Reduced-order models for geometrically nonlinear vibrations of thin structures

Yichang Shen

To cite this version:

Yichang Shen. Reduced-order models for geometrically nonlinear vibrations of thin structures. Vibrations [physics.class-ph]. Institut Polytechnique de Paris, 2021. English. NNT : 2021IPPAE012 . tel-03352699

HAL Id: tel-03352699
https://theses.hal.science/tel-03352699

Submitted on 23 Sep 2021

INSTITUT
POLYTECHNIQUE
DE PARIS

NNT : 2021IPPAE012

Thèse de doctorat

Reduced-order models for geometrically nonlinear vibrations of thin structures

Thèse de doctorat de l'Institut Polytechnique de Paris
préparée à l'École nationale supérieure de techniques avancées

École doctorale n°626 École doctorale de l'Institut Polytechnique de Paris (EDIPP)
Spécialité de doctorat: Ingénierie, mécanique et énergétique

Thèse présentée et soutenue à Palaiseau, le 16/09/2021, par

YICHANG SHEN

Composition du Jury :

Jean-François Deü Professeur au Conservatoire Nationale des Arts et Métiers	Président
Bruno Cochelin Professeur à l'école centrale marseille	Rapporteur
Évangéline Capiez-Lernout Maitre de conférence à l'université Eiffel	Rapporteur
Arnaud Lazarus Maitre de conférences à Sorbonne Université	Examinateur
Sébastien Baguet Maitre de conférence à l'INSA Lyon	Examinateur
Cyril Touzé Professeur à l'ENSTA Paris	Directeur de thèse
Ting Yu Ingénieur-chercheur à l'EDF lab	Encadrante de thèse
Olivier Thomas Professeur à l'ENSAM Lille	Invité

Acknowledgements

When writing this acknowledgement, the memories of the past three years seem to be vividly in my mind.

First of all, I would like to sincerely thank my supervisor Prof. Cyril Touzé for his generous support and expert guidance over the past 3 years. Even during the time that we need to work remotely, his valuable instruction and help are essential for me to continue this PhD project. During my PhD journey, I learned valuable knowledge thanks to his strong teaching skills, also, his rigorous and efficient work style have set a good example for me.

I also would like to thank the following knowledgeable people whose guidance and helps have proved invaluable to this work (in random order): Prof. Olivier Thomas, Dr. Loic Salle, Prof. Attilio Frangi, Dr. Natacha Béreux, and Dr. Ting Yu. In addition, I would like to thank my friend Dr. Alessandra Vizzaccaro, as this thesis is benefited from our joint work.

In the meantime, I am also very grateful to the jury members, Prof. Bruno Cochelin, Dr. Évangéline Capiez-Lernout, Prof. Jean-François Deü, Dr. Arnaud Lazarus, and Dr. Sébastien Baguet, for spending their precious time on reading my thesis and giving me their recognition and positive comments on my work, also for their questions and suggestions during the defence.

I have had the pleasure to meet so many good colleagues and friends during the last three years when I was in France, their accompany and support mean a lot to me, so thanks to all of them.

Finally, I would like to give special thanks to China Scholarship Council for the full three-year funding supports, also to my parents for their love and support all the time.

Contents

Résumé

Cette thèse s'intéresse aux modèles d'ordre réduit (ROM) pour les vibrations non linéaire géométrique de structures minces.

Les structures minces, comme les poutres, les plaques, les coques, se retrouvent dans de très nombreux domaines applicatifs de l'ingénierie, on peut citer par exemple l'aéronautique [1, 2], les systèmes de production d'énergie comme par exemple les éolienne [3], ou encore les systèmes micro-électro-mécaniques (MEMS) [4, 5]). Dans beaucoup des problèmes cités, la non-linéarité géométrique joue un rôle dont l'importance a tendance à croitre, avec la conception de structures de plus en plus minces et souples, qui peuvent atteindre plus facilement des grandes amplitudes vibratoires. Bien que la réponse non linéaire de telles structures puisse être étudiée expérimentalement, de nombreux efforts sont consacrés à la prédiction de la réponse non linéaire en utilisant la simulation par éléments finis (EF) (*e.g.* [6]). Dans ce cadre-là, le coût de calcul associé est important en particulier à cause de la discrétisation spatiale et temporelle fine qui est requise afin de rendre compte des dynamiques non linéaires observées. Ainsi l'analyse prédictive par le calcul de solutions complètes est quasiment hors de portée, ce qui impose une limitation claire en termes d'analyse et de conception paramétrique. Afin de traiter le problème, on peut transformer le modèle d'ordre complet par des méthodes de réduction de modèle, conduisant à des modèles d'ordre réduit dont la complexité de calcul est moindre, avec l'idée de conserver la même finesse prédictive. Les techniques de réduction sont de plus en plus utilisées de nos jours en tant qu'outil efficace permettant d'accélérer le calcul des modèles éléments finis complets.

Modèle d'ordre réduit

Le but des modèles d'ordre réduit est de pouvoir prédire avec précision les propriétés et caractéristiques non linéaires du modèle complet, avec un modèle beaucoup plus léger, comportant moins d'inconnues, et dont la résolution numérique se fait en un temps de calcul plus rapide et avec des accès mémoire moins gourmands. Concernant l'application de ces techniques aux modèles élément fini, il convient de souligner deux problématiques particulières liées à la mise en équation du problème, et à la variétyé de solutions apparaissant dès qu'une dynamique non linéaire entre en jeu.

Le premier problème est de calculer efficacement les forces internes non linéaires dans la base réduite. A cette fin, il est aussi important de distinguer, au niveau de la technique de réduction, les méthodes appelées intrusives et non-intrusives, qui seront discutées plus en détail dans la section 2.2. Par méthode non-intrusive, nous entendons une méthode de calcul qui utilise les sorties communes de tout code EF standard (commercial) (tel que les calculs statiques par exemple) pour établier le modèle d'ordre réduit. A contrario, une méthode intrusive nécessite que l'utilisateur insère ses propres lignes de calcul au sein du code EF, ce qui nécessite un accès complet à un code ouvert.

Le deuxième problème important est lié à la dynamique non linéaire, qui fait apparaitre des phénomènes tels que des instabilités, des bifurcations, pouvant mener à des solutions quasipériodiques et chaotiques. Ainsi, les modèle d'ordre réduit doivent pouvoir récupérer ces caractéristiques non linéaires. À cette fin, l'optimisation de la base de réduction, qui doit être à la fois de petite taille et conserver les caractéristiques linéaires et non linéaires les plus importantes de la réponse, devient un problème important [7]. En ce qui concerne le type de base impliquée dans les modèles EF, les méthodes de réduction non intrusives peuvent être généralement classées en deux familles. La première famille comprend les méthodes linéaires, comme par exemple la méthode POD [8, 9, 10], la projection de mode linéaire et utilisant la condensation statique [11, 12] avec les coefficients non linéaires calculés par un calcul annexe [13]. Ces méthodes sont les plus utilisées ces dernières années avant le début de cette thèse, en raison de leur facilité de calcul et de leur signification physique claire [14, 15]. La deuxième famille est constituée des méthodes non linéaire, par exemple, la méthode ICE [16, 17, 18, 19, 4] et les dérivées modales (MD) [20, 21].

Mode non linéaire et variétés invariantes

Le concept de modes normaux non linéaires (NNM) est considéré ici comme un excellent outil pour construire des modèles d'ordre réduit. Les NNM ont été introduits pour la première fois dans les années 1960 par Rosenberg [22, 23]. Il offre un cadre conceptuel clair pour comprendre l'organisation de la dynamique dans l'espace des phases et interpréter une large classe de phénomènes dynamiques non linéaires. Bien que de nombreuses définitions différentes des NNM aient été données dans le passé, la plupart d'entre elles partagent des propriétés équivalentes dans un cadre conservatif. Un certain nombre de travaux antérieurs considèrent les NNM comme une famille d'orbites périodiques, ce qui permet de trouver une relation entre la relation amplitude-fréquence et l'organisation des orbites dans l'espace des phases [22, 24]. Une proposition alternative est de considérer une NNM comme une variété invariante dans l'espace des phases, tangente aux espaces propres linéaires près de l'origine [25]. Cette propriété d'invariance de la variété est un point clé dans la perspective de la réduction du modèle, qui garantit que les trajectoires du modèle réduit existeront également pour le système complet.

La principale difficulté concernant le calcul des NNMs pour les problème discrétisés en éléments finis est que le calcul des NNMs pour les modèles de grande taille est coûteux, en particulier pour les non-linéarités distribuées. De plus, toutes les applications antérieures de la méthode considèrent comme point d'entrée le système exprimé dans sa base modale, avec accès à l'ensemble des coefficients de couplage non linéaire modaux, ce qui est la plupart du temps inatteignable en pratique. Au début de cette thèse, il y avait donc un manque identifié dans la littérature pour développer des applications plus directes de techniques basées sur les variétés invariantes pour produire des modèles réduits précis, spécifiquement adapté au cas de la discrétisation par éléments finis. L'un des objectifs de cette thèse était donc d'explorer cette direction de recherche.

Contribution scientifique

Ce manuscrit de thèse est organisée de la manière suivante :

Après ce premier chapitre introductif, un état de l'art sur le calcul des modèles d'ordre réduit est présenté dans la partie I, en insistant sur les connaissances disponibles au début de la thèse. L'accent est délibérément mis sur les structures discrétisées avec la méthode des éléments finis comme cadre d'étude, et la portée est limitée aux non-linéarités géométriques. Les méthodes linéaires et non linéaires sont passées en revue au cours des chapitres 3 et 4.

La partie II présente la première contribution de cette thèse, qui consiste en un analyse poussée de la relation existant entre la méthode de condensation implicite (méthode ICE selon la dénomination anglaise Implicit COndensation and Expansion) et la réduction en utilisant les variétés invariantes du système. PLus précisément, les qualités et limites de la méthode ICE sont analysées en comparant directement avec l'utilisation de variétés invariantes comme référence au calcul de sous-espaces réduits (Chapitre 5). Ensuite, le chapitre 6 s'intéresse à la méthode de réduction utilisant une variété quadratique construite à partir de dérivées modales.

De nouveau, une comparaison aux variétés invariantes est fournie afin de bien en comprendre les intérêts et limites. A titre illustratif, deux exemples sont ensuite présentés. Le premier exemple, de nature académique, est le cas d'une poutre linéaire reposant sur uen fondation élastique non linéaire. Il permet de montrer comment les différents traitements des non-linéarités quadratiques par ces méthodes peuvent affecter les prédictions. Le second exemple est le cas d'une coque sphérique peu profonde à bord libre, dont les vibrations sont modélisées à l'aide des hypothèses cinématiques de von Kármán .

La partie III contient de nombreux exemples numériques permettant d'illustrer le comportement des différentes méthodes de réduction non linéaire, en se focalisant désormais sur le cas des structures discrétisées avec la méthode des éléments finis. Au chapitre 7, trois méthodes de réduction non linéaire pour les poutres minces vibrant avec de grandes amplitudes sont comparées : la méthode ICE, les méthodes utilisant une variété quadratique construite à partir de dérivées modales (et utilisant soit les dérivées modales complètes, soit les dérivées modales statiques), et la méthode de la forme normale, permettant une réduction directe sur les variétés invariantes du système. Les exemples sléectionnés permettent de montrer comment els différentes méthodes sont capables de gérer l'ajout de courbure, une résonance interne 1:1 ou encore la non-liénarité inertielle en utilisant une poutre encastrée-libre. Au chapitre 8, des structures plus complexes (coques) sont étudiées de la même manière. La coque est étudiée avec différentes dimensions, et la prédiction du type de non-linéarité obtenue par différentes méthodes est comparée et étudiée.

La troisième contribution de la thèse est présentée dans la partie IV : l'étude de la forme normale pour un système non linéaire présentant une résonance 1:2 et une non-linéarité cubique. Ce travail conclut d'abord qu'avec une résonance 1:2 dans la réduction de forme normale, de nouveaux termes cubiques apparaissent dans les coordonnées liées aux variétés invariantes, la relation non linéaire entre ces nouvelles coordonnées et les coordonnées physiques sera également affectée (Chapitre 9). Ensuite, au chapitre 10, le calcul a été fait sur le changement de non-linéarité du système au croisement de la divergence due à la présence de la résonance 1:2. La méthode des échelles multiples a été utilisée pour calculer les relation amplitude/fréquence du système conservatif, et le comportement raidissant/assouplissant pour le cas d'un désaccord important et au voisinage de la résonance 1:2 a été étudié. Enfin, la réponse non linéaire des poutres encastrées avec une discrétisation EF au voisinage de la résonance 1:2 est étudiée.

A la fin de la thèse, une conclusion et des discussions sur les travaux futurs permettent de conclure.

Chapter 1

Introduction

This thesis is concerned with the reduced-order models (ROM) for geometrically nonlinear vibration of thin structures.

Thin structures, like beams, plates, shells, have a large range of applications (*e.g.* aircraft [1, 2], wind energy systems [3], micro electro-mechanical systems (MEMS) [4, 5]). In their design procedure, geometric nonlinearity plays an important role because of their large deflection and leads to complicated motions with typical nonlinear phenomena. Although the nonlinear response of such structures can be investigated experimentally, many efforts are devoted to predict the nonlinear response by using finite element (FE) simulation (*e.g.* [6]). Consequently, a large number of expansion functions is needed for the discretization of the structure for obtaining convergence through the Galerkin method [26]. As a consequence, full-order nonlinear analysis of complex structures featuring important nonlinearity is computational expensive, setting a clear limitation in terms of analysis and parametric design. In order to deal with the problem, one can transform the full-order model by reduction methods, leading to a ROM with less computational complexity. ROM techniques become more and more attractive nowadays as an efficient tool to speed up the computation of FE models.

1.1 Reduced-order model

A ROM is generally desired to be able to accurately capture the nonlinear properties and characteristics with only a small approximation error as compared to the full-order model, also, it is needed to be computationally efficient and robust. With regard to building ROM for complex geometrically nonlinear structures with FE discretization, there are two most important issues.

The first issue is to efficiently compute the reduced nonlinear internal forces, and based on the way of doing this, ROM techniques for FE discretization are generally divided into two groups: intrusive and non-intrusive methods, which will be discussed in Section 2.2. By non-intrusive method, we mean a computational method which uses the common outputs of any standard (commercial) FE package (such as static computations) to derive the ROM. On the other hand, an intrusive method needs the user to insert his own computation at the elementary level, such that a full access to the code is needed.

The second important issue is that in the nonlinear dynamics stage, one can observe nonlinear dynamical phenomenon like instabilities, bifurcations, arising more complex dynamics including quasiperiodic solutions, chaotic solutions and even wave turbulence. Thus the ROMs need to be able to retrieve these nonlinear features. For that purpose, optimization of the reduction basis, which is required to be both of limited size and convey the most important linear and nonlinear features of the response, becomes a significant problem [7]. With regard to the type of basis involved in FE models, the non-intrusive reduction methods can be generally classified into two families. The first family is the methods with linear basis, for example, the POD method [8, 9, 10], the projection of linear mode and using static condensation [11, 12] with the nonlinear coefficients computed by STiffness Evaluation Procedure (STEP) [13]. These methods are much more used in the past years before the start of this thesis, because of their ease of computation and their clear physical meaning [14, 15]. The second family is the methods with nonlinear mapping, for instance, the ICE method [16, 17, 18, 19, 4] and modal derivatives (MD) [20, 21]. However, recently it is found that deriving a nonlinear manifold can give a better representation of the dynamics instead of adding new vectors in the basis, such that it is worth investigating further about their theoretical foundation and their advantages and disadvantages.

1.2 Nonlinear normal mode and invariant manifold methods

The concept of nonlinear normal modes (NNMs) is considered here as an excellent tool for building ROM. NNMs have been first introduced in the 1960s by Rosenberg in order to deal with numerous vibratory problems [22, 23]. It offers a sound conceptual framework in order to understand the organization of the dynamics in the phase space and interpreting a wide class of nonlinear dynamical phenomena. Although many different definitions of NNMs have been given in the past, most of them share equivalent properties in a conservative framework. A number of previous work consider NNMs as a family of periodic orbits, which allows one to find a relationship between the backbone curve and the organization of orbits in phase space [22, 24]. An alternative proposal is to consider an NNM as an invariant manifold in phase space, tangent at the linear eigenspaces near the origin [25]. This invariance property of the manifold is a key point in the perspective of model reduction, which ensures the trajectories of the ROM will also exist for the full system.

The main difficulty of generating NNMs for FE problem is that the calculation of NNMs for large-scale models is expensive, particularly for distributed nonlinearities, and the reason lies in the fact that application of the method as it was presented in [27, 25, 28] needs as input the nonlinear modal coupling coefficients. This difficulty impedes a large application of such methods for FE problem such that at the start of this PhD, most of the examples in the literature dealt with simplified structural models defined by a partial differential equation. Three years ago, there was thus an identified lack in the literature to develop more direct applications of invariant-based techniques to produce accurate ROMs for FE structure. One of the objective of this thesis was thus to investigate this research direction.

1.3 Outline and scientific contribution

This thesis is organized as follows:

After this introductory Chapter 1, the state of the art in the computation of ROMs for geometrically nonlinear structures is surveyed in Part I. A special focus on the ROM with the geometrical nonlinear FE structures (Chapter 2) and the methods with the linear modal basis for the reduction of nonlinear systems are subsequently introduced (Chapter 3) with a clamped plate example. At last, the reduction methods with nonlinear mapping are reviewed (Chapter 4).

Part II presents the first contribution of the thesis, that is to analyse the relationship between the stress manifold produced by the implicit condensation and expansion (ICE) method and the invariant manifolds defining NNMs (Chapter 5), also the relationship between quadratic manifold built from modal derivatives and the direct normal form approach (Chapter 6), thus, to assess the quality and merits of each method in producing efficient ROMs for geometrically nonlinear structures. For illustrative reason, two examples are subsequently shown, the methods were first compared on an academic, analytical example, a linear beam resting on a nonlinear elastic foundation, in order to analyze how the different treatments of quadratic nonlinearities by these methods can affect the predictions. Then, A free-edge shallow shell modelled with von Kármán assumption is investigated for extending the conclusion to a more complex structure. All these achievements will help the scholars or engineers, who want to build the ROMs for their problem, to know the advantage and drawbacks of each method and to select the methods they will use.

Part III contains numerous numerical examples for illustrating the assessment and comparison of the nonlinear reduction methods and lead to the second contribution that offers a more complete picture of the advantages and drawbacks of each method and validate the theoretical comparison results among the reduction methods. In Chapter 7, three nonlinear reduction methods for thin beam structures vibrating with large amplitudes were compared: the ICE method, the quadratic manifold (QM) methods using either full modal derivatives (MDs) or only static modal derivatives (SMDs), and the direct normal form (DNF) method. The FE-based beam examples were selected in order to emphasize the ability of the methods to handle curvature (on a curved beam), 1:1 internal resonance (on a clamped-clamped beam with two polarizations), and inertia nonlinearity (on a cantilever beam). In Chapter 8, more complex structures (shells) have been investigated in the same manner. The shell is studied with different dimensions, and the prediction of the type of nonlinearity obtained by different methods are compared and investigated.

The third contribution of the thesis is shown in Part IV: the investigation of normal form for nonlinear system with 1:2 resonance and cubic nonlinearity. This work first concludes that with 1:2 resonance in the normal form reduction, extra new cubic terms will come up in the coordinates that are linked to the invariant manifolds, also the nonlinear relation between these new coordinates and the physical coordinates will be affected (Chapter 9). Then, In Chapter 10, the computation has been done on the change of nonlinearity of the system at the cross of 1:2 divergence. The multiple scales method has been employed for computing the backbone curves of the conservative system, and the hardening/softening behaviour for the case of large detuning and in the vicinity of 1:2 resonance have been researched respectively. Finally, the nonlinear response of the clamped-clamped beams with FE discretization in the neighbourhood of 1:2 internal resonance is investigated, and the detuning between the resonant modes is parametrized by changing the extent of curvature.

At the end of the thesis, a conclusion and discussions of future works will be given.

Part I

State of art

Chapter 2

Reduced-order model with nonlinear finite element model

2.1 Nonlinear finite element model

Thin structures experiencing large displacements are considered, so that geometrical nonlinearities are excited. The usual framework assumes also small strains and a linear behaviour law, so that the relationship between the second Piola Kirchhoff stress tensor $\mathbf{S}$ and the the Green-Lagrange strain tensor $\mathbf{G}$ reads, following the Saint-Venant Kirchhoff law [29, 30] :

$$\mathbf{S} = \mathbf{A} : \mathbf{G}, \quad \text{with} \quad \mathbf{G} = \frac{1}{2}\left(\nabla \mathbf{u} + \nabla^t \mathbf{u} + \nabla \mathbf{u} \cdot \nabla^t \mathbf{u}\right), \tag{2.1.1}$$

where $\mathbf{A}$ is the tensor of constant stiffness terms describing the material law, and $\mathbf{u}$ the three-dimensional displacement. The weak form is then written in the reference configuration and reads:

$$\int_{\Omega_0} \rho \ddot{\mathbf{u}} \cdot \mathbf{w} \mathrm{d}\Omega + \int_{\Omega_0} \mathbf{P} : \nabla^t \mathbf{w} \mathrm{d}\Omega = \int_{\Omega_0} \rho \hat{\mathbf{F}} \cdot \mathbf{w} \mathrm{d}\Omega + \int_{\mathcal{S}_0} \mathbf{f} \cdot \mathbf{w} \mathrm{d}\mathcal{S}, \quad \forall\, \mathbf{w} \in \mathcal{C}^0, \tag{2.1.2}$$

where $\mathbf{w}$ is a continuous test function, $\mathbf{P}$ is the first Piola-Kirchhoff stress tensor, $\mathbf{P} = (1 + \nabla \mathbf{u}) \cdot \mathbf{S}$, ρ is the density in the reference configuration, and $\rho \hat{\mathbf{F}}$ and $\mathbf{f}$ are respectively volumic and surface external forces exerted on the body occupying the domain Ω_0 with boundary surface $\mathcal{S}_0$.

Most of the developments in this thesis are concerned with a space discretization relying on the finite element (FE) procedure. In that context, the equivalent semi-discrete, finite dimensional expression of Eq. (2.1.2), generally reads:

$$\mathbf{M}\ddot{\mathbf{q}} + \mathbf{K}\mathbf{q} + \hat{\mathbf{\Gamma}}(\mathbf{q}) = \mathbf{F}, \tag{2.1.3}$$

with $\mathbf{q}$ the vector of generalized displacements (displacements at the nodes) with dimension N, $\mathbf{M}$ the mass matrix, $\mathbf{K}$ the tangent stiffness matrix, $\hat{\mathbf{\Gamma}}(\mathbf{q})$ representing the nonlinear restoring force and $\mathbf{F}$ the external forces. It can be shown in particular that in the context of geometrically nonlinear structures, the nonlinear part of the stiffness $\hat{\mathbf{\Gamma}}(\mathbf{q})$ is polynomial, more precisely, with 3D element the nonlinear restoring force contains only quadratic and cubic terms [31, 32], and for shell/plate elements, it is possible to have higher order terms due to the extra physical assumptions.

The linear modal basis is defined by the vectors ϕ_i such that

$$\mathbf{K}\phi_i = \omega_i^2 \mathbf{M}\phi_i. \tag{2.1.4}$$

In the modal basis, the equations of motion can be rewritten, using the linear change of coordinates $\mathbf{q} = \mathbf{P}_\phi \mathbf{X}$, with $\mathbf{P}_\phi$ the matrix of eigenvectors and $\mathbf{X}$ the modal coordinates :

$$\ddot{X}_p + \omega_p^2 X_p + \sum_{i=1}^{N}\sum_{j\geq i}^{N} g_{ij}^p X_i X_j + \sum_{i=1}^{N}\sum_{j\geq i}^{N}\sum_{k\geq j}^{N} h_{ijk}^p X_i X_j X_k = \tilde{F}_p, \quad \forall p = 1, ..., N. \tag{2.1.5}$$

with $\tilde{\mathbf{F}} = \mathbf{P}_\phi^t \mathbf{F}$ the vector of modal forcings, g_{ij}^p and h_{ijk}^p the quadratic and cubic nonlinear modal coupling coefficients.

The main problem when using the FE approach is that the nonlinear coupling coefficients are *a priori* not available, and require an additional direct or indirect method to obtain them [31, 32, 33]. Also, the number of modes can be prohibitively large to derive reduced-order models, as underlined in *e.g.* [12, 11]. Consequently, ad-hoc methods are proposed in the literature in order to overcome these problems and directly propose reduced-order models with a limited number of selected coordinates and number of coupling coefficients to compute.

2.2 Non-intrusive/intrusive methods

Based on the method of computing the reduced nonlinear internal forces, nonlinear ROM techniques for FE structures are generally classified into indirect and direct methods, also called non-intrusive and intrusive method.

The intrusive methods are the methods that can be used in any standard FE code (even commercial FE packages) with its already existing capacities in order to build a ROM [31], this is because the nonlinear restoring forces are computed without entering inside the programs at the elementary level and generally by a direct projection of the full-order equations to a reduced eigenspace by using a prescribed reduction basis. On the other hand, when applying a direct method, one needs to enter inside the program to write new lines of computation in order to obtain the needed quantities to build ROMs, however, this may be difficult for most commercial FE software since the complete access to the code is not available.

The following Fig. 2.2.1 shows the classification of the reduction methods and only the non-intrusive methods were considered throughout this work. As shown in the figure, one can divide roughly the reduction techniques proposed in the literature into two different categories: the first one use the linear change of coordinates and is reviewed in Section 3, while the second family with nonlinear mappings is discussed in Section 4.

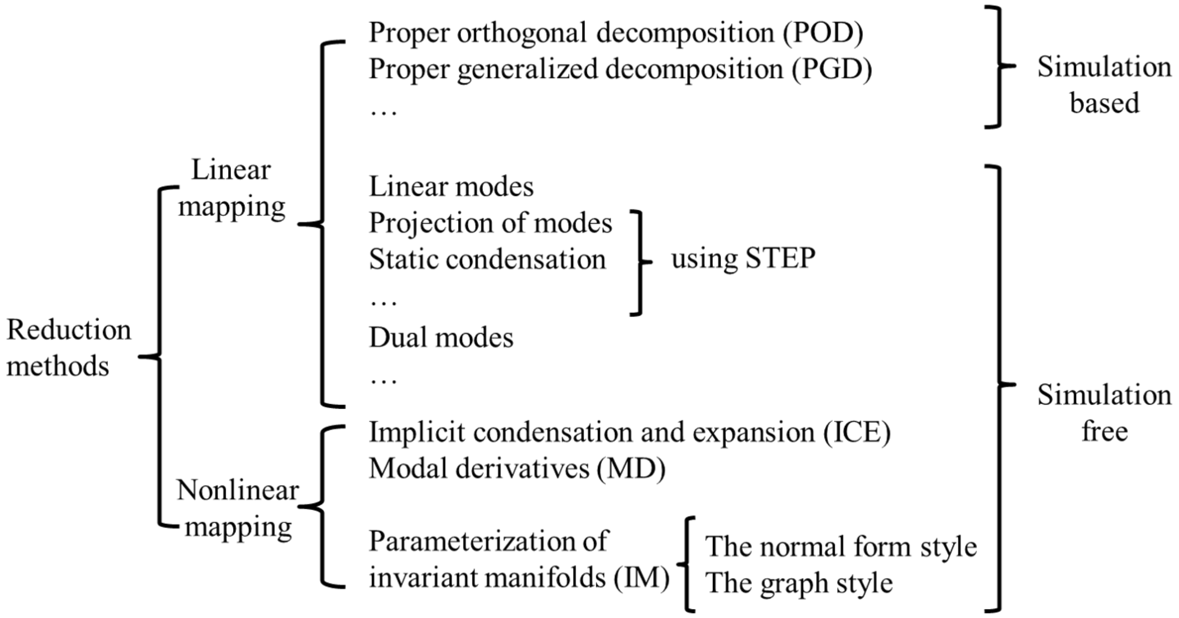

Figure 2.2.1: The classification of the reduction methods.

Chapter 3

Non-intrusive reduction methods with linear mapping

In the past decades, numerous methods have been proposed that rely on a linear change of coordinates. They can be roughly divided into two groups: Simulation-based methods and simulation-free methods.

3.1 Simulation-based methods

Many reduction methods share the common points that simulations of the full, high dimensional system are run in a first step, of which the results are analysed in a second step to build the reduced basis for the nonlinear system, such kind of methods are so-called simulation-based method. One of the most widely used simulation-based methods is the Proper Orthogonal Decomposition (POD) [8, 9, 10], which is a multivariate statistical method that aims at obtaining a compact representation of the data. The POD method optimally extracts the spatial information necessary to characterize the spatio-temporal complexity and inherent dimension of a system, from a set of temporal snapshots of the response, gathered from either numerical simulations or experimental data. The key idea of the POD is to reduce a large number of interdependent variables to a much smaller number of uncorrelated variables while retaining as much as possible of the variation in the original variables. An orthogonal transformation to the basis of the eigenvectors of the sample covariance matrix is performed, and the data are projected onto the subspace spanned by the eigenvectors corresponding to the largest eigenvalues. The most beneficial characteristic of the POD is that it optimally minimizes the average squared distance between the original signal and its reduced linear representation.

There are also other simulation-based methods, like Proper Generalized Decomposition (PGD) method [34, 35] and so on. However, these methods share the same drawback that they need a full order simulation at the first step, which may be difficult when dealing with the system in a very large number of degree of freedoms.

Among all the reduction methods with linear mapping, except for simulation-based methods, there are also simulation-free methods that based on using linear mapping, for example, the simple projection of the modes and static condensation. These methods have the advantage that full-order modal analysis is not needed when developing ROMs, instead, one has to compute the nonlinear coupling coefficients, which are shown in Eq. (2.1.5), of all the modes on the modal basis. For that purpose, one widely used approach is the STiffness Evaluation Procedure (STEP).

3.2 Stiffness evaluation procedure

The STiffness Evaluation Procedure (STEP) was first proposed by Muravyov and Rizzi [13]. In the method, selected static displacements are prescribed to the FE model, the FE procedure then computes the required reaction forces induced by the statically assigned displacements and the nonlinear coefficients are obtained by solving a set of linear equations given by the input displacements and output nonlinear restoring forces. It should be noted that STEP is generally seen as a non-intrusive procedure for computing the nonlinear coefficients of the FE model.

Now the procedure is given as follows. The total restoring force $\boldsymbol{F}_T$ in physical coordinates is given by the summation of nonlinear nodal restoring force and linear restoring force as:

$$\boldsymbol{F}_T = \boldsymbol{F}_L + \boldsymbol{F}_{NL} = \boldsymbol{K}\boldsymbol{q}_c + \hat{\boldsymbol{\Gamma}}(\boldsymbol{q}_c). \tag{3.2.1}$$

By prescribing nodal displacement $\boldsymbol{q}_c$ as the input, the total nodal force $\boldsymbol{F}_T$ in the nonlinear static solution (which could be directly solved by FE software) and the linear force $\boldsymbol{F}_L = \boldsymbol{K}\boldsymbol{q}_c$ in the linear static solution could be solved, thus, the nonlinear nodal force $\boldsymbol{F}_{NL}$ is determined by:

$$\boldsymbol{F}_{NL} = \boldsymbol{F}_T - \boldsymbol{F}_L = \boldsymbol{\Phi}^T\boldsymbol{\Gamma}(\boldsymbol{q}_c), \tag{3.2.2}$$

the nonlinear nodal force $\boldsymbol{F}_{NL}$ for rth mode could also be expressed as

$$F_{NL}^{r}=\sum_{i=1}^{N}\sum_{j=i}^{N}g_{ij}^{r}X_iX_j+\sum_{i=1}^{N}\sum_{j=i}^{N}\sum_{k=j}^{N}h_{ijk}^{r}X_iX_jX_k.\ r=1,2,...,N. \tag{3.2.3}$$

To illustrate the technique, one can begin by prescribing the displacement fields from each single generalized coordinate while all other coordinates are zero

$$\boldsymbol{q}_c=\boldsymbol{\phi}_iX_i \quad \text{and} \quad \boldsymbol{q}_c=-\boldsymbol{\phi}_iX_i. \tag{3.2.4}$$

The nonlinear nodal force contributions F_{NL}^{r} are determined by using Eq. (3.2.2), these may be written in modal coordinates as

$$\begin{aligned}\hat{\boldsymbol{F}}_{NL_1}&=\boldsymbol{\Phi}^T\boldsymbol{F}_{NL_1}=\boldsymbol{\Phi}^T\boldsymbol{\Gamma}(\boldsymbol{\phi}_iX_i)=[g_{ii}^{r}]X_i^2+[h_{iii}^{r}]X_i^3,\\ \hat{\boldsymbol{F}}_{NL_2}&=\boldsymbol{\Phi}^T\boldsymbol{F}_{NL_2}=\boldsymbol{\Phi}^T\boldsymbol{\Gamma}(-\boldsymbol{\phi}_iX_i)=[g_{ii}^{r}]X_i^2-[h_{iii}^{r}]X_i^3.\end{aligned} \tag{3.2.5}$$

Note that the other nonlinear terms do not appear in equation (3.2.5) since $X_j=0$ for $j\neq i$. All the stiffness coefficients corresponding to only one mode can be determined , *i.e.*, g_{ii}^{r} and $h_{iii}^{r}, r=1,2,...,N$. Then, prescribing the displacement fields as:

$$\boldsymbol{q}_c=\boldsymbol{\phi}_iX_i+\boldsymbol{\phi}_jX_j,\ \boldsymbol{q}_c=-\boldsymbol{\phi}_iX_i-\boldsymbol{\phi}_jX_j \quad \text{and} \quad \boldsymbol{q}_c=\boldsymbol{\phi}_iX_i-\boldsymbol{\phi}_jX_j,\ j>i, \tag{3.2.6}$$

results in the following equations

$$\begin{aligned}\hat{\boldsymbol{F}}_{NL_1}&=\boldsymbol{\Phi}^T\boldsymbol{\Gamma}(\boldsymbol{\phi}_iX_i+\boldsymbol{\phi}_jX_j),\\ \hat{\boldsymbol{F}}_{NL_2}&=\boldsymbol{\Phi}^T\boldsymbol{\Gamma}(-\boldsymbol{\phi}_iX_i-\boldsymbol{\phi}_jX_j),\\ \hat{\boldsymbol{F}}_{NL_3}&=\boldsymbol{\Phi}^T\boldsymbol{\Gamma}(\boldsymbol{\phi}_iX_i-\boldsymbol{\phi}_jX_j).\end{aligned} \tag{3.2.7}$$

Summing the $\hat{F}_{NL_1}$ and $\hat{F}_{NL_2}$, subtracting $\hat{F}_{NL_1}$ and $\hat{F}_{NL_3}$, subtracting $\hat{F}_{NL_2}$ and $\hat{F}_{NL_3}$ respectively, results in

$$\begin{aligned}\hat{F}_{NL_1}^{r}+\hat{F}_{NL_2}^{r}&=2g_{ii}^{r}X_i^2+2g_{jj}^{r}X_j^2+2g_{ij}^{r}X_iX_j,\\ \hat{F}_{NL_1}^{r}-\hat{F}_{NL_3}^{r}&=2h_{jjj}^{r}X_j^3+2g_{ij}^{r}X_iX_j+2h_{iij}^{r}X_i^2X_j,\\ \hat{F}_{NL_2}^{r}-\hat{F}_{NL_3}^{r}&=-2h_{iii}^{r}X_i^3-2g_{ij}^{r}X_iX_j-2h_{ijj}^{r}X_iX_j^2,\end{aligned} \tag{3.2.8}$$

from above equations, all coefficients of the type g_{ij}^{r}, h_{ijj}^{r} and $h_{iij}^{r}, j>i, r=1,2,...,N$ can be found. For the case of coefficients with three unequal lower indices, *i.e.* h_{ijk}^{r}, can be determined by prescribing the displacement field

$$\boldsymbol{q}_c=\boldsymbol{\phi}_iX_i+\boldsymbol{\phi}_jX_j+\boldsymbol{\phi}_kX_k,\ k>j>i, \tag{3.2.9}$$

and resulting equation

$$\begin{aligned}\hat{\boldsymbol{F}}_{NL} =&\boldsymbol{\Phi}^T\boldsymbol{\Gamma}(\boldsymbol{\phi}_iX_i + \boldsymbol{\phi}_jX_j + \boldsymbol{\phi}_kX_k)\\ =&[g^r_{ii}]X_i^2 + [g^r_{jj}]X_j^2 + [g^r_{kk}]X_k^2 + [g^r_{ij}]X_iX_j + [g^r_{ik}]X_iX_k + [g^r_{jk}]X_jX_k\\ &+ [h^r_{iii}]X_i^3 + [h^r_{jjj}]X_j^3 + [h^r_{kkk}]X_k^3 + [h^r_{ijj}]X_iX_j^2 + [h^r_{ikk}]X_iX_k^2 + [h^r_{jkk}]X_jX_k^2\\ &+ [h^r_{iij}]X_i^2X_j + [h^r_{iik}]X_i^2X_k + [h^r_{jjk}]X_j^2X_k + [h^r_{ijk}]X_iX_jX_k.\end{aligned} \tag{3.2.10}$$

In Eq. (3.2.10), $h^r_{ijk}, r = 1, 2, ..., N$ can be found in this manner because all the other types of coefficients have already been solved. In practice, for using the STEP, these values for $\boldsymbol{q}_c$ must be large enough to trigger geometric nonlinearity in the system, but not too large, in order to avoid the convergence problem of the solution in the FE model and excitation of large rotation, thus, X_i should be properly chosen when applying the STEP. A detailed study on the selection of X_i had been presented in [12], shows that the solution of coefficients is converged when $0.0001h < max\,|\boldsymbol{\phi}_i|\,X_i < 1h$, and it is recommanded that X_i are chosen as 1/20 of the thickness of the investigated structures:

$$max\,|\boldsymbol{\phi}_i|\,X_i \approx \frac{1}{20}h. \tag{3.2.11}$$

To compute the nonlinear coefficients with this STEP for the number of N modes, Eqs. (3.2.4), (3.2.6) and (3.2.9) indicate the number of different displacements needed as the inputs in the STEP, thus, the total number of operations could be computed by

$$OP_s = 2N + 3\begin{pmatrix} N \\ 2 \end{pmatrix} + \begin{pmatrix} N \\ 3 \end{pmatrix}, \tag{3.2.12}$$

where the binomial coefficients is

$$\begin{pmatrix} n \\ k \end{pmatrix} = \frac{n!}{k!(n-k)!}. \tag{3.2.13}$$

3.3 STEP with tangent stiffness matrix

The STEP is an important computation tool for building ROM in the framework of the linear eigenspace and attracts much attention from the academics and industry. There are contributions proposed for optimizing the STEP in order to speed up the calculation for obtaining the nonlinear coupling coefficients.

One of the enhanced STEP, which computes the nonlinear coefficients with a tangent stiffness matrix, is proposed in [36] and introduced here. For the FE model, in which the nonlinear model is developed, the tangent stiffness matrix could be released out of a nonlinear static analysis by the FE package. The tangent stiffness matrix of the full-order model from a nonlinear static solution is then mapped into the reduced space of generalized coordinates using the previously defined reduction basis, *i.e.*, by prescribing nodal displacement $\boldsymbol{q}_c$ as the input,

$$\hat{\boldsymbol{K}}^t(X) = \boldsymbol{\Phi}^T \boldsymbol{K}^t(\boldsymbol{q}_c)\boldsymbol{\Phi}, \tag{3.3.1}$$

where $\hat{\boldsymbol{K}}^t$ and $\boldsymbol{K}^t$ are the tangent stiffness matrices for the modal space and model FE degree of freedom space, respectively. The tangent stiffness matrix is the Jacobian of the nonlinear restoring force vector with respect to generalized coordinates, given by

$$\hat{\boldsymbol{K}}^t = \boldsymbol{J}_{F_T}(X) = \begin{bmatrix} \frac{\partial F_T^1}{X_1} & \cdots & \frac{\partial F_T^1}{X_N} \\ \vdots & \ddots & \vdots \\ \frac{\partial F_T^N}{X_1} & \cdots & \frac{\partial F_T^N}{X_N} \end{bmatrix}, \tag{3.3.2}$$

where F_T^r is given by

$$F_T^r = F_L^r + F_{NL}^r = \omega_r^2 X_r + \sum_{i=1}^{N}\sum_{j=i}^{N} g_{ij}^r X_i X_j + \sum_{i=1}^{N}\sum_{j=i}^{N}\sum_{k=j}^{N} h_{ijk}^r X_i X_j X_k, \tag{3.3.3}$$

and the (r, n) component of tangent stiffness matrix is given by

$$\begin{aligned} \hat{K}_{(r,n)}^t = \frac{\partial F_T^r}{\partial X_n} &= \frac{\partial}{\partial X_n}[\omega_r^2 X_r + \sum_{i=1}^{N}\sum_{j=i}^{N} g_{ij}^r X_i X_j + \sum_{i=1}^{N}\sum_{j=i}^{N}\sum_{k=j}^{N} h_{ijk}^r X_i X_j X_k] \\ &= \omega_r^2 \delta_{rn} + \sum_{j=1}^{n-1} g_{jn}^r X_j + 2g_{nn}^r X_n + \sum_{j=n+1}^{N} g_{nj}^r X_j \\ &+ 2\sum_{j=1}^{n-1} h_{jnn}^r X_n X_j + 2\sum_{j=n+1}^{N} h_{nnj}^r X_n X_j + \sum_{j=1}^{n-1} h_{jjn}^r X_j^2 + \sum_{j=n+1}^{N} h_{njj}^r X_j^2 + 3h_{nnn}^r X_n^2 \\ &+ \sum_{j=1}^{n-1}\sum_{k=j}^{n-1} h_{jkn}^r X_j X_k + \sum_{j=1}^{n-1}\sum_{k=n+1}^{N} h_{jnk}^r X_j X_k + \sum_{j=n+1}^{N}\sum_{k=j}^{N} h_{njk}^r X_j X_k. \end{aligned} \tag{3.3.4}$$

When prescribing the displacement fields from each single generalized coordinate while all other coordinates are zero:

$$\boldsymbol{q}_c = \boldsymbol{\phi}_i X_i, \tag{3.3.5}$$

such that in Eq. (3.3.4), $X_j = 0$ for $j \neq i$, thus, one can rewrite Eq. (3.3.4) as:

$$\begin{aligned} \hat{K}^t_{(r,n)} &= \omega_r^2 \delta_{rn} + g^r_{ni} X_i + h^r_{nii} X_i^2,\ i > n, \\ \hat{K}^t_{(r,n)} &= \omega_r^2 \delta_{rn} + 2 g^r_{ii} X_i + 3 h^r_{iii} X_i^2,\ i = n, \\ \hat{K}^t_{(r,n)} &= \omega_r^2 \delta_{rn} + g^r_{in} X_i + h^r_{iin} X_i^2,\ i < n. \end{aligned} \tag{3.3.6}$$

Repeat the last step with $\boldsymbol{q}_c = -\boldsymbol{\phi}_i X_i$, Eqs. (3.3.6) would change to

$$\begin{aligned} \hat{K}^t_{(r,n)} &= \omega_r^2 \delta_{rn} - g^r_{ni} X_i + h^r_{nii} X_i^2,\ i > n, \\ \hat{K}^t_{(r,n)} &= \omega_r^2 \delta_{rn} - 2 g^r_{ii} X_i + 3 h^r_{iii} X_i^2,\ i = n, \\ \hat{K}^t_{(r,n)} &= \omega_r^2 \delta_{rn} - g^r_{in} X_i + h^r_{iin} X_i^2,\ i < n. \end{aligned} \tag{3.3.7}$$

By considering the simultaneous formulas (3.3.6) and (3.3.7), all the coefficient corresponding to no more than two modes could be solved. Then, the prescribed displacement fields read:

$$\boldsymbol{q}_c = \boldsymbol{\phi}_i X_i + \boldsymbol{\phi}_j X_j,\ j > i, \tag{3.3.8}$$

such that in Eq. (3.3.4), only two generalized coordinates will not be zero, *i.e.* $X_i \neq 0, X_j \neq 0$. Specifically, for $n > j > i$, one has

$$\hat{K}^t_{(r,n)} = \omega_r^2 \delta_{rn} + g^r_{in} X_i + g^r_{jn} X_j + h^r_{iin} X_i^2 + h^r_{jjn} X_j^2 + h^r_{ijn} X_i X_j. \tag{3.3.9}$$

The above equation could be used to determine cubic terms like h^r_{ijn}. To compute the nonlinear coefficients with tangent stiffness matrix for the number of N modes, from Eqs. (3.3.5) and (3.3.8), the total number of operations could be computed by

$$OP_t = 2N + \begin{pmatrix} N \\ 2 \end{pmatrix}. \tag{3.3.10}$$

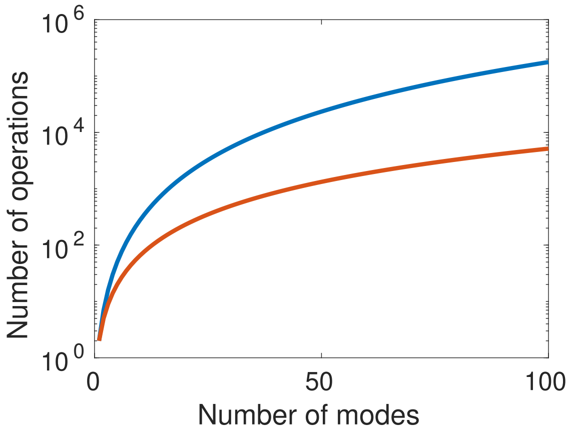

Figure 3.3.1: The relationship between the number of operations and the size of modal basis for the original version of STEP (blue) and STEP with tangent stiffness matrix (red).

Fig. 3.3.1 shows the comparison on the number of operation needed for using ordinary STEP and STEP with tangent stiffness matrix, with different size of modal basis. As compared to the ordinary STEP, it is shown that smaller number of operation are required by using STEP with tangent stiffness matrix for computing coefficients, especially when large number of modes is involved. It should be noted that the STEP with tangent stiffness matrix takes more time in each operation in the FE model, but it can significantly reduce time and storage cost when calculating a large number of coefficients.

Tab. 3.3.1 shows the computation times with different number of modes by the two procedures on a simply supported rectangular plate meshed with 2D DKT elements for 441 nodes. The computation is run by Code_Aster [37] on the 12-core processor computer with 16 GB of RAM and CPU @ 2.20GHz. It is shown that the ordinary STEP is more appealing when a small number of modes are involved in the modal basis, and in the context of computing coefficients with a large number of modes , it is suggested to using the STEP with tangent stiffness matrix.

Procedure	Number of modes		
	10 modes	15 modes	20 modes
STEP	1.5 minutes	6 minutes	76 minutes
STEP-TSM	4 minutes	11 minutes	28 minutes

Table 3.3.1: The time for computing the nonlinear coefficients by applying STEP or STEP with tangent stiffness matrix (STEP-TSM).

There are also many other kinds of STEP that have been proposed, for example the E-STEP [38]. Relying on STEP, many methods, which give the optimal approximating linear manifold in the configuration space, are frequently applied to nonlinear problems. The linear nature of the methods are appealing because the theory of linear operators is available, but it also exhibits its major limitation that it may fail to retrieve most of the nonlinear phenomenons with even a large modal basis [39]. In the next section, an application of a circular plate is shown for giving a more illustrative view of these reduction methods with linear mapping.

3.4 Example: Application to a clamped circular plate

In order to better illustrate the reduction methods on linear modal basis, the case of a clamped circular plate was first investigated by the author of the thesis in [11] and recalled here. The plate has a radius $R = 0.3$ m, a thickness $h = 0.005$m, and the material properties are: density $\rho = 7800$ kg/m^3, Young's modulus $E = 210$ GPa and Poisson ratio $v = 0.3$. For computing all the modes and applying the different proposed methodologies, a coarse mesh is chosen. The plate is discretized with 540 HEX20 elements on the face and 2 HEX20 elements in the thickness, with a total of 1931 nodes and 4928 degrees of freedom.

3.4.1 Static condensation

In the plate case with 3D element discretization, the eigenmodes can be separated into two groups. The first group is the bending modes with lower frequencies, and their deformed shapes are dominated by transverse displacements. The second group gathers all the other modes, called non-bending modes, which generally have higher frequencies. The bending coordinates $(m \in \{1, N_B\})$, which are directly excited by the external forcing, can be considered of the order magnitude of a small parameter ϵ: $X_m = o(\epsilon)$, while the non-bending coordinates $(s \in \{N_B + 1, N\})$ are not directly excited and should vibrate at a lower order of magnitude, are assumed to scale as ϵ^2: $P_s = o(\epsilon^2)$. In the context of investigating a flat and symmetric structure (like the plate in this case), one can insert these two scaling into Eq. (2.1.5) with damping C included and keeping only the leading order, and thus obtain the following equation of motion with (a) for the bending modes and (b) for non-bending modes [11]:

$$\ddot{X}_m + \omega_m^2 X_m + C_m \dot{X}_m + \sum_{i=1}^{N_B} \sum_{l=N_B+1}^{N} g_{il}^m X_i P_l + \sum_{i=1}^{N_B} \sum_{j=i}^{N_B} \sum_{k=j}^{N_B} h_{ijk}^m X_i X_j X_k = \tilde{F}_m, \tag{3.4.1a}$$

$$\ddot{P}_s + \omega_s^2 P_s + C_s \dot{P}_s + \sum_{i=1}^{N_B} \sum_{j=i}^{N_B} g_{ij}^s X_i X_j = 0. \tag{3.4.1b}$$

with N the number of dofs and N_B the number of non-bending modes.

In the context where the dynamics are dominated by the bending modes, the static condensation can be applied for generating ROMs. Because the non-bending modes have natural frequencies very large as compared with the excited bending modes, *i.e.* $\omega_s \gg \omega_m$, the dynamical part of Eq. (3.4.1b) can be neglected, and thus, one can directly express the non-bending coordinate as:

$$P_s = -\sum_{i=1}^{N_B} \sum_{j=i}^{N_B} \frac{g_{ij}^s}{\omega_s^2} X_i X_j. \tag{3.4.2}$$

Substituting Eq. (3.4.2) into Eq. (3.4.1a), the nonlinear dynamics of the plate can be rewritten with involving only bending coordinates:

$$\ddot{X}_m + \omega_m^2 X_m + C_m \dot{X}_m + \sum_{i=1}^{N_B} \sum_{j=i}^{N_B} \sum_{k=j}^{N_B} \Upsilon_{ijk}^m X_i X_j X_k = \tilde{F}_m, \tag{3.4.3}$$

where Υ_{ijk}^m read

$$\Upsilon_{ijk}^m = h_{ijk}^m - \sum_{s=NB+1}^{N} \hat{C}_{ijk}^{ms}, \tag{3.4.4}$$

and $\hat{C}_{ijk}^{ms}$ is expressed by:

$$\hat{C}_{ijk}^{ms} = \begin{cases} \frac{g_{is}^m g_{jk}^s + g_{js}^m g_{ik}^s + g_{ks}^m g_{ij}^s}{\omega_s^2}, & i < j < k, \\ \frac{g_{is}^m g_{ik}^s + g_{ks}^m g_{ii}^s}{\omega_s^2}, & i = j < k, \\ \frac{g_{is}^m g_{kk}^s + g_{ks}^m g_{ik}^s}{\omega_s^2}, & i < j = k, \\ \frac{g_{is}^m g_{ii}^s}{\omega_s^2}, & i = j = k. \end{cases} \tag{3.4.5}$$

In this example, a ROM, with modal basis including a single bending mode and all the other non-bending modes, is considered, such that the nonlinear cubic term of Eq. (3.4.4) simply reduces to:

$$\Upsilon_{mmm}^m = h_{mmm}^m - \sum_{s=NB+1}^{N} \hat{C}_{mmm}^{ms}, \tag{3.4.6}$$

where the correction factors now read:

$$\hat{C}^{ms}_{mmm} = \frac{g^m_{ms} g^s_{mm}}{\omega_s^2} = \frac{2(g^s_{mm})^2}{\omega_s^2}. \tag{3.4.7}$$

With the coefficients g^s_{mm} and h^m_{mmm} computed by the STEP, the static condensation technique can be used and building the ROMs with nonlinear dynamics given in Eq. (3.4.3).

3.4.2 Modal coupling

A convergence study on the modal coupling is investigated for the first axisymmetric bending mode (0,1) having no nodal line and one nodal circle, and the first asymmetric (1,0) mode with one nodal line and no nodal circle. The case of the first axisymmetric mode is less complex as compared with the asymmetric mode for symmetry reasons.

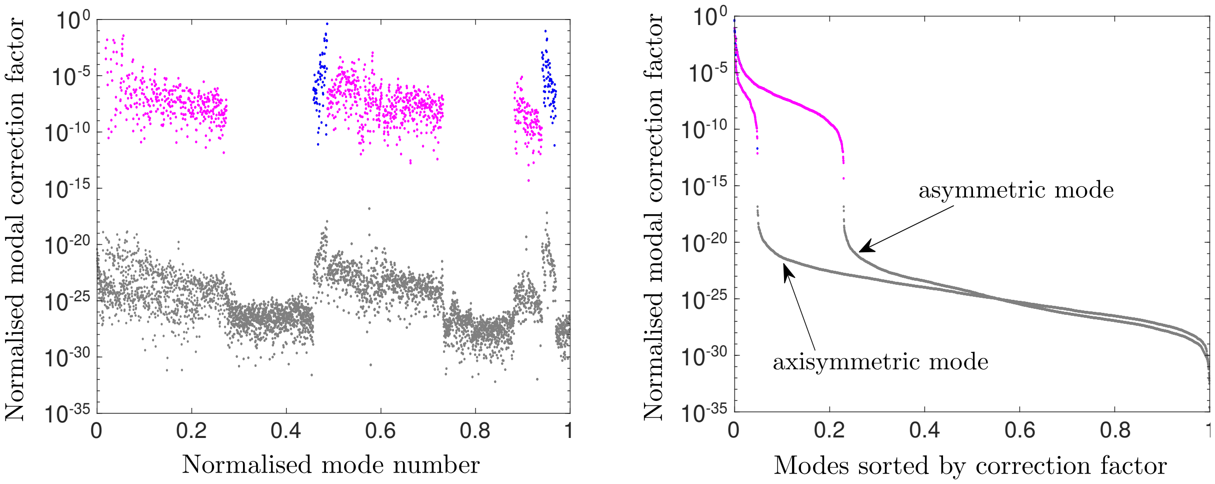

Figure 3.4.1: (a) Normalised modal correction factor for the clamped circular plate, as a function of the normalised mode number (normalization by the number of dofs), for the first asymmetric (1,0) mode of the plate. (b) The correction factors are now sorted by decreasing values, and two cases are shown : the case of the first asymmetric mode, corresponding to sorting (a), and the case of the first axisymmetric mode, showing a faster convergence. Grey points are negligible modes in terms of coupling, magenta points are the important in-plane coupled modes while blue points are the important thickness modes.

Fig. 3.4.1(a) shows the behaviour of the normalised modal correction factor, *i.e.*, the correction factor given in Eq. (3.4.7) normalized by the cubic coefficients h^m_{mmm}, expressed by $2(g^n_{mm}/\omega_n)^2/h^m_{mmm}$, where m refers to the master mode ($m = 1$ is the fundamental axisymmetric (0,1) mode, $m = 2$ is the asymmetric (1,0) mode) and $n \in \{1, N\}$. In Fig. 3.4.1(a) only the case of the first asymmetric mode ($m = 2$) is shown for the sake of brevity, but the trend of first axisymmetric mode was very similar. It is shown that a strong coupling with numerous non-bending modes in high-frequency regime is observed, consequently, the normalised modal correction factors show a very slow convergence. Table 3.4.1 shows the deformed shape of the first nine modes, sorted according to their correction factor, which are thus the most important in the coupling with the bending (1,0) mode. These modes are all in high frequency range, two purely in-plane modes are found in (e) and (h), and all the other ones involve important deformation in the thickness of the plate, and thus called thickness modes, their presence being the direct consequence of 3D effects.

Fig. 3.4.1(b) shows the normalized correction factor now sorted by order of decreasing values, and for the two cases of the axisymmetric fundamental mode and first asymmetric mode. It shows in particular that the convergence on the corrected cubic coefficient is more rapidly achieved for the axisymmetric mode, where less than 10% of the modes are needed. On the other hand, the convergence is more difficult for the first asymmetric mode. Concerning the coupling with high-frequency modes and thickness modes for these two first bending modes, it is interesting to note that the subset of coupled modes is almost exactly the same in the two cases, showing in particular that the coupling with the thickness modes is not very dependent on the selected bending mode. In fact, the two cases investigated here share more than 90% of the same coupled modes.

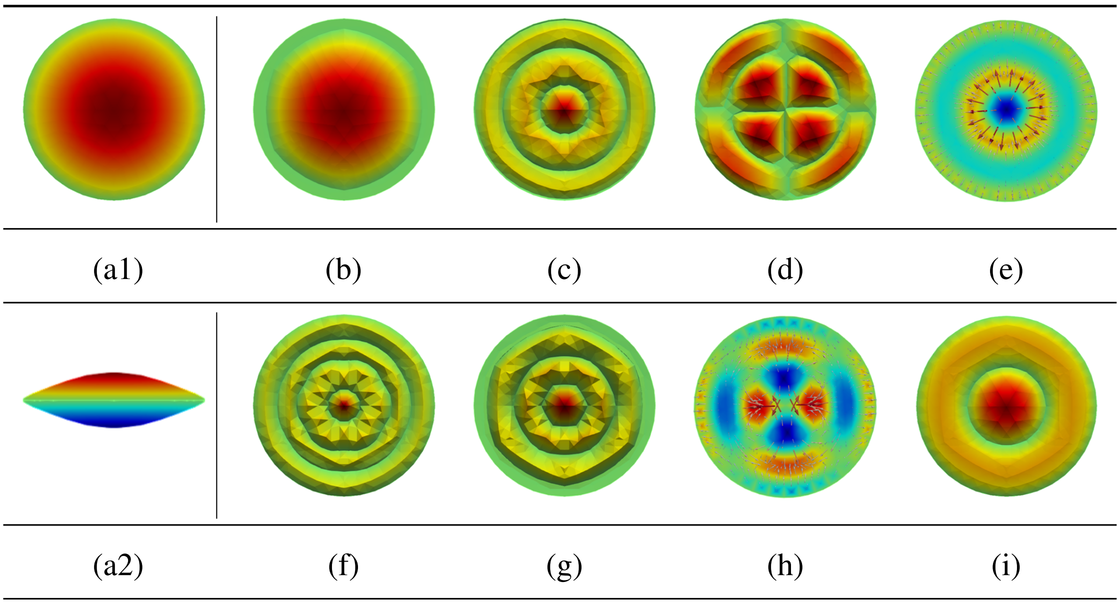

(a1) (b) (c) (d) (e)

(a2) (f) (g) (h) (i)

Table 3.4.1: Mode shapes of the 9 most relevant modes coupled with the first flexural asymmetric (1,0) mode. Only two of them are in-plane modes: (e) and (h), while all the others are thickness modes. (a2) is a side view of the top view (a1) of the first thickness mode, in order to show the strong dependence on thickness deformation.

3.4.3 Results and discussion

	Corrected cubic Coefficients				
	Υ^2_{222}	Υ^4_{222}	Υ^4_{224}	Υ^2_{444}	Υ^4_{444}
M-STEP	6.4763e+10	-2.8539e+09	1.5374e+11	-57.3021	3.8776e+11
Static condensation	6.4762e+10	-2.8535e+09	1.5372e+11	5.3298e+03	3.8775e+11

Table 3.4.2: Corrected cubic coefficient Υ^p_{ijk}, for two flexural modes, *i.e.* $i, j, k, m = 2$ or 4, where 2 refers to the first (1,0) asymmetric mode while 4 refers to the second (2,0) asymmetric mode; anf for two different methods : the modified STEP, and the static condensation where all the coupled modes are statically condensed.

Now we are shortly introducing the modified STEP so called M-STEP [40, 11]. Different from the STEP that imposes displacement to the entire physical subspaces, when applying the

M-STEP, displacements are imposed on selected degrees of freedom only, normally on the middle line/plane of the structures, the idea is to include automatically the effects of non-bending modes (slave modes), by a kind of implicit condensation of their motion, embedded into the prescribed displacement on the middle line/plane. The interested reader can find the formulation and the quality indicator for the convergence of the method in [11].

The numerical results for the corrected cubic coefficient Υ^p_{ijk} are shown in Table 3.4.2, with the expression given in Eq. (3.4.4) with $m = 2$ for the first asymmetric (1,0) mode and $m = 4$ for the second asymmetric (2,0) mode (the bending modes being sorted by increasing frequencies, $m = 1$ is the fundamental axisymmetric (0,1) mode, $m = 2, 3$ for the two configurations of the asymmetric (1,0) mode and $m = 4, 5$ for the second asymmetric (2,0) mode). This choice has been guided by the fact that these two asymmetric modes are coupled [41] and thus cubic nonlinear coefficients are important when deriving a ROM. The two methods presented: M-STEP and static condensation of all the linear modes, give the same results, except for Υ^2_{444} shows a different result for the M-STEP, however the value is very small as compared to the other ones so that this coefficient is negligible.

In the example, we have shown that in the case of 3D elements, a strong coupling with non-bending mode occurred, especially the thickness modes, thus it is difficult to achieve the convergence of the ROM derived by using linear basis. It is also shown that by using simple projection of modes or static condensation, with the coefficient calculated by the STEP, is sometimes really inefficient, also, the computation of all the linear modes, including the thickness modes appearing at very high frequencies, is generally out of reach. The M-STEP works well in this case since it leads to an accurate ROM with only two master coordinates, however, it should be noted that the method has a disadvantage that it only can be used when the structures are flat and symmetry.

This example indicates the difficulty of building ROM by using linear basis, that is the modal basis can be difficult to be determined and has a large size for some cases. On the other hand, reduction methods with nonlinear mapping on phase space will not have such drawback and are reviewed in the next section.

Chapter 4

Reduction methods with nonlinear mapping

4.1 Nonlinear mappings applied to modal equations

In this section, reduction methods applied to modal equations for generating the NNMs are reviewed. The NNMs are defined as invariant manifolds in phase space, which are tangent to their linear counterpart at the origin, aimed at extending the usual linear decomposition to non-linear regimes [42], thus, NNM is a valuable concept for interpreting certain essentially nonlinear dynamic phenomenon that have no counterpart in linear theory and cannot be analysed by linearised methods.

An important advantage of the reduction methods deriving NNMs is that the invariant property is kept during the computation and the trajectories of the ROMs will also exist for the full system [43, 44, 45]. Based on the styles of parametrization [46], these methods for deriving the invariant manifold can be roughly divided into two groups: invariant manifold approach by Shaw and Pierre (the graph style) and the normal form.

4.1.1 Invariant manifold approach by Shaw and Pierre

In this section, we use the definition of NNMs as proposed by Shaw and Pierre [27, 25, 47, 48]. The method relies on the center manifold theorem [49, 50], and allows a clear conceptual definition of an NNM as an invariant manifold in phase space, tangent to the linear eigenspaces at the origin. One of the main advantages of the method is to provide a clear continuation of linear eigenspaces to nonlinear regimes, as well as giving efficient reduced-order subspaces for building ROMs since the key property of invariance is conserved. The drawback is that the solution of the graph style is restricted in amplitude, because the method is not able to go on the possible foldings of the invariant manifolds [46]. The main procedure of applying the method is shown as the following:

For the sake of simplicity, the modal Eq. (2.1.5) can also be rewritten as:

$$\ddot{X}_p + \omega_p^2 X_p + f_p(X_1, X_2, ..., X_N) = \tilde{F}_p, \tag{4.1.1}$$

and the starting point is to put Eq. (4.1.1) in first-order form (dynamical system), for the rth mode:

$$\begin{aligned} \dot{X}_r &= Y_r, \\ \dot{Y}_r &= -\omega_r^2 X_r - f_r(X_1, ..., X_N). \end{aligned} \tag{4.1.2}$$

The invariant manifold is defined by functional relationships a_s and b_s relating the slave coordinates to the master ones by, $\forall\ s\ \in [m+1, N]$:

$$X_s = a_s(X_1, Y_1, ..., X_m, Y_m), \tag{4.1.3a}$$

$$Y_s = b_s(X_1, Y_1, ..., X_m, Y_m), \tag{4.1.3b}$$

where the master coordinates X_μ, Y_μ with $\mu = 1, ..., m$ represent the coordinates in nonlinear reduction basis, and the slave coordinates X_s, Y_s are the coordinates that are coupled with the master ones. Following the guidelines of the center manifold theorem, one arrives at the two following equations, describing the geometry of the $2(N-m)$ dimensional invariant manifold in phase space :

$$\sum_{t=1}^{m} \left(\frac{\partial a_s}{\partial X_t} Y_t + \frac{\partial a_s}{\partial Y_t} \left[-\omega_t^2 X_t - f_t \right] \right) = b_s, \tag{4.1.4a}$$

$$\sum_{t=1}^{m} \left(\frac{\partial b_s}{\partial X_t} Y_t + \frac{\partial b_s}{\partial Y_t} \left[-\omega_t^2 X_t - f_t \right] \right) = -\omega_s^2 a_s - f_s. \tag{4.1.4b}$$

Once the unknown functions a_s and b_s have been obtained, the dynamics of the ROM reads:

$$\forall\ t \in\ [1, m], \quad \ddot{X}_t + \omega_t^2 X_t + f_t(X_1, ..., X_m, a_{m+1}(X_1, Y_1, ..., X_m, Y_m), ..., a_N(X_1, Y_1, ..., X_m, Y_m)) = 0. \tag{4.1.5}$$

4.1.2 Normal form approach

In this section, The NNMs are computed by using the normal form theory, as defined in [51, 52]. The main idea is to define a nonlinear change of coordinates, from the modal coordinates to new ones defined as the normal coordinates. The nonlinear mapping is inherited from Poincaré and Poincaré-Dulac theorems [53, 54], based on the idea of finding out a nonlinear change of coordinate capable of eliminating as much as possible of nonlinear terms. In the best case, when no nonlinear resonance exists, the system can be linearized (Poincaré theorem). When nonlinear resonance is present, some monomials cannot be cancelled and stay in the so-called normal form of the system, obtained after applying the nonlinear change of coordinates (Poincaré-Dulac theorem). In the framework of mechanical systems, explicit computation of the normal form for geometrically nonlinear systems encompassing quadratic and cubic nonlinearities have been provided in [51, 52]. In this section, only the main results are recalled, the interested reader is referred to these publications [51, 52, 55, 56] for more theoretical details.

Normal form theory allows definition of new co-ordinates that describe invariant manifolds, as well as the nonlinear relationship between these new normal coordinates and the initial modal ones. The nonlinear change of coordinates is identity-tangent, at third order, it reads:

$$X_p = R_p + \sum_{i=1}^{N}\sum_{j\geq i}^{N}(a^p_{ij}R_iR_j + b^p_{ij}S_iS_j) + \sum_{i=1}^{N}\sum_{j\geq i}^{N}\sum_{k\geq j}^{N} r^p_{ijk}R_iR_jR_k + \sum_{i=1}^{N}\sum_{j=1}^{N}\sum_{k\geq j}^{N} u^p_{ijk}R_iS_jS_k, \tag{4.1.6a}$$

$$Y_p = S_p + \sum_{i=1}^{N}\sum_{j=1}^{N}\gamma^p_{ij}R_iS_j + \sum_{i=1}^{N}\sum_{j\geq i}^{N}\sum_{k\geq j}^{N} \mu^p_{ijk}S_iS_jS_k + \sum_{i=1}^{N}\sum_{j=1}^{N}\sum_{k\geq j}^{N} \nu^p_{ijk}S_iR_jR_k, \tag{4.1.6b}$$

where N is the number of retained modes in the linear analysis, X_p, Y_p is the modal coordinate and the modal velocity respectively, (R_p, S_p) is the new normal coordinates, and all the coefficients of $r^p_{ijk}, u^p_{ijk}, \gamma^p_{ij}, \mu^p_{ijk}, \nu^p_{ijk}$ are analytic and their expressions are given in [51].

The dynamics in phase space spanned by invariant manifolds is then given, up to the third order, by:

$$
\begin{aligned}
&\forall p = 1, ..., N : \\
&R_p = \dot{S}_p && \text{(4.1.7a)} \\
&S_p = -\omega_p^2 - (A^p_{ppp} + h^p_{ppp})R_p^3 - B^p_{ppp}R_pS_p^2 \\
&- R_p \left[\sum_{j>p}^{N} [(A^p_{jpj} + A^p_{pjj} + h^p_{pjj})R_j^2 + B^p_{pjj}S_j^2] + \sum_{j<p} [(A^p_{iip} + A^p_{pii} + h^p_{iip})R_i^2 + B^p_{pii}S_i^2] \right] \\
&- S_p \left[\sum_{j>p}^{N} B^p_{jpj}R_jS_j + \sum_{j<p} B^p_{iip}R_iS_i \right] . && \text{(4.1.7b)}
\end{aligned}
$$

Coefficients A^p_{ijk}, B^p_{ijk} arise from the cancellation of non-resonant quadratic terms. Now Eqs. (4.1.7) contain the invariance property, and it is possible to truncate the system to a low-dimensional subspace without neglecting interactions.

It should be noted that the method as presented here is limited by the fact that starting point are modal equation, so a direct computation from physical space is needed.

4.2 Methods directly applicable to finite element model

Two non-intrusive methods are shortly reviewed in this section. Different from the methods developing the invariant manifold, the nonlinear mappings derived by these methods do not have the invariance property, they are widely used mainly because they can be directly computed from the FE model. The first one is the implicit condensation and expansion method that leads to the stress manifold, and the second one is the (static) modal derivatives with the quadratic manifold derived.

4.2.1 Implicit condensation and expansion method

The implicit condensation and expansion (ICE) method has been first introduced by McEwan, Gordon and Hollkamp [16, 17, 18, 19], and recently used by Kuether *et al.* [57], and Frangi and Gobat [4]. It is sometimes also called the applied force method (AMF) since it relies on applying a set of selected static forces on the FE model as a first step for deriving the ROM. In the processing using the ICE method, a stress manifold is built from the set of prescribed applied loads [4]. This explains in particular why the coefficients from the ICE method strongly depends on the amplitude of the applied load, since following the curvature of the stress manifold.

Let us briefly recall the main steps needed for deriving the ICE method. The interested reader is referred to [19, 4, 58] for further details. The first step is to impose body forces $\mathbf{Q}$ that are proportional to the inertia of a number of selected linear modes, $\mathbf{Q} = \beta_i \mathbf{M} \phi_i$ in Eq. (2.1.3), with $i = 1...m$, m being the number of master coordinates retained in the ROM. A static problem is then solved with the FE code, and the obtained displacement field is projected onto the eigenmodes in order to get the modal displacements X_p corresponding to the imposed force, for $p = 1...m$. A mapping is thus constructed with entries β_i and outputs X_p. Assuming that the functional relationship is invertible, one obtains $X_p(\beta_i)$, from which the ROM can be built. At the last step, a fitting procedure is executed in order to derive functional forms from the computed clouds of points, to obtain the $\boldsymbol{\beta}(\mathbf{X})$ from the map $\mathbf{X}(\boldsymbol{\beta})$.

The reduced-order dynamics derived by ICE method is m-dimensional and reads:

$$\ddot{\mathbf{X}} + \boldsymbol{\Omega}^2 \mathbf{X} + \mathbf{C}\dot{\mathbf{X}} + \boldsymbol{\beta}(\boldsymbol{X}) = \mathbf{F}, \tag{4.2.1}$$

One main advantage is that the method takes implicitly into account the axial-bending nonlinear coupling that causes geometric nonlinearities, it is thus particularly appealing when working with thin flat structures. The main drawback of the method is the fact that a fitting procedure is needed after the application of the forces in order to get the nonlinear restoring force on the stress manifold. Although this is not problematic when working with a single master coordinates, using of more and more master modes cause difficulty to implement the method in a general m-dimensional case.

4.2.2 Modal derivatives

Modal derivatives have been first introduced in [59] with the idea of accounting for the variation of the eigenmodes with amplitude. In that respect, let us denote as $\tilde{\phi}_i(\mathbf{q})$ the amplitude-dependent eigenvector. The ij-th modal derivative $\boldsymbol{\Theta}_{ij}$ is thus introduced as the derivative of $\tilde{\phi}_i$ with respect to the j-th coordinate used for the reduced basis so that one can write [20, 21, 60, 61]:

$$\boldsymbol{\Theta}_{ij} \doteq \left. \frac{\partial \tilde{\phi}_i(\mathbf{q})}{\partial X_j} \right|_{\mathbf{q}=0}. \tag{4.2.2}$$

In order to derive an explicit problem from which the MD will be solution of, it is convenient to rewrite the eigenvalue system defined in Eq. (2.1.4) and stating the explicit dependence of mode shape and eigenfrequency on amplitude $\mathbf{u}$, thus obtaining:

$$\left(\frac{\partial \boldsymbol{F}(\mathbf{q})}{\partial \mathbf{q}} - \tilde{\omega}_i^2(\mathbf{q})\boldsymbol{M}\right)\tilde{\phi}_i(\mathbf{q}) = \mathbf{0}, \tag{4.2.3}$$

where the tangent stiffness matrix $\mathbf{K}$ has been replaced by the derivative of the full nonlinear restoring force $\mathbf{F}$ with respect to amplitude. Note also that it has been assumed that the mass matrix is not amplitude-dependent. Expanding Eq. (4.2.3) in Taylor series for small vibration, one can observe that the first term will reproduce the usual linear eigenproblem while the next term will make appear the modal derivative $\boldsymbol{\Theta_{ij}}$. Since the frequency dependence on amplitude also appears, a second equation is used to close the problem, and the developments shown in [20, 21, 60] advocate to use the mass normalization equation: $\tilde{\phi}_i^T \mathbf{M} \tilde{\phi}_i = 1$. Expanding also in Taylor series produces a second equation; finally grouping the two gives the system from which one can compute MD as:

$$\begin{bmatrix} \boldsymbol{K} - \omega_i^2 \boldsymbol{M} & -\boldsymbol{M}\phi_i \\ -\phi_i^T \boldsymbol{M} & 0 \end{bmatrix} \begin{Bmatrix} \boldsymbol{\Theta_{ij}} \\ \frac{\partial \omega_i^2}{\partial X_j} \end{Bmatrix} = \begin{Bmatrix} -2\boldsymbol{G}(\phi_j, \phi_i) \\ 0 \end{Bmatrix}. \tag{4.2.4}$$

The solution of Eq. (4.2.4) is generally difficult to obtain because of the singularity of the $\boldsymbol{K} - \omega_i^2 \boldsymbol{M}$ at the eigenmode directions. Also, obtaining all the terms in Eq. (4.2.4) with a FE software is not straightforward since some of them do not correspond to standard operations. Consequently, most of the results one can found in the literature with MD simplify the problem given by Eq. (4.2.4) by neglecting the inertia, thus defining the so-called *static* modal derivatives (SMD), which are the solution of the simpler problem

$$\mathbf{K}\boldsymbol{\Theta_{ij}} = -2\boldsymbol{G}(\phi_j, \phi_i). \tag{4.2.5}$$

As remarked in [20, 21, 61], the computation of this SMD can be performed in a non-intrusive manner with a standard FE code.

The main advantage of MDs, the same as the ICE method, is that it also does not require manual selection of membrane-dominated modes demanded to accurately develop the nonlinear ROM. Instead, the most important nonlinear features of the full-order response are conveyed by non-intrusive MDs, which are systematically derived from the originating vibration modes and are easy to compute. Another advantage, in contrary to the ICE method, is that the MDs are selected in a load-independent manner and render the ROM valid for a range of loading conditions.

Part II

Comparisons and assessments of nonlinear reduction methods

Chapter 5

Comparison of Implicit condensation and invariant manifold

The main idea of this chapter is to propose a comparison between two methods to derive reduced-order models (ROM) for geometrically nonlinear structures. The implicit condensation and expansion (ICE) method relies on a series of applied static loadings, from this set, a stress manifold is constructed for building the ROM. On the other hand, nonlinear normal modes rely on invariant manifold theory in order to keep the key property of invariance for the reduced subspaces. In the course of the development, the problem related to the fitting procedure in the ICE method will be illustrated in the case where a large number of master modes is selected. A simplified procedure, relying on normal form theory and identification of only resonant monomial terms in the nonlinear stiffness, is proposed and contrasted with the current method. All the findings are illustrated on beams and plates examples. These contents have been published as a journal paper, and this Chapter is organized as follows: Section 5.1 recalls the theoretical settings and explains the ICE method and the invariant manifold approach. In particular, it is shown that in the specific case where all the coefficients of the model are fully known, then the ICE method simplifies to the standard static condensation of current use to simplify the high-frequency components of a vibrating structure. From a theoretical point of view, contrasting the two methods is then equivalent to comparing static condensation with NNM-based reduction. It is then shown in a general framework that if one assumes a slow/fast decomposition between the master and slave coordinates, then the static condensation approach reduces to the invariant manifold approach, at the leading order. Section 5.2 confirms these general findings by simplifying to a two degrees-of-freedom (dofs) system, for which explicit analytical expressions can be derived thanks to asymptotic expansions, leading to an accurate term-by-term comparison. Section 5.3 extends the results to the case of continuous structures. Beam examples with plate/shell and three-dimensional elements are tested, as well as a plate with simply supported boundary conditions. In this section, a thorough discussion on the construction of multi-mode ROMs with the ICE method is given, and a proposition in order to reduce the burden of the fitting procedure, is developed. Using normal form theory and the recognition that only resonant monomial terms have a strong influence on the dynamics, it is proposed to fit only these resonant monomials in the nonlinear restoring force.

5.1 Theoretical settings

5.1.1 ICE method and stress manifold

The Implicit Condensation and Expansion (ICE) method [16, 17, 18, 19, 57, 4] has been first introduced in Section 4.2.1, more details are now given in order to draw out more accurate description and comparison. As compared to the STEP method, where a series of static prescribed displacements are used in order to get the values of the modal coupling coefficients g^p_{ij} and h^p_{ijk} given in Eq. (2.1.5), the ICE method relies on a series of applied static forcings. Whereas the STEP method gives a direct access to the modal coupling coefficients, the values obtained with the ICE method are different and depend on the level of applied force and are thus load dependent. This is directly related to the fact that the coordinates used to build ROMs from the ICE method are not the modal coordinates. Instead, a stress manifold is built from the series of applied loads, and new coordinates are used to describe the dynamics onto this manifold. In other words, ICE method allows to directly pass from the physical space (nodes of the FE structure) to the curved stress manifold and the reduced variables describe the dynamics onto this stress manifold; without resorting to an intermediate step where modal coordinates are needed. Since the stress manifold is curved and amplitude-dependent, it is fully logical to obtain coefficients that are load-dependent. On the other hand, if one refers to the STEP applied to eigenmodes, then the computed coupling coefficients should not depend on amplitude since related to planar linear eigensubspaces. This explains why the coefficients from STEP do not depend upon amplitude in the large range where the nonlinearity is correctly excited, see *e.g.* [12] for a quantitative analysis of this behaviour. Using applied forces instead of prescribed displacements allows one to get a better track of how the nonlinear couplings generated by the nonlinear internal force transfer energies between oscillators. But the drawback of the method relies on the fact that a fitting procedure is needed after application of the forces in order to get the nonlinear restoring force on the stress manifold.

The procedure is as follows. First one imposes body forces $\mathbf{F}$ that are proportional to the inertia of the linear modes, $\mathbf{F} = \beta_i \boldsymbol{\phi}_i(\mathbf{x})$ in Eq. (2.1.3), for a selected number i of modes, $i = 1...m$, where m is the number of modes selected in the final ROM. A static problem is then solved and the obtained displacement field is projected onto the eigenmodes in order to get the modal displacements X_p corresponding to the imposed force. A mapping is thus constructed with entries β_i and outputs X_p. Assuming that the functional relationship can be inverted, one obtains $X_p(\beta_i)$, from which the ROM can be built. For this last step, a fitting procedure is needed so as to derive functional forms from the computed clouds of points.

As noted by different authors [19, 57], the method allows to make an *implicit* condensation of the non modeled degrees of freedom. The procedure is thus particularly appealing when working with thin structures, in order to implicitly take into account the axial-bending nonlinear coupling that gives rise to geometric nonlinearities. One may also notice that, in the specific cases of small models where the equations of motion are fully known (*i.e.* if one is able to get the full-model equations as in (2.1.5) for all the degrees of freedom, which is generally out of reach for complex structures meshed with FE), the implicit condensation becomes explicit, so that the method is equivalent to the usual static condensation.

In the context of drawing out a full comparison of ICE method with NNMs, we will first use full models where all coefficients are known, so that ICE method reduces to static condensation. Let us first separate the degrees of freedom of the modal displacement $\mathbf{X}$ between the first m master coordinates $X_1, ..., X_m$, and the remaining slave coordinates $X_{m+1}, ..., X_N$, such that the modal equations (2.1.5) for master coordinates X_t and slave coordinates X_s can be rewritten as:

$$\begin{aligned} \ddot{X}_t + \omega_t^2 X_t + f_t(X_1, X_2, ..., X_N) &= \tilde{F}_t, \\ \ddot{X}_s + \omega_s^2 X_s + f_s(X_1, X_2, ..., X_N) &= \tilde{F}_s. \end{aligned} \tag{5.1.1}$$

Let us also assume that for the slave coordinate $s \in [m+1, N]$, inertia $\ddot{X}_s$ can be neglected. This hypothesis is generally justified by the fact that the slave coordinates correspond to high-frequency modes with fast oscillations. The method then assumes that a functional relationship c_s exists between the master coordinates and the slave coordinates:

$$\forall\, s \in\, [m+1, N], \quad X_s = c_s(X_1, X_2, ..., X_m). \tag{5.1.2}$$

These relationships define the stress manifold in phase space, and only depend on the displacements. The functions c_s are determined from:

$$\forall\, s \in\, [m{+}1, N], \quad \omega_s^2 c_s(X_1, ..., X_m){+}f_s(X_1, ..., X_m, c_{m+1}(X_1, ..., X_m), ..., c_N(X_1, ..., X_m)) = 0, \tag{5.1.3}$$

then, the reduced-order model for the master coordinates reads:

$$\forall\, t \in\, [1, m], \quad \ddot{X}_t + \omega_t^2 X_t + f_t(X_1, ..., X_m, c_{m+1}(X_1, ..., X_m), ..., c_N(X_1, ..., X_m)) = 0. \tag{5.1.4}$$

5.1.2 Invariant manifolds

In this section, the NNMs is parametrized in graph style as proposed by Shaw and Pierre [27, 25, 47, 48], as introduced in Section 4.1.1. The starting point is to put Eq. (5.1.1) in first-order form (dynamical system), for the rth mode:

$$\begin{aligned} \dot{X}_r &= Y_r, \\ \dot{Y}_r &= -\omega_r^2 X_r - f_r(X_1, ..., X_N). \end{aligned} \tag{5.1.5}$$

The invariant manifold is defined by functional relationships a_s and b_s relating the slave coordinates to the master ones by, $\forall\ s\ \in [m+1, N]$:

$$X_s = a_s(X_1, Y_1, ..., X_m, Y_m), \tag{5.1.6a}$$

$$Y_s = b_s(X_1, Y_1, ..., X_m, Y_m). \tag{5.1.6b}$$

From Eqs. (5.1.6), the derivation of X_s, Y_s read as:

$$\begin{aligned} \dot{X}_s &= \sum_{t=1}^{m} \left(\frac{\partial a_s}{\partial X_t} \dot{X}_t + \frac{\partial a_s}{\partial Y_t} \dot{Y}_t \right), \\ \dot{Y}_s &= \sum_{t=1}^{m} \left(\frac{\partial b_s}{\partial X_t} \dot{X}_t + \frac{\partial b_s}{\partial Y_t} \dot{Y}_t \right). \end{aligned} \tag{5.1.7}$$

Such that by following the guidelines of the center manifold theorem, one arrives at the two following equations, describing the geometry of the $2(N-m)$ dimensional invariant manifold in phase space :

$$\sum_{t=1}^{m}\left(\frac{\partial a_s}{\partial X_t}Y_t+\frac{\partial a_s}{\partial Y_t}\left[-\omega_t^2X_t-f_t\right]\right) = b_s, \tag{5.1.8a}$$

$$\sum_{t=1}^{m}\left(\frac{\partial b_s}{\partial X_t}Y_t+\frac{\partial b_s}{\partial Y_t}\left[-\omega_t^2X_t-f_t\right]\right) = -\omega_s^2a_s-f_s. \tag{5.1.8b}$$

The solutions of these partial differential equations are generally difficult to obtain. No analytical solutions exist and the early developments proposed asymptotic expansions in order to compute the first nonlinear dependences of invariant manifolds upon amplitudes [27, 25, 47, 48]. Numerical methods have also been formulated to get effective ROMs based on invariant manifolds up to very large amplitudes [28, 62, 63, 64]. Whatever the method, once the unknown functions a_s and b_s have been obtained, the dynamics of the ROM reads:

$$\forall\, t\in\,[1,m],\quad \ddot{X}_t+\omega_t^2X_t+f_t(X_1,...,X_m,a_{m+1}(X_1,Y_1,...,X_m,Y_m),...,a_N(X_1,Y_1,...,X_m,Y_m))=0. \tag{5.1.9}$$

One can note that the static condensation and invariant manifold approaches share similarities in the way reduced-order models are derived. However, this general presentation shows that the invariant manifold approach appears to be more general. Indeed, whereas static condensation works out only on displacements, the invariant manifold approach includes also the velocities as independent variables, so that two unknown functions are to be found, each of which depending on two master coordinates. Furthermore, no assumption on neglecting any inertia is introduced when computing the NNMs. This suggests that the two methods should have similarities only in the case where a clear slow/fast decomposition (defined in the next section) holds between slave and master coordinates, and that the stress manifold would not be able to take into account internal resonance relationship, a key feature in nonlinear vibrations. Finally, the NNM approach allows conserving the key property of invariance for the reduced subspaces, an attribute that is not embedded in the stress manifold.

5.1.3 Slow/fast decomposition

Let us assume that a slow/fast decomposition of the system is at hand, which means that the slave coordinates X_s, for $s\in[m+1,N]$, have a radian eigenfrequency ω_s which is much larger than those of the master coordinates X_t, for $t \in [1,m]$: $\omega_s \gg \omega_t$. In order to take the assumption into account in the equations of motion, one can introduce a small parameter ε and scale the linear and nonlinear restoring forces of the slave variables by $1/\varepsilon$ in order to express the fact that the slave coordinates are much more stiff and thus corresponds to fast oscillations. Therefore the dynamics of the system (5.1.1) without external forcing, can be rewritten as:

$$\forall\, t \in [1,m], \quad \ddot{X}_t + \omega_t^2 X_t + f_t(X_1, X_2, ..., X_N) = 0, \tag{5.1.10a}$$

$$\forall\, s \in [m+1,N], \quad \ddot{X}_s + \frac{1}{\varepsilon}\omega_s^2 X_s + \frac{1}{\varepsilon} f_s(X_1, X_2, ..., X_N) = 0. \tag{5.1.10b}$$

With this formulation, Eq. (5.1.10b) justifies the assumption of neglecting the inertia of the fast variable so that one arrives easily at Eq. (5.1.3) allowing the computation of the stress manifold.

The equations describing the geometry of the invariant manifold, Eqs. (5.1.8), rewritten with the slow/fast assumption, read:

$$\sum_{t=1}^{m} \left(\frac{\partial a_s}{\partial X_t} Y_t + \frac{\partial a_s}{\partial Y_t} \left[-\omega_t^2 X_t - f_t \right] \right) = b_s, \tag{5.1.11a}$$

$$\sum_{t=1}^{m} \left(\frac{\partial b_s}{\partial X_t} Y_t + \frac{\partial b_s}{\partial Y_t} \left[-\omega_t^2 X_t - f_t \right] \right) = -\frac{1}{\varepsilon}\omega_s^2 a_s - \frac{1}{\varepsilon} f_s. \tag{5.1.11b}$$

Eq. (5.1.11b) shows that thanks to the slow/fast assumption, a_s is, at first order, solution of the following, obtained by neglecting the ε terms:

$$\forall\, s \in [m+1,N], \quad \omega_s^2 a_s(X_1, Y_1, ..., X_m, Y_m) + f_s\left(X_1, ..., X_m, a_{m+1}, ..., a_N\right) = 0. \tag{5.1.12}$$

This equation is completely equivalent to Eq. (5.1.3), showing that with the slow/fast assumption, the function a_s shall thus tend to the c_s obtained with the static condensation, the only difference being the dependence on the velocities of a_s, that is not assumed for the c_s functions. Based on this observation, one can also assume that the a_s, as being solutions of the same problem as the c_s, will not depend on the velocities, so that $\forall\, t \in [1,m]$, $\partial a_s / \partial Y_t = 0$. Reporting this in Eq. (5.1.11a) shows that a simple relationship should hold between a_s and b_s as:

$$b_s = \sum_{t=1}^{m} \frac{\partial a_s}{\partial X_t} Y_t. \tag{5.1.13}$$

All these relationships shows that static condensation and invariant manifolds should propose equivalent results when a slow/fast decomposition of the system can be assumed. However, if the slave modes are not stiff as compared to the master, then the ICE method should be used with care, and a better approach is to use invariant manifolds in order to propose efficient ROMs.

5.1.4 Type of nonlinearity

In this section, we compare how both methods allow predicting the type of nonlinearity, defined as the hardening/softening dependence of the oscillation frequency upon amplitude. Indeed, the ability of a method to correctly predict the backbone curve of a nonlinear oscillator is key, and reduced-order models need to be able to give a correct prediction at least to the first order. For that purpose, let us assume that a single master coordinate, labelled p, is retained, all other coordinates for $s \neq p$ belonging to the slave variables. The reduced-order model will then consist of a single oscillator equation from which one can derive the type of nonlinearity. Also, the leading order term that dictates the hardening/softening behaviour can be found from a perturbative solution where the single nonlinear oscillator equation is truncated to the cubic order [14, 51]. Consequently the general equations describing the stress manifolds, the invariant manifolds, and the dynamics within them, can be truncated up to order three.

In the case of the static condensation, one has to solve Eq. (5.1.2) up to quadratic term only since, when replacing in Eq. (5.1.4), the slave coordinates are at least of second order. The first-order term for Eq. (5.1.2) is easy to derive and one can write immediately, for all $s \neq p$

$$X_s = c_s(X_p) \simeq -\frac{g^s_{pp}}{\omega_s^2} X_p^2 + \mathcal{O}(X_p^3). \tag{5.1.14}$$

Consequently the dynamics of the master mode on the stress manifold reads

$$\ddot{X}_p + \omega_p^2 X_p + g^p_{pp} X_p^2 + \left(h^p_{ppp} - \sum_{\substack{s=1 \\ s\neq p}}^{N} \frac{g^p_{ps} g^s_{pp}}{\omega_s^2} \right) X_p^3 + \mathcal{O}(X_p^4) = 0 \tag{5.1.15}$$

The frequency-amplitude relationship can be derived from this equation by a perturbative approach, see *e.g.* [14, 51]. One arrives at the following generic formula

$$\omega_{\text{NL}} = \omega_p \left(1 + \Gamma^p_{[M]} a^2 \right), \tag{5.1.16}$$

where ω_{NL} is the nonlinear frequency, depending on amplitude a, and $\Gamma^p_{[M]}$ is a coefficient dictating the type of nonlinearity (hardening oscillator for $\Gamma^p_{[M]} > 0$, softening for $\Gamma^p_{[M]} < 0$) with $[M]$ refers to the method (SC, IM). Applying the first-order formula from a perturbation method to Eq. (5.1.15), the type of nonlinearity for the static condensation approximation Γ^p_{SC} reads

$$\Gamma^p_{\text{SC}} = \frac{1}{8\omega_p^2} \left(3h^p_{ppp} - \frac{10(g^p_{pp})^2}{3\omega_p^2} - \sum_{\substack{s=1 \\ s\neq p}}^{N} \frac{3 g^p_{ps} g^s_{pp}}{\omega_s^2} \right). \tag{5.1.17}$$

In the case of the invariant manifold approach, Eqs. (5.1.6) can be rewritten with the assumption of a single master NNM, for all $s \neq p$, and up to the second order:

$$X_s = a_s(X_p, Y_p) = A^p_{s,1} X_p^2 + A^p_{s,2} X_p Y_p + A^p_{s,3} Y_p^2, \tag{5.1.18a}$$

$$Y_s = b_s(X_p, Y_p) = A^p_{s,4} X_p^2 + A^p_{s,5} X_p Y_p + A^p_{s,6} Y_p^2. \tag{5.1.18b}$$

where the individual expressions of the coefficients can be found in [25, 48, 65], and read:

$$A^p_{s,1} = \frac{(\omega_s^2 - 2\omega_p^2)}{\omega_s^2(4\omega_p^2 - \omega_s^2)} g^s_{pp}, \tag{5.1.19a}$$

$$A^p_{s,3} = \frac{-2}{\omega_s^2(4\omega_p^2 - \omega_s^2)} g^s_{pp}, \tag{5.1.19b}$$

$$A^p_{s,5} = \frac{2}{4\omega_p^2 - \omega_s^2} g^s_{pp}, \tag{5.1.19c}$$

$$A^p_{s,2} = A^p_{s,4} = A^p_{s,6} = 0. \tag{5.1.19d}$$

Consequently the reduced-order dynamics writes

$$\ddot{X}_p + \omega_p^2 X_p + g^p_{pp} X_p^2 + \left(h^p_{ppp} + \sum_{\substack{s=1 \\ s\neq p}}^{N} g^p_{ps} A^p_{s,1} \right) X_p^3 + \left(\sum_{\substack{s=1 \\ s\neq p}}^{N} g^p_{ps} A^p_{s,3} \right) X_p Y_p^2 = 0, \tag{5.1.20}$$

and the type of nonlinearity is dictated by Γ^p_{IM} (where IM stands for invariant manifold):

$$\Gamma^p_{\mathrm{IM}} = \frac{1}{8\omega_p^2} \left(3h^p_{ppp} - \frac{10(g^p_{pp})^2}{3\omega_p^2} - \sum_{\substack{s=1 \\ s\neq p}}^{N} \frac{3\omega_s^2 - 8\omega_p^2}{\omega_s^2 - 4\omega_p^2} \frac{g^p_{ps} g^s_{pp}}{\omega_s^2} \right). \tag{5.1.21}$$

Comparing the two predictions given by Eqs. (5.1.17) and (5.1.21), one can observe that the only difference relies in the summed term, taking into account the important contributions of the slave modes to the type of nonlinearity. Interestingly, one can notice that under the slow/fast assumption, if for all s, $\omega_s \gg \omega_p$, then the asymptotic value of Γ^p_{IM} is equal to Γ^p_{SC}. More precisely, assuming that a single slave mode s is present in order to decompose their contributions, the ratio R between the summed terms appearing in (5.1.17) and (5.1.21) simply writes

$$R = \frac{\omega_s^2 - \frac{8}{3}\omega_p^2}{\omega_s^2 - 4\omega_p^2} = \frac{\rho^2 - \frac{8}{3}}{\rho^2 - 4}, \tag{5.1.22}$$

where the ratio $\rho = \omega_s/\omega_p$ has been introduced. Fig. 5.1.1 shows the variations of R as a function of ρ. Firstly, as noted in previous articles, the formula obtained from the invariant

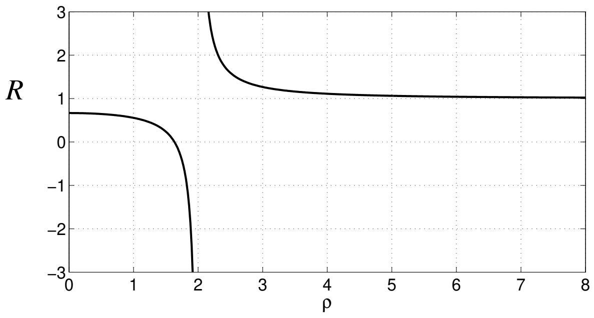

Figure 5.1.1: Correction factor R defined in Eq. (5.1.22) as a function of $\rho = \omega_s/\omega_p$ the ratio between the eigenfrequencies of the slave mode s and the master mode p. From this figure, one can conclude that the static condensation gives a correct prediction on the type of nonlinearity when $\omega_s > 6\omega_p$.

manifold approach is correct, mainly because the reduction subspace is a NNM having the property of invariance embedded in its definition, so that trajectories simulated in the reduced subspace also exist for the complete system. Consequently Fig. 5.1.1 shows how the prediction given by static condensation diverge from the correct prediction when R is different to 1. One can observe that the static condensation does not take into account 2:1 internal resonance. In this region, when $\rho \simeq 2$, a strong coupling between the two modes exist and it becomes meaningless to define Γ since no single-mode motions exist anymore [51].

From Fig.5.1.1, a quantitative criterion can be derived in order to set the minimal frequency gap between master and slave eigenfrequencies such that ICE method could be applied safely. One can observe that with static condensation 10% of error is predicted when $\omega_s > 4\omega_p$, and 4% of error when $\omega_s > 6\omega_p$. Of course this is not meant to be understood as a strict lower bound. A quantified rule of thumb can be stated as: eigenfrequencies of the slave modes should be six times large than those of the master.

5.2 Slow/fast decomposition in a two dofs system

In this section, we first begin by giving more insights to the general formulas. By restricting on a two dofs system and using asymptotic expansions to derive the first terms of the solution of the invariant manifold and the static condensation, one can realize a term-by-term comparison and contrast the similarities between the two methods.

5.2.1 Asymptotic expansions

Restricting to two degrees of freedom, the initial system simply writes:

$$\begin{aligned} \ddot{X}_1 + \omega_1^2 X_1 + f_1(X_1, X_2) = 0, \\ \ddot{X}_2 + \omega_2^2 X_2 + f_2(X_1, X_2) = 0, \end{aligned} \tag{5.2.1}$$

where $f_p(X_1, X_2)$ are the nonlinear internal force for $p = 1,\ 2$, which are of the polynomial type with quadratic and cubic terms so that their general expressions read:

$$f_p(X_1, X_2) = g_{11}^p X_1^2 + g_{12}^p X_1 X_2 + g_{22}^p X_2^2 + h_{111}^p X_1^3 + h_{112}^p X_1^2 X_2 + h_{122}^p X_1 X_2^2 + h_{222}^p X_2^3. \tag{5.2.2}$$

Let us assume that X_1 is the master coordinate and X_2 the slave. Applying static condensation, one looks for a relationship $X_2 = c(X_1)$, where c is solution of Eq. (5.1.3) which can be rewritten here as:

$$\omega_2^2 c(X_1) + g_{11}^2 X_1^2 + g_{12}^2 X_1 c(X_1) + g_{22}^2 c(X_1)^2 + h_{111}^2 X_1^3 + h_{112}^2 X_1^2 c(X_1) + h_{122}^2 X_1 c(X_1)^2 + h_{222}^2 c(X_1)^3 = 0. \tag{5.2.3}$$

The solution for c can be found based on an asymptotic expansion:

$$X_2 = c(X_1) = k_2 X_1^2 + k_3 X_1^3 + k_4 X_1^4 + ... + k_9 X^9 + \mathcal{O}(X^9), \tag{5.2.4}$$

which is stopped here at order 9 but no maximal order of the polynomial expansion can be inferred from Eq. (5.2.4) which produces new order each time the expansion for c is pushed further. Term-by-term identification of the coefficients of same power gives a direct analytical solution for the k_i coefficients introduced in (5.2.4). The quadratic and cubic coefficients read:

$$k_2 = \frac{-g_{11}^2}{\omega_2^2}, \tag{5.2.5a}$$

$$k_3 = \frac{-h_{111}^2 \omega_2^2 + g_{12}^2 g_{11}^2}{\omega_2^4}, \tag{5.2.5b}$$

$$k_4 = (-g_{11}^2 (g_{12}^2)^2 - (g_{11}^2)^2 g_{22}^2 + g_{12}^2 h_{111}^2 \omega_2^2 + g_{11}^2 h_{112}^2 \omega_2^2)/\omega_2^6, \tag{5.2.5c}$$

$$\begin{aligned} k_5 = &(g_{11}^2 (g_{12}^2)^3 + 3(g_{11}^2)^2 g_{12}^2 g_{22}^2 - (g_{12}^2)^2 h_{111}^2 \omega_2^2 - 2 g_{11}^2 g_{22}^2 h_{111}^2 \omega_2^2 - 2 g_{11}^2 g_{12}^2 h_{112}^2 \omega_2^2 \\ &- (g_{11}^2)^2 h_{122}^2 \omega_2^2 + h_{111}^2 h_{112}^2 \omega_2^4)/\omega_2^8, \end{aligned} \tag{5.2.5d}$$

while the other k_6 to k_9 coefficients are too complexed, are thus given in Appendix A.

For the invariant manifolds, general expressions for the coefficients of the asymptotic expansions have already been derived in [25, 48, 65]. The two unknown functions describing the geometry of the invariant manifold can be written up to order three as:

$$X_2 = a_2(X_1, Y_1) = A^1_{11}X_1^2 + A^1_{12}X_1Y_1 + A^1_{22}Y_1^2 + B^1_{111}X_1^3 + B^1_{112}X_1^2Y_1 + B^1_{122}X_1Y_1^2 + B^1_{222}Y_1^3, \tag{5.2.6a}$$

$$Y_2 = b_2(X_1, Y_1) = A^2_{11}X_1^2 + A^2_{12}X_1Y_1 + A^2_{22}Y_1^2 + B^2_{111}X_1^3 + B^2_{112}X_1^2Y_1 + B^2_{122}X_1Y_1^2 + B^2_{222}Y_1^3. \tag{5.2.6b}$$

where the general expressions for the quadratic terms and the cubic coefficients can be derived from Eqs. (5.1.19), with the full expressions read:

$$A^1_{11} = \frac{(\omega_2^2 - 2\omega_1^2)}{\omega_2^2(4\omega_1^2 - \omega_2^2)} g^2_{11}, \tag{5.2.7a}$$

$$A^1_{22} = \frac{-2}{\omega_2^2(4\omega_1^2 - \omega_2^2)} g^2_{11}, \tag{5.2.7b}$$

$$A^2_{12} = \frac{2}{4\omega_1^2 - \omega_2^2} g^2_{11}, \tag{5.2.7c}$$

$$A^1_{12} = A^2_{11} = A^2_{22} = 0, \tag{5.2.7d}$$

while the cubic coefficients of the invariant manifold asymptotic expansion write:

$$B^1_{111} = \frac{\omega_2^2(4\omega_1^2 - \omega_2^2)(7\omega_1^2 - \omega_2^2)h^2_{111} + (9\omega_1^2\omega_2^2 - 18\omega_1^4 - \omega_2^4)g^2_{11}g^2_{12} + (2\omega_2^4 - 12\omega_1^4 - 10\omega_1^2\omega_2^2)g^1_{11}g^2_{11}}{\omega_2^2(4\omega_1^2 - \omega_2^2)(\omega_2^2 - \omega_1^2)(\omega_2^2 - 9\omega_1^2)}, \tag{5.2.8}$$

$$B^1_{122} = \frac{6\omega_2^2(4\omega_1^2 - \omega_2^2)h^2_{111} + (8\omega_2^2 - 18\omega_1^2)g^2_{11}g^2_{12} - 20\omega_2^2 g^1_{11}g^2_{11}}{\omega_2^2(4\omega_1^2 - \omega_2^2)(\omega_2^2 - \omega_1^2)(\omega_2^2 - 9\omega_1^2)}, \tag{5.2.9}$$

$$B^2_{112} = \frac{3\omega_2^2(4\omega_1^2 - \omega_2^2)(3\omega_1^2 - \omega_2^2)h^2_{111} + (11\omega_1^2\omega_2^2 - 3\omega_2^4 - 18\omega_1^4)g^2_{11}g^2_{12} - 10\omega_2^2(3\omega_1^2 - \omega_2^2)g^1_{11}g^2_{11}}{\omega_2^2(4\omega_1^2 - \omega_2^2)(\omega_2^2 - \omega_1^2)(\omega_2^2 - 9\omega_1^2)}, \tag{5.2.10}$$

$$B^2_{222} = B^1_{122}, \tag{5.2.11}$$

$$B^2_{111} = B^2_{122} = B^1_{112} = B^1_{222} = 0. \tag{5.2.12}$$

Higher-order terms can also be found for the invariant manifold approach but their derivation leads to difficult and lengthy expressions needing for a symbolic computation processor. Comparing the expressions up to order three, one can observe that the coefficients $A^1_{11}, A^1_{22}, A^2_{12}$ derived from the invariant manifold approach show singularities when internal resonances exist between the eigenfrequencies ($\omega_2 \approx 2\omega_1$), also $B^1_{111}, B^1_{122}, B^2_{112}, B^2_{222}$ show singularities when $\omega_2 \approx \omega_1$, $\omega_2 \approx 2\omega_1$, and $\omega_2 \approx 3\omega_1$, and this feature, *i.e.*, the singularity of the coefficients, is not expressed in the static condensation. In the next section we will show how a slow/fast assumption reveals the similarities between the two approaches.

5.2.2 Slow-fast decomposition

The general expressions given in the previous section can be simplified and directly compared if one assumes that a slow/fast decomposition is at hand between the two degrees of freedom of the system, *i.e.* if $\omega_2 \gg \omega_1$. All expansions are also compared up to the third-order for consistency. The geometry of the stress manifold as given by the ICE method is obtained from Eq. (5.2.4) up to cubic terms and reads:

$$X_2 = c(X_1) = \frac{-g^2_{11}}{\omega_2^2} X_1^2 + \frac{-h^2_{111}\omega_2^2 + g^2_{12} g^2_{11}}{\omega_2^4} X_1^3 \tag{5.2.13}$$

The dependence on the eigenfrequencies is much more pronounced in the expressions giving the geometry of the invariant manifold in phase space, as a consequence that the inertia of the slave coordinate is not abruptly neglected. Assuming a slow/fast decomposition, *i.e.* $\omega_2 \gg \omega_1$ for this two-dofs system, we give here the limited values of all the coefficients A^p_{ij} and B^p_{ijk} $(i, j, k, p = 1, 2)$ appearing in Eqs. (5.2.6). We begin with the quadratic coefficients A^p_{ij}:

$$A^1_{11} \xrightarrow{\omega_2 \gg \omega_1} -\frac{g^2_{11}}{\omega_2^2}, \tag{5.2.14a}$$

$$A^1_{22} \xrightarrow{\omega_2 \gg \omega_1} \frac{2g^2_{11}}{\omega_2^4}, \tag{5.2.14b}$$

$$A^1_{12} \xrightarrow{\omega_2 \gg \omega_1} -\frac{2g^2_{11}}{\omega_2^2}, \tag{5.2.14c}$$

$$A^1_{12} = A^2_{11} = A^2_{22} = 0. \tag{5.2.14d}$$

For the cubic coefficients we have :

$$B^1_{111} \xrightarrow{\omega_2 \gg \omega_1} \frac{-\omega_2^2 h^2_{111} + g^2_{11} g^2_{12} - 2g^1_{11} g^2_{11}}{\omega_2^4}, \tag{5.2.15a}$$

$$B^1_{122} \xrightarrow{\omega_2 \gg \omega_1} \frac{6\omega_2^2 h^2_{111} - 8g^2_{11} g^2_{12} + 20g^1_{11} g^2_{11}}{\omega_2^6}, \tag{5.2.15b}$$

$$B^2_{112} \xrightarrow{\omega_2 \gg \omega_1} \frac{-3\omega_2^2 h^2_{111} + 3g^2_{11} g^2_{12} - 10g^1_{11} g^2_{11}}{\omega_2^4}, \tag{5.2.15c}$$

$$B^2_{222} = B^1_{122}, \tag{5.2.15d}$$

$$B^2_{111} = B^2_{122} = B^1_{112} = B^1_{222} = 0. \tag{5.2.15e}$$

Consequently the nonlinear relationships between slave and master coordinates simplifies to :

$$X_2 = \frac{-g^2_{11}}{\omega_2^2} X_1^2 + \frac{2g^2_{11}}{\omega_2^4} Y_1^2 + \frac{-\omega_2^2 h^2_{111} + g^2_{12} g^2_{11} - 2g^1_{11} g^2_{11}}{\omega_2^4} X_1^3 + \frac{6\omega_2^2 h^2_{111} - 8g^2_{11} g^2_{12} + 20g^1_{11} g^2_{11}}{\omega_2^6} X_1 Y_1^2, \tag{5.2.16a}$$

$$Y_2 = -\frac{2g^2_{11}}{\omega_2^2} X_1 Y_1 + \frac{-3\omega_2^2 h^2_{111} + 3g^2_{11} g^2_{12} - 10g^1_{11} g^2_{11}}{\omega_2^4} X_1^2 Y_1 + \frac{6\omega_2^2 h^2_{111} - 8g^2_{11} g^2_{12} + 20g^1_{11} g^2_{11}}{\omega_2^6} Y_1^3. \tag{5.2.16b}$$

Now comparing Eqs. (5.2.13) with (5.2.16a), one can see that the quadratic terms in X_1^2 are the same. As announced, no dependence on the velocity master variable Y_1 exists for the stress manifold, however this dependence is proportional to $1/\omega_2^4$ in (5.2.16a) for the quadratic term in Y_1^2, and can thus be considered as negligible as compared to the term in X_1^2, scaling as $1/\omega_2^2$. For the cubic term in X_1^3, one can see that the coefficient is almost the same in the two expressions. Rewriting the difference in the last two terms in the X_1^3 coefficient in (5.2.16a) as $g^2_{11}(g^2_{12} - 2g^1_{11})$, and recalling that the slow/fast assumption should also hold for the nonlinear stiffness so that $g^2_{12} \gg g^1_{11}$, one thus meet the conclusion that both X_1^3 coefficients tends to have the same values assuming the slow/fast decomposition. Finally the last cubic term in $X_1 Y_1^2$ in (5.2.16a) is also one order of magnitude smaller, scaling as $1/\omega_2^4$, and can thus be neglected.

Consequently, the conclusion drawn in Section 5.1.3 holds, and the present developments show that the results given by the static condensation tend to those given by the invariant manifold approach if a slow/fast decomposition is present. The dependence on the velocity also tends to disappear, being one order of magnitude smaller. One can also see that Eq. (5.1.13), given in the general case and now specifying to

$$b_2 \simeq \frac{\partial a_2}{\partial X_1} Y_1, \tag{5.2.17}$$

also holds, if and only if one also assumes $g^2_{12} \gg g^1_{11}$, which is the case if the slow/fast dynamics is assumed.

Finally one can also compare the reduced-order dynamics given by the two methods, up to order three, if $\omega_2 \gg \omega_1$. The dynamics of the master coordinate X_1 with the static condensation method is given by Eq. (5.1.4) and reads:

$$\ddot{X}_1 + \omega_1^2 X_1 + g^1_{11} X_1^2 + \left(h^1_{111} - \frac{g^1_{12} g^2_{11}}{\omega_2^2} \right) X_1^3 = 0. \tag{5.2.18}$$

On the other hand, the dynamics on the invariant manifold is given by:

$$\ddot{X}_1+\omega_1^2X_1+g_{11}^1X_1^2+\left(\frac{(\omega_2^2-2\omega_1^2)}{\omega_2^2(4\omega_1^2-\omega_2^2)}g_{12}^1g_{11}^2+h_{111}^1\right)X_1^3+\left(\frac{-2}{\omega_2^2(4\omega_1^2-\omega_2^2)}g_{12}^1g_{11}^2\right)X_1Y_1^2=0, \tag{5.2.19}$$

which simplifies to the following with $\omega_2 \gg \omega_1$:

$$\ddot{X}_1+\omega_1^2X_1+g_{11}^1X_1^2+\left(h_{111}^1-\frac{g_{12}^1g_{11}^2}{\omega_2^2}\right)X_1^3+\frac{2g_{12}^1g_{11}^2}{\omega_2^4}X_1Y_1^2=0, \tag{5.2.20}$$

Comparing Eq. (5.2.20) with (5.2.18), one can observe that the cubic term in X_1^3 is exactly the same, confirming again that the stress manifold should be able to give reliable results only under the slow/fast assumption. The supplementary term in $X_1Y_1^2$ for the invariant manifold based ROM scales as $1/\omega_2^4$ and should thus be negligible. The next section will illustrate all these findings on an example system.

5.2.3 Example system

In order to illustrate the previous results, the system composed of a mass connected to two nonlinear springs is selected, as shown in Fig.5.2.1. Note that the idea of using this system as a benchmark has been first proposed by B. Cochelin in 2002, it then has been used in a number of studies so that numerous results are already present in the literature on this example [51, 52, 64, 45, 66].

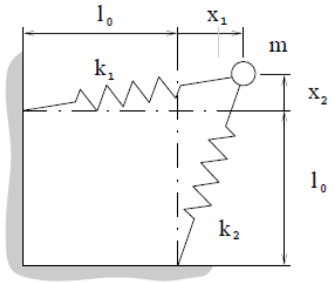

Figure 5.2.1: A mass connected to two nonlinear springs.

The equation of motion for the system reads:

$$\begin{aligned}\ddot{X}_1+\omega_1^2X_1+\frac{\omega_1^2}{2}(3X_1^2+X_2^2)+\omega_2^2X_1X_2+\frac{\omega_1^2+\omega_2^2}{2}X_1(X_1^2+X_2^2)=0,\\ \ddot{X}_2+\omega_2^2X_2+\frac{\omega_2^2}{2}(3X_2^2+X_1^2)+\omega_1^2X_1X_2+\frac{\omega_1^2+\omega_2^2}{2}X_2(X_1^2+X_2^2)=0.\end{aligned} \tag{5.2.21}$$

An advantage of the present two-dofs system is that the coefficients are fully parameterized by the two eigenfrequencies ω_1 and ω_2 only, since the expressions of the quadratic and cubic coupling nonlinear terms simply writes as functions of ω_1 and ω_2. The aim of this section is to compare the results provided by the static condensation with those obtained using NNMs, in terms of geometry of the manifold used to reduce the dynamics, and expression of the dynamics onto this reduced subspace. As we are in a case where the model is fully known, then the ICE method is equivalent to the static condensation.

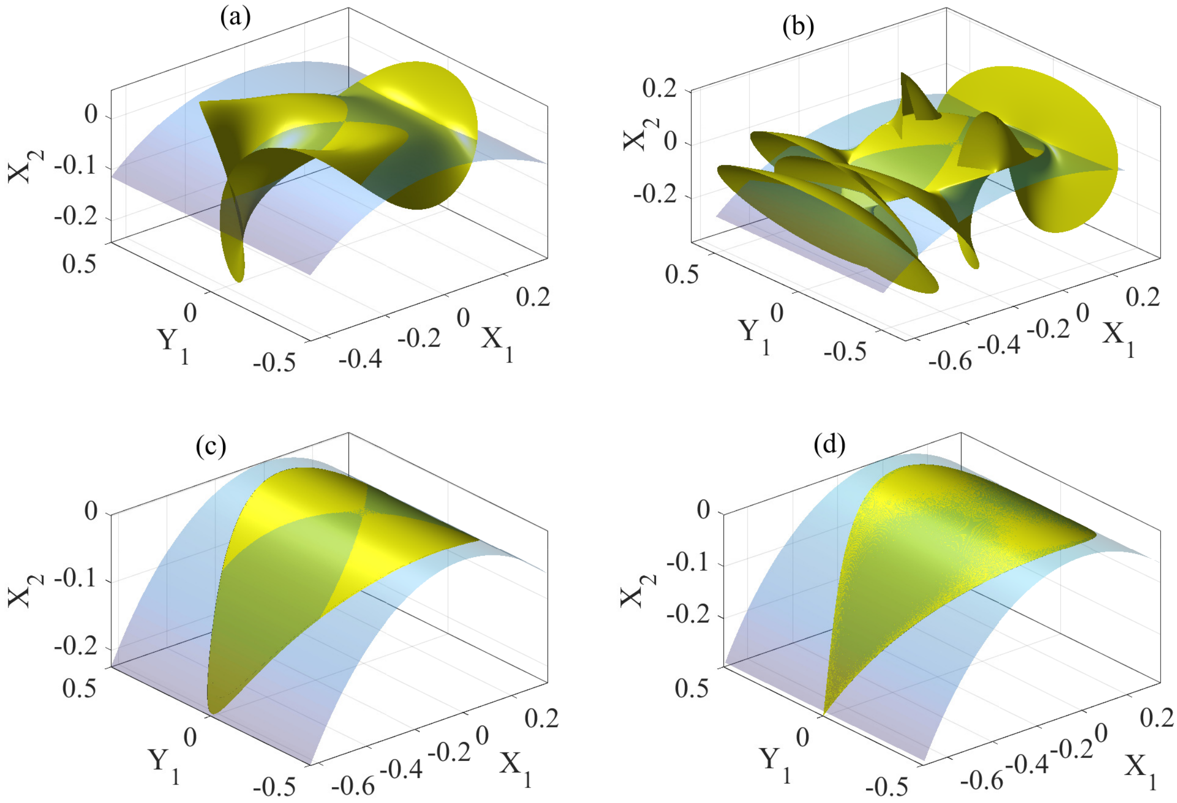

Figure 5.2.2: Comparison of stress manifold obtained with static condensation (light blue), and invariant manifold obtained from numerical continuation of periodic orbits (yellow) in phase space (X_1, Y_1, X_2) for the two-dofs system of Eq. (5.2.21). In each figure, $\omega_1 = 1$ while ω_2 is increased to meet the slow/fast assumption. (a) $\omega_2 = 2.5$, (b) $\omega_2 = 5$, (c) $\omega_2 = 10$ and (d): $\omega_2 = 100$.

Fig. 5.2.2 shows a comparison of the stress manifold obtained from the static condensation with the invariant manifold obtained from the definition of an NNM as a collection of periodic orbits in phase space. The stress manifold has been obtained by solving numerically Eq. (5.1.3) for $s = 2$, with X_1 the master coordinate. The numerical solution of this nonlinear equation allows obtaining an exact expression for the stress manifold, without any assumption on amplitudes. On the other hand, the invariant manifold is also computed numerically without any approximation so that the exact NNM is represented. The manifold is computed using numerical continuation of periodic orbits from the original system given by Eqs. (5.2.21). The continuation method uses an asymptotic-numerical method implemented in the software Manlab [67], where the unknowns are represented thanks to the harmonic balance method [68, 69, 70]. In order to ensure convergence, the computation has been realized with 30 harmonics.

In order to compare the results when the frequency gap between the two eigenfrequencies is increased so as to meet the slow/fast assumption, four cases are tested and reported in Fig. 5.2.2. In each case ω_1 is set to 1 while ω_2 is increased. As already underlined, the stress manifold does not depend on the velocity of the master variable Y_1 so that the curvatures in this direction are not well approximated. When $\omega_2 = 2.5$ and $\omega_2 = 5$, Figs. 5.2.2(a-b) clearly shows that the shape of the invariant manifold can be very complex with numerous foldings, a feature that is completely missed by the static condensation. On the other hand, from $\omega_2 = 10$, the slow/fast assumption is sufficiently met so that the geometry of the two reduced spaces tends to be equivalent. These figures allow confirming the limit exhibited in Section 5.1.4 on the type of nonlinearity, with a factor 6 between slave and master eigenfrequencies. Note that the shape of the invariant manifolds in Figs. 5.2.2(c-d) is obtained by continuation of periodic orbits and the computation has been made up to very large amplitudes where the periodic orbits saturate to the specific shape shown. This figure, obtained with the exact stress and invariant manifolds, evidences the fact that when the slow/fast assumption is verified, then the two reduction subspaces tend to share the same geometry. Note however that the geometry in phase space does not give precise information on the frequencies of the periodic orbits living inside, an issue that will be investigated later.

In order to gain more insight, further comparisons are made using the asymptotic expansions obtained in the previous section. The static condensation gives the following formula for the stress manifold up to the third order :

$$X_2 = c_2(X_1) = -\frac{1}{2}X_1^2 + \frac{\omega_1^2}{2\omega_2^2}X_1^3. \tag{5.2.22}$$

The expansion up to order 9 can be computed using the formulas given in Appendix A which are not analytically detailed because of the lengthy expressions. In order to draw out a comparison, the geometry of the invariant manifold can be explicited by replacing in Eqs. (5.2.6) the coefficients by their values. Focusing solely on $X_2 = a_2(X_1, Y_1)$ for the sake of comparison in the plane (X_1, X_2), the first equation describing the geometry of the manifolds reads

$$X_2 = a_2(X_1, Y_1) = A^1_{11} X_1^2 + A^1_{22} Y_1^2 + B^1_{111} X_1^3 + B^1_{122} X_1 Y_1^2. \tag{5.2.23}$$

The coefficients A^1_{11}, A^1_{22}, B^1_{111} and B^1_{122} are given below, together with their approximate value when one considers the slow/fast assumption $\omega_2 \gg \omega_1$:

$$\begin{aligned}
A^1_{11} &= \frac{\omega_2^2 - 2\omega_1^2}{2(4\omega_1^2 - \omega_2^2)} \xrightarrow{\omega_2 \gg \omega_1} -\frac{1}{2}, \\
A^1_{22} &= \frac{-1}{4\omega_1^2 - \omega_2^2} \xrightarrow{\omega_2 \gg \omega_1} \frac{1}{\omega_2^2}, \\
B^1_{111} &= \frac{(\omega_2^4 - 18\omega_1^4 - 3\omega_1^2\omega_2^2)\omega_1^2\omega_2^2}{\omega_2^2(4\omega_1^2 - \omega_2^2)(\omega_2^2 - \omega_1^2)(\omega_2^2 - 9\omega_1^2)} \xrightarrow{\omega_2 \gg \omega_1} \frac{\omega_1^2}{-\omega_2^2}, \\
B^1_{122} &= \frac{(-11\omega_2^2 - 9\omega_1^2)\omega_1^2\omega_2^2}{\omega_2^2(4\omega_1^2 - \omega_2^2)(\omega_2^2 - \omega_1^2)(\omega_2^2 - 9\omega_1^2)} \xrightarrow{\omega_2 \gg \omega_1} \frac{11\omega_1^2}{\omega_2^2}.
\end{aligned} \tag{5.2.24}$$

These expressions show clearly that the invariant manifold approach method gives more general results that tend to retrieve those given by static condensation at the leading order only, when a slow/fast assumption holds. Indeed, replacing the values of the coefficients A^1_{11}, A^1_{22}, B^1_{111} and B^1_{122} obtained with the slow/fast assumption in (5.2.23), one obtains

$$X_2 = a_2(X_1, Y_1) \simeq -\frac{1}{2} X_1^2 + \frac{1}{\omega_2^2} Y_1^2 - \frac{\omega_1^2}{\omega_2^2} X_1^3 + \frac{11\omega_1^2}{\omega_2^2} X_1 Y_1^2, \tag{5.2.25}$$

an expression that can be directly compared to (5.2.22), showing that additional terms implying the velocities are present in the invariant manifold, but scales according to $1/\omega_2^2$ which is assumed to be negligible. Also the cubic term in X_1^3 is not the same for the two methods but again is scaling according to $1/\omega_2^2$ and is thus negligible. Consequently, the leading order term is the first quadratic term in Eqs. (5.2.22) and (5.2.25) so that a cut of both stress and invariant manifold in the plane (X_1, X_2), and in the slow/fast limit, should show a parabola scaling as $-\frac{1}{2}X_1^2$.

This result is illustrated in Fig. 5.2.3. In the first panel, Fig. 5.2.3(a), the two eigenfrequencies are set as $\omega_1 = 1$ and $\omega_2 = 2.5$. The cut in the (X_1, X_2) plane clearly shows that only the invariant manifold method up to order three is able to recover the correct curvature of the exact invariant manifold for moderate amplitudes of vibrations, while the static condensation gives an erroneous geometry whatever the amplitude. When increasing ω_2 so as to meet the

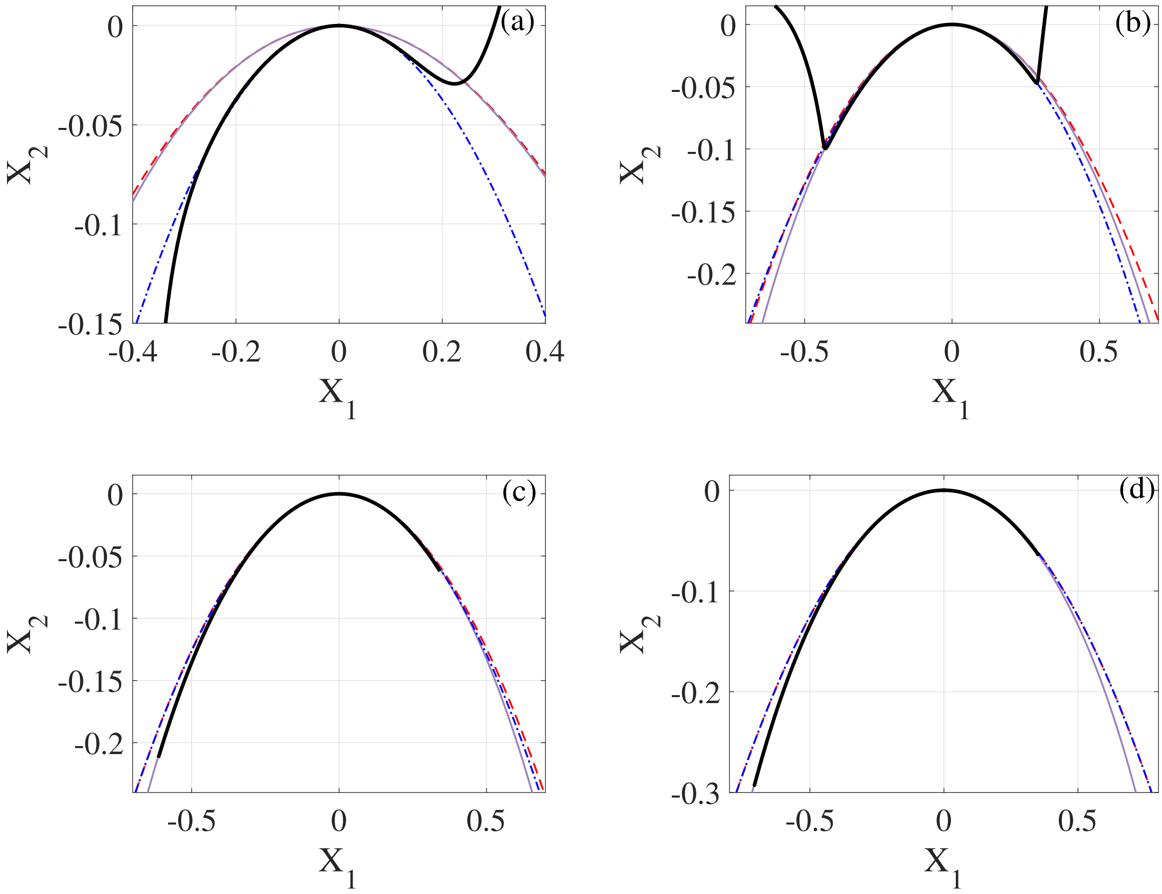

Figure 5.2.3: Comparisons of stress and invariant manifolds in the plane (X_1, X_2) for the two-dofs system of Eq. (5.2.21). The static condensation up to order 3 (red dashed curve) and up to order 9 (continuous violet line) is compared to the exact invariant manifold obtained from numerical continuation of periodic orbits (black thick line, reference solution) and its third-order analytical approximation (blue dash-dotted curve). Increasing values of the frequency ratio are considered in order to meet the slow/fast assumption, with $\omega_1 = 1$, and (a): $\omega_2 = 2.5$, (b): $\omega_2 = 5$, (c) $\omega_2 = 10$ and (d): $\omega_2 = 100$.

slow/fast assumptions, Figs. 5.2.3(b-d) shows that all curves collapses to the same parabola following the first-order term underlined before : $X_2 = -\frac{1}{2}X_1^2$. The results also clearly show that static condensation up to order three is as accurate as the invariant manifold up to order three when $\omega_2 \gg \omega_1$. However a better accuracy on the geometry can be obtained when pushing the development of the static condensation up to order 9, a calculation which is far easier to conduct as getting up to order 9 for the invariant manifold. We can also underline that in the range of amplitudes considered (corresponding to large amplitudes and complicated nonlinear dynamics for this system), the static condensation up to order 9 is completely equivalent to the exact value obtained by numerically solving the equation defining c_2. The exact curve for the static condensation has not been reported in Fig. 5.2.3 since it was fully merged with the ninth order approximation.

To conclude this analysis we now compare the results given by the reduced-order dynamics. Indeed, projecting the equations of motion on the correct subspace is one important point but of utmost importance is also how the periodic orbits and their frequencies are predicted by the reduced models. Using static condensation up to order three, Eq. (5.2.22), leads to the following reduced-order dynamics :

$$\ddot{X}_1 + \omega_1^2 X_1 + \frac{3\omega_1^2}{2} X_1^2 + \frac{\omega_1^2}{2} X_1^3 = 0. \tag{5.2.26}$$

This equation can be compared to the reduced dynamics given by the invariant manifold approach, Eq. (5.2.19), which reads, by replacing the quadratic and cubic coefficients by their values :

$$\ddot{X}_1 + \omega_1^2 X_1 + \frac{3\omega_1^2}{2} X_1^2 + \frac{\omega_1^2(4\omega_1^2 + \omega_2^2)}{2(4\omega_1^2 - \omega_2^2)} X_1^3 + \frac{\omega_2^2}{\omega_2^2 - 4\omega_1^2} X_1 Y_1^2 = 0. \tag{5.2.27}$$

Using now the slow/fast assumption in Eq. (5.2.27), one obtains :

$$\ddot{X}_1 + \omega_1^2 X_1 + \frac{3\omega_1^2}{2} X_1^2 - \frac{\omega_1^2}{2} X_1^3 + X_1 Y_1^2 = 0. \tag{5.2.28}$$

Consequently even with the slow/fast assumption, one can observe in this case that the reduced-order dynamics given by the two methods, Eqs. (5.2.26) and (5.2.28) differ one from another. Again, static condensation does not give rise to any velocity-dependent terms. Since a term-by-term comparison could be misleading about the dynamics produced by the two ROMs, a better idea is to compare the outcomes of the two methods, focusing on the prediction of the type of nonlinearity, as already exemplified in Section 5.1.4. Using the value of Γ_{SC}^p given in Eq. (5.1.17) and replacing the quadratic coefficients by their values, one arrives at $\Gamma_{\mathrm{SC}}^p = -3/4$ for static condensation, *i.e.* a constant value that do not depend on the parameter of the system. On the other hand, using Eq. (5.1.21) shows that

$$\Gamma_{\mathrm{IM}} = \frac{-3\omega_1^2 + \omega_2^2}{4\omega_1^2 - \omega_2^2}. \tag{5.2.29}$$

Interestingly, the type of nonlinearity predicted by the invariant manifold approach has a divergence at the 2:1 internal resonance, a classical feature due to the strong coupling arising in the two modes in this region, and tends to -1 when $\omega_2 \gg \omega_1$. This means that even if the two approaches tend to the same reduced subspaces when the slow/fast assumption holds, a persistent error in the prediction of the type of nonlinearity is given by the static condensation. This conclusion is a bit different from the one obtained in Section 5.1.4, which is due to the particular values of the quadratic coefficients g_{ij}^p. Indeed, being fully dependent on ω_1 and ω_2, their relative values when applying the slow/fast assumption has a direct consequence on the results. Note also that whereas the static condensation always predicts a softening behaviour, there is a small tongue of hardening behaviour since Γ_{IM}^p can reach positive values. This feature thus cannot be correctly predicted by the static condensation.

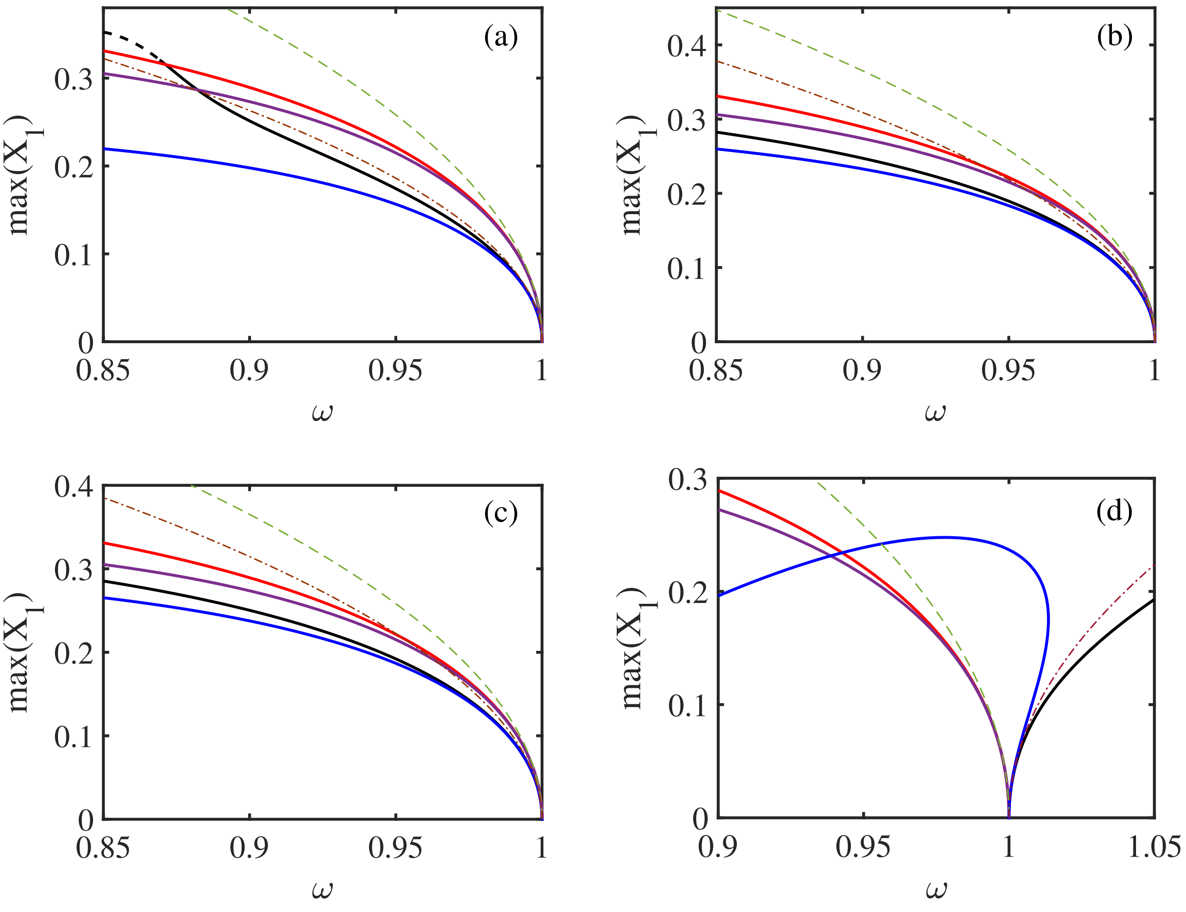

Figure 5.2.4: Comparison of backbone curves for the two-dofs system and different reduced-order models, computed with direct continuation on the equations of motion. The exact solution from the full model, Eqs. (5.2.21) (black curve with unstable part dashed), is compared to the predictions given by the static condensation up to order three, Eq. (5.2.26) (red curve) and up to order 9 (purple curve), as well as the invariant manifold approach up to order 3, Eq. (5.2.27) (blue line). Also shown as an eyeguide are the first-order backbone curves from the type of nonlinearity coefficients $\Gamma_{SC} = -3/4$ (dashed green line) and Γ_{IM} given by Eq. (5.2.29) (brown dash-dotted line). The parameters are set as $\omega_1 = 1$ and ω_2: (a): $\omega_2 = 2.5$, (b): $\omega_2 = 5$, (c): $\omega_2 = 10$ and (d): $\omega_2 = \sqrt{3.5}$.

These findings are illustrated in Fig. 5.2.4. One can clearly see that even with the slow/fast assumption, there is a persistent small error induced by using static condensation in order to predict the amplitude-frequency relationship, whereas the invariant manifold approach is always able to catch the first-order curvature of the backbone accurately. One can also remark that in each of the case studied, the backbone predicted using invariant manifold is close to the reference solution, except in Fig. 5.2.4(a) where the discrepancy is more prominent and increases with amplitude. The reason for that is connected to the appearance of a more complex behaviour including a 1:2 internal resonance. Indeed, Fig. 5.2.4(a) refers to the case with $\omega_1 = 1$ and $\omega_2 = 2.5$. Since the behaviour is softening, nonlinear frequencies are decreasing and upon increasing amplitudes one tends to meet 1:2 condition between the two nonlinear frequencies. This results in a change of behaviour of the full model solution that is not caught by the reduced order model since it is built outside such a resonance condition. Taking properly the internal resonance into account would need to have two master coordinates. Note that in Fig. 5.2.4(d), the invariant manifold and full model predict a hardening behaviour while static condensation predicts softening behaviour for such case. It also should be noted that here invariant manifold is limited to order 3, and the change from hardening to softening is due to the truncation, to obtain more accurate results one needs to compute the invariant manifold to higher-order (at least order 5).

5.3 Numerical examples on continuous structures

In this section, the comparison between the implicit condensation and expansion (ICE) method and the invariant manifold is further discussed on typical beam and plate examples discretized with the finite element method, so that a better assessment of the advantages and drawbacks of each method can be proposed. First a beam example is selected, and reduction to a single mode is achieved with either 2D or 3D elements. Then a simply supported plate is studied, and the question of increasing the number of master modes in the ICE method is investigated. A proposition is tested in order to decrease severely the number of coefficients to be fitted when considering an important number of master modes.

5.3.1 A clamped-clamped beam

In this section, a clamped-clamped beam is investigated as a first test example. Material properties are selected as: density $\rho = 7800\text{kg.m}^{-3}$, Young modulus $E = 2.1e{+}11\,\text{Pa}$, whereas the Poisson ratio is selected as $\nu = 0$ in order to better mimic the assumptions of the theory of beams (see *e.g.* [4]).

To begin with, a simple case of a single master mode (the fundamental bending mode) is investigated, and the comparison between the ICE method and the NNM approach is discussed.

The ICE method is derived by first applying a set of static loadings along the master mode of interest. Denoting ϕ_1 the fundamental mode, a set of body forces proportional to the first mode, $\boldsymbol{F} = \beta_1\phi_1$, for increasing values of the parameter β_1, are imposed to the structure, *i.e.* to Eq. (2.1.3). One can retrieve the modal displacement by projecting the solution of the finite element procedure along ϕ_1, so that a nonlinear relationship between the displacement and the scaling factors β_1 is numerically obtained. Fitting this relationship allows one to retrieve the nonlinear restoring force for the reduced-order model. In this paper, all the calculations have been realized with the open-source finite element software Code_Aster. Two different cases are selected: a thin beam meshed with 2D DKT elements, and a thick beam meshed with 3D elements, in order to underline the differences between using either surface or volume finite elements.

A thin beam discretized with DKT plate elements We first investigate the case of a thin beam, discretized with DKT elements. The dimensions are selected as: length $L = 1$m, width $b = 0.05$m and thickness $h = 0.001$m. The beam has been meshed with 100 elements in the length and 4 elements in the width, so as to guarantee the convergence of the first 10 eigenfrequencies of the structure. Previous investigations using the STEP method, see *e.g.* [12, 11, 71], show that a suitable reduced-order model can be obtained by selecting the first bending mode together with the first three even axial modes (modes number 2, 4 and 6). Indeed, the fundamental bending mode is quadratically coupled to in-plane modes and the symmetry of the problem imposes that coupling occurs only with even in-plane modes. Next, after generating this 4-mode reduced-order model with the STEP method, one can also apply either static condensation or invariant manifold approach in order to reduce the dynamics to a single dof.

The construction of the reduced model with the ICE method is illustrated in the insert in Fig. 5.3.1, where the fitting procedure for a single coordinate is shown. A total of 50 values of β_1 have been selected, where the load scales β_1 as defined from the ICE method, see section 5.1.1, are chosen to obtain displacements in the range of ±1.5 times of thickness. The curve is fitted with a polynomial expansion so that the ROM given by the ICE method reads

$$\ddot{X}_1 + \omega_1^2 X_1 + \gamma_{111}^1 X_1^3 = F_1, \tag{5.3.1}$$

with $\gamma_{111}^1 = 5.2310e+09$. Note that since the beam is a flat, symmetric structure, only the cubic term appears for symmetry reasons.

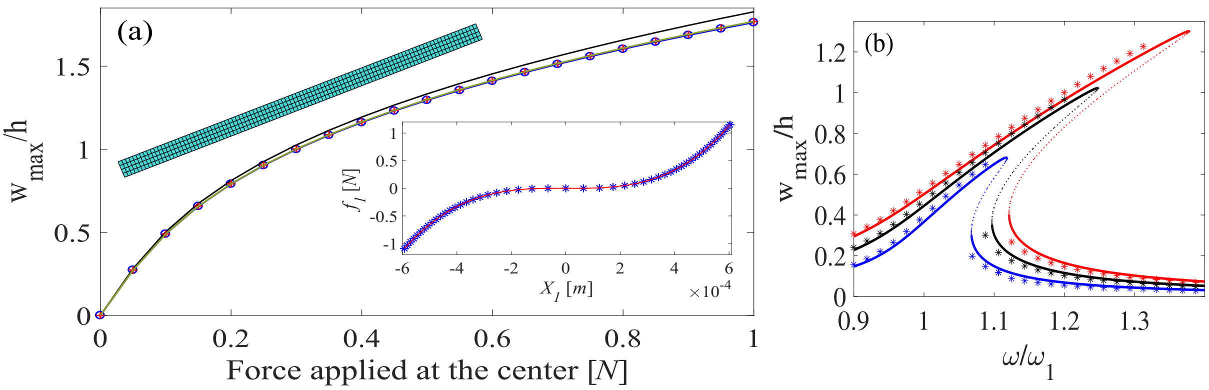

Figure 5.3.1: (a): Comparison of ROMs for a clamped-clamped beam, statically excited at the center with an increasing load. The FE solution (black line) is compared to three reduced order models: a single mode obtained with the ICE method (blue line with circle), a four mode projection using the STEP method (red line with cross), and the reduction to a single NNM from this four mode solution (green line). Insert: illustration of the fitting procedure for the ICE method: blue stars represent the outputs obtained from static applied force on the FE model, red curve is the fitted polynomial of order 3. (b): Frequency response curves of a clamped-clamped beam in the vicinity of the fundamental eigenfrequency, for three different amplitudes of the forcing: 0.00525N (blue), 0.00875N (black), 0.01225N (red), with pointwise excitation located at center. A ROM constructed with the ICE method, Eq. (5.3.1) gives the predictions plotted with continuous lines obtained by numerical continuation, and is compared to direct time integration on the full FE model (stars).

Application of the STEP method using the four linear modes described above allows computing the associated quadratic and cubic coefficients. Quadratic coefficients appear due to the membrane/bending coupling [12]. Next one can apply static condensation, leading to an equation having the form of Eq. (5.3.1), with a computed coefficient now reading

$$\tilde{\gamma}^1_{111} = h^1_{111} - \sum_{p=2}^{4} \frac{g^1_{1p} g^p_{11}}{\omega_p^2}, \tag{5.3.2}$$

where the h and g are the modal coupling nonlinear coefficients computed from the STEP method. In this case one has $\tilde{\gamma}_{111} = 5.2308e+09$, clearly showing the equivalence between implicit and explicit condensation. Finally, starting from the ROM obtained with the STEP method, one can apply the reduction to a single NNM, thus obtaining a reduced dynamics reading

$$\ddot{X}_1 + \omega_1^2 X_1 + \bar{\gamma}^1_{111} X_1^3 + B^1_{111} X_1 \dot{X}_1^2 = F_1, \tag{5.3.3}$$

where $\bar{\gamma}^1_{111} = 5.2308e + 09$ and $B^1_{111} = 1.2506$. Comparing the values of the coefficients appearing in the reduced dynamics, on can conclude that the three methods give exactly the same results, which is in line with the findings of the previous section. Indeed, in-plane modes have very high eigenfrequencies so that the slow/fast assumption definitely holds. This is illustrated in Fig. 5.3.1 (a) with a static test, where the displacement resulting from a static force applied at the center of the beam is computed with the three reduced models, and compared to the result given by the full FE solution, showing a good agreement up to 1.5 times the thickness.

A dynamical test is also performed by computing the nonlinear frequency response curve in the vicinity of the first eigenfrequency. Fig. 5.3.1 (b) shows the obtained results, where the full FE solution have been obtained using direct numerical integration (resulting in dotted points), whereas the response of the reduced models has been obtained by numerical continuation using Manlab. A Rayleigh damping of the form $C_s = 1.34\mathrm{M}$ has been selected, corresponding to a damping ratio of 2 percent for the first mode.

A thick beam discretized with 3D elements The second example addresses a thick beam meshed with 3D elements, in order to illustrate some of the problems one can encounter when using 3D elements in a STEP method, and how the ICE method circumvents these issues. The convergence problems of the STEP method with 3D elements has been fully analyzed in [11]. The selected beam has the following dimensions: length $L = 1m$, width $b = 0.03m$, thickness $h = 0.03$m, and is discretized with 40 elements in the length and 4 elements in the cross-section, with three-dimensional hexahedral 20 nodes finite elements. A static test with an applied force at the center of the beam is used to compare the different methods. The results are shown in Fig. 5.3.2, where the full order solution is compared with different reduced-order models, in a range of displacements up to 2.5 times the thickness.

In order to illustrate the convergence problems encountered when using the linear eigenmodes as basis functions with 3D elements, a first ROM is built by using the fundamental bending mode, plus the same 3 in-plane modes identified in the previous section as the most meaningful for rendering the transverse/in-plane coupling in the case of 2D elements (axial modes 2, 4 and 6). This ROM is composed of a single oscillator equation obtained from explicit static condensation of these axial modes, where all the nonlinear coefficients are computed using the STEP method. The results plotted in red dashed line show that the ROM fails to retrieve

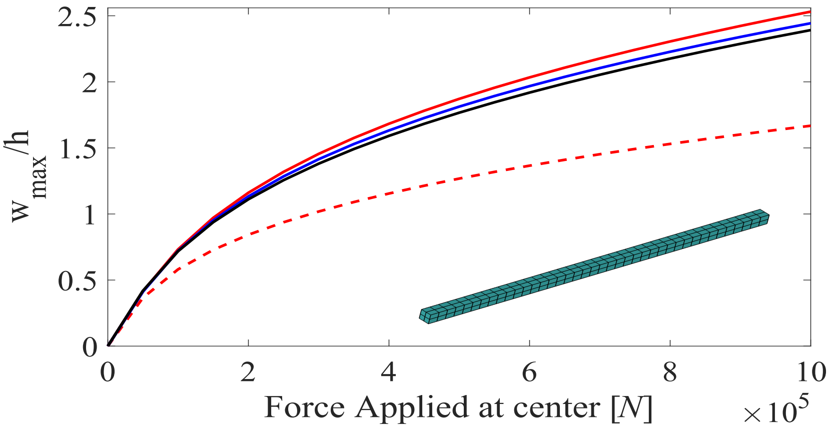

Figure 5.3.2: Static response of a thick beam discretized with 3D elements: displacement at $x = 0.5L$ versus the amplitude of the force in Newton. The reference solution, obtained with the full FE model (black line), is compared to two models using explicit static condensation: the first one composed of four eigenmodes (fundamental flexural, in-plane modes number 2,4 and 6, red dashed line), the second one composed of 87 eigenmodes (fundamental bending plus static condensation of 86 strongly coupled non-bending modes including thickness modes, red solid line); and a model obtained with the ICE method (single mode, blue solid line).

the correct nonlinear stiffness of the beam, putting in evidence that in the case of 3D elements other major couplings arise with other non-bending modes. Indeed, as fully analyzed in [11], strong interactions occur with thickness modes having very high frequencies. Identifying these high-frequency modes is still possible in this simple case of a clamped-clamped beam with a coarse mesh, but would become impractical with more complex geometries and refined mesh. In order to achieve convergence in this case, a set of 86 non-bending modes (including in-plane and thickness modes) are needed, and the explicit static condensation of these to the first flexural mode allows retrieving the correct stiffness. On the other hand, the ICE method, which performs implicit condensation and derives coefficients up to third order in the example, allows finding out directly the correct result. This examples clearly stresses the main advantage of using implicit condensation, since a very rapid convergence is obtained without requiring major efforts in identifying all the coupled modes.

5.3.2 A simply supported rectangular plate

In this section we investigate a simply supported rectangular plate with the aim of developing ROMs with the ICE method including a large number of modes. Indeed, the previous section has shown the main advantage of the ICE method which, thanks to the implicit condensation, guarantees a fast convergence. However a drawback of the method consists in the multidimensional fitting procedure which is required once the set of applied static loadings have been computed. While in the case of a single master mode the fitting is easy and gives good results, when switching to a larger number of master modes two main issues arise: first, the loadings must be selected with care; second, a multivariate function has to be fitted on a multidimensional cloud of points. The objective of this section is to investigate these two issues on the illustrative example of the plate. In the course of the section, the dimensions of the plate are: length $L_x = 0.254m$, width $L_y = 0.3556m$, thickness $h = 0.00102m$, with material properties: density $\rho = 2763kg/m^3$, Young modulus $E = 7.3e{+}10\,\text{Pa}$, and Poisson ratio $v = 0.3$. For the FE model, the plate was discretized with 20 elements in the length and 20 elements in the width.

Construction of multivariate ROMs based on the ICE method In order to build a ROM with m master modes, a combination of loads associated to these is needed. The force vector to be applied in the static computation generally reads $\boldsymbol{F} = \pm\beta_1\phi_1 \pm ... \pm \beta_t\phi_t \pm ... \pm \beta_m\phi_m$, but numerous practical questions need to be solved for selecting the correct combinations with meaningful amplitudes. Previous studies advocated that a third-order polynomial is a correct choice in this multivariate procedure [16, 17, 19, 57]. However, a number of different methods can be used for performing this STEP, as for example local interpolations. Also, deriving a functional relationship is not mandatory and a purely numerical fitting can also be used. To reduce the number of tests, we select here third-order polynomials for this fitting procedure and refer to previous studies for some details, see *e.g.* [57].

A key point for the computational burden is the number of static loads one has to perform before the fitting procedure. When a cubic polynomial fitting is targeted, then one can simply use, in the force vectors to be applied, combinations with only one mode, $\boldsymbol{F} = \pm\beta_t\phi_t$, two modes, $\boldsymbol{F} = \pm\beta_t\phi_t \pm \beta_s\phi_s$, or three modes can be used, since this is sufficient in order to fit quadratic and cubic polynomial terms. The number n of operation associated is :

$$n = 2m + 4 \times C_m^2 + 8 \times C_m^3, \tag{5.3.4}$$

where $C_m^p = \begin{pmatrix} m \\ p \end{pmatrix}$ is the binomial coefficient and m the number of master coordinates retained in the ROM. Note that n scales as m^3 and can be rapidly out of reach if ones targets ROMS with, let say, 20 to 50 modes.

Another key point is also the amplitude of the factors β_p to be selected. As discussed in numerous studies, these amplitudes need not be too small so that the nonlinearity is excited, but not too large also since the FE static computation may then encounter convergence issues. Here we follow the prescription given by [19, 57, 4]. One main idea is to select the β_p's such that the resulting displacement of the structure is in a good range to excite sufficiently the nonlinearity, and the larger the value is (before having convergence issues), the better it is. A last point discussed in [57] is to add reduction factors ($1/2$ for combinations with two modes, and $1/3$ for combinations with three modes), in order to achieve a coherent range of amplitudes for each loading case. This method will be tested next and we will refer to these as the correction factors.

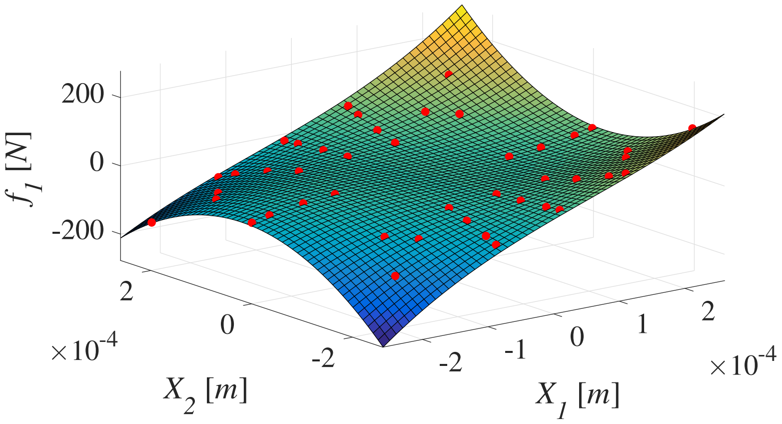

Figure 5.3.3: Illustration of the fitting procedure with two master modes, for the case of the simply supported plate. The red points represent the outputs obtained from static forces applied on the FE model with 44 load cases derived by different combination of $\pm\beta_1\phi_1 \pm \beta_4\phi_4$, with β values as 0, 0.3, 0.5, 0.8, 1. The surface represents the fitted polynomial of order 3.

The fitting procedure is illustrated in Fig. 5.3.3, for the case $m = 2$, and for the simply supported plate studied in this section. It shows how a third-order multivariate polynomial is fitted from the points obtained from the static load cases. Augmenting the number of variables makes the problem more and more difficult, since the number of load cases is increasing drastically,and the fitting procedure is more and more sensitive to small variations.

When increasing the number of modes with a third-order polynomial representation of the restoring force, a specific problem is related to the number of cubic coefficients that have to be fitted (and consequently the number of applied loads needed). Indeed, the number of cubic coefficients for m master modes is equal to $m \times (C_m^3 + 2 \times C_m^2 + m)$. This number scales as m^4 and thus dramatically increases with the number of master modes. In order to reduce the computing cost, one possibility would be to identify only the monomials corresponding to the resonant terms. As known from normal form theory [72, 51, 55], not all the monomial terms in the restoring force do have the same importance, and one can distinguish between resonant terms, that will have a strong influence on the nonlinear dynamics and bifurcations of the problems, and non-resonant monomials that could be easily cancelled thanks to a nonlinear change of coordinates. Among the resonant terms, one can also separate the trivially resonant terms, always present since linked to a trivial resonance relationship, from the resonant terms linked to an internal resonance relationship, see [51, 55] for more details. Trivially resonant terms are all the monomials of the form $X_p X_i^2$, for the p-th oscillator equation, with i ranging from 1 to m. Counting only the trivially resonant terms, one can see that the number of coefficients that have to be identified scales as m^2, a drastic reduction with respect to the global estimate. This also has an implication on the number of static loads $\tilde{n}$ to apply which reduces to:

$$\tilde{n} = 2m + 4 \times C_m^2, \tag{5.3.5}$$

which now scales as m^2. Of course identifying only the resonant monomial terms will have drastic consequences on the fine representation of the nonlinear restoring force. However, normal form theory ensures that these monomials are the most important from the dynamical systems point of view, so that even if less precise fittings could be awaited, one is sure that no important bifurcation or nonlinear phenomena will be missed. And since the number of operations is so importantly decreased to build the ROM, it is worth testing the behaviour of such a ROM as compared to the one with all the nonlinear terms retained.

In the next sections we will discuss the choice of the scaling factors and the identification of the complete set of nonlinear terms as opposed to the reduced set of resonant ones.

Simply supported rectangular plate, static excitation The first numerical example considers the case of the simply supported plate with a static force applied at the center. This test is more challenging than the beam case, since the number of eigenmodes needed to represent correctly the static bending of the rectangular plate is far larger. In the beam case most of the energy is concentrated in the first bending mode, while this is not the case for the plate. Indeed figure. 5.3.4 (a) shows the modal amplitudes for a static load of 70 N applied at the center of the plate and clearly points out that, although most of the energy is concentrated in the fundamental mode, all other ones have a meaningful contribution. As a consequence, a large number of master modes are needed to achieve convergence in the reduced-order model, making this test example interesting for testing different computational strategies.

ROMs with a maximum of 8 master modes have been tested. The number of static loads to be applied and the number of coefficients to identify are given in Table 5.3.1 for 3, 5 and 8 master modes, and for the two different strategies proposed (fitting either all the monomials up to cubic order, or only the resonant terms), showing that the computational burden is already important for 8 modes, especially in the offline phase where one has to apply numerous load cases to the FE model. On the other, fitting only resonant terms leads to a drastic reduction.

		Number of load set cases	Number of coefficients
All terms	3 modes:	26	48
	5 modes:	130	175
	8 modes:	576	960
Only resonant terms	3 modes:	18	9
	5 modes:	50	25
	8 modes:	128	64

Table 5.3.1: The number of load cases and the number of coefficients to be fitted with the different fitting strategies proposed, with either all the monomials, or only the resonant terms.

Also, two different strategies for selecting the β_i's coefficients in the applied load cases, have been tested, and shown in Table 5.3.2 gathering these coefficients for the first 8 modes of interest, sorted by order of increasing frequencies, and selected according to Fig. 5.3.4(a). For load case 1, the amplitudes β_i have been selected such that for a linear plate, the corresponding maximal displacement for each applied force on a single mode, is equal to 2.4 times the thickness. In the simulation and due to the nonlinear restoring force, the computed static displacement is a bit smaller than the targeted one. Also in load case 1, the reduction factors (1/2 if the forcing is a combination of two modes, and 1/3 if a combination of three modes) have been applied, so that the resulting displacements from combinations of 2 and three modes are not too large. For load case 2, a different strategy has been used, without reduction factors, and with decreasing targeted linear resulting displacements, ranging from $1.5h$ for the first mode to $0.5h$ for mode 23.

Scalar weighting factors β_i	β_1	β_4	β_8	β_{11}	β_{12}	β_{19}	β_{22}	β_{23}	Reduction factors
Load case 1	5.24e-5	1.95e-4	3.32e-4	4.73e-4	4.80e-4	7.56e-4	8.91e-4	9.07e-4	yes
Load case 2	3.28e-5	9.75e-5	1.38e-4	1.77e-4	1.60e-4	2.20e-4	2.23e-4	1.88e-4	no

Table 5.3.2: Scalar weight factors β_i [m], selected for the two different load cases tested, for the simply supported plate.

Fig. 5.3.4(b) shows the results obtained with ROMs generated by the ICE method with an increasing number of bending master modes selected in the basis. The results are given for ICE method fitted with all nonlinear terms (solid lines), or retaining only the resonant monomial terms (dotted lines). The results given by the two strategies for the load cases 1 and 2 reported in Table 5.3.2 have not been reported since they were not distinguishable, showing in this case that the effect of the selection of the β_i coefficients is negligible, once the amplitude is large enough to excite the nonlinearity.

As expected, the figure highlights the slow convergence of the method. When all the nonlinear terms are fitted in the polynomial, the convergence trend is clear and the restoring force tends slowly to that of the full model. As in the case of the beam, a comparison with the STEP method has also been drawn for the plate, showing again the advantage of the implicit condensation. Indeed, in order to achieve the same accuracy as the ROM given by the ICE method

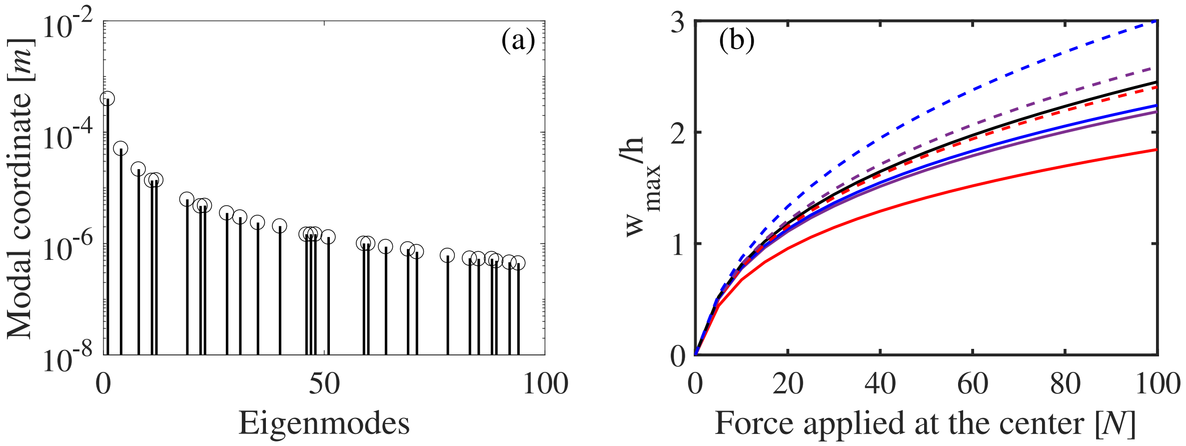

Figure 5.3.4: (a): Amplitudes of the first 100 modal coordinates X_p as a function of the mode number, for a static load of 70 N applied at center of the simply supported plate. (b): Comparisons of ROMs on the static force applied at center. reference solution (full FE model, black line) is compared to the ICE method fitting with all terms (solid lines), or only with resonant terms (dashed lines). Convergence study, ICE method with all terms with 1 mode (red line), 5 modes (modes 1, 4, 8, 11 and 12, purple line) and 8 modes (adding modes 19, 22 and 23, blue line). With only resonant terms, ROM with 3 modes (1, 4 and 8, red dashed line), 5 modes (purple dashed line) and 8 modes (blue dashed line).

with 4 master modes, it was necessary to include 141 membrane modes in the STEP method, resulting in a model with 145 modes.

The behaviour of the ROM built with only resonant terms fitted in the ICE procedure is different. First its convergence is not clearly stated with the test realized, and a larger number of master modes should be used. The conclusion is that this ROM is softer than the one with all the nonlinear terms, which appears logical. Even though most of the nonlinear terms are not meaningful in terms of the dynamical behaviour of the structure with respect to the most important phenomena such as bifurcations, retaining less terms in the polynoms leads to a softer nonlinear restoring force as that of the full model. Hence one has to keep in mind that fitting only resonant terms will produce a model that is generally not as stiff as it should be, but would be able to reproduce qualitatively the dynamics of the structure. Coming back to Fig. 5.3.4(b), it seems clear that the ROM with only resonant monomials converges to a behaviour where the internal force of the structure is not stiff enough as compared to the reference. In order to further analyze this point, the next section is devoted to dynamical simulations.

Simply supported rectangular plate, dynamic response In this last section, we try to gain more insight on the ICE method and an increasing number of dofs focusing on the dynamic response obtained by numerical integration, for the specific case of the free vibrations of the plate when dynamically excited. The input force is applied at $(0.4L_x, 0.35L_y)$ and its time variation is defined by

$$F(t) = \begin{cases} \frac{F_{\text{max}}}{2}[1+\cos(\pi(t-t_0)/T_{\text{wid}})], & \text{if} \quad |t-t_0| \leq T_{\text{wid}}, \\ 0, & \text{if} \quad |t-t_0| > T_{\text{wid}}. \end{cases} \tag{5.3.6}$$

The temporal content $F(t)$ of the excitation is illustrated in Fig. 5.3.5 and depends on two parameters: F_{max} is the maximum amplitude of the strike force (in Newton), and is used to calibrate the level of geometric nonlinearities excited in the response. In the simulations, the values selected for F_{max} are 7 N, 15 N and 50 N. T_{wid} is the interaction time, and is used as a parameter to control the number of modes directly excited by the strike force. Indeed, denoting as $f_m = 1/T_{\text{wid}}$ the frequency associated to this interaction time, all the modes below f_m are thus directly excited by the strike force. Two values of T_{wid} have been selected: $T_{\text{wid}} = 0.005\ s$ and $T_{\text{wid}} = 0.0025\ s$, so as to excite the first three and eight bending eigenmodes, respectively. The first eight eigenfrequencies of the plate are listed in Table 5.3.3.

Mode	1st	2nd	3rd	4th	5th	6th	7th	8th
Frequency[Hz]	58.25	117.30	174.10	215.94	233.00	331.33	353.77	367.19

Table 5.3.3: Natural frequencies of the first eight modes of the simply supported plate.

In order to test the sensitivity of the ROM constructed with ICE method to the scaling factors β_i used to define the load sets, we have also selected three different strategies summarized in Table 5.3.4. Load case 1 has been selected as in the previous section, based on the advice given in [57], with a targeted linear displacement equal to 2.4 times the thickness. Note however that in the dynamic response the first eight modes (at least) are participating to the vibration so that the ROM is built for these master coordinates. Load case 2 and 3 have been selected so as to obtain the largest resulting static displacement possible in the full FE model without encountering convergence issues due to the appearance of large rotations. The difference lies in the use of reduction factors or not, when a combination of modes is used in the applied force.

Finally, three families of ROMs are constructed, with either 3, 5 or 8 master modes, in order to test the robustness of the method with respect to an increasing number of modes.

Scalar weighting factors β_t	β_1	β_2	β_3	β_4	β_5	β_6	β_7	β_8	Reduction factors
Load case 1	4.34e-5	8.82e-5	1.31e-4	1.62e-4	1.75e-4	2.49e-4	2.67e-4	2.77e-4	no
Load case 2	3e-4	3e-4	3e-4	3e-4	3e-4	3e-4	3e-4	3e-4	no
Load case 3	9e-4	9e-4	9e-4	9e-4	9e-4	9e-4	9e-4	9e-4	yes

Table 5.3.4: Scalar weighting factors β_i used for computing the ROM with ICE method for the simply supported plate, for the case of the dynamical response.

The two strategies proposed in order to fit the nonlinear multivariate restoring force, *i.e.* by identifying only the resonant monomials or all the nonlinear terms, have been tested and compared. Note also that apart from the trivially resonant terms that always need to be taken into account in the reduced model, whatever the relationships between the eigenfrequencies, some additional monomials shall also be taken into account if the eigenfrequencies of the studied structure present internal resonance relationships. Note that since a flat symmetric structure is studied, only the third-order internal resonance relationships need to be verified, since the restoring force shall not contain quadratic terms. For the selected rectangular plate with simply supported boundary conditions, whose first eight eigenfrequencies are given in Table 5.3.4, one can observe that the following third-order relationships of closeness to internal resonance are verified:

$$\omega_3 \approx 3\omega_1 \tag{5.3.7a}$$

$$\omega_3 \approx 2\omega_2 - \omega_1 \tag{5.3.7b}$$

$$\omega_5 \approx 2\omega_1 + \omega_2 \tag{5.3.7c}$$

$$\omega_5 \approx 2\omega_3 - \omega_2 \tag{5.3.7d}$$

$$\omega_5 \approx \omega_2 + \omega_3 - \omega_1, \tag{5.3.7e}$$

$$\omega_6 \approx 2\omega_1 + \omega_4 \tag{5.3.7f}$$

$$\omega_6 \approx \omega_3 + \omega_4 - \omega_1 \tag{5.3.7g}$$

$$\omega_6 \approx \omega_4 + \omega_5 - \omega_2 \tag{5.3.7h}$$

$$\omega_7 \approx 3\omega_2 \tag{5.3.7i}$$

This means in particular that all the resonant monomial terms corresponding to these relationships need to be added to the ROM. For example from $\omega_3 \approx 3\omega_1$, one has to take into account a term of the form $h^3_{111}X_1^3$ in the equation for X_3, and a term $h^1_{113}X_1^2X_3$ in the equation for X_1. If the relationships involves three eigenfrequencies like $\omega_3 \approx 2\omega_2 - \omega_1$, then three additional terms are needed: $h^3_{122}X_1X_2^2$ in the equation for X_3, $h^1_{223}X_2^2X_3$ in the equation for X_1, and $h^2_{123}X_1X_2X_3$ in the equation for X_2. Finally four terms are needed if the internal resonance relationship involves 4 eigenfrequencies. Consequently, in the ROM composed of 8 master mode, a number of 28 more monomials have been added.

All these choices for running the simulations resulted in a series of 108 time simulations (3 values for the force amplitude, 2 values for the interaction time, 3 load cases to construct the ROM, 3 cases with different number of master modes, and two different strategies with either all nonlinear terms or only the resonant monomial terms) that have been thoroughly analyzed with different indicators, in the time and frequency domain, to understand the quality of the ROMS obtained. In all the simulation, the time step is set to be 0.0001s, the simulation time is 0.5s, the damping of the ROM is selected as $C_s = 5 + 0.00001\omega_s^2$, while in the FE model a Rayleigh damping matrix is used with $\mathbf{C} = 5\mathbf{M} + 0.00001\mathbf{K}$, leading to damping ratios ζ between about 0.8 and 1.3 percent for all eight modes in the excitation band.

In the next paragraph, we show only two representative examples of the results obtained and give our comments based on the analysis of the 108 simulations.

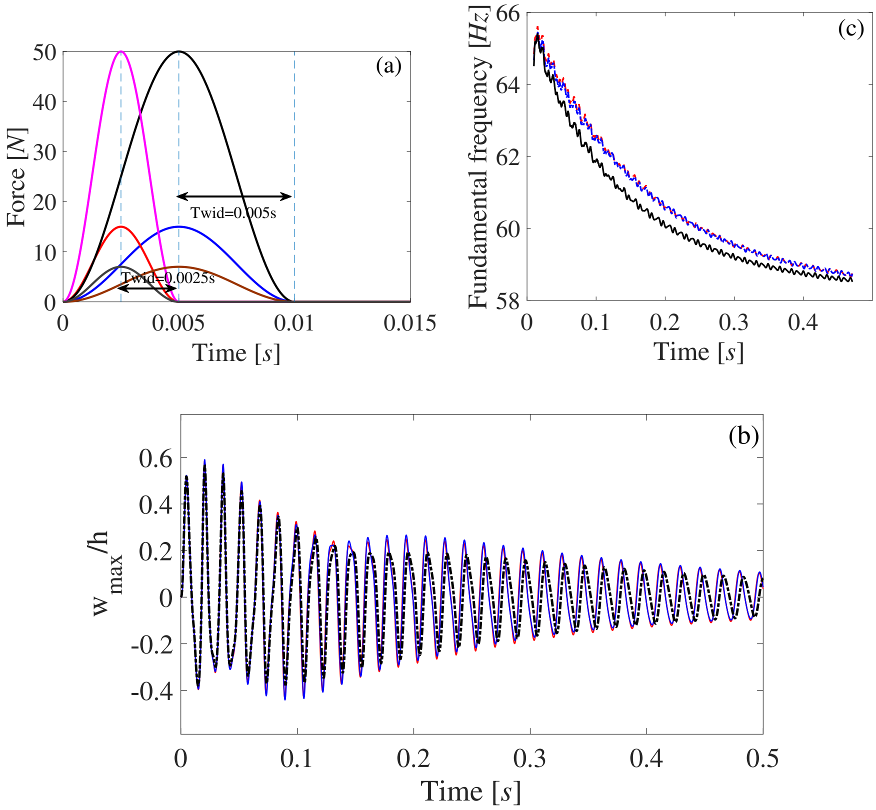

Figure 5.3.5: (a): Temporal content of the striking force given in Eq.(5.3.6), for the two different values of T_{wid} and three different amplitude $Fmax$ used in the simulations. (b): Time response of the plate subjected to a strike force. The full model (reference FE solution) is plotted in black. Displacements of two ROMS with 8 master modes and either all the nonlinear terms fitted (red curve), or only the resonant terms (blue curve). (c): Fundamental frequency variation in the case of fitting with all the terms (red) and with only resonance terms (blue); the black curve shows the reference FE solution.

Example 1: $F_{max} = 7$N, $T_{wid} = 0.0025$s, 8 master modes The first example is a case of small excited nonlinearity ($F_{max} = 7$N) resulting in a maximal amplitude displacement of $0.6h$ with h the thickness of the plate. A small T_{wid} is selected so that the first 8 modes are directly excited by the load, consequently two ROMs with 8 master modes are compared : one with all the polynomial terms fitted, and one with only the resonant terms. For both ROMs, load case 3 is analyzed in the following. The results are shown in Fig.5.3.5(b) for the time series of the displacement, while Fig.5.3.5(c) shows the evolution of the fundamental frequency of each displacements (full model versus the two tested ROMs), obtained directly with the yin algorithm [73]. In this case of moderate nonlinearity, it can be observed that the two ROMs are able to recover finely the temporal dynamics. The nonlinear frequency shift decreases from 66 to 58.2 Hz (hardening behaviour) is also very well recovered by the two ROMs. And the fact that only resonant terms are selected has no clear visible effects since the two ROMs gives hardly the same result. Regarding the different results obtained when changing the load cases reported in Table 5.3.4, it has been found that when all the terms are fitted, the three methods gives almost the same result, with a small deviation for load case 2. When fitting only the resonant monomials, load case 3 gave the best result. The variability of the resulting ROMs with respect to load cases was more important when fitting only resonant terms, mainly because the geometric nonlinearity in the restoring force is a little less excited in this case.

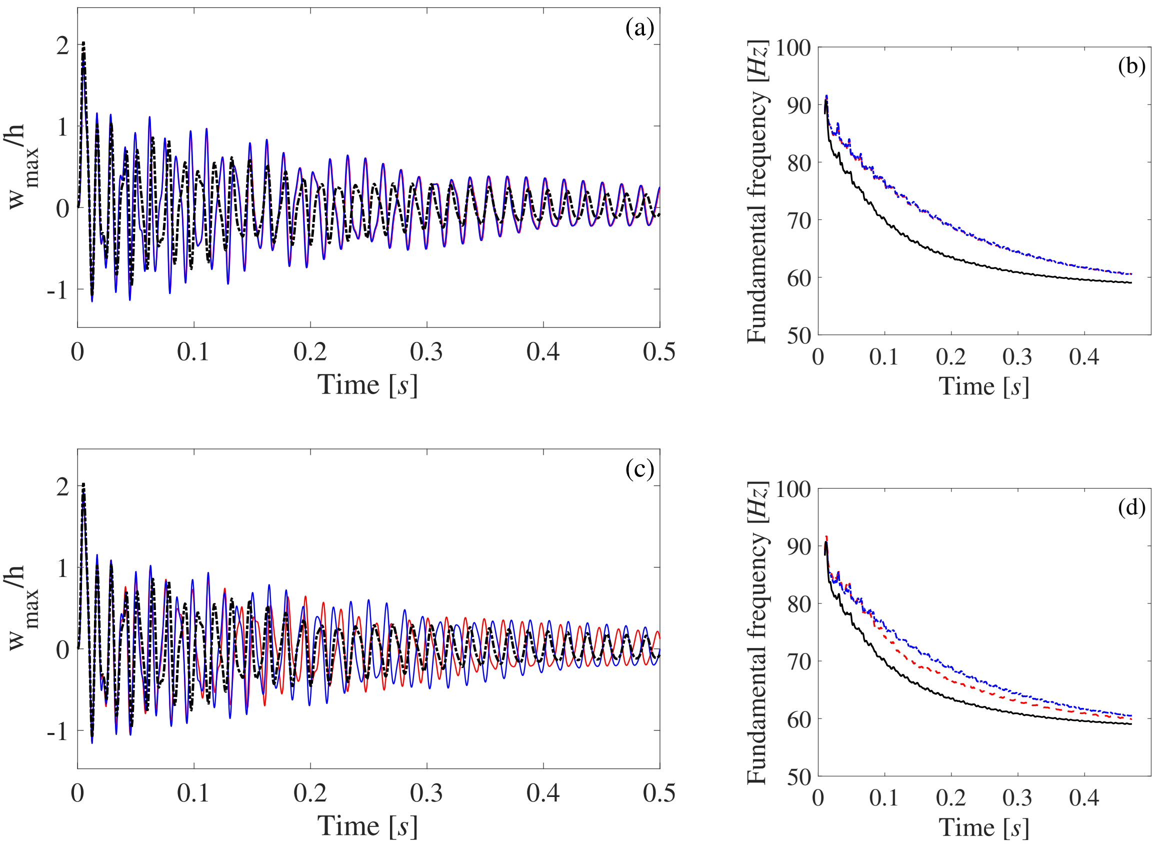

Figure 5.3.6: (a,c): Time response of the plate subjected to a strike force. (b)-(d) : variation f the fundamental frequency. (a-b): 3 master modes in the ROMS, (c-d) : 8 master modes. Comparison of the full FE (reference) solution in black, ROM with all the nonlinear terms fitted (red) and only resonant terms (blue).

Example 2: $F_{max} = 50$N, $T_{wid} = 0.005$s, 3 or 8 master modes The second example considers a stronger nonlinearity, with $F_{max} = 50$N, resulting in a maximum displacement of two times the thickness. A larger $T_{wid} = 0.005$s is selected, so that only the first three modes are directly excited by the load, however since the nonlinearity is strongly excited, energy exchanges occur and other modes are then excited via nonlinear couplings. Consequently two results are reported: Fig. 5.3.6(a-b) is concerned with a ROM composed of 3 master modes, while 8 master modes are taken into account in Fig. 5.3.6(c-d). One can first observe on the time series of the displacements that whatever the ROM used, it has not been found possible to retrieve exactly the result of the full model. However the global trends are recovered in term of maximum amplitude, global decrease in time, frequency content. The decrease of the fundamental frequency is now much more pronounced with an impressive frequency shift of 50%. Fitting with 3 modes, Fig. 5.3.6(a-b) shows that the non-resonant terms can be easily discarded to the ROM since the results are fully comparable. But none of the ROM is able to recover exactly the frequency shift.

Increasing the number of master modes to 8 shows that the two ROMs depart in the solution they compute, and the ROM with all nonlinear terms performs better, in particular with regard to the variation of the fundamental frequency. In each of these cases, the load case 3 from Table 5.3.4 has been used. It has been found that whatever the fitted model, load case 2 has the best results but very close to load case 3 used in the figure, while load case 1 gives the worst predictions.

Based on the full analysis of the 108 simulations (where also indicators on decay time, accuracy of frequency spectrum, indicators on time series and phases of the signals, have been analysed) the results show that the methods are very sensitive to either the load case, or the model used. No clear trends have been found, since some load cases could give better results for the estimation of the phase, but not on the decay time, just to give an example. The only clear trend found is that as long as the nonlinearity is small (example 1), and that a small number of modes (typically 3) are concerned, then all the methods converge and are able to finely recover the dynamical solutions. Increasing either the nonlinearity, and/or the number of modes involved in the dynamics, then all methods depart slowly from the full-order model solution. Even though all methods give generally good qualitative predictions, quantitative discrepancies appear and have a strong dependence on the input parameters and load cases. A general conclusion also is that even though fitting only the resonant terms does not give the best results when increasing the nonlinearity and the number of master modes, the results are qualitatively acceptable. Since the computational burden is so drastically reduced, the method still presents an advantage.

Our final conclusion on all these simulations is that the main drawback of the ICE method relies in this fitting procedure, which is very sensitive to a number of parameters that are difficult to control, so that it appears difficult to give clear advice on a best strategy that would work in any case and would be able to retrieve all the nonlinear characteristics of a full system.

5.4 Conclusion

This Chapter addressed the understanding of the implicit condensation and expansion (ICE) method, with detailed comparisons to the results provided using nonlinear normal modes (defined as invariant manifolds in phase space) so as to better understand the advantages and drawbacks of the method. One of the main advantage is to propose an *implicit* condensation of the non-modeled degrees of freedom (or slave variables), which has very important consequences when dealing with structures discretized with the FE approach, and for which there is no direct and simple access to the full expression of the restoring force. This main advantage leads to the fact that using the ICE method is much more efficient than using the STEP method. Indeed, the STEP method allows computing the nonlinear modal coupling coefficients, which are not dependent of the amplitude of the prescribed displacement. But the drawback is that, using the modal basis, all the known problems related to its very slow convergence for nonlinear structures, are present. This point has been clearly underlined in this contribution, in line with the results already presented by previous authors.

A second important conclusion is that the ICE method, being an implicit condensation, can not, in any case, perform better than the usual static condensation. This fact has been analysed by comparing the geometry of the reduction subspaces in phase space, together with the predictions of hardening/softening behaviour. The stress manifold, used in the ICE method to fit the nonlinear restoring force, does not depend on the velocities, and is not invariant. These two features are of great importance for producing accurate ROMS, and are embedded in the definition of NNM as invariant manifold, which produces better ROMs. In particular, our theoretical analysis shows that if a slow/fast assumption is at hand, then the results of the static condensation tend to those given by invariant manifold at the leading order only. Based on the prediction of the type of nonlinearity, a quantification of the slow/fast assumption has been proposed, with a ratio of 6 between the eigenfrequencies of master and slave coordinates.

Several numerical experiments have been addressed to better understand the behaviour of the ROMs produced with ICE method with regard to two important problems at hand when increasing the number of master modes: the strategies used to impose the prescribed forces, and the fitting procedure. In particular, it has been proposed to derive lighter ROMs by fitting only the resonant terms in the polynomial expression of the restoring force, thus drastically reducing the associated computational burden. Our main conclusion from all these experiments is that the method is generally very sensitive to the numerous parameters involved in the process (selection of β_i coefficient, fitting procedure). Even though the obtained ROMs perform qualitatively well, quantitative differences are unavoidable, and are increasing with the level of nonlinearity and the number of master modes. For all these reasons, our results clearly point out that the main drawback of the method is in this fitting procedure, which needs a particular and dedicated attention. Also, all of our tests show that there is no clear guideline of which method can be used safely as giving always better results. Depending on the nonlinear characteristics one wants to reproduce accurately with a ROM (which can be for example: a correct static behaviour, a correct estimate of the nonlinear frequency shift, an accurate prediction of an important bifurcation point, a correct reproduction of the nonlinear couplings, etc ...), all the tested methods have shown to give, for some indicators, good results, but not for some other.

All these findings argue for using ROMs derived from the general theorems from dynamical system theory. Indeed, they are not dependent on a putative assumption of slow/fast separation between master and slave coordinates, and can be directly computed from the model, so that they belong to the class of simulation-free methods (which is not the case for *e.g.* POD or PGD based methods). Also, recent contributions propose their derivation in a setting that fits to the FE formulation, see *e.g.* the derivations with either the spectral submanifold method [74] or the normal form approach [75, 76]. In particular, general formula are given for an arbitrary number of master modes in [76]. As a consequence, these methods bypass the fitting procedure of the ICE method which is its main drawback, particularly when increasing the number of master modes.

Chapter 6

Comparison of quadratic manifold and direct normal form

6.1 Direct normal form

6.1.1 Foreword

Before the author starts the thesis, application of the method for deriving NNMs to full FE models has been rarely discussed in the literature, see *e.g.* [77] for an example. The main reason lies in the fact that application of the method as it was presented in [27, 25, 28] needs as input the nonlinear coupling coefficients, obtained for example from a STEP. However, recent developments overcome this limitation, see *e.g.* [74] for a direct approach using spectral submanifolds (with general third-order formula equivalent to the ones given with the invariant manifold method proposed by Shaw and Pierre), and [75, 76] for a direct method based on normal form.

The work presented in this Section comes from a collaborative project with Imperial College London and ENSAM Lille starting from January 2019. This part of the work was processed during Vizzaccaro was visiting the IMSIA, before, the author of this thesis had a one-week scientific exchange in Imperial College London. The development of direct normal form (DNF) approach was mainly done by Vizzaccaro [75, 76], then, the approach is used and assessed by the author [78, 79]. The subsequent text is to simply explain the method.

6.1.2 Nonlinear mapping and reduced dynamics

The Direct normal form (DNF) approach allows direct computation of the nonlinear mapping enabling to pass from the physical space (dofs of the FE mesh) to the invariant manifolds of the system that are tangent to their linear counterpart at the origin (Nonlinear Normal Modes in the sense of Shaw and Pierre [27, 25]). The method builds on earlier results where the normal form was computed from the problem expressed in the modal basis, *i.e.*, the equation of motion of the initial model expressed as Eq. (2.1.5) [51, 52], such that develops a nonlinear mapping up to the third-order, which has been presented in Section 4.1.2. The main advantage of the direct approach proposed in [76] is to bypass the step of eigenmode projection, since this can be out of reach in complex FE mesh with millions of dofs. Instead, the method uses as a starting point Eq. (2.1.3), *i.e.* the physical space and the dofs of the FE mesh. The equations of motion in physical coordinates are given here again:

$$\mathbf{M}\ddot{\mathbf{q}} + \mathbf{K}\mathbf{q} + \hat{\mathbf{\Gamma}}(\mathbf{q}) = \mathbf{F}, \tag{6.1.1}$$

where the internal force vector reads $\hat{\mathbf{\Gamma}}(\mathbf{q}) = \mathbf{G}(\mathbf{q},\mathbf{q}) + \mathbf{H}(\mathbf{q},\mathbf{q},\mathbf{q})$. The detailed expressions of the quadratic and cubic polynomial terms, *i.e.* $\mathbf{G}(\mathbf{q},\mathbf{q})$ and $\mathbf{H}(\mathbf{q},\mathbf{q},\mathbf{q})$, representing the nonlinear internal restoring force are given by:

$$\mathbf{G}(\mathbf{q},\mathbf{q}) = \sum_{r=1}^{N}\sum_{s=1}^{N} \mathbf{G}_{rs} q_r q_s, \tag{6.1.2}$$

$$\mathbf{H}(\mathbf{q},\mathbf{q},\mathbf{q}) = \sum_{r=1}^{N}\sum_{s=1}^{N}\sum_{t=1}^{N} \mathbf{H}_{rst} q_r q_s q_t, \tag{6.1.3}$$

where $\mathbf{G}_{rs}$ and $\mathbf{H}_{rst}$ are the N-dimensional vectors of coefficients G^p_{rs} and H^p_{rst}, for $p = 1, ..., N$. Using the matrix of eigenvectors, this problem can be rewritten in the modal basis as in Eq. (2.1.5), using similar notations for the quadratic and cubic tensors of coefficients. The p-th modal equation thus writes:

$$\ddot{X}_p + 2\zeta_p\omega_p\dot{X}_p + \omega_p^2 X_p + \sum_{i=1}^{N}\sum_{j=i}^{N} g^p_{ij} X_i X_j + \sum_{i=1}^{N}\sum_{j=i}^{N}\sum_{l=j}^{N} h^p_{ijl} X_i X_j X_l = F_p, \tag{6.1.4}$$

and the relationships between $\mathbf{G}$ and $\mathbf{g}$, $\mathbf{H}$ and $\mathbf{h}$ reads:

$$\mathbf{g}_{ij} = \mathbf{P}_{\phi}^{T}\mathbf{G}(\boldsymbol{\phi_i}, \boldsymbol{\phi_j}), \tag{6.1.5a}$$

$$\mathbf{h}_{ijk} = \mathbf{P}_{\phi}\mathbf{H}(\boldsymbol{\phi_i}, \boldsymbol{\phi_j}, \boldsymbol{\phi_k}), \tag{6.1.5b}$$

where $\mathbf{P}_\phi$ is the matrix of eigenvectors $\boldsymbol{\phi_i}$.

Two versions of the DNF are presented in [76], a second-order and a third-order development. Also, a method to take into account Rayleigh damping is proposed so that one can get a reduced dynamics where the losses of the reduced dynamics do not neglect those of the slave modes. At present, the inclusion of the Rayleigh damping in the form of $\mathbf{C} = \zeta_M \mathbf{M} + \zeta_K \mathbf{K}$ is only possible with the second-order DNF. For that reason, the presentation retained here will focus to the case of the second-order DNF with inclusion of damping.

The nonlinear mapping up to second-order reads:

$$\mathbf{u} = \sum_{i}^{n} \boldsymbol{\phi}_i X_i + \sum_{i=1}^{n}\sum_{j=1}^{n} \bar{\boldsymbol{a}}_{ij} X_i X_j + \sum_{i=1}^{n}\sum_{j=1}^{n} \bar{\boldsymbol{b}}_{ij} \dot{X}_i \dot{X}_j + \sum_{i=1}^{n}\sum_{j=1}^{n} \bar{\boldsymbol{c}}_{ij} X_i \dot{X}_j, \tag{6.1.6}$$

where n is the number of master modes used to build the ROM, and X_i together with its velocity $Y_i = \dot{X}_i$ are the coordinates used to span the i-th invariant manifold. In Eq. (6.1.6), $\boldsymbol{\phi}_i$ is the eigenvector and $\bar{\boldsymbol{a}}_{ij}$, $\bar{\boldsymbol{b}}_{ij}$ and $\bar{\boldsymbol{c}}_{ij}$ are second-order tensors, the full expressions are given in [76] and expressed as:

$$\bar{\boldsymbol{a}}_{ij} = \frac{1}{2}(\bar{\boldsymbol{Z}}\boldsymbol{d}_{ij} + \bar{\boldsymbol{Z}}\boldsymbol{s}_{ij}), \tag{6.1.7a}$$

$$\bar{\boldsymbol{b}}_{ij} = \frac{1}{2\omega_i\omega_j}(\bar{\boldsymbol{Z}}\boldsymbol{d}_{ij} - \bar{\boldsymbol{Z}}\boldsymbol{s}_{ij}), \tag{6.1.7b}$$

$$\begin{aligned}\bar{\boldsymbol{c}}_{ij} =& (\zeta_M + 3\omega_i^2\zeta_K)\bar{\boldsymbol{b}}_{ij} - (2\zeta_K)\bar{\boldsymbol{a}}_{ij} + (-\zeta_M + 2\omega_i^2\zeta_K)(\bar{\boldsymbol{Z}}\boldsymbol{ss}_{ij} + \bar{\boldsymbol{Z}}\boldsymbol{dd}_{ij})\\ &+ (-\zeta_M + 2\omega_j^2\zeta_K)(\omega_i/\omega_j)(\bar{\boldsymbol{Z}}\boldsymbol{ss}_{ij} - \bar{\boldsymbol{Z}}\boldsymbol{dd}_{ij}),\end{aligned} \tag{6.1.7c}$$

where

$$\bar{\boldsymbol{Z}}\boldsymbol{ss}_{ij} = ((+\omega_i + \omega_j)^2\mathbf{M} - \mathbf{K})^{-1}\mathbf{M}\bar{\boldsymbol{Z}}\boldsymbol{s}_{ij}, \tag{6.1.8a}$$

$$\bar{\boldsymbol{Z}}\boldsymbol{dd}_{ij} = ((-\omega_i + \omega_j)^2\mathbf{M} - \mathbf{K})^{-1}\mathbf{M}\bar{\boldsymbol{Z}}\boldsymbol{d}_{ij}, \tag{6.1.8b}$$

and

$$\bar{\boldsymbol{Z}}\boldsymbol{s}_{ij} = ((+\omega_i + \omega_j)^2\mathbf{M} - \mathbf{K})^{-1}\mathbf{G}(\boldsymbol{\phi}_i, \boldsymbol{\phi}_j), \tag{6.1.9a}$$

$$\bar{\boldsymbol{Z}}\boldsymbol{d}_{ij} = ((-\omega_i + \omega_j)^2\mathbf{M} - \mathbf{K})^{-1}\mathbf{G}(\boldsymbol{\phi}_i, \boldsymbol{\phi}_j). \tag{6.1.9b}$$

With the nonlinear mapping up to second-order, the normal form is able to give the reduced dynamics up to the third-order. For the nonlinear mapping in third-order, the interested reader can find the details in [21]. By taking into account the Rayleigh damping with an assumption of small damping ratios on the master modes, the nonlinear dynamics reads, $\forall\, p = 1, ...m$:

$$\ddot{R}_p+(\zeta_M+\zeta_K\omega_p^2)\dot{R}_p+\omega_p^2R_p+\sum_{i=1}^{m}\sum_{j=1}^{m}\sum_{k=1}^{m}[(A^p_{ijk}+h^p_{ijk})R_iR_jR_k+B^p_{ijk}R_i\dot{R}_j\dot{R}_k+C^p_{ijk}R_iR_j\dot{R}_k] = F_p, \tag{6.1.10}$$

where the coefficients $A^p_{ijk}, B^p_{ijk}, C^p_{ijk}$ arise from the cancellation of non-resonant quadratic terms, their full expression reads [76]:

$$A^p_{ijk} = 2\phi_p^T\mathbf{G}(\boldsymbol{\phi}_i, \bar{\boldsymbol{a}}_{jk}), \tag{6.1.11a}$$

$$B^p_{ijk} = 2\phi_p^T\mathbf{G}(\boldsymbol{\phi}_i, \bar{\boldsymbol{b}}_{jk}), \tag{6.1.11b}$$

$$C^p_{ijk} = 2\phi_p^T\mathbf{G}(\boldsymbol{\phi}_i, \bar{\boldsymbol{c}}_{jk}). \tag{6.1.11c}$$

The reduced dynamics given in (6.1.10) is expressed on the $2m$ dimensional invariant manifold. For that reason, there is no need of fulfilling a slow/fast assumption to produce correct predictions.

Also, the reduction to a single master coordinate is able to predict the correct hardening/softening behaviour, in such context, the reduced dynamics reads as:

$$\ddot{R}_p + (\zeta_M + \zeta_K\omega_p^2)\dot{R}_p + \omega_p^2R_p + (A^p_{ppp} + h^p_{ppp})R_p^3 + B^p_{ppp}R_p\dot{R}_p^2 + C^p_{ppp}R_p^2\dot{R}_p = F_p. \tag{6.1.12}$$

This result has been applied for analyzing the type of nonlinearity of shallow spherical-cap shells in [41, 79].

6.2 Reduction with quadratic manifold

In this section, the quadratic manifold (QM) method, which is first introduced in [20, 21] based on modal derivatives reviewed in Section 4.2.2, is presented. The main idea is to derive a nonlinear mapping, using the modal derivatives, as a quadratic dependence on the master coordinates, to pass from the FE nodes to a reduced subspace built on a quadratic manifold. In the section, we explain how the quadratic manifold is built.

The modal derivatives have been first introduced with the aim of completing the linear mode basis with additional vectors in order to take into account the new spanning directions given by the curvature of the invariant manifold in phase space, and have been used as such in numerous context, see e.g. [71]. However it then appeared logical to embed these added vectors in a nonlinear mapping. Indeed, from the definition of the modal derivatives, it is possible to define a nonlinear mapping from the initial physical dofs to the master coordinates, stating that the quadratic part of the mapping is conveyed by the introduced MD or SMD. Following [20, 21, 61], one can write such a relationship in a compact form as

$$\mathbf{q} = \Xi(\mathbf{X}) = \mathbf{\Phi}\mathbf{X} + \frac{1}{2}\bar{\mathbf{\Theta}}(\mathbf{X},\mathbf{X}) = \sum_{i=1}^{m} \phi_i X_i + \frac{1}{2}\sum_{i=1}^{m}\sum_{j=1}^{m} \bar{\mathbf{\Theta}}_{ij} X_i X_j, \tag{6.2.1}$$

where Ξ stands for the quadratic nonlinear mapping, with $\mathbf{\Phi}$ the $N \times m$ matrix of the master eigenvectors only, *i.e.* it is the restriction of $\mathbf{P}_\phi$ to the m selected master modes; and $\bar{\mathbf{\Theta}}_{ij} = (\mathbf{\Theta}_{ij} + \mathbf{\Theta}_{ji})/2$ is the symmetrized MD. The reduced-order dynamics is obtained by applying the second-order nonlinear mapping (6.2.1) to the original equations of motion (2.1.3). To that purpose, one can introduce the tangent space of the manifold $\mathbf{P}_\Xi$ as the derivative of the nonlinear mapping with respect to displacements, thus reading [20, 21]:

$$\mathbf{P}_\Xi = \frac{\partial \Xi}{\partial \mathbf{X}} \tag{6.2.2}$$

where $\mathbf{P}_\Xi$ is a matrix whose k-th column $[\mathbf{P}_\Xi]_k$ writes

$$[\mathbf{P}_\Xi]_k = \frac{\partial \Xi}{\partial \mathbf{X}_k} = \phi_k + \sum_{j=1}^{m} \bar{\mathbf{\Theta}}_{jk} X_j. \tag{6.2.3}$$

Derivating (6.2.1) two times with respect to t leads to:

$$\dot{\mathrm{q}} = \dot{\Xi} = \mathbf{P}_\Xi \dot{\mathbf{X}}, \tag{6.2.4a}$$

$$\ddot{\mathrm{q}} = \ddot{\Xi} = \mathbf{P}_\Xi \ddot{\mathbf{X}} + \left(\frac{\partial \mathbf{P}_\Xi}{\partial \mathbf{X}} \dot{\mathbf{X}}\right) \dot{\mathbf{X}}. \tag{6.2.4b}$$

Substituting for these in Eq. (2.1.3), the reduced-order dynamics reads :

$$\mathbf{P}_\Xi^t \mathbf{M}\ddot{\Xi} + \mathbf{P}_\Xi^t \mathbf{C}\dot{\Xi} + \mathbf{P}_\Xi^t \mathbf{K}\Xi + \mathbf{P}_\Xi^t \mathbf{G}(\Xi,\Xi) + \mathbf{P}_\Xi^t \mathbf{H}(\Xi,\Xi,\Xi) = \mathbf{P}_\Xi^t \mathbf{Q}. \tag{6.2.5}$$

One can note in particular that the quadratic and cubic terms $\mathbf{G}(\Xi,\Xi)$ and $\mathbf{H}(\Xi,\Xi,\Xi)$ will produce higher orders (up to power four for the first and power six for the second), and these higher orders will not be balanced by additional terms taken into account in the nonlinear mapping, which is a common feature in such asymptotic developments. Consequently it might appear more reasonable to truncate also Eq. (6.2.5) to the third order to maintain consistency. Following [61], one finally obtains, in full indicial notation, and by including Rayleigh damping, the third-order reduced dynamics, reading $\forall p = 1, ..., m$:

$$\begin{aligned}
&\ddot{X}_p + \omega_p^2 X_p + (\zeta_M + \zeta_K \omega_p^2)\dot{X}_p \\
&+ \sum_{i,j=1}^{m} \left((g_{ij}^p + \frac{\omega_p^2}{2}\bar{\theta}_{ij}^p) X_i X_j + \bar{\theta}_{ij}^p (\dot{X}_i \dot{X}_j + X_i \ddot{X}_j) + \bar{\theta}_{pi}^j (\omega_j^2 X_i X_j + X_i \ddot{X}_j) \right) \\
&+ \zeta_M \sum_{i,j,k=1}^{m} \left(2(\bar{\theta}_{ij}^p)\dot{X}_i X_j + \sum_{s=1}^{m} (\bar{\theta}_{pk}^s \bar{\theta}_{ij}^s)\dot{X}_i X_j X_k \right) + \zeta_K \omega_p^2 \sum_{i,j,k=1}^{m} \left(2(\bar{\theta}_{ij}^p)\dot{X}_i X_j + \sum_{s=1}^{m} (\bar{\theta}_{pk}^s \bar{\theta}_{ij}^s)\dot{X}_i X_j X_k \right) \\
&+ \sum_{i,j,k=1}^{m} \left(\left(h_{ijk}^p + \sum_{s=1}^{m} \left(g_{is}^p \bar{\theta}_{jk}^s (g_{ij}^s + \frac{\omega_s^2}{2}\bar{\theta}_{ij}^s) \right) \right) X_i X_j X_k + \sum_{s=1}^{m} (\bar{\theta}_{pk}^s \bar{\theta}_{ij}^s)(\dot{X}_i \dot{X}_j X_k + \ddot{X}_i X_j X_k) \right) = F_p.
\end{aligned} \tag{6.2.6}$$

In these equations, g_{ij}^p and h_{ijk}^p are the modal coupling coefficients that can be obtained by applying the STEP, and $\bar{\boldsymbol{\theta}}_{ij}$ is the symmetrized expression of the MD in the modal space, which is connected to the MD via:

$$\bar{\boldsymbol{\Theta}}_{ij} = \mathbf{P}_\phi \bar{\boldsymbol{\theta}}_{ij} = \sum_{s=1}^{N} \phi_s \bar{\theta}_{ij}^s. \tag{6.2.7}$$

In the right-hand side of Eq. (6.2.6), only F_p appears since it has been assumed that for the case under study, the forcing term is oriented along a master coordinate that is orthogonal to the symmetrized MD $\bar{\boldsymbol{\Theta}}$.

Assuming that only mode p is present as reduced coordinates, thus $X_i = 0$, for all $i \neq p$, Eq. (6.2.6) simplifies to the single dof reduction, read as:

$$\begin{aligned}
&\ddot{X}_p + \omega_p^2 X_p + (\zeta_M + \zeta_K \omega_p^2)\dot{X}_p + (g_{ij}^p + \frac{\omega_p^2}{2}\theta_{ij}^p) X_p^2 + \theta_{ij}^p (\dot{X}_i \dot{X}_j + X_i \ddot{X}_j) + \theta_{pi}^j (\omega_j^2 X_i X_j + X_i \ddot{X}_j) \\
&+ h_{ppp}^p + \sum_{s=1}^{n} \left(g_{ps}^p \theta_{pp}^s X_p^3 + (g_{pp}^s + \frac{\omega_s^2}{2}\theta_{pp}^s) X_p^3 + (\theta_{pp}^s)^2 (\dot{X}_p^2 X_p + \ddot{X}_p X_p^2) \right) = F_p.
\end{aligned} \tag{6.2.8}$$

6.3 Comparisons on the nonlinear dynamics and prediction of the type of nonlinearity

Theoretical comparison between NF and MDs on modal equations was first done by Vizzaccaro et al [61], then, further numerical comparisons between DNF and MDs on the FE model applications have been done by the author [78]. This section gives the comparison of the two nonlinear mappings, and the reduced-order dynamics as well as prediction of type of nonlinearity are the interested characteristic of the ROMs derived by the two methods. Only the main conclusions presented here aims to make the research framework more complete, for more details, one can find in the articles [61, 79].

The restriction to a single master dof is provided in Eqs. (6.1.12) for DNF and (6.2.8) for MD/SMD, so that one could draw out a term-by-term comparison between the reduced-order dynamics provided by the two methods. On the reduced-order dynamics for each of the methods, the general nonlinear oscillator equation describing the dynamics on the reduced subspace can be written under the general form as: In each case, the dynamics is reduced to a single-degree of freedom equation from which one can infer the hardening/softening behaviour. Let p be the master mode of interest, one can show that the reduced dynamics given by the three (MD, SMD, NF) methods, and also the static condensation (SC) for comparison reason, writes:

$$\ddot{R} + \omega_p^2 R_p + C_1 R_p^2 + C_2 \frac{\dot{R}_p^2}{\omega_p^2} + C_3 \frac{\ddot{R}_p R_p}{\omega_p^2} + C_4 R_p^3 + C_5 \frac{\dot{R}_p^2 R_p}{\omega_p^2} + C_6 \frac{\ddot{R}_p R_p^2}{\omega_p^2} = 0, \tag{6.3.1}$$

where the expression of C_1 to C_6 are different depending on the method, and are recalled in Tab. 6.3.1.

	C_1	C_2	C_3	C_4	C_5	C_6
MD	g_{pp}^p	0	0	$h_{ppp}^p - \sum_{\substack{s=1\\s\neq p}}^{n} \frac{2(g_{pp}^s)^2(\omega_s^2-2\omega_p^2)}{(\omega_s^2-\omega_p^2)^2}$	$\sum_{\substack{s=1\\s\neq p}}^{n} \frac{4(g_{pp}^s)^2\omega_p^2}{(\omega_s^2-\omega_p^2)^2}$	$\sum_{\substack{s=1\\s\neq p}}^{n} \frac{4(g_{pp}^s)^2\omega_p^2}{(\omega_s^2-\omega_p^2)^2}$
SMD	$-2g_{pp}^p$	$-2g_{pp}^p$	$-4g_{pp}^p$	$h_{ppp}^p - \sum_{s=1}^{n} \frac{2(g_{pp}^s)^2}{\omega_s^2}$	$\sum_{s=1}^{n} \frac{4(g_{pp}^s)^2\omega_p^2}{\omega_s^4}$	$\sum_{s=1}^{n} \frac{4(g_{pp}^s)^2\omega_p^2}{\omega_s^4}$
NF	0	0	0	$h_{ppp}^p - \sum_{s=1}^{n} \frac{2(g_{pp}^s)^2(\omega_s^2-2\omega_p^2)}{\omega_s^2(\omega_s^2-4\omega_p^2)^2}$	$\sum_{s=1}^{n} \frac{4(g_{pp}^s)^2\omega_p^2}{\omega_s^2(\omega_s^2-4\omega_p^2)^2}$	0
SC	g_{pp}^p	0	0	$h_{ppp}^p - \sum_{s=1}^{n} \frac{2(g_{pp}^s)^2}{\omega_s^2}$	0	0

Table 6.3.1: Table of coefficients of the reduced dynamics given by the four methods: MD for modal derivatives, SMD for static modal derivatives, NF for normal form and SC for static condensation.

From Tab. 6.3.1, it is shown that the normal form approach is able to cancel the quadratic nonlinearity and produce a cubic-order reduced dynamics, depending on two separate coefficients only.

Most importantly, when a slow/fast assumption is fulfilled ($\omega_s \gg \omega_p$), one can observe that the coefficients provided by the normal form and the MD method tend to equal to the values given by the SMD approach. More specifically, normal form has only two coefficients C_4 and C_5, and their expressions exactly match those from the SMD and MD in the case of slow/fast decomposition, with $C_4^{SF} = h^p_{ppp} - \sum_{s=1}^{n} \frac{2(g^s_{pp})^2}{\omega_s^2}$ and $C_5^{SF} = \sum_{s=1}^{n} \frac{4(g^s_{pp})^2\omega_p^2}{\omega_s^4}$, so that the only difference, between the reduced-order dynamics given by invariant manifold and quadratic manifold, lies in the additional terms C_1, C_2, C_3 and C_6.

Because the meaning of the reduced variables is not the same, to better understand the differences on the reduced-order dynamics, a further comparison has been done on the predictions of type of nonlinearity given by each reduction method. A first-order perturbative development allows definition of the angular frequency of free oscillations ω_{NL}, the expression is shown in Eq. (5.1.16) and recalled here: $\omega_{\text{NL}} = \omega_p(1 + \Gamma^p_{[M]} a^2)$, where a is the amplitude of the response of the pth master coordinate, ω_p is the nature frequency, and $\Gamma^p_{[M]}$ the coefficient governing the type of non-linearity with $[M]$ refers to the method. $\Gamma^p_{[M]} > 0$ indicates the hardening behaviour while $\Gamma^p_{[M]} < 0$ implies softening behaviour. The general expression for $\Gamma^p_{[M]}$ with all the C_i coefficients read as:

$$\Gamma^p_{[M]} = -\frac{1}{24\omega_p^4}(10C_1^2 + 10C_1C_2 + 4C_2^2 - 7C_2C_3 + C_3^2 - 11C_1C_3) + \frac{1}{8\omega_p^2}(3C_4 + C_5 - 3C_6). \quad (6.3.2)$$

with C_1 to C_6 different coefficients, which values are summarized in Tab. 6.3.1 for the these different methods. For the QM method based on MD and SMD, general formula have been derived in [61]. The Γ coefficients for these two cases read, first assuming a QM build on full modal derivatives:

$$\Gamma^p_{\text{MD}} = -\frac{5}{12\omega_p^2}(\frac{g^p_{pp}}{\omega_p})^2 + \frac{3}{8\omega_p^2}\left(h^p_{ppp} - \sum_{\substack{s=1 \\ s\neq p}}^{N} 2(\frac{g^s_{pp}}{\omega_s})^2 \left(1 + \frac{\omega_p^2(4\omega_s^2 - 3\omega_p^2)}{3(\omega_s^2 - \omega_p^2)^2}\right)\right). \quad (6.3.3)$$

If the QM is built from the simplified expression given by SMD, then the formula simplifies to:

$$\Gamma^p_{\text{SMD}} = -\frac{5}{12\omega_p^2}(\frac{g^p_{pp}}{\omega_p})^2 + \frac{3}{8\omega_p^2}\left(h^p_{ppp} - \sum_{\substack{s=1 \\ s\neq p}}^{N} 2(\frac{g^s_{pp}}{\omega_s})^2 \left(1 + \frac{4\omega_p^2}{3\omega_s^2}\right)\right). \quad (6.3.4)$$

Finally for the DNF, since in that case the initial problem has been projected onto the linear modes, then the full expressions of normal form given in [51, 56] allows writing directly the

Γ^p_{IM} coefficient, which is already given in Eq. (5.1.21) and can be rewritten as:

$$\Gamma^p_{\text{IM}} = -\frac{5}{12\omega_p^2}(\frac{g^p_{pp}}{\omega_p})^2 + \frac{3}{8\omega_p^2}\left(h^p_{ppp} - \sum_{\substack{s=1\\s\neq p}}^{N} 2(\frac{g^s_{pp}}{\omega_s})^2\left(1 + \frac{4\omega_p^2}{3(\omega_s^2 - 4\omega_p^2)}\right)\right). \tag{6.3.5}$$

From Eqs. (6.3.3) to (6.3.5), one can notice that the summed terms, with the form of one plus a term at the end of the right-hand side, provide the only differences among the three equations. In order to be more illustrative, the Γ^p_{SC} of static condensation is also given with considering the symmetry relationship of coefficients $g^p_{ps} = 2g^s_{pp}$ [13]:

$$\Gamma^p_{\text{SC}} = -\frac{5}{12\omega_p^2}(\frac{g^p_{pp}}{\omega_p})^2 + \frac{3}{8\omega_p^2}\left(h^p_{ppp} - \sum_{\substack{s=1\\s\neq p}}^{N} \frac{(g^s_{pp})^2}{\omega_s^2}\right). \tag{6.3.6}$$

Introducing C_{MD}, C_{SMD} and C_{NF} as the correction factors, *i.e.* the term in the summation, given by each method, and the correction term obtained by using static condensation is given following

$$C_{\text{SC}} = 2(\frac{g^s_{pp}}{\omega_s})^2. \tag{6.3.7}$$

By making all correction factors divide by C_{SC}, such that the g^s_{pp} is vanishing and one can then draw a comparison about the terms with expression depending only on the eigenfrequencies. Assuming that there is only one slave mode s and letting $\rho = \omega_s/\omega_p$ be the ratio between the eigenfrequency of the slave modes and that of the master mode, one then obtains:

$$\frac{C_{\text{MD}}}{C_{\text{SC}}} = 1 + \frac{4}{3}\frac{\rho^2 - 3/4}{3(\rho^2 - 1)^2}, \tag{6.3.8a}$$

$$\frac{C_{\text{SMD}}}{C_{\text{SC}}} = 1 + \frac{4}{3\rho^2}, \tag{6.3.8b}$$

$$\frac{C_{\text{NF}}}{C_{\text{SC}}} = 1 + \frac{4}{3(\rho^2 - 4)}. \tag{6.3.8c}$$

One can observe that these formulas show that all the methods predict the same first two terms in the expansion. Furthermore, with a slow/fast assumption ($\rho \to \infty$) fulfilled, the ratios tends to 1 in this case such that the static condensation also tends to the same results. For illustrative purpose, Fig. 6.3.1 shows the ratio of the correction factors expressed in Eq. (6.3.8), It is found that $\frac{C_{\text{MD}}}{C_{\text{SC}}}$ and $\frac{C_{\text{SMD}}}{C_{\text{SC}}}$ tend to equal to $\frac{C_{\text{NF}}}{C_{\text{SC}}}$ when ρ is increasing, with more detail, the error between the results derived from MD and NF is about 10% when $\rho = 4$ and less than 1% when $\rho =$

6. Generally, one can conclude that all methods are almost converged in terms of type of nonlinearity when $\omega_s > 4\omega_p$.

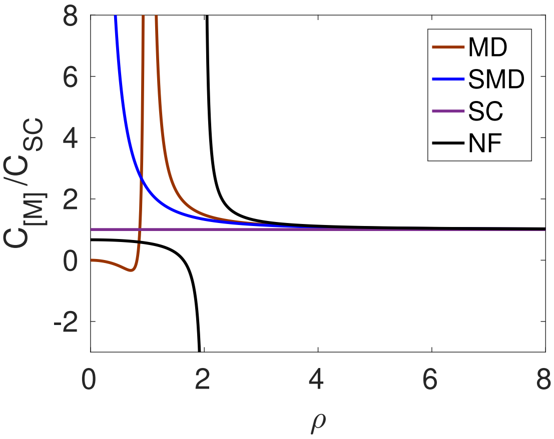

Figure 6.3.1: The ratios $\frac{C_{[\mathrm{M}]}}{C_{\mathrm{SC}}}$ with respect to the ratio of eigenfrequencies ρ, as expressed in Eq. (6.3.8). Blue: $\frac{C_{\mathrm{SMD}}}{C_{\mathrm{SC}}}$, brown: $\frac{C_{\mathrm{MD}}}{C_{\mathrm{SC}}}$, purple: $\frac{C_{\mathrm{SC}}}{C_{\mathrm{SC}}}$, and black: $\frac{C_{\mathrm{NF}}}{C_{\mathrm{SC}}}$. This figure is first shown in [61].

6.4 Example: A linear beam on a nonlinear elastic foundation

In order to give a first illustration of the capabilities of the different methods, an academic, analytical example is first used: a simply supported linear beam resting on a nonlinear elastic foundation. This example has already been studied in *e.g.* [80, 81, 56], in order to underline the use of invariant manifolds for producing accurate reduced-order models. The nonlinear elastic foundation being composed of quadratic and cubic power law, simple analytical formula are easily derived allowing full computation of modal coupling coefficients, so that a comprehensive comparison on the ability of the different reduction methods to predict the correct type of nonlinearity can be achieved.

6.4.1 Model equations and type of nonlinearity

In non-dimensional form, the undamped transverse vibrations of the linear beam on a nonlinear elastic foundation are governed by [80, 81, 56]:

$$\frac{\partial^2 w}{\partial t^2} + \frac{\partial^4 w}{\partial x^4} + \alpha_2 w^2 + \alpha_3 w^3 = 0, \tag{6.4.1}$$

where $w(x,t)$ is the transverse displacement, and α_2 and α_3 are the two free parameters that balance the relative importance of quadratic and cubic couplings. Simply supported boundary conditions are assumed, reading:

$$w(x,t) = 0,\ \frac{\partial^2 w}{\partial x^2} = 0, \quad \text{for } x = 0, 1. \tag{6.4.2}$$

The eigenmodes and the eigenfrequencies are easily computed as:

$$\phi_n(x) = \sqrt{2}\sin(n\pi x),\ \omega_n = n^2\pi^2. \tag{6.4.3}$$

Denoting as X_p the modal co-ordinate associated to the p-th linear mode, modal projection yields the equation of motion in the form of Eq. (2.1.5), where individual quadratic and cubic modal coupling coefficients respectively read:

$$\begin{aligned} g^p_{ij} &= \alpha_2 \int_0^1 \phi_i(x)\phi_j(x)\phi_p(x)dx, \\ h^p_{ijk} &= \alpha_3 \int_0^1 \phi_i(x)\phi_j(x)\phi_k(x)\phi_p(x)dx. \end{aligned} \tag{6.4.4}$$

The reduction methods (ICE, MD, SMD, NF) will be compared on their ability to correctly predict the type of nonlinearity (hardening/softening behaviour), when reducing the dynamics to a single master coordinate. Depending on the reduction method used, different values of Γ are obtained, which are already expressed in Eqs. (6.3.3) to (6.3.6) and reading as:

$$\Gamma^p_{\text{MD}} = -\frac{5}{12\omega_p^2}(\frac{g^p_{pp}}{\omega_p})^2 + \frac{3}{8\omega_p^2}\left(h^p_{ppp} - \sum_{\substack{s=1\\ s\neq p}}^{N} 2(\frac{g^s_{pp}}{\omega_s})^2\left(1 + \frac{\omega_p^2(4\omega_s^2 - 3\omega_p^2)}{3(\omega_s^2-\omega_p^2)^2}\right)\right). \tag{6.4.5a}$$

$$\Gamma^p_{\text{SMD}} = -\frac{5}{12\omega_p^2}(\frac{g^p_{pp}}{\omega_p})^2 + \frac{3}{8\omega_p^2}\left(h^p_{ppp} - \sum_{\substack{s=1\\ s\neq p}}^{N} 2(\frac{g^s_{pp}}{\omega_s})^2\left(1 + \frac{4\omega_p^2}{3\omega_s^2}\right)\right). \tag{6.4.5b}$$

$$\Gamma^p_{\text{IM}} = -\frac{5}{12\omega_p^2}(\frac{g^p_{pp}}{\omega_p})^2 + \frac{3}{8\omega_p^2}\left(h^p_{ppp} - \sum_{\substack{s=1\\ s\neq p}}^{N} 2(\frac{g^s_{pp}}{\omega_s})^2\left(1 + \frac{4\omega_p^2}{3(\omega_s^2-4\omega_p^2)}\right)\right). \tag{6.4.5c}$$

$$\Gamma^p_{\text{SC}} = -\frac{5}{12\omega_p^2}(\frac{g^p_{pp}}{\omega_p})^2 + \frac{3}{8\omega_p^2}\left(h^p_{ppp} - \sum_{\substack{s=1\\ s\neq p}}^{N} \frac{(g^s_{pp})^2}{\omega_s^2}\right). \tag{6.4.5d}$$

Apart from the methods mentioned above, for this example we will also consider the prediction given if one reduces the dynamics to the eigenmode subspace. Assuming only linear modal coordinate p present in the dynamics (*i.e.* $X_i = 0$ for all $i \neq p$), and denoting as Γ^p_{LN} the coefficient for that case, one arrives easily at [51, 56]:

$$\Gamma^p_{\mathrm{LN}} = -\frac{5}{12\omega_p^2}(\frac{g^p_{pp}}{\omega_p})^2 + \frac{3}{8\omega_p^2}h^p_{ppp}. \tag{6.4.6}$$

By comparing the coefficients Γ^p_{LN}, Γ^p_{ICE}, Γ^p_{NNM}, Γ^p_{MD}, Γ^p_{SMD} respectively given by Eqs. (6.4.5) and (6.4.6), it is obvious that regions of hardening or softening behaviour in the parameter plane (α_2,α_3) are different so that all the studied methods will predict different results. The aim of the next section is to highlight this and compare the predictions to a full-order solution in order to understand the ability of the reduction methods to correctly retrieve the first important nonlinear characteristics in nonlinear oscillations.

6.4.2 Results

Fig. 6.4.1 shows the hardening/softening regions for the first three modes of the beam as predicted by the different methods proposed, in the parameter space (α_2, α_3). Only the sign of the prediction (hardening/softening) is reported, the lines showing the points of cancellation where the formulas Eqs. (6.4.5) and (6.4.6) are vanishing. In each case, the upper left part of the plane (corresponding to large values of the cubic nonlinearity α_3) are linked to a hardening behaviour since a large cubic positive term is dominating. On the other hand, in the lower right part of the figure (large values of quadratic nonlinearity α_2), a softening behaviour is at hand. The continuous line denotes the hardening/softening transition as predicted by the different methods. Five curves are compared each time. The first one corresponds to the reduction to a single linear normal mode, Eq. (6.4.6). Although this simplification is known from a long time to produce incorrect predictions in most of the cases, it is reported here for the sake of completeness. The prediction given by static condensation (ICE method), Eq. (6.4.5d) is reported in purple, while both predictions using MD or SMD QM, Eqs. (6.4.5a)-(6.4.5b), are given in brown and blue. Finally the prediction given by the normal form approach, Eq. (6.4.5c), is in red. As known from theoretical results, see *e.g.* [51, 56], at first-order the prediction given by normal form gives the correct result, so that all the other methods can be compared to this reference. This will be again confirmed numerically next, by comparing to full-order solutions.

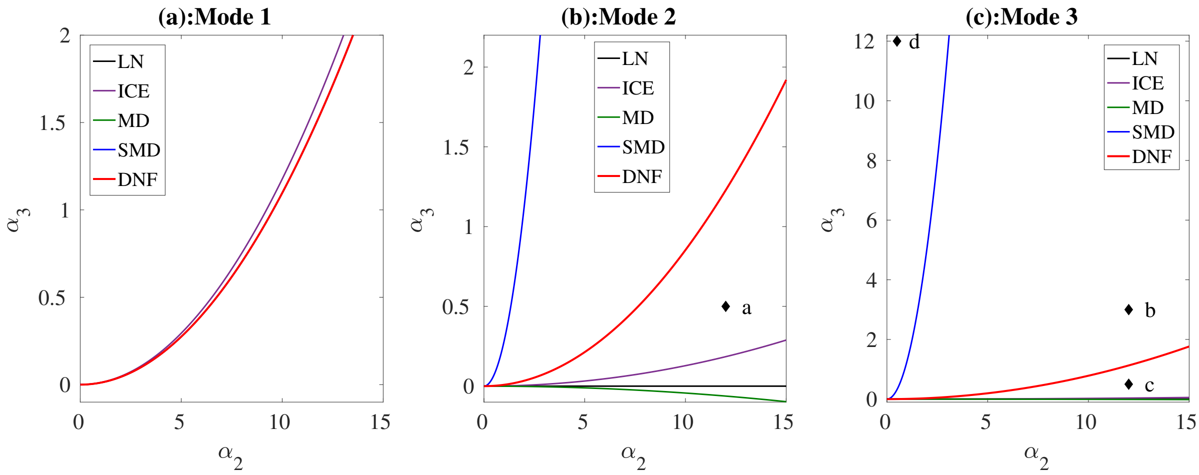

Figure 6.4.1: Hardening/softening regions in the parameter plane (α_2,α_3) for the first three modes of a simply supported beam resting on a nonlinear elastic foundation. In the legend, LN: single linear mode; ICE: implicit condensation and expansion; MD: QM with full modal derivatives; SMD: QM with static modal derivatives; DNF: single nonlinear normal mode built from normal form.

For the first mode, one can observe that the predictions given by all five methods are fully coincident. This means in particular that the first invariant manifold shows only very slight curvature and is very close to the linear eigensubspace, such that restriction to a single linear mode is already correct. In that context, one also understands easily that all other reduction methods are able to catch back a simple linear behaviour and thus offers a good prediction. Only the ICE method gives a very slight departure which remains however negligible. For mode 1, one can also observe that the slow/fast assumption is well retrieved, since the ratio ω_2/ω_1 is equal to 4, meaning that all the slave modes fulfill the criteria given in [61, 58] about slow/fast assumption for ICE and QM methods.

For all the other modes, all the methods gives very different predictions, as shown in Fig. 6.4.1 for modes 2 and 3. As already reported in [56], restriction to a single linear mode gives a completely erroneous prediction, meaning that the invariant manifolds have important curvatures and strongly depart from the linear subspace. This feature is well illustrated by Fig. 6.4.2, one can observe that the first mode is almost not coupled with mode 3 since the manifold is almost flat as shown in Fig. 6.4.2(a), that is the reason all the reduction methods work well and give the same correct prediction in the case of mode 1, as shown in Fig. 6.4.1(a). While the third mode is strongly coupled with the first mode, leading to a curved manifold as shown in Fig. 6.4.2(b), and the coupling relationship cannot be retrieved by other methods because of slow/fast assumption is not fulfilled, such that in Fig. 6.4.1(c) only the DNF gives the correct prediction.

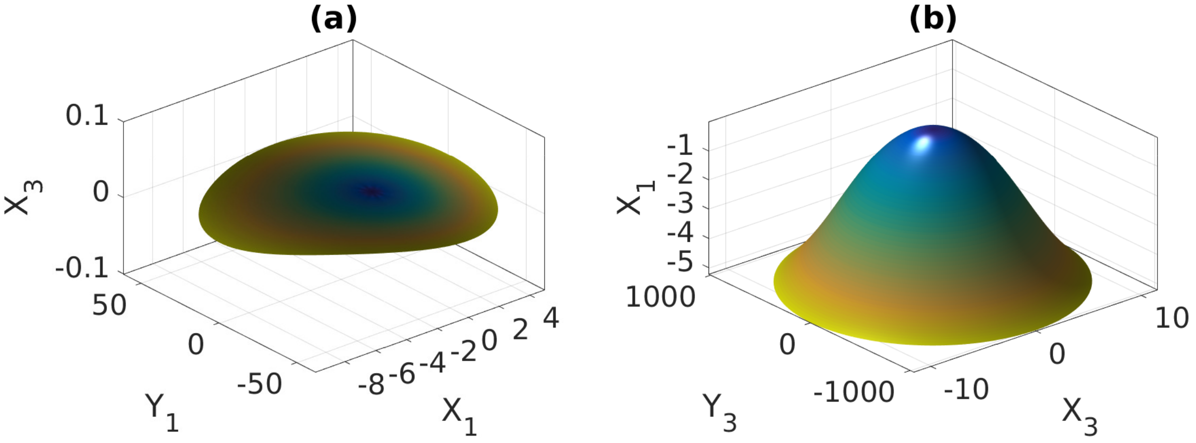

Figure 6.4.2: The invariant manifold of the full model obtained from numerical continuation of periodic orbits in phase space (a): (X_1, Y_1, X_3) and (b): (X_3, Y_3, X_1). The parameters of the system are chosen as $\alpha_2 = 12, \alpha_3 = 0.5$.

Regarding the slow/fast assumption, one can now easily understands, by forming the ratio ω_n/ω_2 and ω_n/ω_3 for modes 2 and 3 as shown in Tab. 6.4.1, that the assumption is not fulfilled anymore. For mode 2 one has for example $\omega_1/\omega_2 = 1/4$ and $\omega_3/\omega_2 = 2.25$: two slave modes do not meet the slow/fast assumption. For mode 3, 4 slave modes do not fulfill the constraint since the ratio between the master mode and slave modes are smaller than 4. Consequently, all the three reduction methods that need this frequency separation (ICE, QM with either MD or SMD), fail to accurately predict the type of nonlinearity.

In order to give more insight to these results, four specific points corresponding to selected values of (α_2, α_3), are retained, and the backbone curves are compared with a reference solution, obtained by keeping ten linear modes in the truncation, a number sufficiently large to achieve comfortable convergence. The four points are denoted with diamonds and letters a, b, c, and d in Fig. 6.4.1. Point a is selected for mode 2, while points b, c and d refers to mode 3. Their specific locations have been selected in order to underline the different possible predictions given by all tested methods. The backbone curves have been obtained numerically with a continuation method using asymptotic-numerical method combined with harmonic balance, implemented in the software Manlab. The reference solution is obtained by using the nonlinear equation

	1st	2nd	3rd	4th	5th	6th	7th	8th	9th	10th
ω_i	9.87	39.48	88.83	157.91	246.74	355.30	483.61	631.65	799.44	986.96
ω_i/ω_1	1	4	9	16	25	36	49	64	81	100
ω_i/ω_2	0.25	1	2.25	4	6.25	9	12.25	16	20.25	25
ω_i/ω_3	0.11	0.44	1	1.78	2.78	4	5.44	7.11	9	11.11
ω_i/ω_4	0.06	0.25	0.56	1	1.56	2.25	3.06	4	5.06	6.25

Table 6.4.1: Natural frequencies of the modes and the corresponding ratio as the criteria of the slow/fast assumption.

of motion of the full-order model (as shown in Eq. (2.1.5)) with ten modes. On the other hand, the reduction methods used the reduced dynamics as given in Eq. (4.2.1) for the ICE method, Eq. (6.2.6) for QM MD and SMD (discarding damping), and Eq. (6.1.10) for DNF (again without damping).

Fig. 6.4.3 reports the obtained results. Fig. 6.4.3(a), corresponding to point a in Fig. 6.4.1, has been selected since only DNF and QM-SMD method should predict softening behaviour, while QM-MD and ICE method should predict hardening. This is verified by the numerical computation. One can observe that only normal form is able to catch the correct behaviour. The softening behaviour computed by QM-SMD is overestimated while MD and ICE method predict an unreliable solution. One can observe that this case corresponds to a quite large value of α_2 as compared to α_3, meaning that quadratic terms are dominating the cubic ones. This example thus clearly illustrates that ICE and QM, with slow/fast assumption not fulfilled, offers an incorrect processing of quadratic terms, finally leading to an incorrect prediction of the type of nonlinearity.

Fig. 6.4.3(b), corresponding to point b in Fig. 6.4.1, shows a case where only QM-SMD predicts a softening behaviour, all other methods giving a hardening one. This result is effectively verified by the numerical computation. The solution given by DNF method is close to the reference solution, but finally departs at large amplitude, as a consequence of the fact that the DNF method is an asymptotic expansion up to order three. In this specific case, even if the slow/fast assumption is not met for mode 3, the prediction given by ICE and QM-MD is good. Even if the exact correct curvature of the backbone is not retrieved at small amplitudes, the prediction

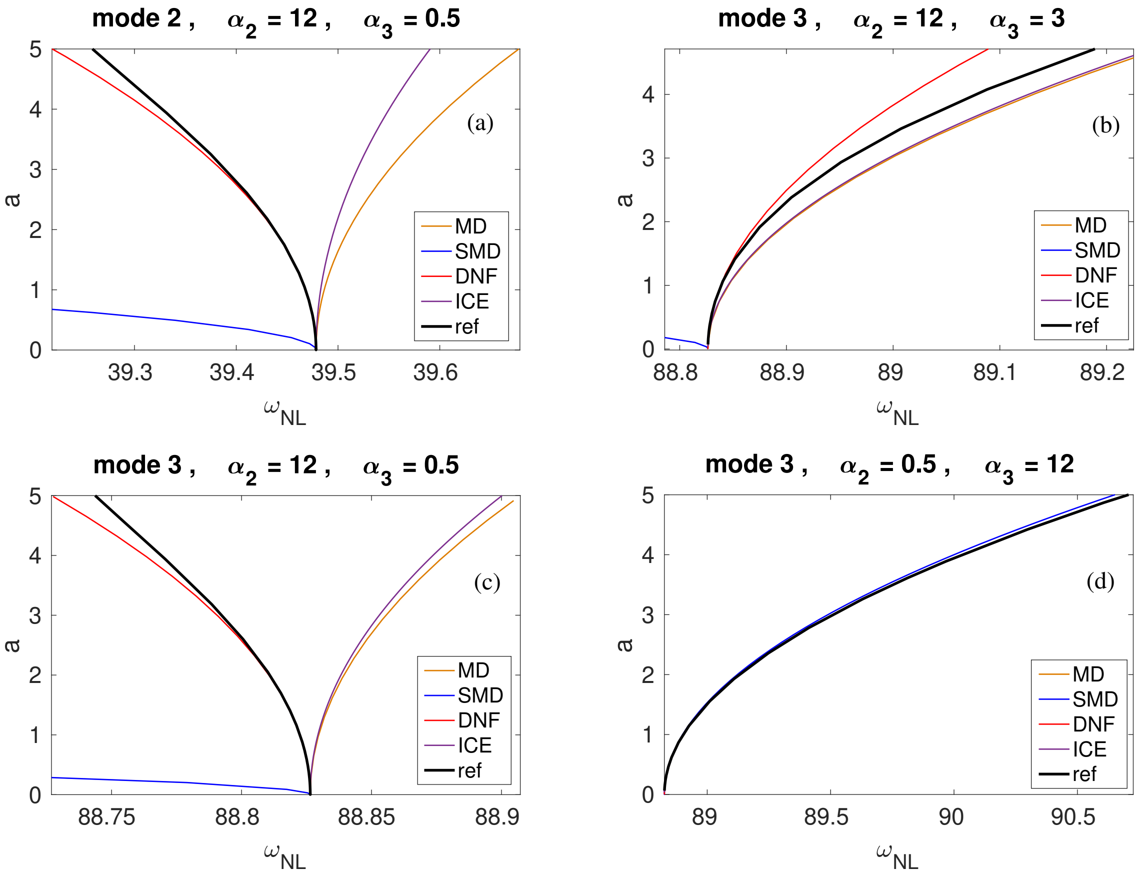

Figure 6.4.3: Backbone curves for the linear beam on nonlinear elastic foundation. (a) second mode, $\alpha_2 = 12, \alpha_3 = 0.5$, (b) third mode, $\alpha_2 = 12, \alpha_3 = 3$, (c) third mode, $\alpha_2 = 12, \alpha_3 = 0.5$. (d) third mode, $\alpha_2 = 0.5, \alpha_3 = 12$. Reference solution (black thick line): continuation on a solution built from 10 linear modes retained.

remains no too far from the reference up to a comfortable amplitude.

Fig. 6.4.3(c) reports a case that is close to Fig. 6.4.3(a) but now for mode 3, underlining again how incorrect predictions can be obtained. Finally, Fig. 6.4.3(d) shows a case where the cubic nonlinearity dominates the quadratic one. In that case one clearly observes that all the methods are able to produce a correct solution.

As a conclusion on this simple analytical example, it has been shown that when the slow/fast assumption is not met, ICE and QM method based on MD or SMD can predict incorrect results for the type of nonlinearity. The incorrect treatment of the quadratic terms by these methods has been also specifically underlined, another concern that is different from the slow/fast assumption involving the eigenfrequencies. It has been shown on selected examples that when the quadratic nonlinearity is dominant, ICE and QM methods can predict incorrect results, *e.g.* a hardening behaviour instead of softening, or too large values of the curvature of the backbone as compared to the reference. On the other hand the DNF method always produces the first-order correct assumption, and can only fail at large amplitudes due to its limitation related to the third-order asymptotic expansion.

6.5 Example: Prediction of the type of nonlinearity of free spherical shells

The aim of this section is to compare three different methods, the quadratic manifold (QM) built from (static) modal derivatives, the stress manifold built form ICE method and the normal form approach, on a shell example. More particularly, the ability of the three methods in the prediction of the type of nonlinearity (*i.e.* the first term in the amplitude-frequency relationship that dictates the hardening or softening behaviour), is investigated. In nonlinear vibrations, predicting the correct type of nonlinearity is the first characteristic that needs to be correctly given by a ROM since being a fundamental property of the nonlinear oscillations. This general result is here illustrated on the specific case of a shallow spherical shell with increasing curvature. For that purpose, the von Kármán model, assuming shallowness, neglecting in-plane and rotary inertia and using an Airy stress function, is used [82], such that geometrically nonlinear vibrations of the shell are described by partial differential equations. Thus, the full shell model can be reduced into a single degree of freedom equation by using different reduction methods and thus leading to ROMs that can be applied to predict the type of nonlinearity of the shell.

It should be noted that the comparison of NF and (S)MDs on the prediction of the type of nonlinearity of the two dofs system (spring-mass system shown in Fig. 5.2.1) in the previous chapter is given in [61], here the investigation is extended to the thin shell.

6.5.1 Modelling

A free-edge spherical shell, made of a homogeneous isotropic material of density ρ, Poisson's ratio ν and Young's modulus E is considered, with the dimension of thickness h, radius of curvature R and outer diameter $2a$ (see Fig. 6.5.1). Large transverse deflections and moderate rotations are considered, so that the model is a generalization of von Kármán's theory for large deflection of plates [82].

The shell is assumed to be thin so that $h/a \ll 1$ and $h/R \ll 1$, and shallow: $a/R \ll 1$. Since we are interested in predicting the type of nonlinearity, damping and forcing are not considered. The equations of motion read [82, 83, 84, 85]:

$$D\Delta\Delta w + \frac{1}{R}\Delta F + \rho h\ddot{w} = L(w, F), \tag{6.5.1a}$$

$$\Delta\Delta F - \frac{Eh}{R}\Delta w = -\frac{Eh}{2}L(w, w), \tag{6.5.1b}$$

where w is the displacement, F the the Airy stress function, Δ the Laplacian, L is a quadratic bi-linear operator and $D = Eh^3/12(1 - v^2)$ is the flexural rigidity, t indicates the time variable and the double dot ($\ddot{\bullet}$) the second derivative with respect to time. The problem is made nondimensional by introducing $r = a\bar{r}$, $t = a^2\sqrt{\frac{\rho h}{D}}\bar{t}$, $w = h\bar{w}$, and $F = Eh^3\bar{F}$. Thus, substituting the above definitions in equations of motion, Eq. (6.5.1), and dropping the overbars in the results, one obtains:

$$\Delta\Delta w + \varepsilon_q\Delta F + \ddot{w} = \varepsilon_c L(w, F), \tag{6.5.2a}$$

$$\Delta\Delta F - \sqrt{\kappa}\Delta w = -\frac{1}{2}L(w, w). \tag{6.5.2b}$$

where the two nondimensional coefficients are $\varepsilon_q = 12(1-v^2)\sqrt{\kappa}$, and $\varepsilon_c = 12(1-v^2)$, making also appear the aspect ratio κ of the shell as $\kappa = \frac{a^4}{R^2h^2}$.

The complete linear analysis has been tackled in [82]. As an important result, the behaviour of the eigenfrequencies with respect to the aspect ratio κ is shown in Fig. 6.5.2. One can

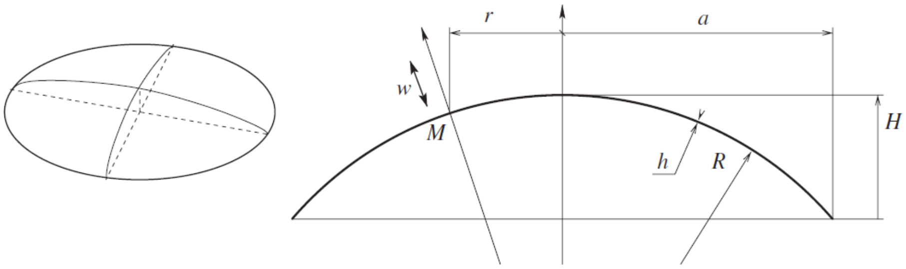

Figure 6.5.1: Geometry of the free-edge shallow spherical shell.

observe in particular that purely asymmetric modes $(k, 0)$, with k nodal diameters and no nodal circle, show a very slight dependence upon κ. On the other hand, axisymmetric modes $(0, n)$ without nodal diameters, as well as mixed mode (k, n) with both $k \neq 0$ and $n \neq 0$, show a huge dependence on curvature. These results are important in order to analyze the type of nonlinearity, depending on the mode considered.

In order to predict the type of nonlinearity, Eqs. (6.5.2) are projected onto the natural basis of the eigenmodes. After projection, the semi-discretized equations of motion read as given in Eq.(2.1.5) without external forcing [82]:

$$\ddot{X}_p + \omega_p^2 X_p + \sum_{i=1}^{+\infty}\sum_{j=1}^{+\infty} g_{ij}^p X_i X_j + \sum_{i=1}^{+\infty}\sum_{j=1}^{+\infty}\sum_{k=1}^{+\infty} h_{ijk}^p X_i X_j X_k = 0, \tag{6.5.3}$$

where X_p refers to the modal amplitude of the pth transverse mode, and ω_p its radian eigenfrequency. The nonlinear coupling coefficients write:

$$g_{ij}^p = -\varepsilon_q \iint_{\varphi_\perp} \phi_p L(\phi_i, \psi_j) dS - \frac{\varepsilon_q}{2} \sum_{b=1}^{+\infty} \frac{1}{\xi_b^4} \iint_{\varphi_\perp} L(\phi_i, \phi_j) \Upsilon_b dS \iint_{\varphi_\perp} \phi_p \Delta \Upsilon_b dS, \tag{6.5.4a}$$

$$h_{ijk}^p = \varepsilon_c \sum_{b=1}^{+\infty} \frac{1}{\xi_b^4} \iint_{\varphi_\perp} L(\phi_i, \phi_j) \Upsilon_b dS \iint_{\varphi_\perp} \phi_i L(\phi_k, \Upsilon_b) dS. \tag{6.5.4b}$$

ϕ_i refers to transverse eigenmodes while ψ_j are obtained from the diagonalization of the Airy stress function. ξ_n and eigenfunction Υ_n are zeros from the eigenproblem, the interested reader can find their detailed expression in [82]. $\varphi_\perp$ is the domain defined by $(r, \theta) \in [0\ 1] \times [0\ 2\pi]$. Eqs. (6.5.3) describe the dynamics of the shell and the trend of nonlinearity can be inferred from these equations.

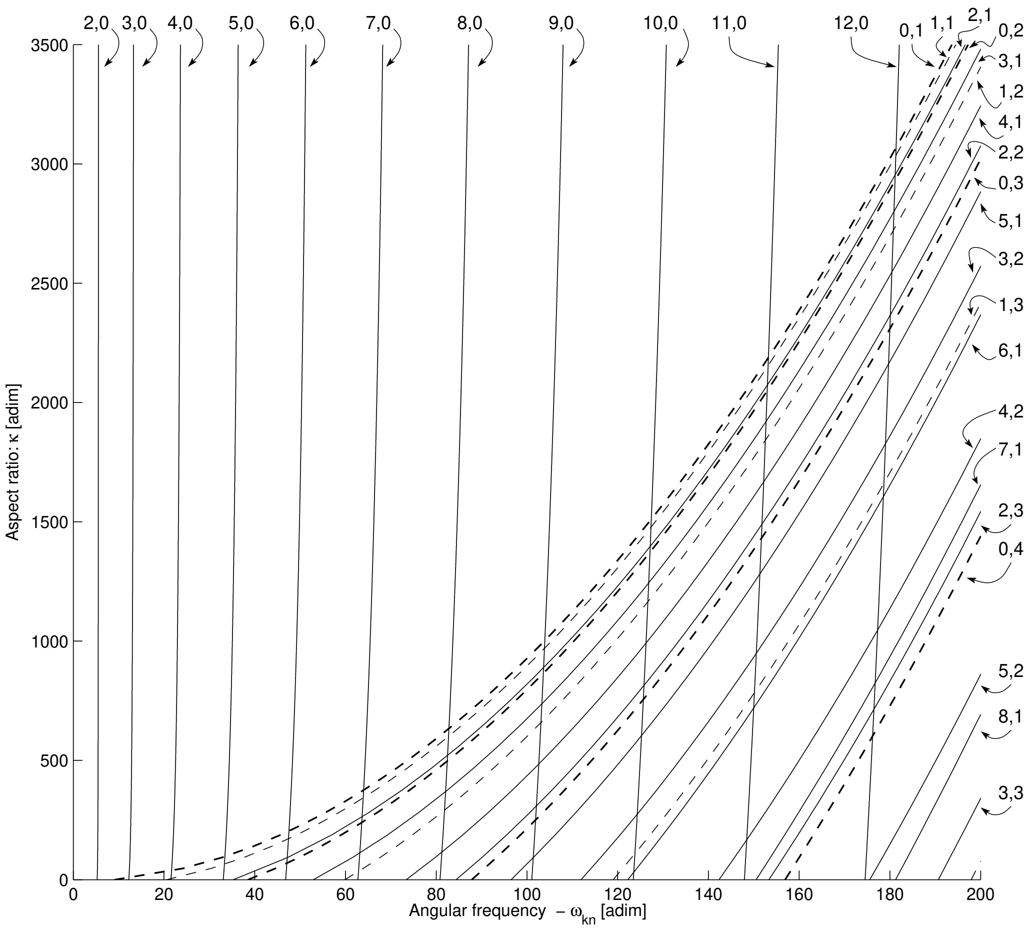

Figure 6.5.2: Dimensionless natural frequencies ω_{kn} of the shell as a function of the aspect ratio κ (figure reprinted from [41]). $\kappa = 0$ corresponds to the flat plate case.

6.5.2 Analytical Prediction of the Type of Nonlinearity

In this section, we compare the prediction of the type of nonlinearity using the semi-analytical derivation obtained from von Kármán model. Three different predictions are contrasted. The first one is given by the normal form approach, and has already been reported in [41]. As known from theoretical results [51], this prediction is correct thanks to the invariance property of nonlinear normal modes (NNMs). Three other solutions are compared to this reference solution, two obtained from the QM approach developed in [20, 21], the first one using full MD, and the second one static modal derivatives (SMD), the last one obtained from the stress manifold derived by ICE method.

As the said in the last section, the MD, SMD and ICE methods are awaited to give correct results only if a slow/fast assumption between master and slave coordinates is at hand. This slow/fast assumption has been quantified in previous section. If $\rho > 4$, the slow/fast assumption is fulfilled, while $\rho < 3$ means that QM and ICE method will probably fail. In order to analyze the fulfilment of this slow/fast assumption, let us introduce ρ_p for spherical shells as:

$$\rho_p = \min_{n \in E_s}(\frac{\omega_n}{\omega_p}), \tag{6.5.5}$$

where E_s is the set of all the slave modes, *i.e.* all the modes except the master coordinate p. The coupling relationship is given in [41], as shown in Tab. 6.5.1.

Master mode	Slave modes E_s
(2,0)	(4,0), (4,1), (4,2), (0,1), (0,2), (0,3) and (0,4),
(3,0)	(6,0), (6,1), (6,2), (0,1), (0,2), (0,3) and (0,4),
(4,0)	(8,0), (8,1), (0,1), (0,2) and (1,1),
(0,1)	(0,2), (0,3), (0,4), (0,5), (0,6) and (0,7),
(0,2)	(0,1), (0,3), (0,4), (0,5), (0,6) and (0,7),
(2,1)	(4,0), (4,1), (4,2), (4,3), (4,4), (0,1), (0,3), (0,4), (0,5), (0,6) and (0,7),

Table 6.5.1: The investigated master mode with its corresponding coupled slave modes. Where $(k, 0)$ are the purely asymmetric modes, $(0, n)$ are the axisymmetric modes and (k, n) are the mixed modes.

The results are shown for 6 different master modes in Fig. 6.5.3 [86, 79]. The first three cases are purely asymmetric modes, (2,0), (3,0) and (4,0); then the first two axisymmetric modes are considered, and finally a mixed mode (2,1) is selected. In the figures, the reference solution is given by the normal form approach (NNM) in magenta. The prediction given by QM MD is in red, QM SMD in yellow and ICE in blue. The figures have two y-axis allowing to also report the variations of ρ_p for the mode of interest, as function of κ.

For mode (2,0), one can observe that MD, SMD and ICE methods fail to recover 1:2 resonance leading to a change of behaviour of the type of nonlinearity. On the other hand, when κ is larger than 20, then ρ_p increases and is close to 4, the slow/fast assumption is retrieved and the three methods give the same results. Modes (3,0) and (4,0) show another important feature, already noted in [61]: the MD method has a divergence in the case of 1:1 resonance, which has no physical explanation and is interpreted as a failure of the method. For purely asymmetric modes, since they show a very slight dependence on curvature, this means that all the slave

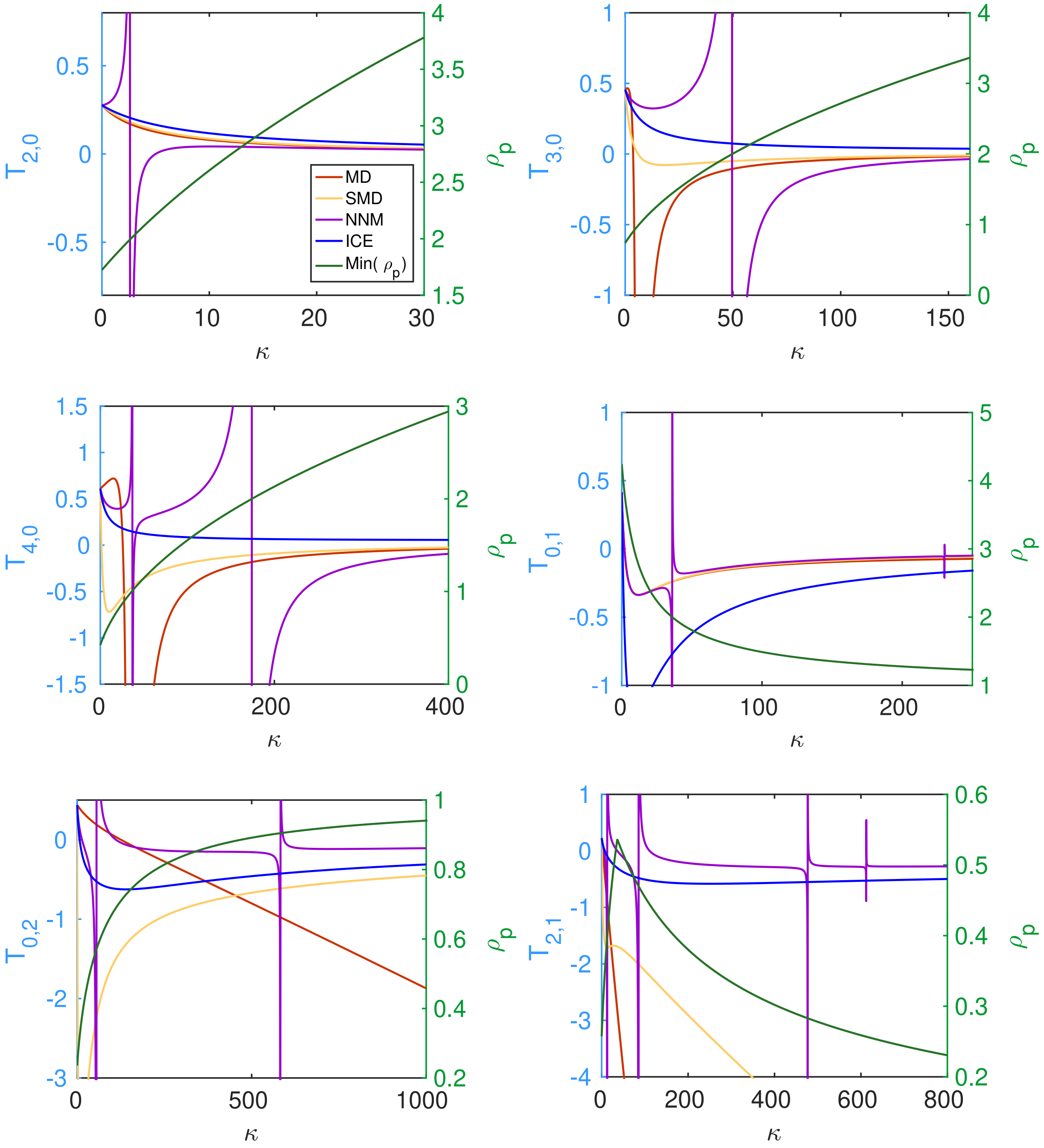

Figure 6.5.3: Type of nonlinearity for 6 modes of the shell: modes (2,0), (3,0), (4,0), (0,1), (0,2), (2,1).

modes have strongly increasing eigenfrequencies with κ. Consequently for all these modes the slow/fast assumption is always finally retrieved, but sometimes at large values of curvature.

Mode (0,1) has the particularity to be very well predicted by using a single linear mode, as shown in [41]. Consequently the MD, SMD, ICE and NF methods behave correctly, even though ρ is decreasing with κ so that slow/fast does not hold. As a matter of fact, for all axisymmetric and mixed modes, the behaviour of their eigenfrequencies shown in Fig. 6.5.2 underlines that slow/fast assumption will never been met. Consequently the prediction of the type of nonlinearity given by MD, SMD and ICE methods completely fails.

6.6 Conclusion

Now, a short summary about the comparison between normal form and modal derivatives is given.

These two methods share two common points: they both introduce nonlinear mapping when building a ROM, also, they are both non-intrusive and simulation-free method. However, it is more interesting to see the differences between these two method. Firstly, in the nonlinear change of coordinate aspect, the quadratic manifold only contains the displacements as unknowns, while the normal form approach takes into account displacements and velocities, which is logical since displacements and velocities have to be considered as independent variables in a dynamical system's perspective, thus, normal form gives a more complete link to the geometry in phase space. Secondly, the quadratic manifold is defined up to the second-order while the expressions of normal form are up to order three and are able to touch higher orders easily. Thirdly, as said before, normal form theory relies of firm mathematical theorems, ensuring a clean conceptual framework, while modal derivatives appear as an ad-hoc, yet efficient, method used in the vibration community, and it has been proved that the modal derivatives works only when slow/fast assumption fulfilled, more details can be found in [61].

The subsequent examples have illustratively demonstrated the comparison of the these methods. The type of nonlinearity for linear beam with elastic foundation and free-edge shallow spherical shells have been studied with a special emphasis on comparing different models and methods. These reduction methods have been contrasted in their ability to correctly predict the type of nonlinearity. For the beam case, the backbone curves obtained by different reduction methods are also compared. For the shell case, the von Kármán model has been used to illustrate how the reduction methods can give different predictions. These results underline that same as the ICE method, modal derivatives approaches also need a slow/fast assumption in order to yield a correct prediction. For numerous modes of the shallow spherical shell, the slow/fast assumption is never met so that the methods (using either MD, SMD or ICE) completely fail in predicting correctly the hardening/softening behaviour, whereas the normal form always gives the correct prediction.

Part III

Applications of reduced order models to continuous structures

Chapter 7

Beams

In Part II, the stress manifold and quadratic manifold are theoretically compared with the invariant manifold, and the comparisons show that these nonlinear mappings without invariant property only work when a slow/fast assumption is fulfilled. In this Part, large FE models are investigated instead of small models, and a special emphasis will put on the numerical solutions of the ROMs, no analytical comparisons will be given anymore. The aim of the Part is to present numerical comparisons of model-order reduction methods for geometrically nonlinear structures in the general framework of FE procedures, *i.e.*, comparing the outcomes provided by the ROMs derived by these methods, in order to offer a more complete picture of the advantages and drawbacks of the methods.

In this Chapter, the reduction methods are compared on finite element beam structures, and all the calculations have been realized with the open-source finite element software Code_Aster. Three different beam examples are selected, in order to test the accuracy of the methods in different contexts. The first example is a clamped-clamped beam becoming an arch by increasing curvature. The second example is a straight beam with 1:1 internal resonance between the two possible polarization of the fundamental mode, selected in order to test the methods on a case where two internally resonant master modes are needed. Finally a cantilever beam is selected so as to illustrate the behaviour of the methods when inertia nonlinearity is important.

7.1 A clamped-clamped beam with increasing curvature

The first example is a clamped-clamped beam, initially straight (case 1), for which two different levels of curvature are added to the neutral line in order to transform the beam to a shallow arch (case 2) and then to a non-shallow arch (case 3). Note that this example has first been introduced in [61], where the comparison between the normal form result and the QM-MD and SMD methods were compared on the backbone curves only. In this section, we extend these results by first adding the ICE method in the comparisons, and second by considering a frequency-response function with damping and forcing. The geometry of the beams and the mesh retained are shown in Fig. 7.1.1. The straight beam has a length L=0.7m, and square cross-section with equal thickness h and width b, $h = b =$ 5cm. The material is linear elastic (Young modulus E = 124 GPa, Poisson's ratio ν = 0.3 and density ρ = 4400 kg.m^{-3}). The height of the static deflection of the shallow arch is 5.5cm, while that of the non-shallow arch is 25cm. Three-dimensional hexahedral finite elements with 20 nodes are used in each case. For the straight beam, 60 elements (4 in the section and 15 in the length), resulting in a total number of 1287 dofs have been selected, while for the arches a total of 96 solid elements (4 in the section and 24 in the length), resulting in 2097 dofs are used.

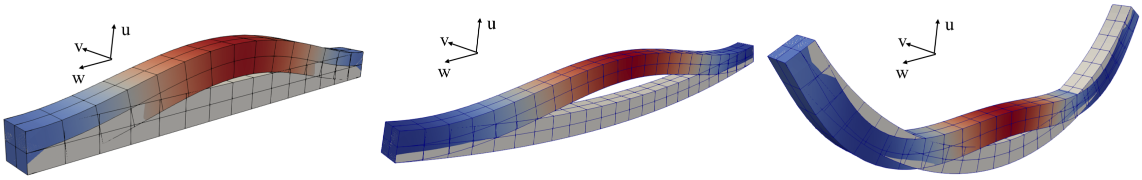

Figure 7.1.1: The three beams under investigation with the mesh used and the deformed shape of the bending mode under study. Flat beam with 60 elements, arches with increasing curvature and 96 elements.

In each case, reduction to a single master mode is targeted, considering the nonlinear vibrations of the first bending mode. For the straight beam, the eigenfrequency of the first bending mode is f_1=545.60 Hz. For the shallow arch, the first bending appears as the second mode (by order of increasing frequency), with an eigenfrequency f_2=372.28 Hz, and for the non-shallow arch it appears in fourth position, with f_4=1004 Hz. Let us first illustrate on this case how the ICE method is used to retrieve the nonlinear stiffness. Fig. 7.1.2 shows the nonlinear relationship found by applying a static load of amplitude β on the first bending mode, and its fitting by polynomial laws of order 3, 5 and 7. A total of 100 values of applied loads have been selected for the flat beam and the shallow arch cases, and 122 for the non-shallow arch. The load scales, as defined from the ICE method, see *e.g.* [19, 4, 57, 58], are chosen to obtain displacements around the range of ± 1.4 times of thickness for the beam case, $-2h$ to $3.8h$ for the shallow arch and $-2.74h$ to $1.56h$ for the non-shallow arch. In each case, the application of the static force gives the displacement as a function of β, from which the fits allow inverting the relationship. In particular, one can observe the appearance of strong even powers in the polynomial expansion for the last two cases, with a non-symmetric restoring force. In these last two cases also, the third-order approximation is not sufficient to correctly retrieve the stiffness behaviour law, and order 5 is at least needed.

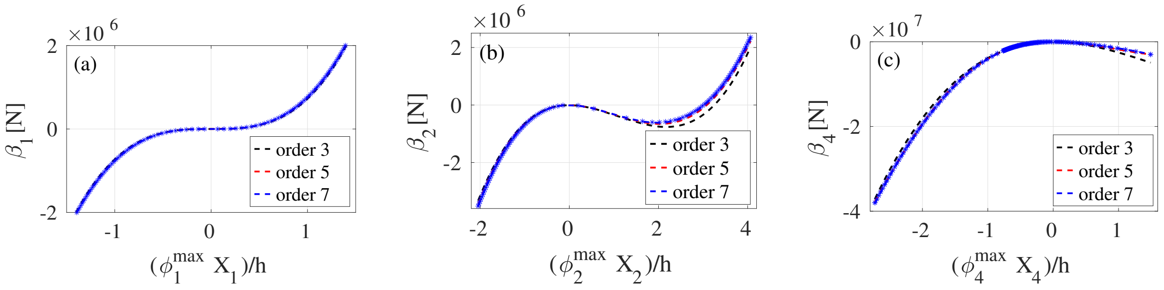

Figure 7.1.2: Illustration of the fitting procedure for the ICE method: blue stars $*$ represent the outputs obtained from static applied force on the FE model, the dashed curve is the fitted polynomial, black: order 3, red: order 5, blue: order 7. (a) straight beam, (b) shallow arch for which the first bending mode appears as the second mode, (c) non-shallow arch (first bending mode in fourth position).

Fig. 7.1.3 displays the backbone curves obtained for the three beams with increasing curvature. A reference solution is obtained via numerical continuation on all the degrees of freedom, using a code with parallel implementation of harmonic balance method and pseudo arc-length [87]. On the other hand, the reduced dynamics being composed of a single master mode, the backbones are obtained numerically by continuation using a method combining harmonic balance and asymptotic-numerical method implemented in Manlab.

In Fig. 7.1.3(a) for the straight clamped-clamped beam, the slow/fast assumption is very well fulfilled and all methods easily catch the correct nonlinear behaviour. The shallow arch results are shown in Fig. 7.1.3(b). In that case, the slow/fast assumption is just below the limit proposed in [61], since the ratio of eigenfrequencies between the first and the third bending modes is equal to 3.44. Also, quadratic nonlinear couplings between bending modes have appeared. For this main reason, the QM-SMD method fails to predict the correct nonlinear behaviour of the backbone, as already remarked in [61]. The QM-MD and DNF reduction give an almost equivalent result in terms of the backbone, which is close to the reference solution but slightly departs when the amplitudes are becoming large. Finally in that case, the ICE method provides the best approximation to the reference solution, mostly because the fitting procedure is able to retrieve correctly the quadratic nonlinearity, and that the slow/fast assumption is not strongly violated. Note that for all the figures, the ICE method has been used in the reduction with the seventh-order fitted polynomial. Consequently the order in the asymptotics is larger than the other methods, which could also explain its better performance in that case.

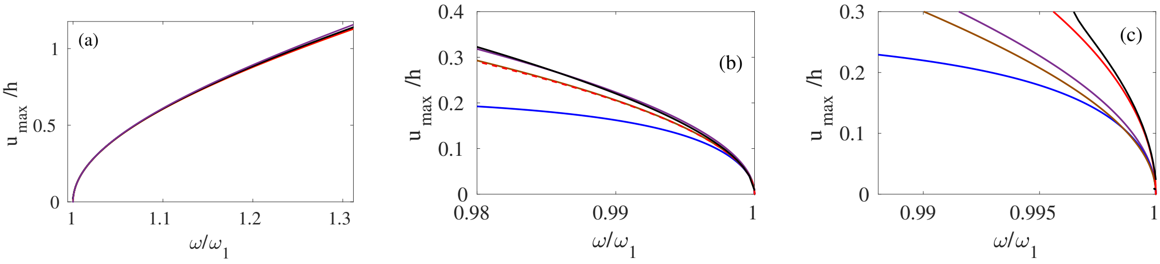

Figure 7.1.3: The backbone curves for (a) the straight beam, (b) the shallow arch, and (c) the non-shallow arch. reference solution with numerical continuation in black. Comparison of reduction methods with a single master coordinate, purple: ICE method, blue: QM-SMD, brown: QM-MD and red: DNF.

In the case of the non-shallow arch, Fig. 7.1.3(c), the frequency ratio between third and first bending is 1.66, meaning that the slow/fast assumption is strongly broken. The consequence is that three methods are not able to retrieve the correct softening nonlinearity anymore: QM-MD and QM-SMD, as well as ICE method, even though the ICE method is still pushed to seventh order. In that case the unfulfillment of the slow/fast assumption is stronger so that whatever the order in the ICE method, it won't converge to the correct value. On the other hand, DNF still predicts the correct nonlinear behaviour, and shows a slight departure at larger amplitude, the only known limitation of the method linked to its asymptotic development.

A further insight is given to these results by computing the frequency-response functions (FRFs) for the three tested beams. In each case, a pointwise harmonic forcing is considered, located at the center of the beam, with an excitation frequency in the vicinity of the first bending mode. Rayleigh damping is added to the FE model, and a stiffness proportional damping is taken into account, such that the damping matrix reads $\mathbf{C} = \zeta_K \mathbf{K}$. The value of the coefficient

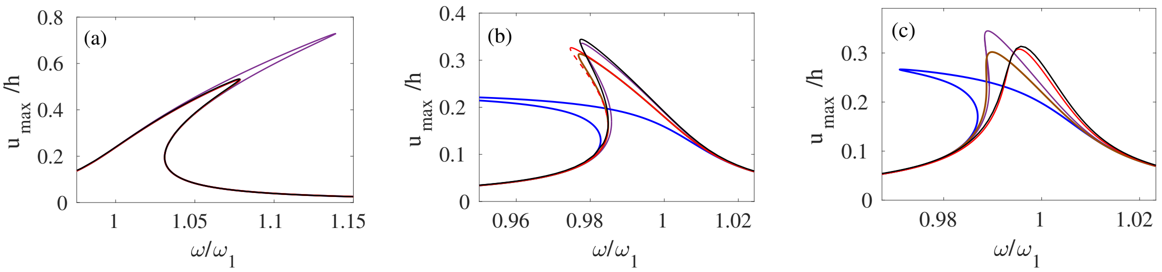

Figure 7.1.4: The FRF for the beam, shallow arch, and non-shallow arch. Red: DNF, Blue: SMD, Brown: MD, Purple: ICE method, Black: reference solution.

b has been selected such that a damping ratio of 0.5% for the first bending mode is at hand, which leads to the following numerical values: $\zeta_K = 2.91e-06s$ for the straight beam, $\zeta_K = 4.27e-06s$ for the shallow arch, and $\zeta_K = 1.58e-06s$ for the non-shallow arch.

Fig. 7.1.4 shows the obtained results where the four reduction methods are compared to the reference. Note that the treatment of the damping factor is strongly different in each case. The ICE method is the less efficient method for treating out the damping. Indeed, working on the fitting procedure of the nonlinear stiffness only, the method does not provide any method to include the damping of the slave modes in the reduced dynamics. Consequently only the damping of the master mode is considered, which generally leads to strongly underestimate the losses in the ROM. This is particularly true for the straight beam case in Fig. 7.1.4(a). On the other hand, for the two arches, the level of damping in the master mode is sufficient to approximately predict the correct maximum value in the FRF.

The other nonlinear reduction methods, QM and DNF, takes the damping of the slave modes in the reduction process thanks to the nonlinear mapping. This leads to a perfect match with the reference solution in the beam case. For the arches, the problems already underlined in the backbone persist for the FRF. In particular the QM-SMD method is not able to predict a correct FRF for the two arches, while QM-MD gives a correct computation for the shallow arch, but departs in the non-shallow arch case. The DNF method generally gives a correct approximation but misses some slight quantitative informations for the two arches, mainly due to the two approximations used to build the ROM: the asymptotics at second-order only, and the treatment of the forcing, not strictly aligned with the nonlinear direction of the manifold but simply to the linear eigenspace. ICE method with order seven has been used in each case, giving an excellent result in the shallow arch case, but generally is awaited to underpredict the losses, as observed in the beam and non-shallow arch cases.

The results of this example exactly agree and validate the conclusion given by the theoretical comparisons among these reduction methods in the last Part, *i.e.*, ICE and QM methods need the fulfilment of the slow/fast assumption between master and slave modes in order to predict correct results. Also, incorrect treatment of the quadratic nonlinear terms in the QM-SMD method leads to problematic results once the second-order terms in the restoring force are important. Furthermore, by investigating this numerical example, one can observe that ICE method is able to rapidly propose a ROM with possible higher orders, but fails as soon as the slow/fast assumption is violated. Also, the method is not able to take into account the losses of the slave mode in the dynamics of the master mode, while DNF always proposes the correct trend in terms of hardening/softening behaviour, is able to take properly the damping of the slave modes into account, and is only limited to its fundamental assumptions linked to the used asymptotic and the treatment of the forcing.

7.2 Clamped beams with 1:1 resonance

The second example is a straight clamped-clamped beam that is allowed to vibrate in the two bending directions, leading to different polarizations and consequently a 1:1 internal resonance. The objective of the comparison is to illustrate the ability of the methods in handling a more complex case with two master modes and bifurcations due to the presence of the internal resonance, with the existence of coupled and uncoupled solutions [88, 89].

Two different cases are investigated, where the constant parameters are: the length of the beam, $L = 1$m, the density $\rho = 4400 kg/m^3$, the Young modulus $E = 1.04e11 Pa$, and the Poisson's ratio $v = 0.3$. For the space discretization, 3D hexahedral 20 nodes brick elements, with 40 elements in the length and 4 in the cross-section, have been used. The difference between the two beams is on their relative values of width b and thickness h. A first case with perfect square section with $h = b = 3$cm gives no detuning between the eigenfrequencies of the two polarizations of the first bending modes which are perfectly equal. On the other hand, a second case with $h = 3$cm and $b = 3.15$cm allows creating a detuning of 4.92$\%$ between these two eigenfrequencies. Table 7.2.1 summarizes the geometrical parameters, and Fig. 7.2.1 shows the mesh retained and the two polarizations of the fundamental bending mode (displacements along these two direction are noted u and v, and w is the in-plane motion).

Case	length(m)	thickness(m)	width(m)	ω_1(rad/s)	ω_2(rad/s)	detuning ε
a	1	0.03	0.03	941.37	941.40	0.0
b	1	0.03	0.0315	941.47	987.83	4.92%

Table 7.2.1: Dimensions and eigenfrequencies of the clamped beams with and without detuning, where $\varepsilon = (\omega_2 - \omega_1)/\omega_1$.

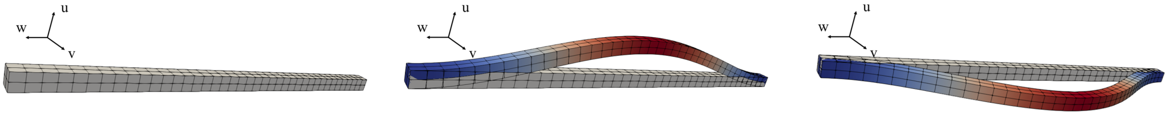

Figure 7.2.1: The beam mesh and the two polarizations of the first bending mode.

Since the reduced dynamics contains two master coordinates, the fitting procedure for the ICE method first needs to create the two-dimensional stress manifold, from which the nonlinear restoring force is deduced. The fitting procedure is illustrated in Fig. 7.2.2. 44 static load cases with different values of (β_1, β_2) are selected where β_i is the modal force amplitude factor applied on mode i. From these, the modal displacements (X_1, X_2) are retrieved from the static deformation, and a stress manifold is obtained, shown in space (X_1, X_2, β_1) in Fig. 7.2.2. The load scales are chosen so as to obtain amplitudes of displacements in the range of ± 1 times of thickness. The perfect and detuned case are considered showing a clear symmetric stress manifold.

7.2.1 Backbone curves

We first report the computation of the backbone curves in the two selected cases, with and without detuning. As in the previous section, a reference solution is derived thanks to numerical continuation on the full-order model, and is compared to the ROMs with two master coordinates. The analytical solution derived in [89] allows for a better understanding of the awaited results. In particular, when a detuning is present, an uncoupled solution with the lowest frequency mode only excited exist until a pitchfork bifurcation point, where this solution becomes unstable in favour of a coupled solution corresponding to an elliptic mode.

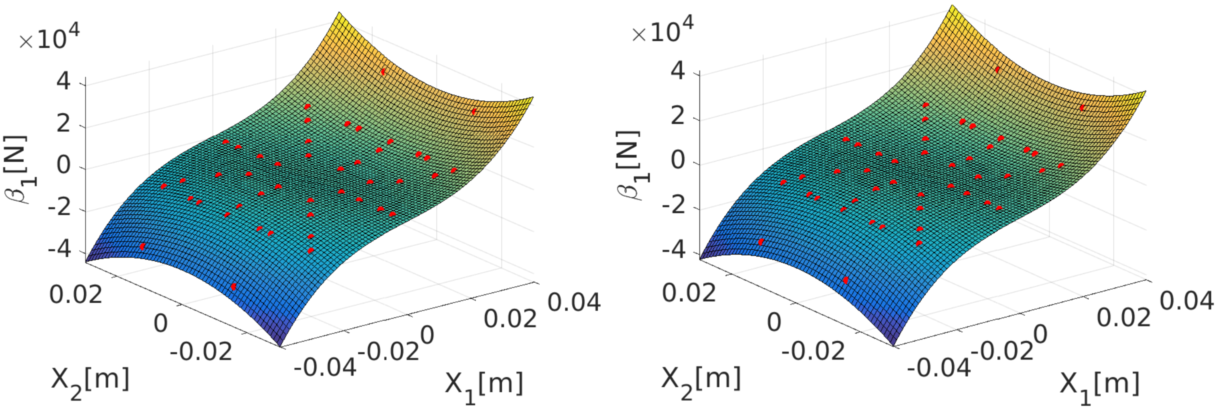

Figure 7.2.2: Illustration of the fitting procedure in ICE method, with two master modes, for the case of the clamped beam without detuning $\varepsilon = 0$ (left), and with detuning $\varepsilon = 4.92\%$ (right).

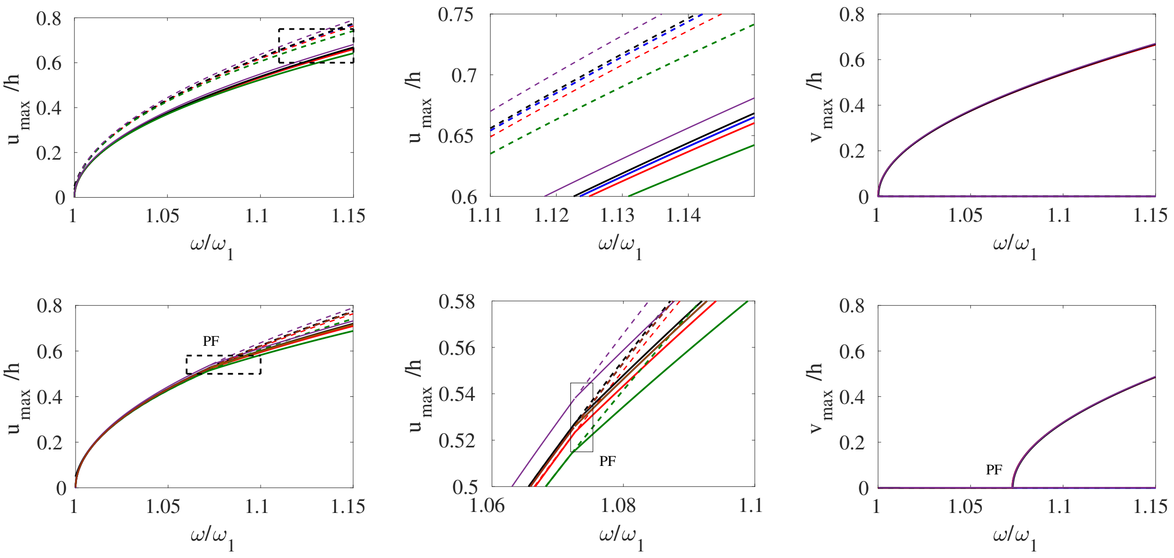

Figure 7.2.3: Backbone curves of the clamped-clamped beam in 1:1 resonance. First row: without detuning, second row: with detuning. Left column: first polarization in u direction, center column: zoom, right column: second polarization in v direction. Comparison of reference full-order solution (black line) to ROMs with two master modes, purple: ICE, blue: QM-SMD, brown: QM-MD, red: DNF. Green curve represents the analytical solution. PF: pitchfork bifurcation point.

Fig. 7.2.3 shows the obtained results. The first row corresponds to the case without detuning while the second row with detuning. In order to correctly represent the two vibration polarizations, the displacements at center of the beam in the two u and v directions (see Fig. 7.2.1) are reported. When there is no detuning, from the first row of Fig. 7.2.3, one can observe that two types of backbone curves are numerically retrieved. A unstable solution, corresponding to an uncoupled mode where only the displacement along u is excited (such that $v = 0$), and a stable coupled solution with both $u \neq 0$ and $v \neq 0$, which represents that the energy of the excited mode is transformed to the corresponding resonant mode. With the detuning, from the second row of Fig. 7.2.3, it can be observed that the backbone curve is stable until arriving at a pitchfork bifurcation point, then, the solution is separated into the uncoupled solution and coupled solution branches where the resonant mode starts to be excited ($v \neq 0$) [89]. The main conclusion is that all the methods are able to correctly retrieve the unforced and undamped dynamics of this problem, with all the specific analytical features in terms of existence, stability and bifurcations of the 1:1 internally resonant dynamics. This is easily explained by looking at the reduced dynamics computed by each of the methods, for the sake of brevity, the equations are given only in the case without detuning, and for undamped-unforced case.

Using the ICE method, the polynomial third-order fitting from the set of imposed forcings allows retrieving the following reduced dynamics:

$$\ddot{R}_1 + 8.8618e5R_1 + 4.3527e8R_1^3 + 4.5018e8R_1R_2^2 = 0, \tag{7.2.1a}$$

$$\ddot{R}_2 + 8.8624e5R_2 + 4.3575e8R_2^3 + 4.4893e8R_2^2R_1 = 0. \tag{7.2.1b}$$

Note that, in the fitting procedure, only the nonlinear terms are assessed. The linear ones are given as known from the eigenanalysis. The small difference between the two squared eigenfrequency is the consequence of the small difference in the computed eigenfrequencies reported in Tab 7.2.1, which is due to numerical roundoff. Only four monomial terms are needed and they correspond to the ones studied in [89].

The ROM computed with the DNF method reads:

$$\ddot{R}_1 + 8.8618e5R_1 + 4.5659e8R_1^3 + 4.5657e8R_1R_2^2 + 0.1265R_1\dot{R}_1^2 + 0.0042R_2\dot{R}_1\dot{R}_2 + 0.1224R_1\dot{R}_2^2 = 0, \tag{7.2.2a}$$

$$\ddot{R}_2 + 8.8624e5R_2 + 4.5657e8R_1^2R_2 + 4.5659e8R_2^3 + 0.1265R_2\dot{R}_2^2 + 0.0042R_1\dot{R}_1\dot{R}_2 + 0.1224R_2\dot{R}_1^2 = 0. \tag{7.2.2b}$$

The linear part is left unchanged (identity-tangent nonlinear mapping). One can observe that the additional monomials (involving squared velocities) are obviously negligible as compared to the four resonant cubic terms already present in Eqs. (7.2.1). This clearly underlines that the dynamics is completely driven by the most simple system with only four resonant monomial terms corresponding to 1:1 internal resonance.

Using the QM-SMD method, a different nonlinear mapping is introduced. As already observed in [61], the QM-SMD method produces much more monomial terms in the reduced dynamics, with additional terms involving the accelerations. The reduced dynamics now reads:

$$\begin{aligned}&\ddot{R}_1 + 8.8618e5R_1 + 4.5670e8R_1^3 + 4.5668e8R_1R_2^2 + 0.1263R_1^2\ddot{R}_1 + 0.1243R_1R_2\ddot{R}_2 + 0.0021R_2^2\ddot{R}_1\\ &+ 0.1263\dot{R}_1^2R_1 + 0.1243\dot{R}_1\dot{R}_2R_2 + 0.0021\dot{R}_2^2R_1 = 0,\end{aligned}\tag{7.2.3a}$$

$$\begin{aligned}&\ddot{R}_2 + 8.8624e5R_2 + 4.5670e8R_2^3 + 4.5668e8R_2^2R_1 + 0.1263R_2^2\ddot{R}_2 + 0.1243R_2R_1\ddot{R}_1 + 0.0021R_1^2\ddot{R}_2\\ &+ 0.1263\dot{R}_2^2R_2 + 0.1243\dot{R}_2\dot{R}_1R_1 + 0.0021\dot{R}_1^2R_2 = 0.\end{aligned}\tag{7.2.3b}$$

Again, one can observe that in this particularly simple case of a straight beam, all the added terms have negligible coefficients. Again the dynamcis is driven by the simple system composed of only four cubic terms. The same is also observed when applying the QM-MD method, leading to the following reduced dynamics:

$$\begin{aligned}&\ddot{R}_1 + 8.8618e5R_1 + 4.5670e8R_1^3 + 4.5668e8R_1R_2^2 + 0.1264R_1^2\ddot{R}_1 + 0.1243R_1R_2\ddot{R}_2 + 0.0021R_2^2\ddot{R}_1\\ &+ 0.1264\dot{R}_1^2R_1 + 0.1243\dot{R}_1\dot{R}_2R_2 + 0.0021\dot{R}_2^2R_1 = 0,\end{aligned}\tag{7.2.4a}$$

$$\begin{aligned}&\ddot{R}_2 + 8.8624e5R_2 + 4.5670e8R_2^3 + 4.5668e8R_2^2R_1 + 0.1264R_2^2\ddot{R}_2 + 0.1243R_2R_1\ddot{R}_1 + 0.0021R_1^2\ddot{R}_2\\ &+ 0.1264\dot{R}_2^2R_2 + 0.1243\dot{R}_2\dot{R}_1R_1 + 0.0021\dot{R}_1^2R_2 = 0.\end{aligned}\tag{7.2.4b}$$

In this particular case, the reduced dynamics given by QM-SMD and QM-MD are completely equivalent, explaining that the methods produce exactly the same predictions. Note however that this result is specific to the studied case and more complex structure generally leads to different formulations for MD and SMD approaches.

As a matter of fact, the dynamical equations contains only the four resonant monomial terms that are also retained in the analytical developments provided in [89]. All the other terms are negligible. The slow/fast assumption is very well fulfilled, and no quadratic terms are present. Consequently all the methods are able to retrieve such a dynamics which is fully driven by only four cubic terms, without invariant-breaking terms.

7.2.2 Frequency response curves

The forced-damped dynamics is now investigated by computing the FRFs. A forcing term aligned with direction u is imposed at the center of the beam in order to excite one polarization, and observe the nonlinear coupling with the second polarization along v. A Rayleigh damping of the form $\mathbf{C} = \zeta_K \mathbf{K}$ is selected, with $\zeta_K = 1.0622e - 5s$, corresponding to a damping ratio of 0.5 percent for the first mode. The reduction methods are compared to the full-order reference solution, all of them being obtained by numerical continuation. Note however that the continuation method implemented in [87] is not able yet to perform the stability computation, neither to locate pitchfork bifurcation points. In order to circumvent the second limitation, a small forcing in the v direction, with an amplitude selected as 1% the amplitude in the u direction, is also applied. Consequently the solution is perturbed with a non-zero solution in the v direction, allowing the continuation method to retrieve the coupled branch. On the other hand, the reduced dynamics FRFs are computed with Manlab, which reports stability and detects pitchfork bifurcations.

Let us first illustrate the results found in the case without detuning, shown in Fig. 7.2.4, where the amplitude of the forcing is set at 300N. The topology of the solution, already reported in other cases (see *e.g.* [52]), is characterized by a pitchfork bifurcation point from which the branch of coupled solutions arise. Along this solution branch, two Neimark-Sacker bifurcation points exist, leading to quasiperiodic solutions in this area. Importantly, all the methods are able to retrieve all these important dynamical features. Small quantitative differences are observable. The ICE method strongly underestimate the damping in the reduced dynamics. This is again a consequence of the treatment of the losses by the reduction method, which is not able to take into account the damping factors of the slave modes. On the other hand, QM and DNF methods produce a very satisfactory prediction of the full dynamics. QM-MD and SMD gives completely equivalent results in this case, the curves being fully overlapped. Indeed, as reported in Eqs. (7.2.1) to (7.2.4) in this particular case, using either MD or SMD in the reduction method for building the quadratic manifold, produces exactly the same equations for the reduced

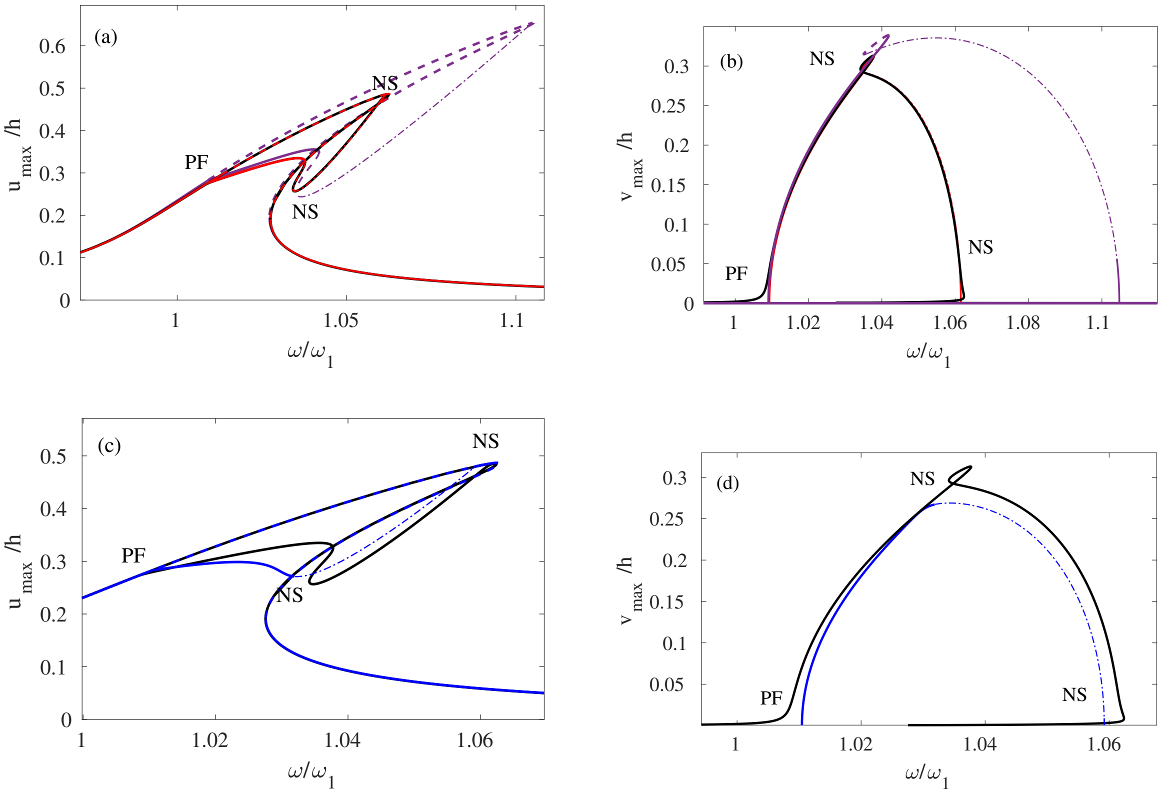

Figure 7.2.4: Frequency-response functions for the beam with 1:1 resonance without detuning. Left column is the solution in u direction (driven mode), and right column in v direction (second polarization, companion mode). The full-order reference solution (black, without stability) is compared to different ROMs. (a)-(b): ICE method (purple) and DNF (red). (c)-(d): QM-SMD (blue). PF: pitchfork bifurcation point. NS: Neimark-Sacker bifurcation. Solid curves: stable part, dashed curve : unstable solution, dash-dotted curve: unstable solution between the NS points (quasiperiodic solution).

dynamics. Consequently in this section, only the results of QM-SMD are shown in the figures. A slightly better quantitative prediction is given by DNF on the second polarization (companion mode), this difference being in any case small. One can also remark that the trick used to get the coupled solution for the full-order model is visible close to the imperfect pitchfork bifurcation points for the second polarization.

For illustrative purpose, the numerical time integration is also given in Fig. 7.2.5. For both full-order solution and ROM solution, Newmark-β scheme is used with $\beta = 0.25$ and $\gamma = 0.5$, and the time step is set to be $\tau = 0.0002$s that corresponds to a sampling rate of 5 kHz, which fully ensures accuracy for the modes that we are investigating with 25 points per period. In each case, the initial conditions correspond to the structure at rest in u and w direction, but has a very small displacement in v direction with $1e-4m$, such that the response of the beam can depart more easily from the uncoupled unstable solution.

From the figure, the ROM derived by the DNF method can perfectly catch the 1:1 internal resonance, more importantly, as compared with the full-order solution, the amplitude in the steady state and also the time needed for the second oscillator v to go from zero up to the steady state are perfectly well reproduced by the time simulation on the ROM. The gains in using ROMs for time integration are very important. The full-order analysis is run by Code_Aster for approximately 5 hours on the 12-core processor computer with 16 GB of RAM and CPU @ 2.20GHz, and the construction as well as utilization of the ROM only takes about 2 minutes for the same simulation.

The results for the beam with detuning $\varepsilon = 4.92\%$ is shown in Fig. 7.2.6, where the Rayleigh damping is now mass-proportional and has been set to $\mathbf{C} = \zeta_M \mathbf{M}$ with $\zeta_M = 9.4147s^{-1}$ (still following the rule of 0.5 percent for the first mode), and the amplitude of the forcing is 1500N, a large value needed in order to enter correctly the coupled branch solution, reaching vibration amplitudes close to 2 times the thickness. One can note that in this case all methods give very close results. In particular, using mass-proportional damping creates damping ratios that decreases with increasing frequencies. Consequently the damping values of the slave modes are smaller and smaller. The consequence is that most of the losses is given by the modal damping factor of the master modes, so that the ICE method is now able to give a correct prediction as compared to the other methods. QM-MD and SMD are again perfectly overlapped for the same reason as before, consequently only QM-SMD curve is shown. The branch of coupled solutions

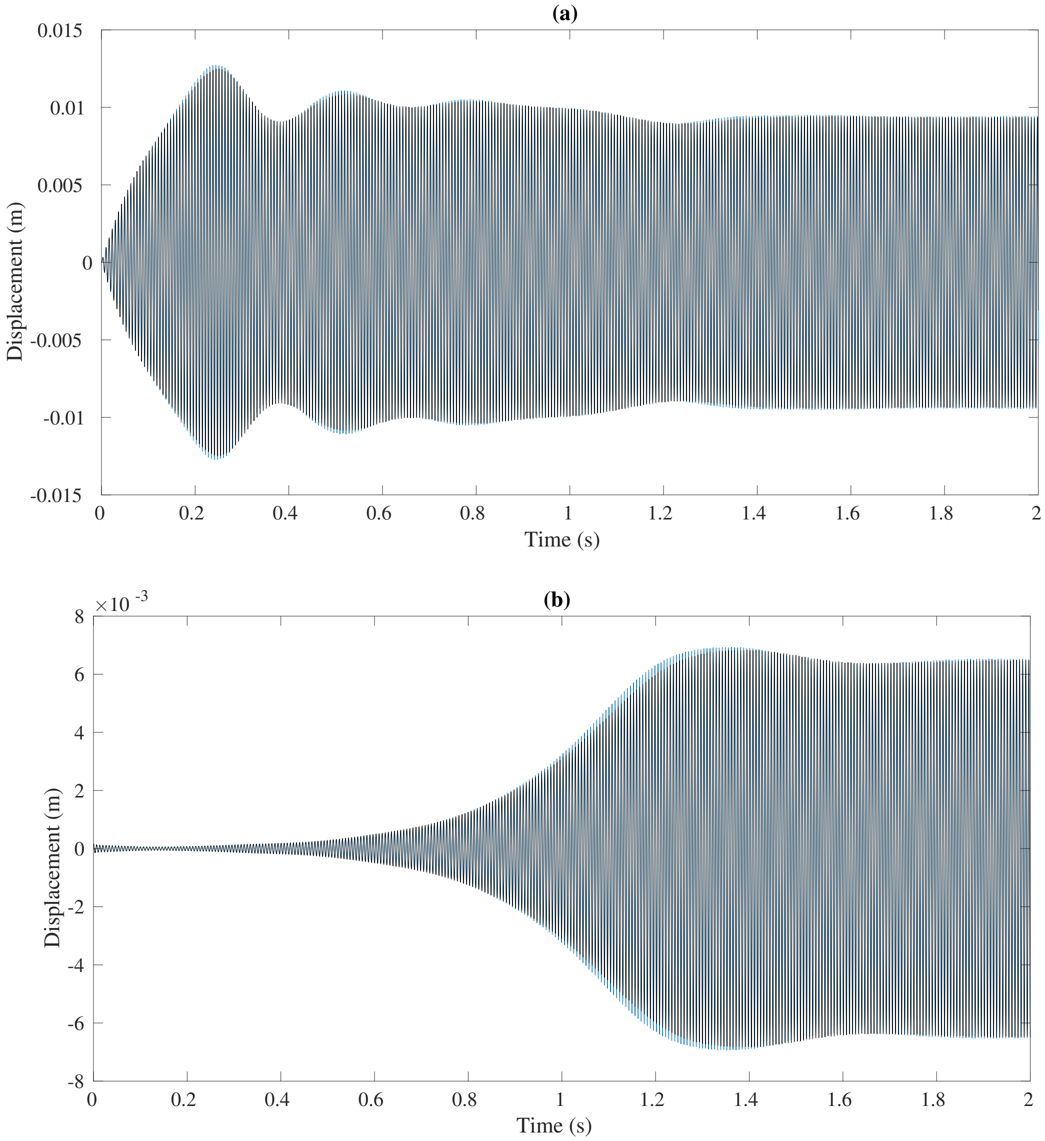

Figure 7.2.5: Time evolution of the displacement of the point at the center the beam, in response to an applied concentrated force with temporal content $f(t) = 300N\sin(1.02\omega_1 t)$. Reference solution (in black) compared to the ROM built with DNF method (in blue) corresponding to the first two master coordinates. (a) displacement in u direction. (b) displacement in v direction.

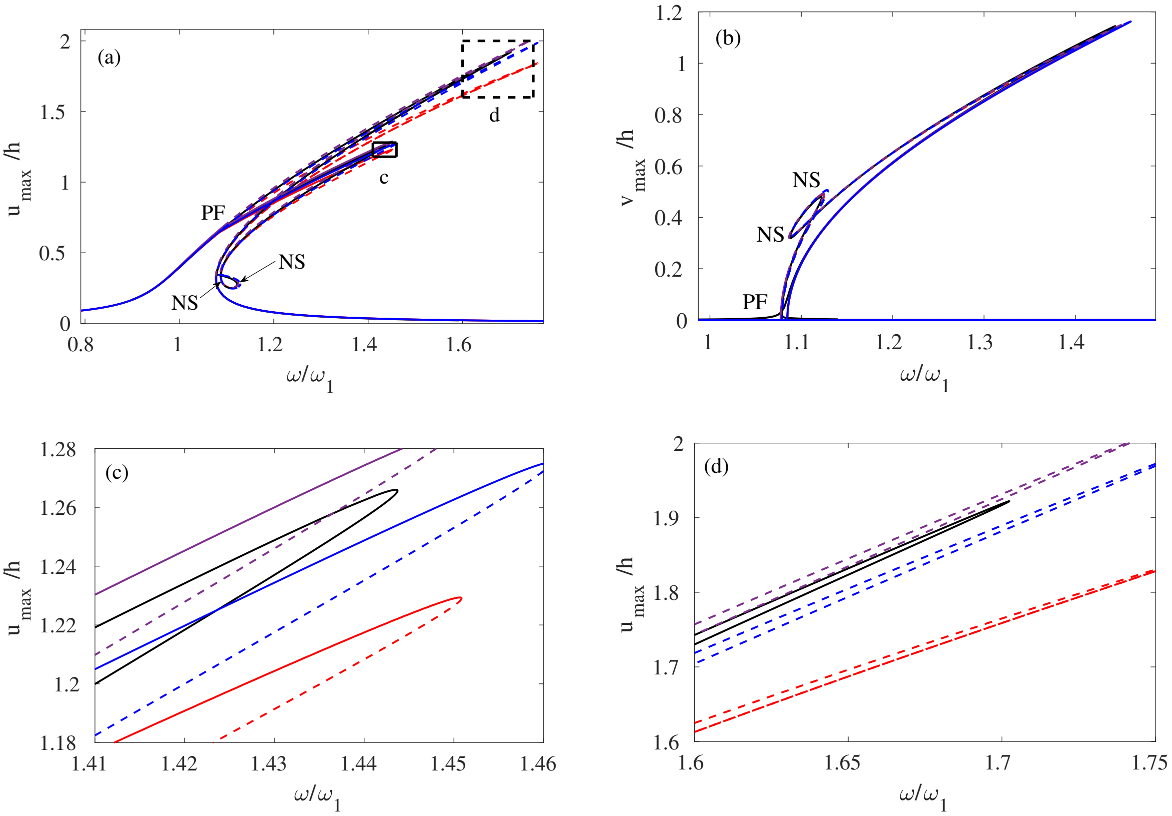

Figure 7.2.6: Frequency-response functions for the beam with 1:1 resonance with detuning 4.92%. (a) u direction (driven mode), (b): v direction (companion mode). (c)-(d) close-up views. Reference full-order solution (black) compared to ROMs obtained with ICE method (purple), DNF (red), QM-SMD (blue).

arise a pitchfork bifurcation, and two Neimark-Sacker bifurcation points exist along this branch, leading to quasiperiodic solutions. Once again, these dynamical features can be retrieved by all the methods .

As a conclusion on this case, one can observe that all the methods are able to well reproduce the 1:1 internally resonant dynamics, by taking into account two master modes. The main reason resides in the fact that the reduced dynamics is only driven by four resonant monomial terms that are easy to retrieve, whatever the method used. Also the slow/fast assumption is very well verified, so that ICE and QM methods can predict correct results. All these conclusions should be different in the case of a shell with 1:1 internal resonance, since in this case the slow/fast assumption and the appearance of strong quadratic couplings would completely change the picture. A preliminary result in this direction is reported in [79], where it is observed that for a spherical-cap shell, QM method is not able to retrieve the correct type of nonlinearity due to the violation of the slow/fast assumption.

7.3 Cantilever beam

The last of the investigated example is a cantilever beam with length $L = 1m$, cross-section with width $b = 0.05m$ and thickness $h = 0.02m$. The material parameters used are density $\rho = 4400kg/m^3$, the elastic modulus $E = 1.04e11Pa$, and Poisson's ratio $\nu = 0.3$. The beam is discretized with 3D hexahedral 20 nodes element. 50 elements in the length and 4 elements in the cross-section are used. For this last example, the backbone curve of the fundamental mode is under study, together with time domain simulations with multi-frequency forcings, in order to test the ability of the ROMs to retrieve the correct type of nonlinearity and their accuracy with more than one master modes in the reduction basis. The first five radian eigenfrequencies of the cantilever beam are $\omega_1 = 99.00(rad/s), \omega_2 = 246.79(rad/s), \omega_3 = 619.31(rad/s), \omega_4 = 1529.1(rad/s), \omega_5 = 1729.3(rad/s)$, showing no obvious internal resonance relationship among them.

Let us first illustrate the computation of the backbone curve of the fundamental bending mode. The ICE procedure is illustrated in Fig. 7.3.1, using a single master coordinate. A total of 100 values of applied load cases have been selected to obtain displacements at the tip of the cantilever in the range of $\pm 0.47m$, meaning that very large displacements, up to almost one half the length, have been considered. One can observe that the fitting with the third-order is not accurate enough, needing for a higher order. In the remainder of the computations, the ROM obtained with ICE method is considered up to order 7.

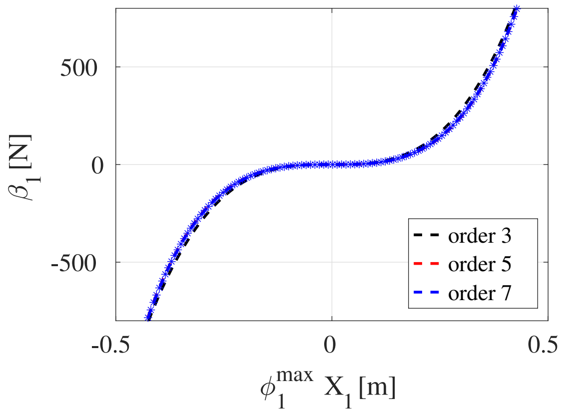

Figure 7.3.1: Illustration of the fitting procedure for the ICE method on the cantilever beam. Blue stars represent the outputs obtained from static applied force on the FE model, the dashed curve is the fitted polynomial, black: order 3, red: order 5, blue: order 7. The range of displacements in the x-axis corresponds to half the length of the cantilever beam.

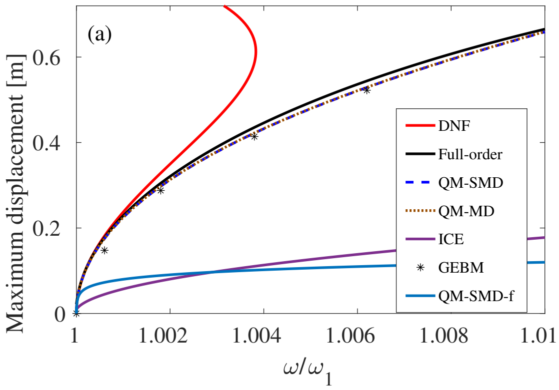

Figure 7.3.2: Backbone curves of the fundamental mode of the cantilever beam. Comparison of reference solution (black) to single-mode reduced dynamics given by ICE method with fitting up to order 7 (purple), DNF (red), QM-MD (dotted brown), QM-SMD (dashed blue) and QM-SMD-f (solid blue). Black stars: reference solution obtained with the geometrically exact beam model (GEBM) taken from Fig. 8 of [90].

Figure (7.3.2) shows the backbone curves. Apart from the classical analytical model initially proposed in [91] and asymptotically truncated to the third order, for which the backbone curves of the first bending modes have been computed for instance in [92, 93], very few numerical attempts to accurately compute those backbone curves for very large amplitudes have been proposed, the only reference being [90], which is based on a geometrically exact beam model (GEBM). Fig. 7.3.2 reports those results with black stars, labelled GEBM, this computation has been made by O. Thomas and in the figure the points are directly taken from [90]. Each point corresponds to the time integration of the beam model, discretized with 20 Timoshenko first order finite elements, under harmonic driving in the steady state at the nonlinear resonance (the point at which the amplitude is maximal), which is very close to the phase resonance corresponding to the backbone curve (see [90] for details about the geometrically exact beam model and [94] for the phase resonance). This reference solution attests a slight hardening behaviour, up to very large amplitudes, equivalent to more than half the length of the beam. The results of this beam model are very close to the reference full-order solution, obtained with the present 3D finite element model of the beam, the slight difference being attributed to the difference in the models (3D and beam model).

Comparing the ROMs, the ICE method gives the most incorrect result with a strong over-prediction of the hardening behaviour. The method being essentially static, it is known that it faces important failures when an inertia nonlinearity is present, However, It should be noted that recently Nocolaidou et al [95] proposed an improvement for the ICE method to overcome such limitation, this will not be introduced in the thesis and one can refer to the article [95] for more details. The DNF method gives the correct behaviour up to a vibration amplitude of approximately 0.2m, meaning that the method is reliable up to 1/5 the beam's length. Then the solution strongly departs from the reference. This limitation is due to the order-three dynamics of the reduction method, and taking into account higher orders would improve the result.

The QM methods, using either MD or SMD, give again identical reduced dynamics in this case. Importantly, it offers the best solution for this specific case, with vibration amplitudes up to more than 0.6 times the length of the beam. One can note that the result presented here is different from the one reported in [21], where the QM-SMD method was found to fail in a similar cantilever case. In order to understand this discrepancy, another implementation of the QM-SMD method has been applied to the same case, and is referred to as ”QM-SMD-f” case (where the added letter -f refers to ”full” QM SMD approach). In this version, the reduced dynamics used to compute the backbone curve is the untruncated one, given by Eq. (6.2.5), with polynomial terms up to order 7, which is the one used in [21], that is different from the one we used throughout the paper, where all reduced dynamics given by QM method have been truncated to order three. Interestingly, the full implementation of the QM-SMD method gives very incorrect results, following the conclusions drawn in [21]. On the other hand, our implementation of the QM method with dynamics truncated up to order three gives an excellent result, underlining that unbalanced higher-order terms have a huge effect on the prediction of the reduced dynamics in this specific case.

In order to further illustrate the comparison, time responses have been computed with harmonic forcings with two and three driving frequencies and located at the free tip of the cantilever, in order to test the ability of the different methods with either two or three master modes. In this last comparison, only QM-based methods and DNF are studied. Indeed, as already reported in [57, 58], the fitting procedure in the ICE method with an increasing number of master modes becomes more and more difficult and subject to important variations depending on the load scales selected. Second, the computations reported in [40] underlines the limits of the ICE method for tackling a problem including inertia nonlinearity as in the present case of a cantilever beam. Finally, the incorrect result found with only one master mode, as well as preliminary computations with two master modes, clearly underlines that the ICE methods gives result that are too far from the reference. Therefore, the results of the ICE method would no longer be shown in this case.

For the numerical time integration, Newmark-β scheme with $\beta = 0.25$, and $\gamma = 0.5$, has been selected. The time step $\tau = 0.0001$s corresponds to a sampling rate of 10 kHz, with 20 points per period, ensuring accuracy up to mode number 6. Also this value is large as compared to the selected forcing frequency, exciting the low-frequency modes in the range $[15, 300]$ Hz. A mass-proportional Rayleigh damping, with $C_f = 2\mathrm{M}$ (in s^{-1}), is taken into account, corresponding to a damping ratio of 1 percent for the first mode. In each case, the initial conditions correspond to the structure at rest.

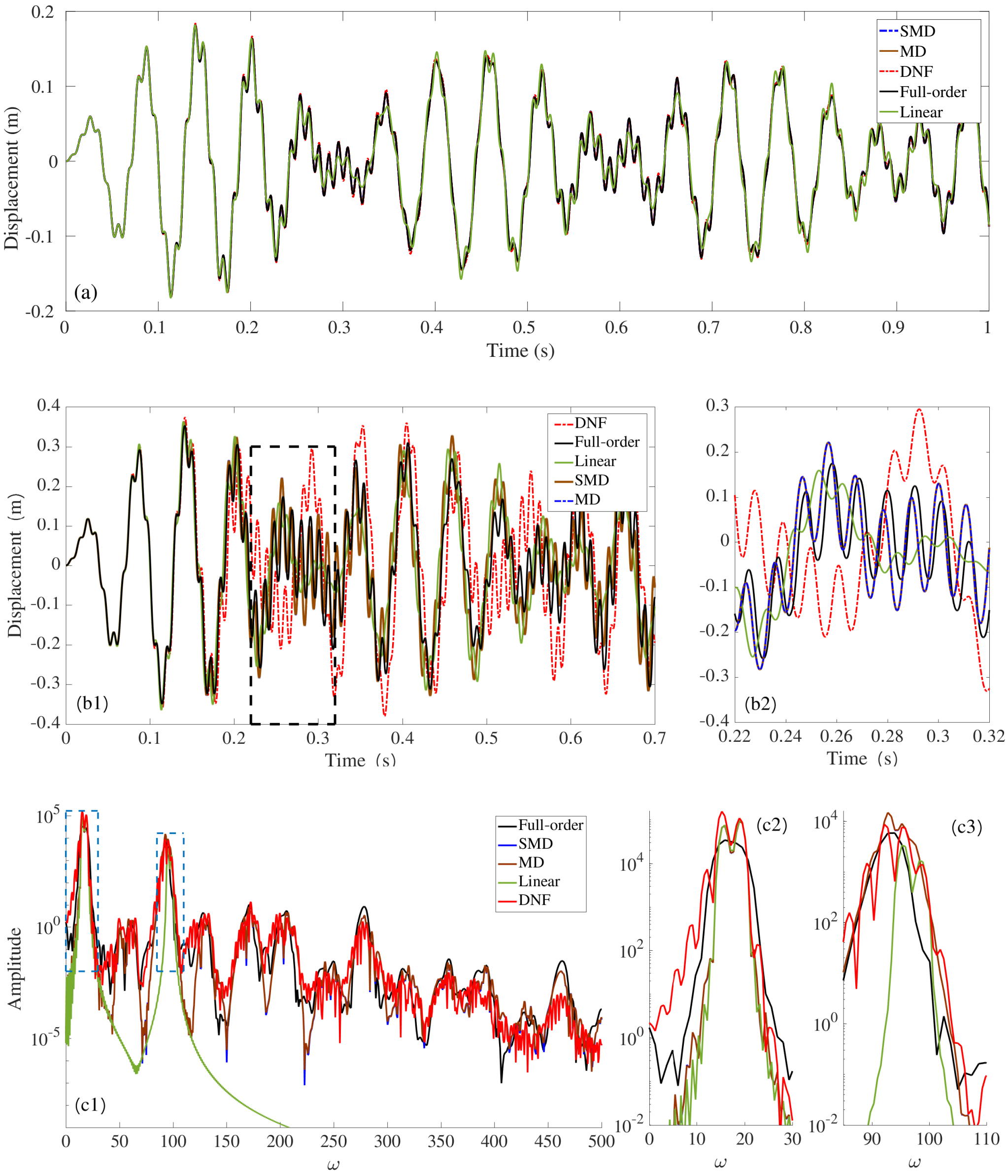

Figure 7.3.3: Time evolution of the vertical displacement of a point at the tip end of the cantilever beam, in response to an applied concentrated force with temporal content $f(t) = F_0(\sin(1.21\omega_1 t) + \sin(0.97\omega_3 t))$. Reference solution (in black compared) to three different ROMs built with two modes corresponding to master coordinates 1 and 3: blue: QM-SMD, brown: QM-MD, red: DNF. Also shown in green is the full-order model assuming linear restoring force. (a) $F_0 = 400$N. (b) $F_0 = 800$N. (c) Frequency content of the time signals shown in (b) for $F_0 = 800$N.

The first case considers a two-frequency harmonic excitation, with driving frequencies in the vicinity of the first and third eigenfrequencies of the structure. More precisely, the temporal content of the external force reads $f(t) = F_0(\sin(1.21\omega_1 t) + \sin(0.97\omega_3 t))$, and two different amplitudes of the forcing are tested, $F_0 = 400$N and $F_0 = 800$N, in order to reach vibration amplitudes respectively up to 0.2m (1/5 the length of the cantilever) and 0.4m. Fig. 7.3.3 shows the obtained results, where the full-order solution assuming a linear restoring force is also shown in green. Neglecting the nonlinear terms in Eq. (8.1.1) allows directly assessing the level of excited nonlinearity. In Fig. 7.3.3(a) with $F_0 = 400$N, the level of nonlinearity is too small and all vibrations data are very close to each other, for the reduced models as well as for the linear assumption. This is not the case anymore for $F_0 = 800$N, and Figs. 7.3.3(b-c) shows both the temporal and frequency content. The importance of the nonlinearities is particularly well assessed in Figs. 7.3.3(c) where one can observe that the linearized system is not able to reproduce the important frequency content outside the excitation frequencies. Now comparing the reduction methods, the QM-MD and SMD methods offer the best comparison to the reference full-order solution, with time traces and spectra that are very close. On the other hand, the DNF method slightly departs from the reference solution. This is again attributed to the second-order truncation used in the present DNF approach, and higher orders should be able to recover better results. However one can note the correct predictive behaviour of the DNF method, which fails to accurately reproduce details in the time trace, but remains very close to the reference in terms of frequency content, meaning that only slight phase problems are present.

The gains in using ROMs for time integration are very important. The full-order analysis is run by Code_Aster for approximately 24 hours on the 12-core processor computer with 16 GB of RAM and CPU @ 2.20GHz, and the construction as well as utilization of the reduced-order models only takes about 3 minutes for the same simulation.

The last case under study is an excitation with three driving frequencies and temporal content selected as $f(t) = \sin(1.21\omega_1 t) + \sin(0.97\omega_3 t) + \sin(0.98\omega_5 t)$, and amplitude 400N. The ROMs have been built with three master coordinates corresponding to modes 1, 3 and 5. Fig. 7.3.4 shows the obtained results, both in the time and frequency domain. In this case the nonlinearity is sufficiently excited with a forcing amplitude of 400N and very important differences already appear between time traces and frequency content. Regarding the ROMs, one can observe that the QM-based methods gives excellent results, almost coincident with the full-order model. On the other hand, the DNF method shows a slight departure to the reference solution. One can note however that this departure is moderate, with small shifts in the time domain but a very good recovery of the frequency content. The full-order analysis is run

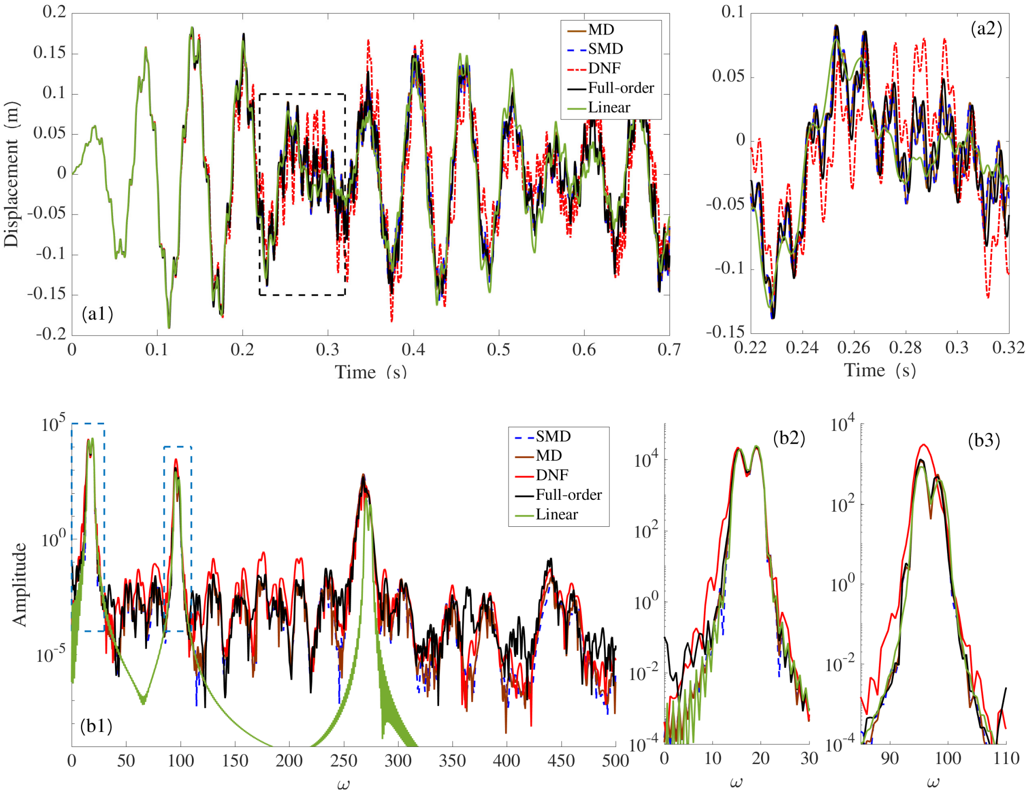

Figure 7.3.4: Vibration response of the cantilever beam to an applied concentrated force at the tip, with amplitude $400N$ and temporal content $f(t) = \sin(1.21\omega_1 t) + \sin(0.97\omega_3 t) + \sin(0.98\omega_5 t)$. (a) full view of the time response in the first 0.7s, (b) close-up view. (c) Fourier spectrum of the vibration up to 500Hz, (d) and (e) close-up views of the first frequency peak (mode 1) and second frequency peak corresponding to mode 3. Reference solution in black compared to three different ROMs built with three modes: blue: QM-SMD, brown: QM-MD, red: DNF. Full-order model with linear restoring force in green.

by Code_Aster for approximately 20 hours on the same computer mentioned previously, the construction as well as utilization of the reduced-order models still only takes about 3 minutes.

To conclude on this example, the three reduction methods (ICE, QM and DNF) have been tested on a cantilever beam. The ICE method is not able to handle successfully this case, mainly due to the importance of the nonlinear inertia effects that are missed in the construction of the ROM. DNF gives good results up to an amplitude of 1/5 the length of the cantilever, in line with the results reported in [76] on a clamped-free fan blade. One advantage of the method is to always predict the correct hardening/softening behaviour at first-order, and to rely on invariant manifolds theory. On the other hand, when reaching very large amplitudes, the limitation of using a third-order asymptotic comes into play. The QM methods have given excellent results in this case, be it used with either full or static modal derivatives. This is in contrast with [21] where an untruncated version of the reduced dynamics was used for that case, such that the higher-order terms introduced in the dynamics by the quadratic part have not been balanced by higher-order terms in the nonlinear mapping. On the other hand, our computations show that, when limited to the third-order, the QM methods give excellent predictions in the cantilever case. This result would need further investigations for offering a complete understanding. Indeed, at present there is no theoretical arguments supporting a better behaviour of the QM method. As demonstrated in [61], QM methods does not project the problem on an invariant manifold, and needs the slow/fast assumption to retrieve correct results. Even though the slow/fast separation is well fulfilled in this case, there is no explanation that the methods could provide such perfect predictions up to very large amplitudes. A reason might come from the acceleration terms that are produced by the method in the reduced dynamics.

Chapter 8

Shells

8.1 Free shallow spherical shells with 1:1 internal resonance

A free-edge spherical shell, which has been analytically investigated in Section 6.5 with von Kármán model, is now studied on the FE model. The schematic of the shell is shown again as Fig. 8.1.1.

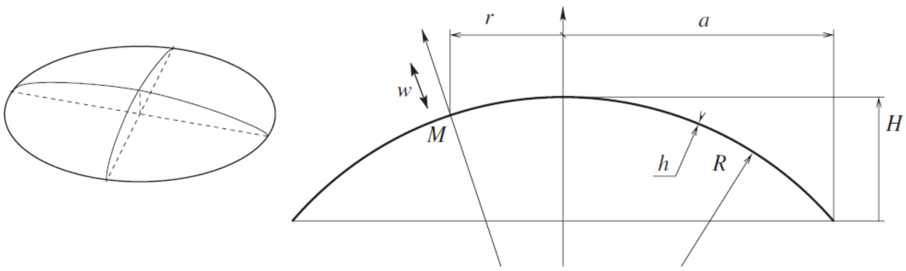

Figure 8.1.1: Geometry of the free-edge shallow spherical shell.

8.1.1 FE Prediction of the Type of Nonlinearity

In this section, a FE procedure is undertaken in order to analyze the type of nonlinearity of shallow spherical shells. For that purpose, free-edge shallow shells have been meshed with both 2D shell elements and 3D brick elements. These meshes will be used in order to highlight the validity of von Kármán's assumption in order to predict hardening/softening behaviour.

For the geometrically nonlinear structures, the equations of motion stemming from the FE discretization write as shown in Eq. (2.1.3), and given again here:

$$\mathbf{M}\ddot{\mathbf{X}} + \mathbf{K}\mathbf{X} + \mathbf{G}(\mathbf{X},\mathbf{X}) + \mathbf{H}(\mathbf{X},\mathbf{X},\mathbf{X}) = \mathbf{0}, \tag{8.1.1}$$

where $\mathbf{X}$ is the vector of generalized displacements at the nodes, $\mathbf{M}$ is the mass matrix, $\mathbf{K}$ is the tangent stiffness matrix, and finally, $\mathbf{G}(\mathbf{X},\mathbf{X})$ and $\mathbf{H}(\mathbf{X},\mathbf{X},\mathbf{X})$ represents quadratic and cubic nonlinear couplings.

This section is devoted to compute the type of nonlinearity from FE models. For that purpose, one has first to select a number of specific cases of curvature since continuous increasing of κ is out of reach. Tab. 8.1.1 summarizes the selected case, where a constant value of radius a=0.15m has been retained. Varying the radius of curvature R and the thickness h gives rise to a number of κ values that can be directly compared with the predictions obtained in the previous section.

In the FE model, the material properties of the shell are the following: $\rho = 4400kg/m^3$, $E = 1.04e + 11Pa$, $\nu = 0.3$. Two types of elements are used in the analysis. In the first case, DKT shell/plate element are used and a mesh composed of 12000 degrees of freedom (dofs), has been built, with three different thicknesses: $1mm, 3mm$ and $5mm$. In the second case, quadratic 3D element are selected and a mesh composed of approximately 50000 dofs, with the thickness $3mm$, has been created. A careful convergence study has underlined that the eigenfrequencies need to be finely computed in order to obtain a reliable result for the type of nonlinearity.

$a(m)$	0.15									
$R(m)$	3.5	2.5	1.5	0.9	0.8	0.7	0.6	0.5	0.4	0.3
$\kappa(h = 0.001m)$	41.3	81.0	225.0	625	791	1033.16	1406.25	2025	3164.06	5625
$\kappa(h = 0.003m)$	4.59	9	25	69.44	87.89	114.80	156.25	225	351.56	625.00
$\kappa(h = 0.005m)$	1.65	3.24	9	25	31.64	41.32	56.25	81	126.56	225.00

Table 8.1.1: Dimensions of the selected shells for the FE analysis with the corresponding κ values.

In order to predict the hardening/softening behaviour for the FE shell models, the direct normal form (DNF) introduced in [76] is used. The type of nonlinearity can be computed from

$\hat{\Gamma}^p_{\text{DNF}}$ that reads in this case:

$$\hat{\Gamma}^p_{\text{DNF}} = \frac{1}{8\hat{\omega}_p^2}[3(\hat{A}^p_{ppp} + \hat{h}^p_{ppp}) + \hat{\omega}_p^2 \hat{B}^p_{ppp}]. \tag{8.1.2}$$

In this equation, $\hat{h}^p_{ppp}$ is the nonlinear cubic coefficient that can be directly computed with a single STEP operation [13]. The other correcting terms $\hat{A}^p_{ppp}$ and $\hat{B}^p_{ppp}$ can be directly computed from the FE model thanks to the DNF approach, that allows to go directly from the physical space (nodes of the FE mesh) to the invariant-based span of the phase space, thanks to the nonlinear mapping given by the normal form approach. The complete expressions for leading these computations are explicit in [76], here we recall the values of the needed coefficients as given by Eqs. (6.1.11):

$$\hat{A}^p_{ppp} = 2\phi_p^T \mathbf{G}(\phi_p, \bar{\boldsymbol{a}}_{pp}), \quad \hat{B}^p_{ppp} = 2\phi_p^T \mathbf{G}(\phi_p, \bar{\boldsymbol{b}}_{pp}), \tag{8.1.3}$$

where the expression of $\bar{\boldsymbol{a}}_{pp}, \bar{\boldsymbol{b}}_{pp}$ can be found in Eq. (6.1.7).

In order to draw out the comparison with the results obtained in the previous sections (von Kármán model) where a nondimensionalisation was carried out, the relationship between the coefficient computed from FE model $\hat{\Gamma}^p_{\text{DNF}}$ and dimensionless Γ^p_{D} is explicit as: $\Gamma^p_{\text{D}} = \hat{\Gamma}^p_{\text{DNF}} h^2 v^2$, where v is the mode shape scaling factor, which is chosen to obtain the same maximal amplitude for the analytical and FE mode shapes, *i.e.* $\hat{\phi}_p = \phi_p v$, with ϕ_p normalized by $\iint_{\varphi_\perp} \phi_p^2 dS = 1$ in analytical von Kármán model.

Fig. 8.1.2 compares the analytical result given by von Kármán model and normal form onto the analytical coefficients, to those obtained from the direct computation on the FE model, where again two different types of elements (DKT shell/plate element and 3D elements) have been used. The same mode as in Fig. 6.5.3 are used. A perfect matching is obtained between the two methods, underlining that the von Kármán model, even though relying on numerous assumptions, is sufficient in order to correctly predict the type of nonlinearity of shallow spherical shell. The results also underlines the efficiency of the DNF approach for computing accurate ROMs for shell models.

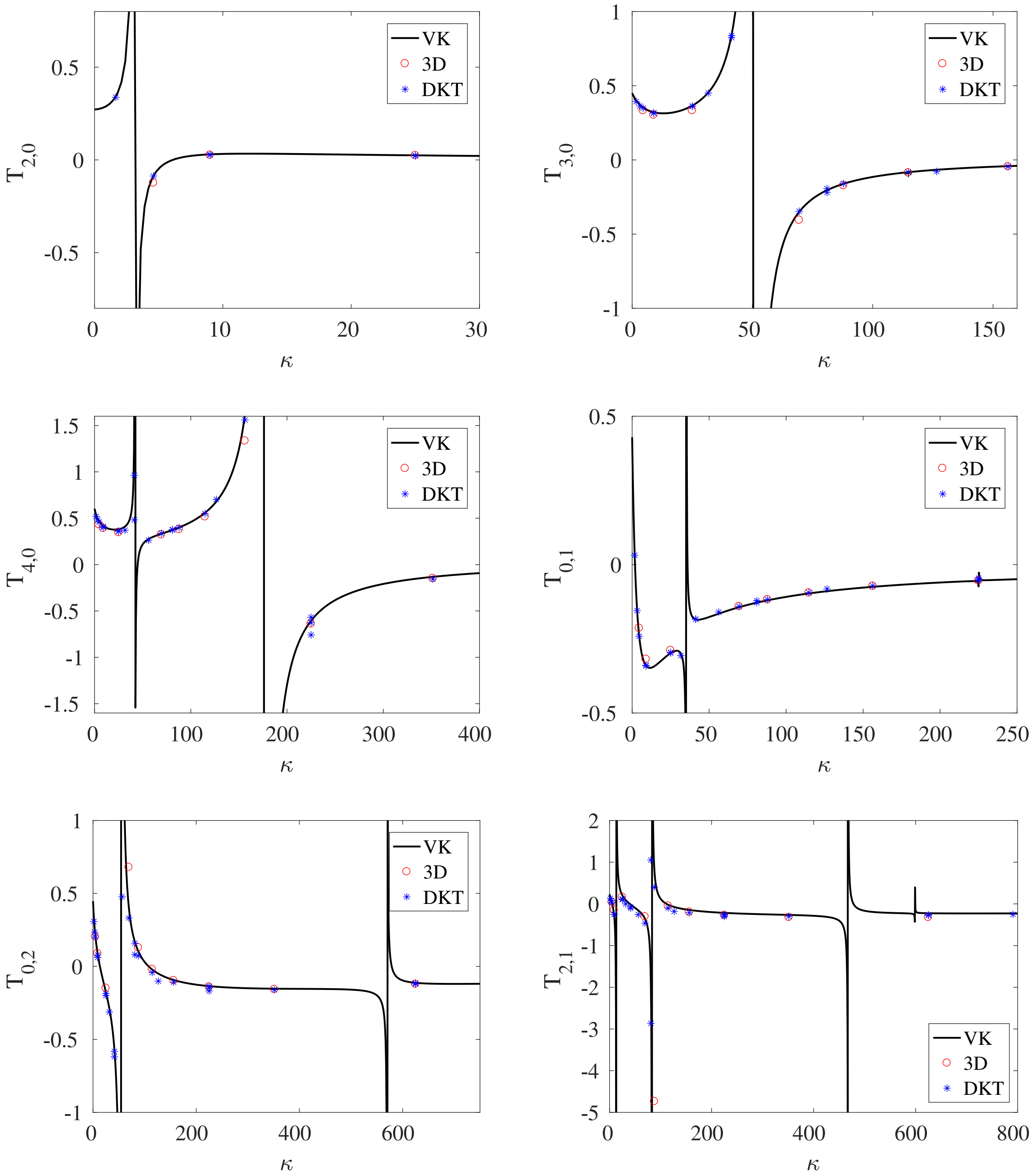

Figure 8.1.2: Type of nonlinearity for 6 modes of the shell: modes (2,0), (3,0), (4,0), (0,1), (0,2), (2,1). Comparison of analytical results from von Kármán model (continuous lines) to numerical predictions obtained by combining FE procedure with DNF.

8.1.2 Backbone curves

The backbone of asymmetric modes of the shells are investigated on the FE models with the same material and mesh given in last section. Two examples have been investigated: a flat plate and a shallow shell with the dimensions shown in the following Tab. 8.1.2, and for each of the case, the first three asymmetric modes will be investigated. The idea is to extend the beam case with 1:1 resonance, as shown in Section 7.2, to the shell and hence draw a comparison of the performance of all the reduction methods when quadratic nonlinearity is involved.

Case	Radius of curvature $R(m)$	thickness $h(m)$	radius $a(m)$	κ
Flat plate	∞	0.003	0.15	0
Shallow shell	1.5	0.003	0.15	25

Table 8.1.2: The dimensions of investigated shells.

However, there is a problem of this test cases, that is we are not able to find the reference solution currently. On the one hand, the thin shells are investigated, such that in FE package the shell/plate elements have to be employed instead of using 3D elements, in such context, we do not have the full-order FE solution yet. On the other hand, there is no analytical solution for such shell test cases, since the normal form for the shell is more complex than for the beam and results of [89] are not available. Consequently, only prelimination results are given in this section.

In Example 1, the flat circular plate with artificial detuning 0.4% is investigated ($\kappa = 0$) such that there is no quadratic nonlinearity between the bending modes and the slow/fast assumption is fulfilled well. The plate is researched with artificial detuning 0.4% by slightly transforming the shape from circular to be elliptical, in order to offer more practical meaning to the example. The backbone curves computed by the ROMs derived from different reduction methods are shown in Fig. 8.1.3. One can observe that for the first three asymmetric modes, the backbone curves computed on the ROM derived by the SMD, MD and DNF are agree well with each other, also, the results have the same characteristics as compared with the cases of the clamped beam with two polarizations, in another words, the 1:1 resonance and pitchfork bifurcations have been retrieved well by the ROMs derived from all the reduction methods, this example validate again the conclusion obtained from the beam case with 1:1 resonance, that is, when slow/fast assumption at hand, the stress manifold and quadratic manifold tend to equal to invariant manifold and thus work well. In Example 2, however, the three methods show different results with increasing of the curvature of the shells, as shown in Fig. 8.1.4. Take the backbone curves of mode (3,0) shown the second row of Fig. 8.1.4 as the example, one can observe that the DNF predicts the hardening behaviour while the prediction given by SMD and MD shows softening behaviour. The reason for arising such difference is that the slow/fast assumption is not fulfilled any more, as the consequence, the results predicted by quadratic manifold (derived by either SMD or MD) should not be correct. Also, it should be noted that these three methods are limited to the third-order asymptotic, and a higher order is needed to retrieve the correct backbone curves. Because of the lack of referencer solution, no more comments will be made and this example is awaited to be investigated in the future.

Example 1: $\kappa = 0$ (free-edge circular plate, with artificial detuning 0.4$\%$), modes (2,0), (3,0), (4,0)

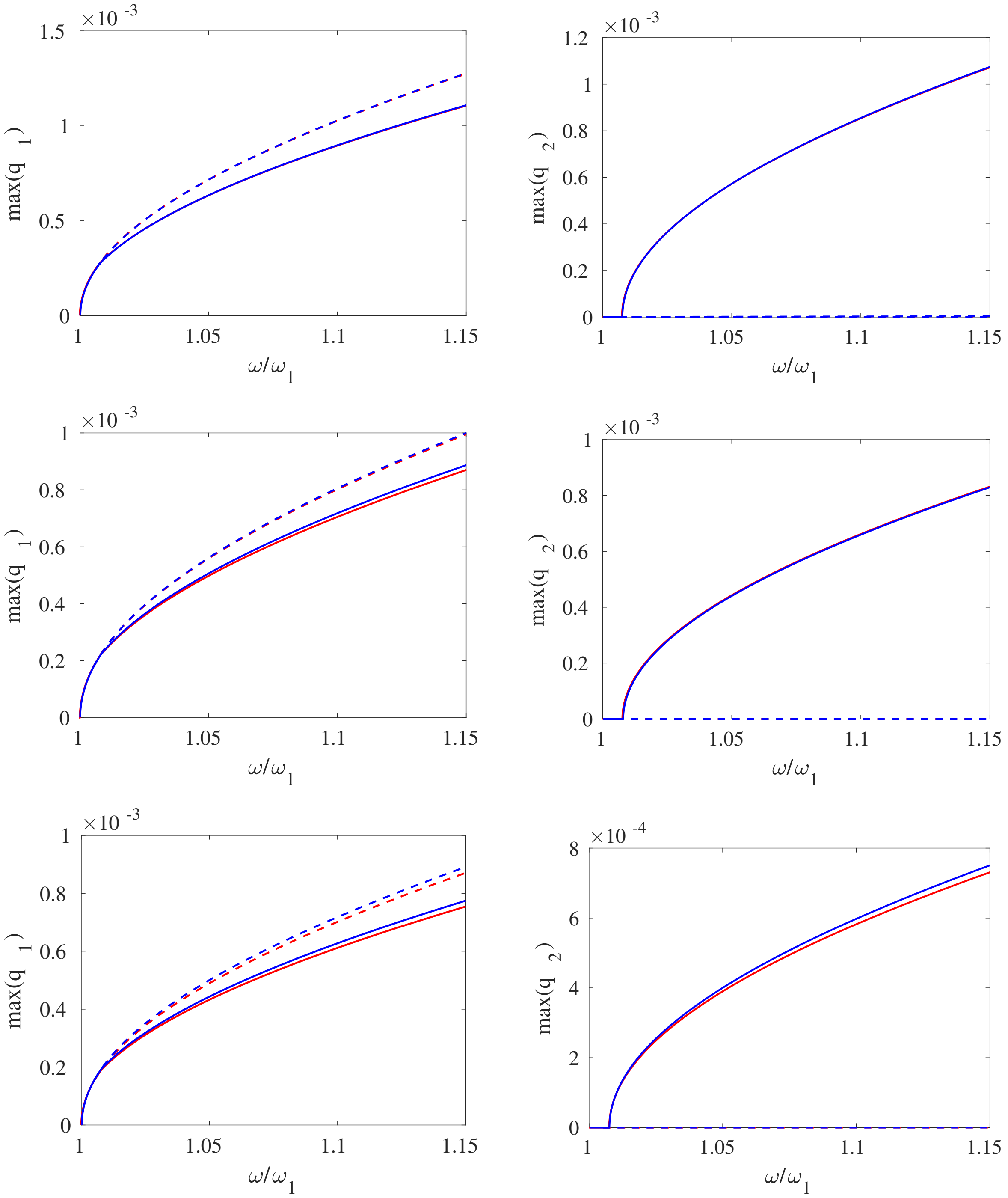

Figure 8.1.3: Backbone curves (red: NNM, blue: QM-SMD, brown: QM-MD) for the mode (2,0)(top), (3,0)(middle), (4,0)(bottom), with unstable part dashed and stable part in solid.

Example 2: $\kappa = 25$**, modes (2,0), (3,0), (4,0)**

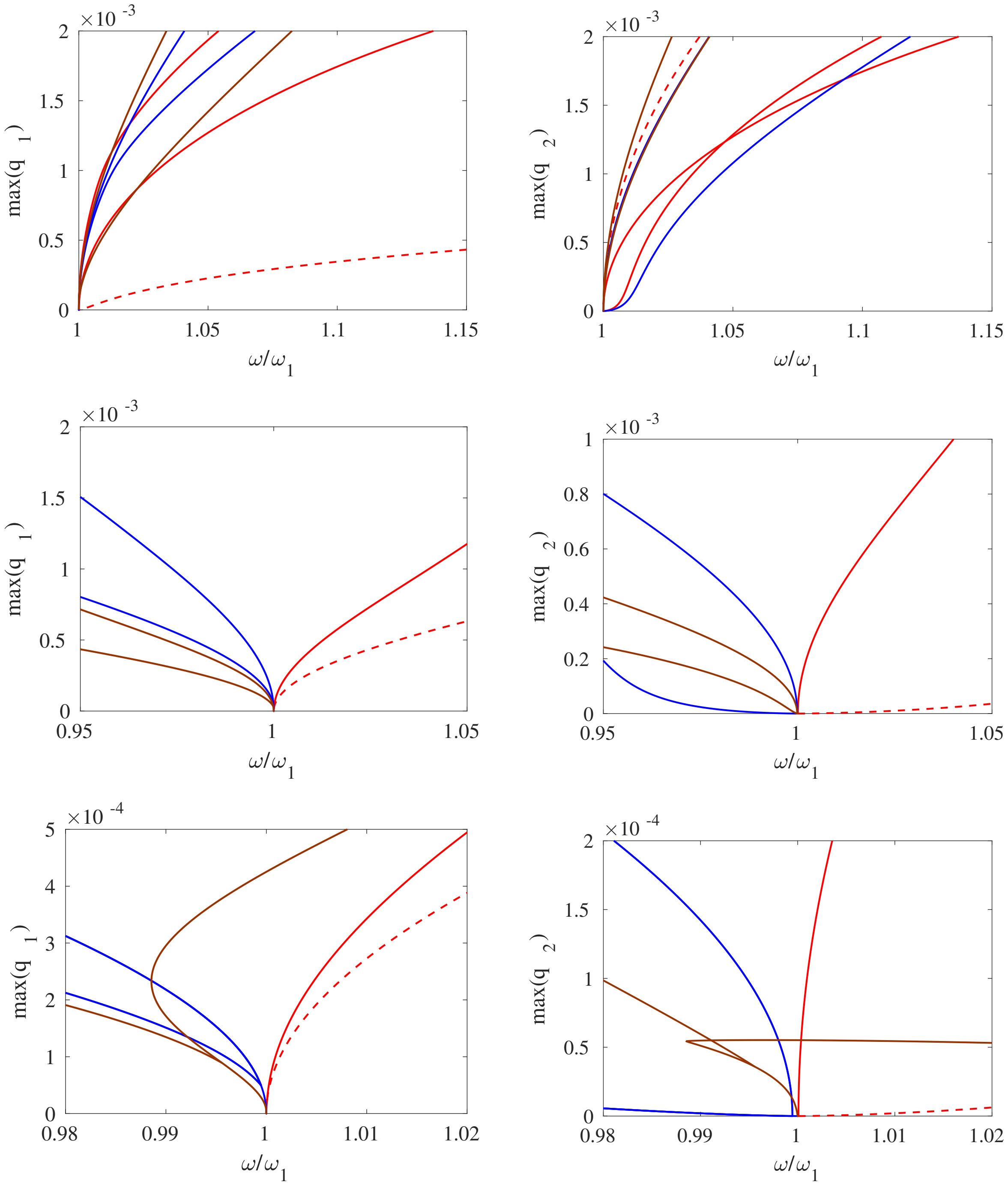

Figure 8.1.4: Backbone curves (red: NNM, blue: QM-SMD, brown: QM-MD) for the mode (2,0)(top), (3,0)(middle), (4,0)(bottom), with unstable part dashed and stable part in solid.

Chapter 9

Conclusion of the numerical tests on the large FE models

In this contribution, three nonlinear reduction methods for thin continuous structures vibrating with large amplitudes were compared: the implicit condensation and expansion (ICE) method, the quadratic manifold (QM) methods using either full modal derivatives (MDs) or only static modal derivatives (SMDs), and the direct normal form (DNF) method. From the theoretical point of view, the three methods propose a reduction of a curved subspace, a feature that is needed to take the nonlinear couplings into account. Only the last two propose a nonlinear mapping to go from the physical space to the reduction space, and only the DNF method relies on invariant manifolds, which is a key feature in order to produce accurate and reliable ROMs. Indeed, when the reduction subspaces are not invariant, the trajectories produced by the ROM do not correspond to any trajectory of the full system, which might be problematic. An important consequence shown in [96, 61, 58] is that the ICE and QM-based methods need a slow/fast separation between the master and slave coordinates in order to predict the correct results.

In Chapter 7, FE-based beam examples were selected in order to offer a more complete picture of the advantages and drawbacks of the methods. In the first example, the curvature was added to a straight clamped–clamped beam, enforcing important nonlinear quadratic couplings together with an unfulfillment of the slow/fast assumption. Similar conclusions to those from the academic, analytical example were drawn. A straight beam with two polarizations was then studied, showing that all of the tested methods were able to correctly retrieve these 1:1 internally resonant dynamics. Finally, a cantilever beam was investigated, showing that ICE method could not catch the correct behavior from the small amplitudes, whereas the DNF method allowed correct prediction of up to 1/5 of the length of the beam, and the QM methods gave excellent results up to larger amplitudes, more than 1/2 of the length for the backbone of the fundamental mode. It has been underlined that these results need further investigation, as they are different from the results reported in [21], and there is no theoretical support yet that can explain such good results.

Chapter 8 aims at enlarging the scope to include more complex structures, more specifically, the case of shells, where the differences between the methods are more pronounced. Firstly, the type of non-linearity for free-edge shallow spherical shells has been studied with a special emphasis on comparing different models (von Kármán model and FE model). For that purpose, the DNF approach has been used, allowing to directly compute and predict the type of nonlinearity from FE models. Both models have been found to give the same predictions, underlining that the assumptions of the von Kármán model are well fulfilled so that the predictions given are correct. Further comparisons on the backbone curves await to be investigated.

As a summary of the different methods, one can underline the following results. For the ICE method, the main advantage resides in its ease of use and in the rapid and correct results it might give when only one master mode is considered and the slow/fast assumption is verified. On the other hand, it is not reliable when the slow/fast assumption is not valid anymore, and as it is a static method in essence, it encounters strong difficulties in a case such as the cantilever beam. Finally, the treatment of the damping is elementary, and the loss factors of the slave modes are not taken into account in the reduced dynamics, generally leading to underprediction of the losses in the reduced dynamics.

The QM methods also need the slow/fast assumption and fail in predicting the correct type of nonlinearity when it is not fulfilled. The QM–SMD method proposes a treatment of the quadratic nonlinearity that can lead to erroneous predictions. On the other hand, the QM-MD method generally gives better results. The QM methods propose an improvement as compared to the ICE method, as shown in the numerous examples derived in this section. In particular, the treatment of the damping is more robust and takes the slave modes into account. Further insight is needed in the case of the cantilever to better understand the behavior of the reduction method.

The DNF method has the invariance property embedded and generally includes the most appealing theoretical features without needing any extra assumptions for its use. It is limited to its third-order asymptotic, so the results are expected to deteriorate at very large amplitudes, which was clearly observed in the cantilever beam example. It offers a general treatment of damping that includes the slave modes. Other limitations are linked to the assumption made to take into account the forcing, which might need further developments.

Part IV

Analysis of the dynamics of a system with 1:2 internal resonance and cubic nonlinearity

Chapter 10

Derivation of the normal form

In this part, two nonlinear oscillators, featuring 1:2 internal resonance (their eigenfrequencies being such that $\omega_2 \approx 2\omega_1$) and cubic nonlinearity, are studied. A particular goal is to revisit the change of hardening/softening behaviour in the crossing of 1:2 resonance, as shown in [41]. The idea is to reuse the example as shown in Fig. 6.5.3 with a complete 2 dofs system, instead of a single dof approximation, to discover if there is an augmented representation that could smooth the diverging behaviour. For that purpose, the starting point is the nonlinear system under its real normal form. Note that in earlier calculation of real normal form presented in [51, 52], the case of second-order internal resonance was not fully tackled. In particular, in the process of the computation, the presence of quadratic resonant monomials creates new cubic coefficients that had not been calculated before. The first step of this chapter is thus to derive the complete real norm form with 1:2 resonance and up to the cubic terms. Then, the normal form dynamics is analysed with a multiple scale approach, and computation of backbone curves and behaviour of hardening/softening is investigated with varying detuning, *i.e.* the equations will be analysed in the vicinity of 1:2 resonance but also very far from it, which is not a common practice.

Rewriting the equations of motion of the system shown in Eq. (2.1.5), the generalized coordinates for the displacement and the velocity read:

$$\begin{aligned}
&\dot{X}_p = Y_p, \\
&\dot{Y}_p = -\omega_p^2 X_p - \sum_{i=1}^{N}\sum_{j\geq i}^{N} g_{ij}^p X_i^p X_j^p - \sum_{i=1}^{N}\sum_{j\geq i}^{N}\sum_{k\geq j}^{N} h_{ijk}^p X_i^p X_j^p X_k^p.
\end{aligned} \tag{10.0.1}$$

In order to better present the results, in this Chapter the computation is started on a two dofs nonlinear system, such that Eq. (10.0.1) is rewritten as:

$$\begin{aligned}
&\dot{X}_1 = Y_1,\\
&\dot{Y}_1 = -\omega_1^2 X_1 - g_{11}^1 X_1^2 - g_{12}^1 X_1 X_2 - g_{22}^1 X_2^2 - h_{111}^1 X_1^3 - h_{112}^1 X_1^2 X_2 - h_{122}^1 X_1 X_2^2 - h_{222}^1 X_2^3,\\
&\dot{X}_2 = Y_2,\\
&\dot{Y}_2 = -\omega_2^2 X_2 - g_{11}^2 X_1^2 - g_{12}^2 X_1 X_2 - g_{22}^2 X_2^2 - h_{111}^2 X_1^3 - h_{112}^2 X_1^2 X_2 - h_{122}^2 X_1 X_2^2 - h_{222}^2 X_2^3,
\end{aligned} \tag{10.0.2}$$

The following sections give the procedure of elimination of the quadratic and cubic terms by using normal form theory and building the reduced nonlinear dynamics.

10.1 Elimination of the quadratic terms

In the section, the nonlinear coordinate change has been defined for cancelling all the non-resonant quadratic terms, since this processing does not involve cubic terms, the system (10.0.2) is truncated to the following equation:

$$\begin{aligned}
&\dot{X}_1 = Y_1,\\
&\dot{Y}_1 = -\omega_1^2 X_1 - g_{11}^1 X_1^2 - g_{12}^1 X_1 X_2 - g_{22}^1 X_2^2,\\
&\dot{X}_2 = Y_2,\\
&\dot{Y}_2 = -\omega_2^2 X_2 - g_{11}^2 X_1^2 - g_{12}^2 X_1 X_2 - g_{22}^2 X_2^2.
\end{aligned} \tag{10.1.1}$$

by changing the coordinates (X_p, Y_p) to (U_p, V_p), and from the previous calculation [51, 56, 55], there is no term in the form of $U_p V_p$ in the expression of X_p, and $U_p U_p$, $V_p V_p$ in the expression of Y_p. Thus, one can obtain the relationship between coordinates as:

$$\begin{aligned}
&X_1 = U_1 + a_{11}^1 U_1^2 + a_{12}^1 U_1 U_2 + a_{22}^1 U_2^2 + b_{11}^1 V_1^2 + b_{12}^1 V_1 V_2 + b_{22}^1 V_2^2,\\
&Y_1 = V_1 + \gamma_{11}^1 U_1 V_1 + \gamma_{12}^1 U_1 V_2 + \gamma_{21}^1 U_2 V_1 + \gamma_{22}^1 U_2 V_2,\\
&X_2 = U_2 + a_{11}^2 U_1^2 + a_{12}^2 U_1 U_2 + a_{22}^2 U_2^2 + b_{11}^2 V_1^2 + b_{12}^2 V_1 V_2 + b_{22}^2 V_2^2,\\
&Y_2 = V_2 + \gamma_{11}^2 U_1 V_1 + \gamma_{12}^2 U_1 V_2 + \gamma_{21}^2 U_2 V_1 + \gamma_{22}^2 U_2 V_2,
\end{aligned} \tag{10.1.2}$$

such that the non-resonant quadratic terms in Eq. (10.1.1) can be cancelled by using the nonlinear change of variables by combining Eqs. (10.1.1) and (10.1.2) and taking assumption of

$$\dot{U}_p = V_p + o(U_p^2, V_p^2) \quad \text{and} \quad \dot{V}_p = -\omega_p^2 U_p + o(U_p^2, V_p^2) \quad \text{for} \quad p = 1, 2. \tag{10.1.3}$$

The coefficients of $a_{ij}^p, b_{ij}^p, \gamma_{ij}^p$ (for i, j, p=1 or 2) in Eq. (10.1.2) are solved, and read as:

$$\begin{aligned}
&a_{11}^1 = \frac{g_{11}^1}{-3\omega_1^2}, b_{11}^1 = \frac{2g_{11}^1}{-3\omega_1^4}, \gamma_{11}^1 = \frac{g_{11}^1}{-3\omega_1^2},\\
&a_{22}^1 = \frac{(2\omega_2^2 - \omega_1^2)g_{22}^1}{-(4\omega_1^2\omega_2^2 - \omega_1^4)}, b_{22}^1 = \frac{2g_{22}^1}{-(4\omega_1^2\omega_2^2 - \omega_1^4)}, \gamma_{22}^1 = \frac{-2\omega_1^2 g_{22}^1}{-(4\omega_1^2\omega_2^2 - \omega_1^4)},\\
&a_{22}^2 = \frac{g_{22}^2}{-3\omega_2^2}, b_{22}^2 = \frac{2g_{22}^2}{-3\omega_2^4}, \gamma_{22}^2 = \frac{g_{22}^2}{-3\omega_2^2},\\
&a_{12}^2 = \frac{g_{12}^2}{(\omega_1^2 - 4\omega_2^2)}, b_{12}^2 = \frac{g_{12}^2}{\omega_1^2(\omega_1^2 - 4\omega_2^2)}, \gamma_{12}^2 = \frac{-g_{12}^2}{(\omega_1^2 - 4\omega_2^2)}, \gamma_{21}^2 = \frac{(\omega_1^2 - 2\omega_2^2)g_{12}^2}{\omega_1^2(\omega_1^2 - 4\omega_2^2)}.
\end{aligned}\tag{10.1.4}$$

However, the solution of the terms $a_{12}^1, b_{12}^1, \gamma_{12}^1, \gamma_{21}^1, a_{11}^2, b_{11}^2, \gamma_{11}^2$ have component of $(\omega_2 - 2\omega_1)$ in their denominator, read:

$$\begin{aligned}
a_{12}^1 &= \frac{\omega_2^2 g_{12}^1}{-\omega_2^2(2\omega_1 - \omega_2)(2\omega_1 + \omega_2)},\ b_{12}^1 = \frac{2g_{12}^1}{-\omega_2^2(2\omega_1 - \omega_2)(2\omega_1 + \omega_2)},\\
\gamma_{12}^1 &= \frac{(\omega_2^2 - 2\omega_1^2)g_{12}^1}{-\omega_2^2(2\omega_1 - \omega_2)(2\omega_1 + \omega_2)},\ \gamma_{21}^1 = \frac{-\omega_2^2 g_{12}^1}{-\omega_2^2(2\omega_1 - \omega_2)(2\omega_1 + \omega_2)},\\
a_{11}^2 &= \frac{(2\omega_1^2 - \omega_2^2)g_{11}^2}{-\omega_2^2(2\omega_1 - \omega_2)(2\omega_1 + \omega_2)},\ b_{11}^2 = \frac{2g_{11}^2}{-\omega_2^2(2\omega_1 - \omega_2)(2\omega_1 + \omega_2)},\ \gamma_{11}^2 = \frac{2g_{11}^2}{4\omega_1^2 - \omega_2^2},
\end{aligned}\tag{10.1.5}$$

thus their solution can be infinity instead of a certain value, and has to be replaced by 0. In such context, by inserting Eq. (10.1.2) into Eq. (10.1.1) and let terms $a_{12}^1, b_{12}^1, \gamma_{12}^1, a_{11}^2, b_{11}^2, \gamma_{11}^2$ equal to 0, one can obtain the nonlinear dynamics with new coordinates (U, V) by:

$$\begin{aligned}
\dot{U}_1 &= V_1,\\
\dot{V}_1 &= -\omega_1^2 U_1 - g_{12}^1 U_1 U_2 - o(U_i^3, V_i^3),\\
\dot{U}_2 &= V_2,\\
\dot{V}_2 &= -\omega_2^2 U_2 - g_{11}^2 U_1^2 - o(U_i^3, V_i^3).
\end{aligned}\tag{10.1.6}$$

Eq. (10.1.6) is the real normal form at order two, which is different from the case without 1:2 resonance. Comparing Eq. (10.1.6) to Eq. (10.1.3), there are two quadratic resonant terms that can not be cancelled. Now inserting Eqs. (10.1.1) into (10.1.2) and let terms $a_{12}^1, b_{12}^1, \gamma_{12}^1, a_{11}^2, b_{11}^2, \gamma_{11}^2$

equal to 0, the following equations are obtained:

$$\dot{U}_1 + 2a^1_{11}U_1V_1 + 2a^1_{22}U_2V_2 + 2b^1_{11}V_1\dot{V}_1 + 2b^1_{22}V_2\dot{V}_2 = V_1 + \gamma^1_{11}U_1V_1 + \gamma^1_{22}U_2V_2, \tag{10.1.7a}$$

$$\begin{aligned}&\dot{V}_1 + \gamma^1_{11}V_1^2 + \gamma^1_{11}U_1\dot{V}_1 + \gamma^1_{22}V_2^2 + \gamma^1_{22}U_2\dot{V}_2 \\ &\quad = -\omega_1^2(U_1 + a^1_{11}U_1^2 + a^1_{22}U_2^2 + b^1_{11}V_1^2 + b^1_{22}V_2^2) - g^1_{11}U_1^2 - g^1_{12}U_1U_2 - g^1_{22}U_2^2,\end{aligned} \tag{10.1.7b}$$

$$\begin{aligned}&\dot{U}_2 + a^2_{12}V_1U_2 + a^2_{12}U_1V_2 + 2a^2_{22}U_2V_2 + b^2_{12}\dot{V}_1V_2 + b^2_{12}V_1\dot{V}_2 + 2b^2_{22}V_2\dot{V}_2 \\ &\quad = V_2 + \gamma^2_{12}U_1V_2 + \gamma^2_{21}U_2V_1 + \gamma^2_{22}U_2V_2,\end{aligned} \tag{10.1.7c}$$

$$\begin{aligned}&\dot{V}_2 + \gamma^2_{12}V_1V_2 + \gamma^2_{12}U_1\dot{V}_2 + \gamma^2_{21}V_2V_1 + \gamma^2_{21}U_2\dot{V}_1 + \gamma^2_{22}V_2^2 + \gamma^2_{22}U_2\dot{V}_2 \\ &\quad = -\omega_2^2(U_2 + a^2_{12}U_1U_2 + a^2_{22}U_2^2 + b^2_{12}V_1V_2 + b^2_{22}V_2^2) - g^2_{11}U_1^2 - g^2_{12}U_1U_2 - g^2_{22}U_2^2,\end{aligned} \tag{10.1.7d}$$

Inserting Eqs. (10.1.6), instead of (10.1.3), into Eq. (10.1.7), and then sorting out the equations, one obtains:

$$\dot{U}_1 = V_1 + 2b^1_{11}g^1_{12}U_1U_2V_1 + 2b^1_{22}g^2_{11}U_1^2V_2, \tag{10.1.8a}$$

$$\dot{V}_1 = -\omega_1^2U_1 - g^1_{12}U_1U_2 + \gamma^1_{11}g^1_{12}U_1^2U_2 + \gamma^1_{22}g^2_{11}U_1^2U_2, \tag{10.1.8b}$$

$$\dot{U}_2 = V_2 + b^2_{12}g^1_{12}U_1U_2V_2 + b^2_{12}g^2_{11}V_1U_1^2 + 2b^2_{22}g^2_{11}U_1^2V_2, \tag{10.1.8c}$$

$$\dot{V}_2 = -\omega_2^2U_2 - g^2_{11}U_1^2 + \gamma^2_{12}g^2_{11}U_1^3 + \gamma^2_{21}g^1_{12}U_1U_2^2 + \gamma^2_{22}g^2_{11}U_1^2U_2. \tag{10.1.8d}$$

Eqs. (10.1.8) show the dynamics with the new cubic terms due to the resonant quadratic terms.

To obtain the normal form dynamics of the system, new coordinate W is introduced in order to simplify the equations, and expressed as:

$$\begin{aligned}W_1 &= V_1 + 2b^1_{11}g^1_{12}U_1U_2V_1 + 2b^1_{22}g^2_{11}U_1^2V_2, \\ W_2 &= V_2 + b^2_{12}g^1_{12}U_1U_2V_2 + b^2_{12}g^2_{11}V_1U_1^2 + 2b^2_{22}g^2_{11}U_1^2V_2,\end{aligned} \tag{10.1.9}$$

the Eq. (10.1.8) can thus be rewritten as:

$$\begin{aligned}\dot{U}_1 =& W_1, \\ \dot{W}_1 =& -\omega_1^2U_1 - g^1_{12}U_1U_2 + \gamma^1_{11}g^1_{12}U_1^2U_2 + \gamma^1_{22}g^2_{11}U_1^2U_2 \\ &+ 2b^1_{11}g^1_{12}(W_1U_2W_1 + U_1W_2W_1 - U_1U_2U_1\omega_1^2) + 2b^1_{22}g^2_{11}(2U_1W_1W_2 - U_1^2U_2\omega_2^2) + o(U_i^4, W_i^4), \\ \dot{U}_2 =& W_2, \\ \dot{W}_2 =& -\omega_2^2U_2 - g^2_{11}U_1^2 + \gamma^2_{12}g^2_{11}U_1^3 + \gamma^2_{21}g^1_{12}U_1U_2^2 + \gamma^2_{22}g^2_{11}U_1^2U_2 \\ &+ b^2_{12}g^1_{12}(W_1U_2W_2 + U_1W_2W_2 - U_1U_2U_2\omega_2^2) + b^2_{12}g^2_{11}(-\omega_1U_1^3 + 2U_1W_1^2) \\ &+ 2b^2_{22}g^2_{11}(2U_1W_1W_2 - U_1^2U_2\omega_2^2) + o(U_i^4, W_i^4).\end{aligned} \tag{10.1.10}$$

It can be found that all the non-resonant quadratic terms have been cancelled in the dynamics given in Eq. (10.1.10), only two quadratic terms kept and new cubic terms created because of 1:2 resonance.

10.2 Elimination of the cubic terms

Now, the calculation for eliminating the cubic terms with the new coordinates is presented. Firstly, replacing the (X_i, Y_i) by (U_i, V_i), *i.e.* substituting Eq. (10.1.2) to Eq. (10.0.2), then combining with Eq. (10.1.9) such that the coordinate transformation from (U_i, V_i) to (U_i, W_i) is made, thus, the system with third order terms now reads as:

$$
\begin{aligned}
&\dot{U}_1 = W_1,\\
&\dot{W}_1 = -\omega_1^2 U_1 - h^1_{111} U_1^3 - h^1_{112} U_1^2 U_2 - h^1_{122} U_1 U_2^2 - h^1_{222} U_2^3\\
&- g^1_{11}(2a^1_{11} U_1^3 + 2a^1_{22} U_2^2 U_1 + 2b^1_{11} U_1 W_1^2 + 2b^1_{22} U_1 W_2^2)\\
&- g^1_{12}(U_1 U_2 + a^2_{12} U_1^2 U_2 + a^2_{22} U_1 U_2^2\\
&+ b^2_{12} U_1 W_1 W_2 + b^2_{22} U_1 W_2^2 + a^1_{11} U_2 U_1^2 + a^1_{22} U_2^3 + b^1_{11} U_2 W_1^2 + b^1_{22} U_2 W_2^2)\\
&- g^1_{22}(2a^2_{12} U_1 U_2^2 + 2a^2_{22} U_2^3 + 2b^2_{12} U_2 W_1 W_2 + 2b^2_{22} U_2 W_2^2)\\
&+\gamma^1_{11} g^1_{12} U_1^2 U_2 + \gamma^1_{22} g^2_{11} U_1^2 U_2 + 2b^1_{11} g^1_{12}(W_1^2 U_2 + U_1 W_2 W_1 - U_1^2 U_2 \omega_1^2) + 2b^1_{22} g^2_{11}(2U_1 W_1 W_2 - U_1^2 U_2 \omega_2^2),\\
&\dot{U}_2 = W_2,\\
&\dot{W}_2 = -\omega_2^2 U_2 - h^2_{111} U_1^3 - h^2_{112} U_1^2 U_2 - h^2_{122} U_1 U_2^2 - h^2_{222} U_2^3\\
&- g^2_{11}(U_1^2 + 2a^1_{11} U_1^3 + 2a^1_{22} U_2^2 U_1 + 2b^1_{11} U_1 W_1^2 + 2b^1_{22} U_1 W_2^2)\\
&- g^2_{12}(a^2_{12} U_1^2 U_2 + a^2_{22} U_1 U_2^2 + b^2_{12} U_1 W_1 W_2 + b^2_{22} U_1 W_2^2 + a^1_{11} U_2 U_1^2 + a^1_{22} U_2^3 + b^1_{11} U_2 W_1^2 + b^1_{22} U_2 W_2^2)\\
&- g^2_{22}(2a^2_{12} U_1 U_2^2 + 2a^2_{22} U_2^3 + 2b^2_{12} U_2 W_1 W_2 + 2b^2_{22} U_2 W_2^2)\\
&+\gamma^2_{12} g^2_{11} U_1^3 + \gamma^2_{21} g^1_{12} U_1 U_2^2 + \gamma^2_{22} g^2_{11} U_1^2 U_2\\
&+b^2_{12} g^1_{12}(W_1 U_2 W_2 + U_1 W_2^2 - U_1 U_2^2 \omega_2^2) + b^2_{12} g^2_{11}(-\omega_1 U_1^3 + 2U_1 W_1^2) + 2b^2_{22} g^2_{11}(2U_1 W_1 W_2 - U_1^2 U_2 \omega_2^2).
\end{aligned}
\tag{10.2.1}
$$

Sorting out above Eq. (10.2.1), one obtains:

$$
\begin{aligned}
\dot{U}_1 =& W_1, \\
\dot{W}_1 =& -\omega_1^2 U_1 - g_{12}^1 U_1 U_2 - (h_{111}^1 + A_{111}^1) U_1^3 - (h_{112}^1 + A_{112}^1 - D_{112}^1) U_1^2 U_2 - (h_{122}^1 + A_{122}^1) U_1 U_2^2 \\
& - (h_{222}^1 + A_{222}^1) U_2^3 - B_{111}^1 U_1 W_1^2 - B_{122}^1 U_1 W_2^2 - (B_{112}^1 - E_{112}^1) U_1 W_1 W_2 \\
& - (B_{211}^1 - E_{211}^1) U_2 W_1^2 - B_{212}^1 U_2 W_1 W_2 - B_{222}^1 U_2 W_2^2, \\
\dot{U}_2 =& W_2, \\
\dot{W}_2 =& -\omega_2^2 U_2 - g_{11}^2 U_1^2 - (h_{111}^2 + A_{111}^2 - D_{111}^2) U_1^3 - (h_{112}^2 + A_{112}^2 - D_{112}^2) U_1^2 U_2 \\
& - (h_{122}^2 + A_{122}^2 - D_{122}^2) U_1 U_2^2 - (h_{222}^2 + A_{222}^2) U_2^3 - (B_{111}^2 - E_{111}^2) U_1 W_1^2 \\
& - (B_{122}^2 - E_{122}^2) U_1 W_2^2 - (B_{112}^2 - E_{112}^2) U_1 W_1 W_2 - B_{211}^2 U_2 W_1^2 \\
& - (B_{212}^2 - E_{212}^2) U_2 W_1 W_2 - B_{222}^2 U_2 W_2^2,
\end{aligned}
\tag{10.2.2}
$$

where the terms $A_{ijk}^p, B_{ijk}^p, (i,j,k,p = 1,2)$ are expressed as:

$$
\begin{aligned}
A_{111}^p &= 2a_{11}^1 g_{11}^p, \\
A_{112}^p &= a_{11}^1 g_{12}^p + a_{12}^2 g_{12}^p, \\
A_{122}^p &= 2a_{22}^1 g_{11}^p + a_{22}^2 g_{12}^p + 2a_{12}^2 g_{22}^p, \\
A_{222}^p &= 2a_{22}^2 g_{22}^p + a_{22}^1 g_{12}^p, \\
B_{111}^p &= 2b_{11}^1 g_{11}^p, \\
B_{112}^p &= b_{12}^2 g_{12}^p, \\
B_{122}^p &= b_{22}^2 g_{12}^p + 2b_{22}^1 g_{11}^p, \\
B_{211}^p &= b_{11}^1 g_{12}^p, \\
B_{212}^p &= 2b_{12}^2 g_{22}^p, \\
B_{222}^p &= 2b_{22}^2 g_{22}^p + b_{22}^1 g_{12}^p.
\end{aligned}
\tag{10.2.3}
$$

It should be noted that the notation is kept the same as the case without internal resonance (*e.g.* [51, 52]), the same formula can be used, the only difference being that some coefficients shown in Eq. (10.1.5) are now zero. The new extra terms D, E, due to 1:2 resonance, are expressed by:

$$\begin{aligned}
D^1_{112} &= \gamma^1_{11} g^1_{12} + \gamma^1_{22} g^2_{11} - 2b^1_{11} g^1_{12} \omega^2_1 - 2b^1_{22} g^2_{11} \omega^2_2, \\
D^2_{111} &= \gamma^2_{12} g^2_{11} - b^2_{12} g^2_{11} \omega^2_1, \\
D^2_{112} &= \gamma^2_{22} g^2_{11} - 2b^2_{22} g^2_{11} \omega^2_2, \\
D^2_{122} &= \gamma^2_{21} g^1_{12} - b^2_{12} g^1_{12} \omega^2_2, \\
E^1_{112} &= 2b^1_{11} g^1_{12} + 4b^1_{22} g^2_{11}, \\
E^1_{211} &= 2b^1_{11} g^1_{12}, \\
E^2_{111} &= 2b^2_{12} g^2_{11}, \\
E^2_{122} &= b^2_{12} g^1_{12}, \\
E^2_{112} &= 4b^2_{22} g^2_{11}, \\
E^2_{212} &= b^2_{12} g^1_{12}.
\end{aligned} \tag{10.2.4}$$

Let us change the coordinates again and try to cancel the cubic terms as many as possible, the following cubic polynomials are introduced for $p = 1, 2$:

$$\begin{aligned}
U_p &= R_p + \sum_{i=1}^{2} \sum_{j \geq i}^{2} \sum_{k \geq j}^{2} r^p_{ijk} R_i R_j R_k + \sum_{i=1}^{2} \sum_{j=1}^{2} \sum_{k \geq j}^{2} u^p_{ijk} R_i S_j S_k, \\
W_p &= S_p + \sum_{i=1}^{2} \sum_{j \geq i}^{2} \sum_{k \geq j}^{2} \mu^p_{ijk} S_i S_j S_k + \sum_{i=1}^{2} \sum_{j=1}^{2} \sum_{k \geq j}^{2} \nu^p_{ijk} S_i R_j R_k.
\end{aligned} \tag{10.2.5}$$

Notice that in the dynamics Eq. (10.2.2) two resonant quadratic terms $U_1 U_2$ and U_1^2 can not be cancelled, and inserting them into Eq. (10.2.5), they will be expressed as the following:

$$U_1 U_2 = R_1 R_2 + o(R_i^4, S_i^4) \quad \text{and} \quad U_1^2 = R_1^2 + o(R_i^4, S_i^4), \tag{10.2.6}$$

consequently, it is clear that this two quadratic terms can only have effects on the normal form dynamics at least on the fourth order in the processing of the coordinate transformation from (U_p, W_p) to (R_p, S_p). Combining the Eqs. (10.2.1) and (10.2.5), the quadratic terms $g^1_{12} U_1 U_2, g^2_{11} U_1^2$ lead to unbalance between the two sides of the equals sign, thus has to be ignored when calculating the cubic coefficients $r^p_{ijk}, u^p_{ijk}, \mu^p_{ijk}, \nu^p_{ijk}$ and then they should be added at the final stage.

10.3 Nonlinear reduced dynamics

After following the processing of the previous sections, a nonlinear transform can be found in order to cancel the maximum number of quadratic and cubic coupling terms present in the original system. The nonlinear transformation for $p = 1, 2$ up to order three reads:

$$\begin{aligned} X_p &= R_p + \sum_{i=1}^{2}\sum_{j\geq i}^{2} a^p_{ij} R_i R_j + \sum_{i=1}^{2}\sum_{j\geq i}^{2} b^p_{ij} S_i S_j + \sum_{i=1}^{2}\sum_{j\geq i}^{2}\sum_{k\geq j}^{2} r^p_{ijk} R_i R_j R_k + \sum_{i=1}^{2}\sum_{j=1}^{2}\sum_{k\geq j}^{2} u^p_{ijk} R_i S_j S_k, \\ Y_p &= S_p + \sum_{i=1}^{2}\sum_{j=1}^{2} \gamma^p_{ij} R_i S_j + \sum_{i=1}^{2}\sum_{j\geq i}^{2}\sum_{k\geq j}^{2} \mu^p_{ijk} S_i S_j S_k + \sum_{i=1}^{2}\sum_{j=1}^{2}\sum_{k\geq j}^{2} \nu^p_{ijk} S_i R_j R_k, \end{aligned} \tag{10.3.1}$$

where the quadratic coefficients $a^p_{ij}, b^p_{ij}, \gamma^p_{ij}$ are given by Eq (10.1.4). For the cubic coefficients $r^p_{ijk}, u^p_{ijk}, \mu^p_{ijk}, \nu^p_{ijk}$, with $i, j, k, p = 1, ..., 2$, their expressions are not directly given here because they are too complex, fortunately, as compared with expressions of the coefficients given in [51] with the assumption of no resonance between eigenvalues, the only difference is that for the resonant modes, the new cubic terms given in Eq. (10.2.4) should be considered during the computation. For example, if one wants to obtain terms $r^2_{112}, u^2_{112}, u^2_{211}, \mu^2_{112}, \nu^2_{112}, \nu^2_{211}$, one need to replace $(A^2_{112} + A^2_{211} + h^2_{112})$ in the equations given in Appendix A of [51] to be $(A^2_{112} + A^2_{211} + h^2_{112} - D^2_{112})$ and B^2_{112} to be $(B^2_{112} - E^2_{112})$.

After the coordinate transformation, the invariant-breaking terms are vanishing, and the dynamics of the system with the new coordinates (R_p, S_p) should be written as:

$$\begin{aligned} \dot{R}_1 =& S_1, \\ \dot{S}_1 =& -\omega_1^2 R_1 - g^1_{12} R_1 R_2 - (h^1_{111} + A^1_{111}) R_1^3 - (h^1_{122} + A^1_{122}) R_1 R_2^2 \\ & - B^1_{111} R_1 S_1^2 - B^1_{122} R_1 S_2^2 - B^1_{212} R_2 S_1 S_2, \\ \dot{R}_2 =& S_2, \\ \dot{S}_2 =& -\omega_2^2 R_2 - g^2_{11} R_1^2 - (h^2_{112} + A^2_{112} - D^2_{112}) R_1^2 R_2 - (h^2_{222} + A^2_{222}) R_2^3 \\ & - (B^2_{112} - E^2_{112}) R_1 S_1 S_2 - B^2_{211} R_2 S_1^2 - B^2_{222} R_2 S_2^2. \end{aligned} \tag{10.3.2}$$

The calculation has been extended to a system of N oscillators where only two of them presenting 1:2 resonance, this calculation is presented in Appendix B.

Chapter 11

Change of nonlinearity at crossing 1:2 resonance

11.1 Multiple scales solution

Starting from Eq. (10.3.2) and sorting non-linearities using the book-keeping parameter ε [14, 97], one obtains:

$$\begin{aligned}\ddot{R}_1 + \omega_1^2 R_1 =& - \varepsilon[g_{12}^1]R_1 R_2 - \varepsilon^2[H_{111}^1 R_1^3 + H_{122}^1 R_1 R_2^2 \\ &+ V_{111}^1 R_1 {\dot{R}_1}^2 + V_{122}^1 R_1 {\dot{R}_2}^2 + V_{212}^1 R_2 \dot{R}_1 \dot{R}_2], \\ \ddot{R}_2 + \omega_2^2 R_2 =& - \varepsilon[g_{11}^2]R_1^2 - \varepsilon^2[H_{112}^2 R_1^2 R_2 + H_{222}^2 R_2^3 \\ &+ V_{112}^2 R_1 \dot{R}_1 \dot{R}_2 + V_{211}^2 R_2 {\dot{R}_1}^2 + V_{222}^2 R_2 {\dot{R}_2}^2].\end{aligned} \tag{11.1.1}$$

The eigenfrequencies are related through: $\omega_2 = 2\omega_1 + \varepsilon\sigma$, where σ is a detuning parameter. To make the equation to be shorter and clear, here H_{ijk}^p are introduced with regard to terms $R_i R_j R_k$, and V_{ijk}^p for $R_i S_j S_k$, and model coordinate R is replaced to be q. The method of multiple scales expresses the solution as a composition of different time scales such that $T_j = \varepsilon^j t$ for $j = 0, 1, 2$ and then holds

$$q_i(t) = q_{i0}(T_0, T_1, T_2) + \varepsilon q_{i1}(T_0, T_1, T_2) + \varepsilon^2 q_{i2}(T_0, T_1, T_2) + O(\varepsilon^3), \tag{11.1.2}$$

with $i = 1, 2$. Applying the multiple scales approach and considering the change of variables, the derivatives with respect to time follow the expressions:

$$\begin{aligned} \frac{\partial}{\partial t} &= \frac{\partial}{\partial T_0} + \varepsilon \frac{\partial}{\partial T_1} + \varepsilon^2 \frac{\partial}{\partial T_2} = D_0 + \varepsilon D_1 + \varepsilon^2 D_2, \\ \frac{\partial^2}{\partial t^2} &= D_0^2 + 2\varepsilon D_0 D_1 + \varepsilon^2 (D_1^2 + 2D_0 D_2), \end{aligned} \tag{11.1.3}$$

thus, the equation of motion is rewritten as

$$\begin{aligned} &(D_0^2 + 2\varepsilon D_0 D_1 + \varepsilon^2(D_1^2 + 2D_0D_2))(q_{10} + \varepsilon q_{11} + \varepsilon^2 q_{12}) + \omega_1^2 (q_{10} + \varepsilon q_{11} + \varepsilon^2 q_{12}) \\ &\quad = -\varepsilon g_{12}^1 (q_{10} + \varepsilon q_{11} + \varepsilon^2 q_{12})(q_{20} + \varepsilon q_{21} + \varepsilon^2 q_{22}) - \varepsilon^2 (H_{111}^1 (q_{10} + \varepsilon q_{11} + \varepsilon^2 q_{12})^3 ...), \\ &(D_0^2 + 2\varepsilon D_0 D_1 + \varepsilon^2(D_1^2 + 2D_0D_2))(q_{20} + \varepsilon q_{21} + \varepsilon^2 q_{22}) + \omega_2^2 (q_{20} + \varepsilon q_{21} + \varepsilon^2 q_{22}) \\ &\quad = -\varepsilon g_{11}^2 (q_{10} + \varepsilon q_{11} + \varepsilon^2 q_{12})^2 - \varepsilon^2 (H_{111}^2 (q_{10} + \varepsilon q_{11} + \varepsilon^2 q_{12})^3 ...). \end{aligned} \tag{11.1.4}$$

We split the resulting terms using ε as sorting parameter. In this way we get three systems of equations:

ε^0 :

$$D_0^2 q_{10} + \omega_1^2 q_{10} = 0, \tag{11.1.5a}$$

$$D_0^2 q_{20} + \omega_2^2 q_{20} = 0. \tag{11.1.5b}$$

ε^1 :

$$D_0^2 q_{11} + \omega_1^2 q_{11} = -2D_0 D_1 q_{10} - g_{12}^1 q_{10} q_{20}, \tag{11.1.5c}$$

$$D_0^2 q_{21} + \omega_2^2 q_{21} = -2D_0 D_1 q_{20} - g_{11}^2 q_{10}^2. \tag{11.1.5d}$$

ε^2 :

$$\begin{aligned} D_0^2 q_{12} + \omega_1^2 q_{12} &= -(D_1^2 + 2D_0 D_2) q_{10} - 2D_0 D_1 q_{11} - [g_{12}^1 q_{11} q_{20} + g_{12}^1 q_{10} q_{21} \\ &+ H_{111}^1 q_{10}^3 + H_{122}^1 q_{10} q_{20}^2 + V_{111}^1 q_{10} (D_0 q_{10})^2 + V_{122}^1 q_{10} (D_0 q_{20})^2 + V_{212}^1 q_{20} (D_0 q_{10})(D_0 q_{20})], \end{aligned} \tag{11.1.5e}$$

$$\begin{aligned} D_0^2 q_{22} + \omega_2^2 q_{22} &= -(D_1^2 + 2D_0 D_2) q_{20} - 2D_0 D_1 q_{21} - [2g_{11}^2 q_{10} q_{11} \\ &+ H_{222}^2 q_{20}^3 + H_{112}^2 q_{10}^2 q_{20} + V_{222}^2 q_{20} (D_0 q_{20})^2 + V_{112}^2 q_{10} (D_0 q_{10})(D_0 q_{20}) + V_{211}^2 q_{20} (D_0 q_{10})^2]. \end{aligned} \tag{11.1.5f}$$

Eqs. (11.1.5a,b) give the solution of:

$$\begin{aligned} q_{10} &= A_1(T_1, T_2) \exp(i\omega_1 T_0) + c.c., \\ q_{20} &= A_2(T_1, T_2) \exp(i\omega_2 T_0) + c.c., \end{aligned} \tag{11.1.6}$$

where c.c. stands for complex conjugate. Near resonance some terms give secular solutions, to get rid of them we define the so-called solvability condition. In this way, also fixing the book-keeping parameter $\varepsilon = 1$, for Eq. (11.1.5c,d) we get the conditions:

$$g_{12}^{1} A_2 \bar{A}_1 e^{iT_0\omega_1 + iT_1\sigma} + 2i\omega_1 D_1 A_1 e^{iT_0\omega_1} = 0, \tag{11.1.7a}$$

$$A_1^2 g_{11}^2 e^{2iT_0\omega_1} + 2(2\omega_1 i + \sigma i) D_1 A_2 e^{2iT_0\omega_1 + iT_1\sigma} = 0. \tag{11.1.7b}$$

Solving above equation for D_1A_1 and D_1A_2

$$D_1 A_1 = \frac{i g_{12}^1 A_2 \bar{A}_1 e^{iT_1\sigma}}{2\omega_1}, \tag{11.1.8a}$$

$$D_1 A_2 = \frac{i A_1^2 g_{11}^2}{2(2\omega_1 + \sigma) e^{iT_1\sigma}}, \tag{11.1.8b}$$

at the meanwhile, when above equation is set up, one also could obtain the complex conjugate of Eqs. (11.1.7), reads as:

$$g_{12}^{1} A_1 \bar{A}_2 e^{-iT_0\omega_1 - iT_1\sigma} - 2i\omega_1 D_1 \bar{A}_1 e^{-iT_0\omega_1} = 0, \tag{11.1.9a}$$

$$\bar{A}_1^2 g_{11}^2 e^{-2iT_0\omega_1} - 2(2\omega_1 i + \sigma i) D_1 \bar{A}_2 e^{2iT_0\omega_1 + iT_i\sigma} = 0, \tag{11.1.9b}$$

and substituting the results into the first-order equation Eq. (11.1.5c,d), one obtains:

$$D_0^2 q_{11} + \omega_1^2 q_{11} = -g_{12}^1 (A_1 A_2 e^{iT_0(\omega_1+\omega_2)} + \bar{A}_1 \bar{A}_2 e^{-iT_0(\omega_1+\omega_2)}), \tag{11.1.10a}$$

$$D_0^2 q_{21} + \omega_2^2 q_{21} = -g_{11}^2 (2A_1\bar{A}_1). \tag{11.1.10b}$$

From the Eq. (11.1.10), it is found that the expression of q_{11}, q_{21} can be divided into two parts: homogeneous solution $q_{11}^{(h)}, q_{21}^{(h)}$, and particular solution $q_{11}^{(p)}, q_{21}^{(p)}$, the latter one for (11.1.10a) should in the form of $Q_1 e^{i(\omega_1+\omega_2)T_0} + c.c.$ and for (11.1.10b) should in the expression of Q_2, where Q_1, Q_2 are constants. To set up the Eq. (11.1.10), Q_1, Q_2 can be solved and the particular solution is expressed by:

$$q_{11}^{(p)} = \frac{-g_{12}^1}{\omega_1^2 - (\omega_1+\omega_2)^2} A_1 A_2 e^{i(\omega_1+\omega_2)T_0} + c.c., \tag{11.1.11a}$$

$$q_{21}^{(p)} = \frac{-g_{11}^2}{\omega_2^2} A_1 \bar{A}_1 + c.c, \tag{11.1.11b}$$

The homogeneous part is the solution that makes the following equations set up:

$$D_0^2 q_{11}^{(h)} + \omega_1^2 q_{11}^{(h)} = 0, \tag{11.1.12a}$$

$$D_0^2 q_{21}^{(h)} + \omega_2^2 q_{21}^{(h)} = 0, \tag{11.1.12b}$$

because the solutions of (11.1.12) can be determined within an arbitrary constant P_p multiple the $e^{i\omega_p T_0}$, $(p = 1, 2)$, read as:

$$q_{11}^{(h)} = P_1 e^{i\omega_1 T_0} + c.c., \tag{11.1.13a}$$

$$q_{21}^{(h)} = P_2 e^{i\omega_2 T_0} + c.c.. \tag{11.1.13b}$$

However, we don't want to introduce a new amplitude for the homogeneous solutions, to determine constant P_p and express them by A_1, A_2, the velocity z is here introduced, and the relationship between z and q is given by: $(z_{p0} + \varepsilon z_{p1} + \varepsilon^2 z_{p2}) = (D_0 + \varepsilon D_1 + \varepsilon^2 D_2)(q_{p0} + \varepsilon q_{p1} + \varepsilon^2 q_{p2})$, $p = 1, 2$, such that

$$z_{11} = D_0 q_{11} + D_1 q_{10}, \tag{11.1.14a}$$

$$z_{21} = D_0 q_{21} + D_1 q_{20}, \tag{11.1.14b}$$

and the linear relationships existing between the homogeneous part of $z_{p1}^{(h)}$ and $q_{p1}^{(h)}$ [98], reads:

$$z_{p1}^{(h)} = -i\omega_p q_{p1}^{(h)} \quad \text{or} \quad z_{p1}^{(h)} = -D_0 q_{p1}^{(h)}, \quad \text{for} \quad p = 1, 2, \tag{11.1.15}$$

thus, combining Eqs. (11.1.14) and (11.1.15), the homogeneous solution of q_{11}, q_{21} can be found by the equation:

$$D_1 q_{p0}^{(h)} + 2D_0 q_{p1}^{(h)} = 0, \quad \text{for} \quad p = 1, 2. \tag{11.1.16}$$

Solving above equations, one obtains the expression of P_1 and P_2 in homogeneous solution:

$$P_1 = \frac{-g_{12}^1}{4\omega_1^2} A_2 \bar{A}_1 e^{iT_1\sigma}, \tag{11.1.17a}$$

$$P_2 = \frac{-g_{11}^2}{4\omega_2^2} A_1^2 e^{-iT_1\sigma}, \tag{11.1.17b}$$

Combining homogeneous solution with particular solutions given in Eq. (11.1.11), the expression of q_{11}, q_{21} can be written as

$$q_{11} = \frac{-g_{12}^1}{4\omega_1^2} A_2 \bar{A}_1 e^{iT_0\omega_1 + iT_1\sigma} + \frac{-g_{12}^1}{\omega_1^2 - (\omega_1 + \omega_2)^2} A_1 A_2 e^{i(\omega_1 + \omega_2)T_0} + c.c., \tag{11.1.18a}$$

$$q_{21} = \frac{-g_{11}^2}{4\omega_2^2} A_1^2 e^{i(2\omega_1)T_0} + \frac{-g_{11}^2}{\omega_2^2} A_1 \bar{A}_1 + c.c.. \tag{11.1.18b}$$

Substituting the Eqs. (11.1.18) into the Eqs. (11.1.5e,f), the resonant terms will appear, causing secular terms in the solution, thus, one has to impose again solvability conditions, which yields:

$$\begin{aligned}&[2i\omega_1 D_2 A_1 - \frac{9}{4\omega_2^2} g^1_{12} g^2_{11} A_1^2 \bar{A}_1 - (\frac{1}{\omega_1^2 - (\omega_1+\omega_2)^2} + \frac{1}{4\omega_1^2})(g^1_{12})^2 A_1 A_2 \bar{A}_2 \\ &\quad + 3H^1_{111} A_1^2 \bar{A}_1 + 2H^1_{122} A_1 A_2 \bar{A}_2 + V^1_{111} A_1^2 \bar{A}_1(-i^2\omega_1^2) + 2V^1_{122} A_1 A_2 \bar{A}_2(-i^2\omega_2^2)] e^{i(T_0\omega_1 + T_1\sigma)} = 0,\end{aligned} \tag{11.1.19a}$$

$$\begin{aligned}&[2i\omega_2 D_2 A_2 - 2(\frac{1}{\omega_1^2 - (\omega_1+\omega_2)^2} + \frac{1}{4\omega_1^2}) g^1_{12} g^2_{11} A_2 A_1 \bar{A}_1 + 3H^2_{222} A_2^2 \bar{A}_2 \\ &\quad + 2H^2_{112} A_1 A_2 \bar{A}_1 + V^2_{222} A_2^2 \bar{A}_2(-i^2\omega_2^2) + 2V^2_{211} A_2 A_1 \bar{A}_1(-i^2\omega_1^2)] e^{iT_0(2\omega_1 + \varepsilon\sigma)} = 0,\end{aligned} \tag{11.1.19b}$$

thus, the modulation equations governing the dependence of the complex-valued amplitudes A_1 and A_2 on the scale T_2 in the form:

$$2i\omega_1 D_2 A_1 = K^1_{11} A_1^2 \bar{A}_1 + K^1_{12} A_1 A_2 \bar{A}_2, \tag{11.1.20a}$$

$$2i\omega_2 D_2 A_2 = K^2_{22} A_2^2 \bar{A}_2 + K^2_{12} A_2 A_1 \bar{A}_1, \tag{11.1.20b}$$

where

$$K^1_{11} = \frac{9}{4\omega_2^2} g^1_{12} g^2_{11} - 3H^1_{111} - V^1_{111}\omega_1^2, \tag{11.1.21a}$$

$$K^1_{12} = (\frac{1}{\omega_1^2 - (\omega_1+\omega_2)^2} + \frac{1}{4\omega_1^2})(g^1_{12})^2 - 2H^1_{122} - 2V^1_{122}\omega_2^2, \tag{11.1.21b}$$

$$K^2_{22} = -3H^2_{222} - V^2_{222}\omega_2^2, \tag{11.1.21c}$$

$$K^2_{12} = 2(\frac{1}{\omega_1^2 - (\omega_1+\omega_2)^2} + \frac{1}{4\omega_1^2})(g^1_{12} g^2_{11}) - 2H^2_{112} - 2V^2_{211}\omega_1^2. \tag{11.1.21d}$$

Using the method of reconstitution [99, 100, 14], we can express the derivative of A with respect to time t as $\dot{A} = D_1 A + \varepsilon D_2 A...$, therefore, substituting (11.1.8), (11.1.20) into this equation, one obtains the modulation equations up to second order as:

$$2i\omega_1 \dot{A}_1 = -g^1_{12} A_2 \bar{A}_1 e^{iT_1\sigma} + K^1_{11} A_1^2 \bar{A}_1 + K^1_{12} A_1 A_2 \bar{A}_2, \tag{11.1.22a}$$

$$2i\omega_2 \dot{A}_2 = -A_1^2 g^2_{11} e^{-iT_1\sigma} + K^2_{22} A_2^2 \bar{A}_2 + K^2_{12} A_2 A_1 \bar{A}_1. \tag{11.1.22b}$$

To solve the above system one needs to expand A_i in polar form, *i.e.*

$$\begin{aligned}A_1(T_1, T_2) &= \frac{a_1(T_1, T_2)}{2}\exp(i\theta_1(T_1, T_2)), \\ A_2(T_1, T_2) &= \frac{a_2(T_1, T_2)}{2}\exp(i\theta_2(T_1, T_2)),\end{aligned} \tag{11.1.23}$$

where a_i, θ_i are unknown amplitude and phase. Also, let us transform Eqs. (11.1.6) and (11.1.18) into polar form, we can thus express the first- and second-order generalized coordinates as

$$\begin{aligned}
q_{10} &= a_1 \cos(\omega_1 T_0 + \theta_1), \\
q_{20} &= a_2 \cos(\omega_2 T_0 + \theta_2), \\
q_{11} &= \frac{1}{2}\frac{g^1_{12}}{4\omega_1^2} a_1 a_2 \cos((\omega_2 - \omega_1)T_0 + \theta_2 - \theta_1) + \frac{1}{2}\frac{g^1_{12}}{\omega_1^2 - (\omega_2 + \omega_1)^2} a_1 a_2 \cos((\omega_2 + \omega_1)T_0 + \theta_2 + \theta_1), \\
q_{21} &= \frac{1}{2} a_1^2 \frac{g^2_{11}}{4\omega_2^2} \cos 2(\omega_1 T_0 + \theta_1) + \frac{1}{2} a_1^2 \frac{g^2_{11}}{\omega_2^2}.
\end{aligned} \qquad (11.1.24)$$

To determine $a_1, a_2, \theta_1, \theta_2$, let us split the real and imaginary part of Eqs. (11.1.22) and rewrite the equations in polar form, one obtains:

$$\frac{\partial a_1}{\partial T_1} + \frac{\partial a_1}{\partial T_2} = -\frac{a_1 a_2 g^1_{12}}{4\omega_1} \sin(\theta_2 - 2\theta_1 + T_1\sigma), \qquad (11.1.25a)$$

$$a_1\left(\frac{\partial \theta_1}{\partial T_1} + \frac{\partial \theta_1}{\partial T_2}\right) = \frac{a_1 a_2 g^1_{12}}{4\omega_1} \cos(\theta_2 - 2\theta_1 + T_1\sigma) - \frac{a_1^3 K^1_{11} + a_1 a_2^2 K^1_{12}}{8\omega_1}, \qquad (11.1.25b)$$

$$\frac{\partial a_2}{\partial T_1} + \frac{\partial a_2}{\partial T_2} = \frac{a_1^2 g^2_{11}}{4\omega_2} \sin(2\theta_1 - \theta_2 - T_1\sigma), \qquad (11.1.25c)$$

$$a_2\left(\frac{\partial \theta_2}{\partial T_1} + \frac{\partial \theta_2}{\partial T_2}\right) = \frac{a_1^2 g^2_{11}}{4\omega_2} \cos(2\theta_1 - \theta_2 - T_1\sigma) - \frac{a_2^3 K^2_{22} + a_1^2 a_2 K^2_{12}}{8\omega_2}. \qquad (11.1.25d)$$

Considering the coupled solutions with both a_1 and a_2 different from zero, such that dividing the both sides of (11.1.25b) by a_1 and (11.1.25d) by a_2, in this case the solvability condition can be simplified in:

$$\frac{\partial a_1}{\partial T_1} + \frac{\partial a_1}{\partial T_2} = -\frac{a_1 a_2 g^1_{12}}{4\omega_1} \sin(\theta_2 - 2\theta_1 + T_1\sigma), \qquad (11.1.26a)$$

$$\frac{\partial \theta_1}{\partial T_1} + \frac{\partial \theta_1}{\partial T_2} = \frac{a_2 g^1_{12}}{4\omega_1} \cos(\theta_2 - 2\theta_1 + T_1\sigma) - \frac{a_1^2 K^1_{11} + a_2^2 K^1_{12}}{8\omega_1}, \qquad (11.1.26b)$$

$$\frac{\partial a_2}{\partial T_1} + \frac{\partial a_2}{\partial T_2} = \frac{a_1^2 g^2_{11}}{4\omega_2} \sin(2\theta_1 - \theta_2 - T_1\sigma), \qquad (11.1.26c)$$

$$\frac{\partial \theta_2}{\partial T_1} + \frac{\partial \theta_2}{\partial T_2} = \frac{a_1^2 g^2_{11}}{4\omega_2 a_2} \cos(2\theta_1 - \theta_2 - T_1\sigma) - \frac{a_2^2 K^2_{22} + a_1^2 K^2_{12}}{8\omega_2}. \qquad (11.1.26d)$$

Eq.(11.1.26) is a non-autonomous system and one can introduce the change of variables to get an autonomous one:

$$\gamma_1 = \theta_1, \qquad (11.1.27a)$$

$$\gamma_{(p)} = 2\theta_1 - \theta_2 - T_1\sigma, \qquad (11.1.27b)$$

then, inserting Eq. (11.1.27) into Eq. (11.1.26), one obtains:

$$\begin{aligned}
\frac{\partial a_1}{\partial T_1}+\frac{\partial a_1}{\partial T_2} =&\frac{a_1 a_2 g_{12}^1}{4\omega_1}\sin(-\gamma_{(p)}), && \text{(11.1.28a)}\\
\frac{\partial \gamma_1}{\partial T_1}+\frac{\partial \gamma_1}{\partial T_2} =&\frac{a_2 g_{12}^1}{4\omega_1}\cos(\gamma_{(p)})-\frac{a_1^2K_{11}^1+a_2^2K_{12}^1}{8\omega_1}, && \text{(11.1.28b)}\\
\frac{\partial a_2}{\partial T_1}+\frac{\partial a_2}{\partial T_2} =&\frac{a_1^2 g_{11}^2}{4\omega_2}\sin(\gamma_{(p)}), && \text{(11.1.28c)}\\
\frac{\partial \gamma_{(p)}}{\partial T_1}+\frac{\partial \gamma_{(p)}}{\partial T_2} =&\frac{a_2 g_{12}^1}{2\omega_1}\cos(\gamma_{(p)})-\frac{a_1^2K_{11}^1+a_2^2K_{12}^1}{4\omega_1} && \text{(11.1.28d)}\\
&-(\frac{a_1^2 g_{11}^2}{4\omega_2 a_2}\cos(\gamma_{(p)})-\frac{a_2^2K_{22}^2+a_1^2K_{12}^2}{8\omega_2})-\sigma.
\end{aligned}$$

Eqs. (11.1.28) admit a solution when $\sin(\gamma_{(p)}) = 0$ and consequently $\cos(\gamma_{(p)}) = \pm 1 = p$. Above Eqs. (11.1.28) are satisfied only when a_1 and a_2 are constants. Combining Eq. (11.1.24) and Eq. (11.1.27), one obtains the expressions of two coordinates:

$$\begin{aligned}
q_1(t) =&a_1\cos(\omega_1T_0+\gamma_1)+\frac{1}{2}\frac{g_{12}^1}{4\omega_1^2}a_1a_2\cos(\omega_1T_0+\gamma_1-\gamma_{(p)})\\
&+\frac{1}{2}\frac{g_{12}^1}{\omega_1^2-(\omega_2+\omega_1)^2}a_1a_2\cos(3\omega_1T_0+3\gamma_1-\gamma_{(p)}), \qquad \text{(11.1.29)}\\
q_2(t) =&a_2\cos(2\omega_1T_0+2\gamma_1-\gamma_{(p)})+\frac{1}{2}a_1^2\frac{g_{11}^2}{4\omega_2^2}\cos 2(\omega_1T_0+\gamma_1)+\frac{1}{2}a_1^2\frac{g_{11}^2}{\omega_2^2}.
\end{aligned}$$

To sort out the Eq. (11.1.29) by merging the same order terms, one can consider $p = 1$, that is $\gamma_{(p)} = 2k\pi, (k = 0, 1, 2, ...)$, the equations are now rewritten as:

$$\begin{aligned}
q_1(t) =&(a_1+\frac{1}{2}\frac{g_{12}^1}{4\omega_1^2}a_1a_2)\cos(\omega_1T_0+\gamma_1)+\frac{1}{2}\frac{g_{12}^1}{\omega_1^2-(\omega_2+\omega_1)^2}a_1a_2\cos(3\omega_1T_0+3\gamma_1),\\
q_2(t) =&(a_2+\frac{1}{2}a_1^2\frac{g_{11}^2}{4\omega_2^2})\cos(2\omega_1T_0+2\gamma_1)+\frac{1}{2}a_1^2\frac{g_{11}^2}{\omega_2^2}.
\end{aligned} \qquad \text{(11.1.30)}$$

and considering $p = -1$, such that $\gamma_{(p)} = (2k + 1)\pi, (k = 0, 1, 2, ...)$, the equations read:

$$\begin{aligned}
q_1(t) =&(a_1-\frac{1}{2}\frac{g_{12}^1}{4\omega_1^2}a_1a_2)\cos(\omega_1T_0+\gamma_1)-\frac{1}{2}\frac{g_{12}^1}{\omega_1^2-(\omega_2+\omega_1)^2}a_1a_2\cos(3\omega_1T_0+3\gamma_1),\\
q_2(t) =&(\frac{1}{2}a_1^2\frac{g_{11}^2}{4\omega_2^2}-a_2)\cos(2\omega_1T_0+2\gamma_1)+\frac{1}{2}a_1^2\frac{g_{11}^2}{\omega_2^2}.
\end{aligned} \qquad \text{(11.1.31)}$$

11.2 Backbone curves of the system: $p+$ mode and $p-$ mode

The fixed points of Eq. (11.1.28) in which $a_1' = 0, a_2' = 0, \gamma_{(p)}' = 0$, one calculated and read as:

$$\frac{\partial \gamma_{(p)}}{\partial T_1} + \frac{\partial \gamma_{(p)}}{\partial T_2} = 0 = \frac{a_2 g_{12}^1}{2\omega_1} p - \frac{a_1^2 K_{11}^1 + a_2^2 K_{12}^1}{4\omega_1} - \left(\frac{a_1^2 g_{11}^2}{4\omega_2 a_2} p - \frac{a_2^2 K_{22}^2 + a_1^2 K_{12}^2}{8\omega_2}\right) - \sigma. \tag{11.2.1}$$

From the above equation, we obtain the relationship between a_1 and a_2:

$$a_1^2 = r(a_2) = \frac{a_2(a_2^2 K_{22}^2 \omega_1 - 2a_2^2 K_{12}^1 \omega_2 + 4a_2 g_{12}^1 p \omega_2 + 16\omega_1^2 \omega_2 - 8\omega_1 \omega_2^2)}{-a_2 K_{12}^2 \omega_1 + 2g_{11}^2 \omega_1 p + 2a_2 K_{11}^1 \omega_2}. \tag{11.2.2}$$

Solving the ODEs (11.1.28) we get expressions for the phase angles:

$$\gamma_1 = \frac{a_2 g_{12}^1}{4\omega_1} p T_1 - \frac{a_1^2 K_{11}^1 + a_2^2 K_{12}^1}{8\omega_1} T_2 + \phi_1, \tag{11.2.3a}$$

$$\gamma_{(p)} = \frac{a_2 g_{12}^1}{2\omega_1} p T_1 - \frac{a_1^2 K_{11}^1 + a_2^2 K_{12}^1}{4\omega_1} T_2 - \left(\frac{a_1^2 g_{11}^2}{4\omega_2 a_2} p T_1 - \frac{a_2^2 K_{22}^2 + a_1^2 K_{12}^2}{8\omega_2} T_2\right) - \sigma T_1 + \phi_p. \tag{11.2.3b}$$

with ϕ_1 and $\phi_{(p)}$ integration constants. Consequently, using Eq. (11.1.27) we get the solution in the original variables:

$$\theta_1 = \frac{a_2 g_{12}^1}{4\omega_1} p T_1 - \frac{a_1^2 K_{11}^1 + a_2^2 K_{12}^1}{8\omega_1} T_2 + \phi_1, \tag{11.2.4a}$$

$$\theta_2 = \frac{a_1^2 g_{11}^2}{4\omega_2 a_2} p T_1 - \frac{a_2^2 K_{22}^2 + a_1^2 K_{12}^2}{8\omega_2} T_2 + 2\phi_1 - \phi_{(p)}. \tag{11.2.4b}$$

By taking assumption that $T_0 = T_1 = T_2 = t$ [14], such that the nonlinear pulsation can be expressed as:

$$\omega_{NL1} = \frac{a_2 g_{12}^1}{4\omega_1} p - \frac{a_1^2 K_{11}^1 + a_2^2 K_{12}^1}{8\omega_1} + \omega_1, \tag{11.2.5a}$$

$$\omega_{NL2} = \frac{a_1^2 g_{11}^2}{4\omega_2 a_2} p - \frac{a_2^2 K_{22}^2 + a_1^2 K_{12}^2}{8\omega_2} + \omega_2, \tag{11.2.5b}$$

and inserting Eq. (11.2.5) into Eq. (11.2.1), one can see that the nonlinear frequencies of these two modes have a relationship : $\omega_{NL2} = 2\omega_{NL1}$. Combining Eq. (11.2.5a) with Eq. (11.2.2), the relationship between a_2 and ω_{NL1} reads as:

$$\omega_{NL1} = \frac{\left(a_2^3(K_{11}^1 K_{22}^2 - K_{12}^1 K_{12}^2) + 2a_2^2(g_{11}^2 K_{12}^1 + g_{12}^1 K_{12}^2)p - 4a_2 g_{12}^1 g_{11}^2 + 8a_2 K_{12}^2 \omega_1^2 - 16 g_{11}^2 p \omega_1^2 - 8a_2 K_{11}^1 \omega_2^2\right)}{8(a_2 K_{12}^2 \omega_1 - 2g_{11}^2 p \omega_1 - 2a_2 K_{11}^1 \omega_2)}, \tag{11.2.6}$$

Finally, considering Eq. (11.2.6) and Eq. (11.2.2) together, one can obtain the relationship among a_1, a_2 and ω_{NL1} and draw the backbone curves of the system. Once again, as noted in previous section, p in the equations could be $+1$ or -1, the solution obtained with $p = 1$ is hence called $p+$ mode, and $p = -1$ will lead to the $p-$ mode.

The necessary condition for having solutions of a_1 is that the right hand side of Eq. (11.2.2) is a positive value. The condition of having solution thus change to be

$$(-a_2K^2_{12}\omega_1+2g^2_{11}\omega_1p+2a_2K^1_{11}\omega_2)(a_2^2K^2_{22}\omega_1-2a_2^2K^1_{12}\omega_2+4a_2g^1_{12}p\omega_2+16\omega_1^2\omega_2-8\omega_1\omega_2^2) \geqslant 0, \tag{11.2.7}$$

To better analysis above inequality, the left hand side of Eq. (11.2.7) can be rewritten in the form of cubic function as:

$$f(a_2) = Aa_2^3 + Ba_2^2 + Ca_2 + D, \tag{11.2.8}$$

where

$$\begin{aligned}
&A = -(K^2_{12}\omega_1 - 2K^1_{11}\omega_2)(K^2_{22}\omega_1 - 2K^1_{12}\omega_2),\\
&B = 2p(2g^1_{12}\omega_2(-K^2_{12}\omega_1 + 2K^1_{11}\omega_2) + g^2_{11}\omega_1(K^2_{22}\omega_1 - 2K^1_{12}\omega_2)),\\
&C = 8\omega_1\omega_2(g^1_{12}g^2_{11}p^2 - (2\omega_1 - \omega_2)(K^2_{12}\omega_1 - 2K^1_{11}\omega_2)),\\
&D = 16g^2_{11}p\omega_1^2(2\omega_1 - \omega_2)\omega_2.
\end{aligned} \tag{11.2.9}$$

It is found that the backbone curves can be divided into two parts depending on value of D, more details can be found in the following sections.

11.2.1 Main branch

It is obvious that when $D \geqslant 0$, there will always be positive values of a_2 that can make the inequality (11.2.7) fulfilled, such that it always has a solution starting with $a_2 \approx 0$ and $\omega_{NL1} \approx \omega_1$, and thus called the main branch of the backbone, as the red curve shown in Fig. 11.2.1. If one assumes $g^2_{11} > 0$, which is often the case for thin structures, for $\sigma > 0$, D will be positive when $p = -1$, so the $p-$mode will be the main branch, and for $\sigma < 0$, the $p+$mode will be the main branch. Finally, when $D = 0$, both $p+$ and $p-$ modes will start from $(0, \omega_1)$ and to be the main branches.

11.2.2 Side branch

For distinguishing from the main branch introduced above, solutions with $D < 0$ are named as the side branch of the backbone, when $\sigma < 0$, the curve of $p-$ mode is side branch, in contrast, when $\sigma > 0$, the side branch will be the curve of $p+$ mode. The blue curve in Fig.11.2.1 shows an example of side branch, which starts from a_1 with a certain value.

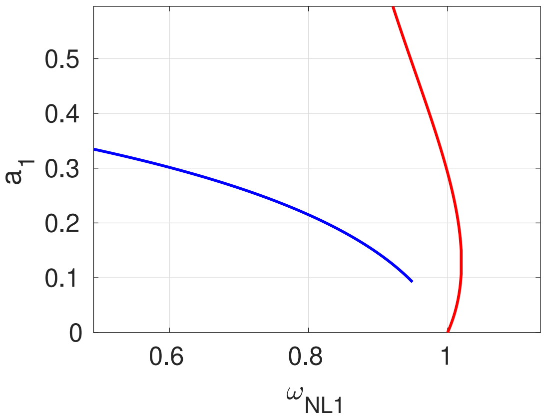

Figure 11.2.1: An example of backbone curve with main branch (red) and side branch (blue).

11.3 Behaviour of the system for large detuning

Firstly, let us investigate the behaviour of the system for large detuning, *i.e.*, ω_2 is away from $2\omega_1$. In such context, the behaviour of the system is fully dependent on the main branch of the backbone, and side branch is less important. The idea is to investigate whether the main branch of backbone curves calculated by normal form with 1:2 internal resonance is close to the results of a single nonlinear normal mode or not.

The first order nonlinear frequency obtained by a single normal mode reads as:

$$\omega_{NL}^{sdof} = \omega_1(1 + \Gamma_{sdof} a_1^2), \tag{11.3.1}$$

where Γ_{sdof}, the indicator of hardening/softening behaviour, is expressed by:

$$\Gamma_{sdof} = \frac{1}{8\omega_1^2}(3h_{111}^1 - \frac{10(g_{11}^1)^2}{3\omega_1^2} - \frac{3\omega_2^2 - 8\omega_1^2}{\omega_2^2 - 4\omega_1^2}\frac{g_{12}^1 g_{11}^2}{\omega_2^2}). \tag{11.3.2}$$

For the purpose of comparison, the nonlinear frequency of the full system with 1:2 resonance, which is given by the Eq. (11.2.5a), can also be written as:

$$\omega_{NL1} = \omega_1(1 + \tilde{\Gamma}_1 a_1^2 + \tilde{\Gamma}_2 a_2^2 + \hat{\Gamma}_2 a_2), \tag{11.3.3}$$

where Γ are the coefficients dictating the type of nonlinearity:

$$\tilde{\Gamma}_1 = -\frac{K^1_{11}}{8\omega_1^2}, \quad \tilde{\Gamma}_2 = -\frac{K^1_{12}}{8\omega_1^2}, \quad \hat{\Gamma}_2 = \frac{g^1_{12}}{4\omega_1^2} p. \tag{11.3.4}$$

One can also express Eq. (11.3.4) by using coefficients g^p_{ij}, h^p_{ijk}, then, one obtains:

$$\tilde{\Gamma}_1 = \frac{1}{8\omega_1^2}(3h^1_{111} - \frac{10(g^1_{11})^2}{3\omega_1^2} - \frac{9g^1_{12}g^2_{11}}{4\omega_2^2}), \tag{11.3.5a}$$

$$\tilde{\Gamma}_2 = \frac{1}{8\omega_1^2}(2h^1_{122} + \frac{(16\omega_2^2 - 4\omega_1^2)g^1_{22}g^1_{11}}{(\omega_1^4 - 4\omega_1^2\omega_2^2)} - \frac{6g^2_{22}g^1_{12}}{3\omega_2^2} + \frac{4g^2_{12}g^1_{22}}{\omega_1^2 - 4\omega_2^2} - (\frac{(g^1_{12})^2}{\omega_1^2 - (\omega_1 + \omega_2)^2} + \frac{(g^1_{12})^2}{4\omega_1^2})), \tag{11.3.5b}$$

$$\hat{\Gamma}_2 = \frac{g^1_{12}}{4\omega_1^2} p. \tag{11.3.5c}$$

For illustrative propose, the numerical example system has been built, with all the nonlinear coefficients selected as constants:

$$\begin{aligned} &g^1_{12} = g^2_{12} = 2, \quad g^1_{11} = g^1_{22} = g^2_{11} = g^2_{22} = 1, \\ &h^1_{111} = h^2_{112} = h^1_{122} = h^2_{222} = 1, \quad h^2_{122} = h^2_{111} = h^1_{222} = h^1_{112} = 0. \end{aligned} \tag{11.3.6}$$

such selection fits the symmetry relationship of coefficients [13]: $g^1_{12} = 2g^2_{11}$, $g^2_{12} = 2g^1_{22}$, $h^2_{112} = h^1_{122}$, and the magnitudes of quadratic and cubic terms are all in a reasonable range.

Fig.11.3.1 compares the main branch of the backbone curves of given by the system with 1:2 resonance and the system reduced to a single dof nonlinear normal modes, with σ far away from 0. From the coefficients given by Eq. (10.1.4), it should be noted that there is also a 2:1 divergence ($\omega_1 = 2\omega_2$) that needs to be avoid when choosing the value of frequencies. In Fig.11.3.1 (a), $\omega_1 = 1$ and ω_2 is set before the divergence (when $\omega_2 = 0.5$), the curves of $p+$ mode (red) show that a_2 is very small when a_1 is not very large. In Fig.11.3.1 (b), when σ is increased to be a very large value, the blue curves are also closer to the plane (ω_{NL1}, a_1). From the two figures, it is shown that when ω_2 is far away from $2\omega_1$, the main branch starting at $\omega_1 = 1$ tends to a sdof solution with $a_2 = 0$ (the black curves).

To give the explanation of such trend, a_2 obtained by Eq. (11.2.6) with regard to ω_{NL1} is

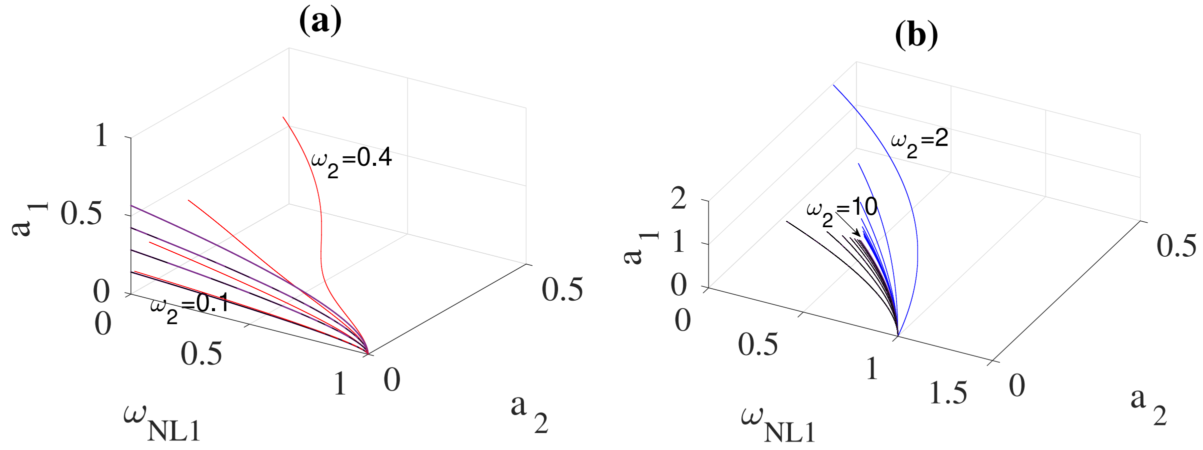

Figure 11.3.1: Main branch of backbone curves of the system, with $\omega_1 = 1$, the coefficients are given in Eq. (11.3.6). (a): $p+$ mode (red) with ω_2 as a variable value changing from 0.1 to 0.4 (before 2:1 divergence). (b): $p-$ mode (blue) with ω_2 as a variable value changing from 2 to 10 (after 1:2 divergence). The purple represent the backbone curves computed by single-mode dynamics.

derived and noted as Da_2, reads:

$$\begin{aligned} Da_2 &= \frac{\partial a_2}{\partial \omega_{NL1}} \\ &\approx \frac{4g_{11}^2\omega_1}{p(g_{12}^1 g_{11}^2 + 2K_{11}^1\omega_2(\omega_2 - 2\omega_1))} + o(a_2). \end{aligned} \tag{11.3.7}$$

Under the assumption that a_2 is small, such that Da_2 will be expressed as a constant value and $o(a^2)$ can be neglected. A large absolute value of Da_2 represent the value of a_2 will increase rapidly when a_1 is increasing, such that the main branch of the backbone curve will be more and more far away from the plane (a_1, ω_{NL1}), for example the case $\omega_2 = 0.4$ in Fig. 11.3.1(a). From the Eq. (11.3.7), when ω_2 is increasing and in a very large value, the absolute value of Da_2 is decreasing and tend to be 0, and the curves will be closer to the plane ($a_2 = 0$). Apart from that trend, Fig. 11.3.1 also demonstrates that when the resonant mode was not excited a lot, *i.e.* a_2 is in a small value, the solution of the main branch match well with the results computed by single-mode dynamics.

Comparing the Eq. (11.3.2) and (11.3.5), It is found the expression of $\tilde{\Gamma}_1$ are quite close to Γ_{sdof}, however, to find regularity in detail, further comparisons were done in the numerical examples, with a new term $\gamma_{[M]}$ introduced with $[M]$ represents the different cases. For normal form of the system with 1:2 resonance: $\gamma_r = \tilde{\Gamma}_1 a_1^2 + \tilde{\Gamma}_2 a_2^2 + \hat{\Gamma}_2 a_2$, and for single normal mode: $\gamma_{sdof} = \Gamma_{sdof1} a_1^2$. When $\gamma_{[M]}$ is positive, indicates the hardening behaviour of backbone curve, and when $\gamma_{[M]}$ is negative, implies softening behaviour.

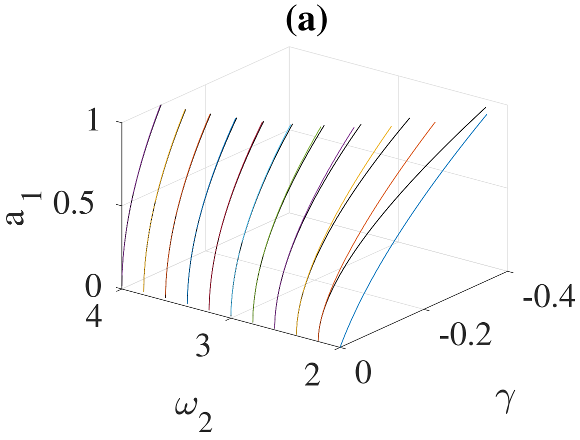

$p-$ mode

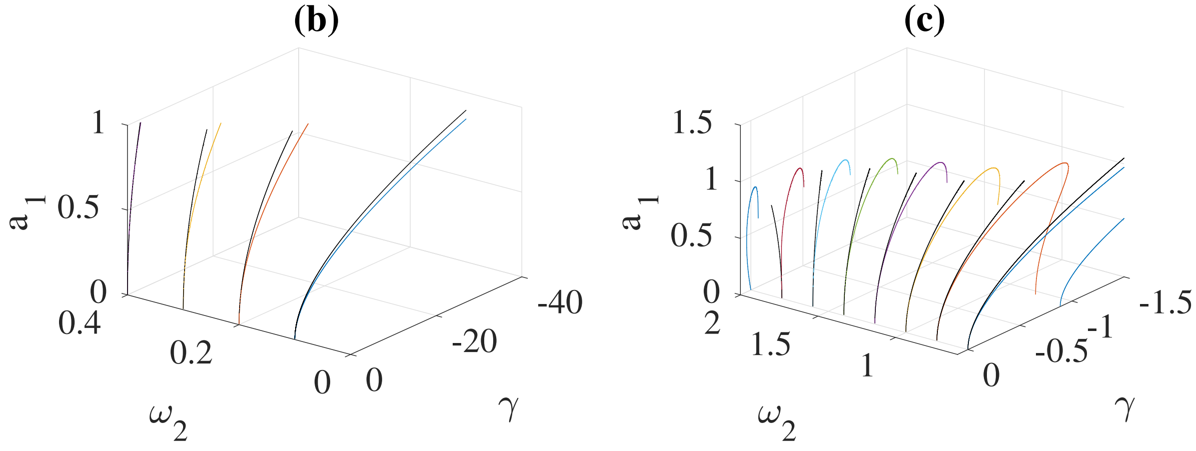

$p+$ mode

Figure 11.3.2: Curves are computed by $\gamma_{[M]}$ as the function of ω_2 and a_1, with $\omega_1 = 1$, the coefficients are given in Eq. (11.3.6), and ω_2 as a variable value changing from 0.1 to 0.4, 0.6 to 2, and 2 to 4. The black curves are the results of single NNM and the colourful curves represent the results of NNM with 1:2 resonance.

In order to predict the type of nonlinearity of the system by investigating the indicator of type of nonlinearity $\gamma_{[M]}$, Fig. 11.3.2 shows the results of comparison of the indicator computed by the normal form reduction with 1:2 resonance results (colourful) and the single NNM (black), with regard to the amplitude of first mode a_1 and the natural frequency of the second mode ω_2. The cases with positive detuning are shown in Fig. 11.3.2(a), where the $p-$ mode is the main branch. The results of the case with negative detuning are plotted in Fig. 11.3.2(b) (before 2:1 resonance) and (c) (after 2:1 resonance), where the main branch is $p+$ mode.

From the figures, it is found that when ω_2 is far from $2\omega_1$, the colourful curves match the corresponding black curves well while when σ is close to 0, the colourful curves match the corresponding black curves only when a_1 is a small value. Furthermore, the differences between colourful curves and the black curves are remarkable when very near 1:2 divergence and two curves even may predict the opposite type of nonlinearity. One should also notice that when $\omega_2 = 2\omega_1$, there is no single normal mode solution for the indicator because of 1:2 divergence.

From this numerical example shown in Fig. 11.3.2, one can conclude that when $\omega_2 \gg 2\omega_1$ or $\omega_2 \ll 2\omega_1$, the indicator $\gamma_{[M]}$ computed by the normal form reduction with 1:2 resonance results and the single NNM are the same and predict the same hardening/softening behaviour, on the other hand, the difference is large in the vicinity of 1:2 divergence, moreover, the single NNM fails to give the prediction when detuning is 0.

11.4 Behaviour in the vicinity of 1:2 resonance

Now we are investigating the behaviour of the system in the vicinity of 1:2 resonance. In such a context, the side branch becomes important because it is close to the main one. The works presented here are related to the results given in [101] without cubic nonlinearity considered, while further developments are done here by researching the behaviour of the main branch and the starting point of the side branch, aims to give a clear view of the crossing 1:2 divergence.

11.4.1 Starting point of side branch

The existence of the real and positive solution for the branch of the backbone could be analysed from the roots of Eq. (11.2.8), which are given by:

$$a_2^{r1} = \frac{-4g_{12}^1 p\omega_2 + \sqrt{16(g_{12}^1)^2 p^2\omega_2^2 - 4(K_{22}^2\omega_1 - 2K_{12}^1\omega_2)(16\omega_1^2\omega_2 - 8\omega_1\omega_2^2)}}{2(K_{22}^2\omega_1 - 2K_{12}^1\omega_2)}, \tag{11.4.1a}$$

$$a_2^{r2} = \frac{-4g_{12}^1 p\omega_2 - \sqrt{16(g_{12}^1)^2 p^2\omega_2^2 - 4(K_{22}^2\omega_1 - 2K_{12}^1\omega_2)(16\omega_1^2\omega_2 - 8\omega_1\omega_2^2)}}{2(K_{22}^2\omega_1 - 2K_{12}^1\omega_2)}, \tag{11.4.1b}$$

$$a_2^{r3} = \frac{2g_{11}^2 p\omega_1}{K_{12}^2\omega_1 - 2K_{11}^1\omega_2}. \tag{11.4.1c}$$

The third root (11.4.1c) is derived from $(-a_2K_{12}^2\omega_1 + 2g_{11}^2\omega_1 p + 2a_2K_{11}^1\omega_2) = 0$, which is the denominator of Eq. (11.2.2), so it will lead to divergence and generate an unstable branch of backbone curves if this root is positive. Such error arises from the truncation of the first order of multiple scale method computations and the third order asymptotic of the normal form of the system, so this situation will not be discussed here.

In the context that cubic nonlinearity is not considered [101], the side branch will always exist and with a starting point $\omega_{NL1}^r = \frac{\omega_2}{2}$, $a_2^r = \frac{2\omega_1(\omega_2-2\omega_1)}{g_{12}^1 p}$. However, now in the case of cubic nonlinearity involved, the position of the starting point of the side branch is expected to be affected and thus change to another position, which theoretically should not be far from the location computed with only quadratic terms. In order to know the exact starting points of the side branches, *i.e.*, the branch starts from $a_2 \neq 0$ and $a_1 \approx 0$, Eq. (11.2.1) can thus be rewritten as

$$\frac{a_2 g_{12}^1}{2\omega_1}p - \frac{a_2^2 K_{12}^1}{4\omega_1} + \frac{a_2^2 K_{22}^2}{8\omega_2} - \sigma = g(a_1, a_1^2) \approx 0. \tag{11.4.2}$$

Solving the above equation and inserting into Eq. (11.2.6), we thus obtain the value a_2^{r1} and a_2^{r2} with expression given in Eqs. (11.4.1a,11.4.1b) that lead $a_1 = 0$, and by inserting these two equations into Eq. (11.2.6), we also obtain the corresponding ω_{NL1}^{r1} for a_2^{r1} and ω_{NL1}^{r2} for a_2^{r2}, read:

$$\begin{aligned}\omega_{NL1}^{r1} =& \frac{1}{2(K_{22}^2\omega_1 - 2K_{12}^1\omega_2)^2} \times \Big(2(K_{22}^2)^2\omega_1^3 + 4(K_{12}^1)^2\omega_2^3 - K_{22}^2\Big((g_{12}^1)^2\omega_2 + 2K_{12}^1\omega_1\omega_2(2\omega_1+\omega_2)\\ &+ g_{12}^1 p\sqrt{\omega_2(2K_{22}^2\omega_1^2(-2\omega_1+\omega_2) + \omega_2((g_{12}^1)^2p^2 + 8K_{12}^1\omega_1^2 - 4K_{12}^1\omega_1\omega_2))}\Big)\Big),\end{aligned} \tag{11.4.3a}$$

$$\begin{aligned}\omega_{NL1}^{r2} =& \frac{1}{2(K_{22}^2\omega_1 - 2K_{12}^1\omega_2)^2} \times \Big(2(K_{22}^2)^2\omega_1^3 + 4(K_{12}^1)^2\omega_2^3 + K_{22}^2\Big(-(g_{12}^1)^2\omega_2 - 2K_{12}^1\omega_1\omega_2(2\omega_1+\omega_2)\\ &+ g_{12}^1 p\sqrt{\omega_2(2K_{22}^2\omega_1^2(-2\omega_1+\omega_2) + \omega_2((g_{12}^1)^2p^2 + 8K_{12}^1\omega_1^2 - 4K_{12}^1\omega_1\omega_2))}\Big)\Big),\end{aligned} \tag{11.4.3b}$$

while the third root a_2^{r3} may also be a starting/ending point with certain value but without corresponding ω_{NL1}^{r3} and a_1 ($\omega_{NL1}^{r3} = \pm\infty, a_1 = \infty$).

The following equation gives the first order nonlinear frequency of the second master mode of the 2-dofs system:

$$\omega_{NL2}^{sdof} = \omega_2(1 + \Gamma_{sdof2}a_2^2). \tag{11.4.4}$$

where

$$\Gamma_{sdof2} = \frac{-K_{22}^2}{8\omega_2^2} = \frac{1}{8\omega_2^2}(3h_{222}^2 - \frac{10(g_{22}^2)^2}{3\omega_2^2} - \frac{3\omega_1^2 - 8\omega_2^2}{\omega_1^2 - 4\omega_2^2}\frac{g_{12}^2 g_{22}^1}{\omega_1^2}). \tag{11.4.5}$$

In the case of $a_1 \approx 0$, combining above equation with Eq. (11.2.5b), It is found that

$$2\omega_{NL1}^r = \omega_2(1 + \Gamma_{sdof2}(a_2^r)^2), \tag{11.4.6}$$

such that the starting points exactly lay on the curve given by $\frac{1}{2}\omega_{NL2}^{sdof}$. In the case of two possible starting points exist: $(a_2^{r1}, \omega_{NL1}^{r1})$, $(a_2^{r2}, \omega_{NL1}^{r2})$, the points with a small value of a_2^r have also a ω_{NL1}^r that is an approximate value of the $\frac{1}{2}\omega_2$ and thus to be the starting point, and the other one is the ending point.

For illustrative purposes, Fig. 11.4.1 shows the results computed by Eq. (11.2.5a) and $\frac{1}{2}\omega_{NL2}^{sdof}$ in the plane of (a_2, ω_{NL1}), with the coefficients of the system given in Eq. (11.3.6) and $\omega_1 = 1$ and ω_2 selected from 1.2 to 2.2. In the figure, The solid curves are computed by Eq. (11.2.5a) with $a_1 = 0$, and the dashed curves are computed by $\frac{1}{2}\omega_{NL2}^{sdof}$. From the figure, the cross point of the same colour solid and dashed curves gives the starting point of the side branch. Also, in this case, it is found that the solution of side branch of the multiple scale method will disappear when $\sigma > 0.24$, so in the next section, we will discuss about the existence of the side branch in the solution of multiple scale method.

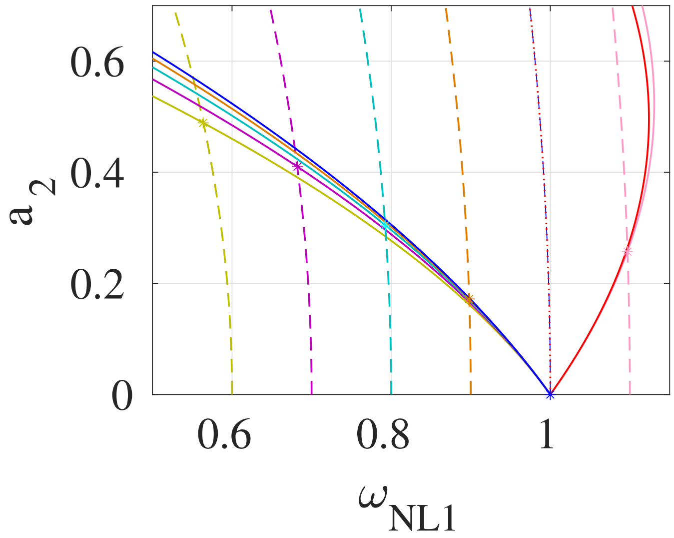

Figure 11.4.1: The solid curves are computed by Eq. (11.2.5a) with $a_1 = 0$, and the dashed curves are computed by $\frac{1}{2}\omega_{NL2}^{sdof}$. The stars are the cross points of the two curves. The coefficients of the system are given in Eq. (11.3.6), with $\omega_1 = 1$ and ω_2 selected every 0.2 (with each kind of colour) from 1.2 to 2.2.

11.4.2 Existence of side branch

Now we are investigating the condition for the existence of the side branch. From the Eqs. (11.4.1a,11.4.1b), it is found that

$$a_2^{r1} a_2^{r2} (a_2^{r1} + a_2^{r2}) = \frac{-32\omega_1 \omega_2^2 g_{12}^1 p \sigma}{(K_{22}^2 \omega_1 - 2K_{12}^1 \omega_2)^2} \geqslant 0, \tag{11.4.7}$$

thus, it is impossible for a_2^{r1} and a_2^{r2} are negative at the same time. In another words, The side branches will exist when the a_2^{r1} and a_2^{r2} are real value such that at least one of them will be positive and to be a starting point of a branch. In the situation where $\sigma > 0$, $(a_2^{r2}, \omega_{NL1}^{r2})$ will be the starting point because of $a_2^{r2} < a_2^{r1}$, on the other hand, $(a_2^{r1}, \omega_{NL1}^{r1})$ will be the starting point when $\sigma < 0$. In the case that the side branch is exists, a_2^{r1} and a_2^{r2} should be the real values and the following equation should be fulfilled:

$$16(g_{12}^1)^2 p^2 \omega_2^2 - 4(K_{22}^2 \omega_1 - 2K_{12}^1 \omega_2)(16\omega_1^2 \omega_2 - 8\omega_1 \omega_2^2) > 0, \tag{11.4.8}$$

thus

$$\sigma(K_{22}^2 \omega_1 - 2K_{12}^1 \omega_2) > \frac{-(g_{12}^1)^2 \omega_2}{2\omega_1}. \tag{11.4.9}$$

The following figure shows the restrictions for the existence of the side branches, where $\Delta = \frac{-(g_{12}^1)^2 \omega_2}{2\omega_1 (K_{22}^2 \omega_1 - 2K_{12}^1 \omega_2)}$. In the yellow and green range, the side branches will have both starting and ending point, an example shown in (a), while in the blue and orange part, there will be only starting point for the side branch. The white represents the range that backbone curves have no side branch, with an example shown in (b) with only $p-$ mode. Besides, in the case of $\sigma > 0$ (blue,yellow), the starting point will be $(a_2^{r2}, \omega_{NL1}^{r2})$, while in the case of $\sigma < 0$ (orange,green), the starting point will be $(a_2^{r1}, \omega_{NL1}^{r1})$.

It should be noted that the above existence range for the side branch is analysed by the first order multiple scale methods, in the context of $\omega_2 \approx 2\omega_1$, so the range shown here is reliable only when the detuning is not very large. In other words, when the detuning is in a large value, the multiple scale method fails to catch the solution of the side branch, which really exists in the original system. Such a counter-example is shown in Fig. 11.4.3, with coefficients selected as Eq. (11.3.6), with $\omega_1 = 1, \omega_2 = 2.5$. From the figure, one can find that the multiple scale solution only retrieve the main branch of the backbone and there is no solution for the side branch, because in such context the left-hand side of Eq. (11.4.8) is negative, while when using continuation method to calculate the backbone curve of the original full order system,

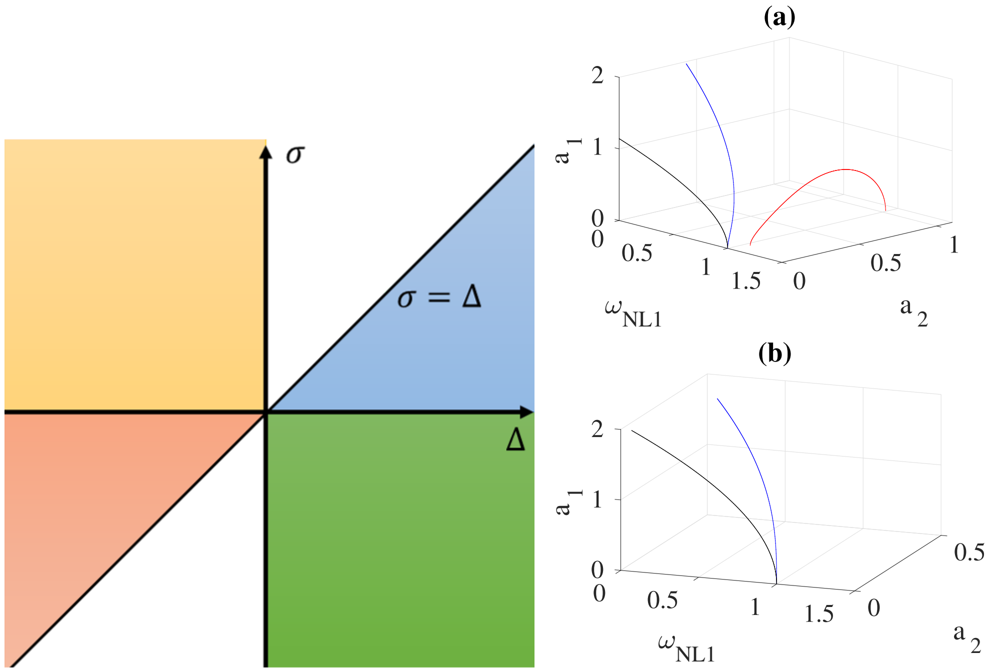

Figure 11.4.2: The schematic representation of the side branch existence range, and examples for two situations. (a): the side branches will have both starting and ending point, (b): Backbone curve has no side branch.

it is shown that the side branch of backbone should exist. This example shows the range of existence of the side branch derived by multiple scale solutions are true and reliable only in the system with not large detuning.

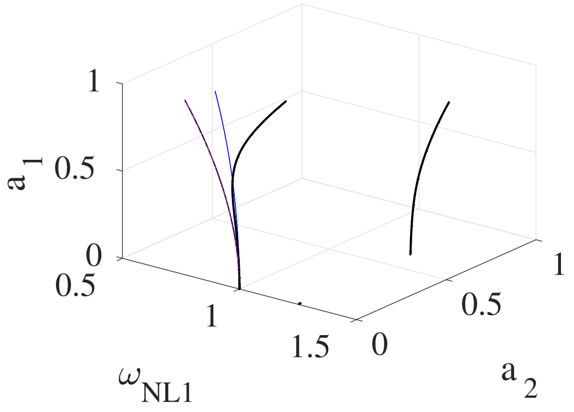

Figure 11.4.3: The backbone curve computed by the multiple scale method, only main branch exist and plotted in blue. The black curves are the backbone of original system computed by continuation method and shows that the side branch exist. The purple is the solution of single NNM.

11.4.3 Hardening/softening behaviour of the main branch

In this section, the change of hardening/softening behaviour in the crossing of 1:2 divergence is investigated and an augmented representation that can smooth the diverging behaviour is searched. The backbone curves of the system in the vicinity of 1:2 resonance computed by multiple scale method on the normal form with 1:2 resonance and the single normal mode are compared, also, the solution of continuation method is included and taken as the reference in order to validate the results of multiple scale solution.

The type of nonlinearity of the main branch (in the context of $a_2 \approx 0$) of the backbone curves can be found from the derivation of a_1 with regard to ω_{NL1}, expressed as following equation:

$$\frac{d(a_1)}{d(\omega_{NL1})} = \frac{d(a_1)}{d(a_2)}\frac{d(a_2)}{d(\omega_{NL1})} = \frac{-16\omega_1\omega_2\sigma}{g^1_{12}g^2_{11}p^2 - 4K^1_{11}\omega_1\omega_2 + 2K^1_{11}\omega_2^2} + o(a_2). \tag{11.4.10}$$

where $\frac{d()}{d()}$ is the notation of derivation, $\frac{d(a_1)}{d(a_2)}$ is obtained from Eq. (11.2.2), and $\frac{d(a_2)}{d(\omega_{NL1})}$ is computed by Eq. (11.2.6). When $\frac{d(a_1)}{d(\omega_{NL1})} > 0$, the system shows a hardening behaviour, if $\frac{d(a_1)}{d(\omega_{NL1})} < 0$, the system would be softening. From Eq. (11.4.10), It should be noted that different from the conclusion given by [101] where only quadratic coefficients are considered, the type of nonlinearity will also depend on the value of coefficients K^1_{11}. To easily investigate the type of nonlinearity of the system, the following equation is introduced:

$$F(\sigma) = -16\omega_1\omega_2\sigma(g^1_{12}g^2_{11}p^2 - 4K^1_{11}\omega_1\omega_2 + 2K^1_{11}\omega_2^2), \tag{11.4.11}$$

which share the same positive or negative characteristic with the Eq. (11.4.10). By inserting the expression of K^1_{11} given by (11.1.21) and considering $\omega_2 = 2\omega_1 + \sigma$, after the first order truncation, the equation reads:

$$F(\sigma) = -32g^1_{12}g^2_{11}\omega_1^2\sigma + o(\sigma^2). \tag{11.4.12}$$

It is indicated that when σ is very small, the backbone curves will show a hardening behaviour when $\sigma < 0$ (in such situation the main branch is the $p+$ mode), while when $\sigma > 0$ (in such case the main branch is the $p-$ mode), the backbone curves show a softening behaviour. Thus, the results exactly match the conclusion of [101] in the context of $\sigma \approx 0$.

In summary, it is known that for the system with 1:2 resonance and cubic nonlinearity, when $\sigma \approx 0$, the results will still in the frame of the conclusion given in [101], *i.e.*, in the context $\sigma < 0$, the $p+$ mode is the main branch and show a softening behaviour, and when $\sigma > 0$, the $p-$ mode will be the main branch and is hardening. On the other hand, when σ far from 0, different from the case presented in [101], the type of nonlinearity also depends on the value of K_{11}^1.

For giving the example, Fig. 11.4.4 shows the backbone curves of the lower frequency mode, coefficients of system are chosen as Eq. (11.3.6) and the ω_1 is selected as 1, and (a) $\omega_2 = 1.9$ such that $\sigma < 0$, (b): $\omega_2 = 2$ in the case of $\sigma = 0$ and (c): $\omega_2 = 2.1, \sigma > 0$. In the figures, the blue ($p-$ mode) and red ($p+$ mode) curves represent the backbone curves computed by multiple scale method with normal form reduction with 1:2 internal resonance, and for validating the solution, backbone curves of the original system (black) are computed by continuation method (Manlab).

In Fig. 11.4.4(a), the side branch of backbone curves (blue) show a softening behaviour when $\sigma = -0.1$. On the other hand, in Fig. 11.4.4(c), when $\sigma = 0.1$ (the side branch is the $p+$ mode which in red), the system shows a hardening behaviour. Such results exactly prove that when σ is very small, generally the effect of cubic nonlinearity can be neglected and the hardening/softening behaviour will in the frame of the conclusion given in [101].

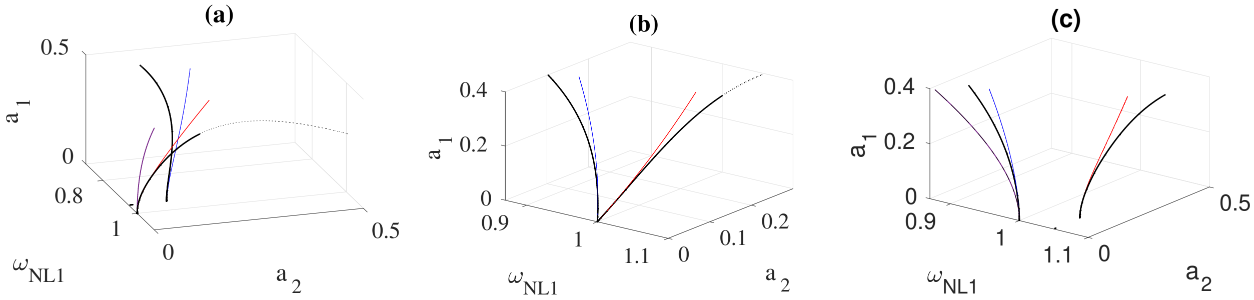

Figure 11.4.4: Backbone curves of the first mode, coefficients of system are chosen as Eq. (11.3.6) and the ω_1 is selected as 1, and the ω_2 is chosen to be 1.9 (a), 2 (b) and 2.1 (c). In the figures, the analytical results of the NF with 1:2 internal resonance are given in blue ($p-$ mode) and red ($p+$ mode), also the result of the single NNM is given in purple, and the results of the original system calculated by the Manlab are shown in black, with the unstable solution dotted.

Also from Fig. 11.4.4, it is found that the multiple scale solutions match well with the full order solution when the amplitude is not very large, also, it is shown that with considering of 1:2 internal resonance, the solution is more accurate than the result obtained by single normal mode as compared to the full order solution. For illustrative purpose, keeping studying the systems with the same coefficients and detuning, Fig. 11.4.5 shows the comparison of the multiple scale solution and HBM continuous solution, *i.e.*, comparing the coefficients in Eq. (11.1.30) and (11.1.31) with corresponding harmonic component computed by Manlab.

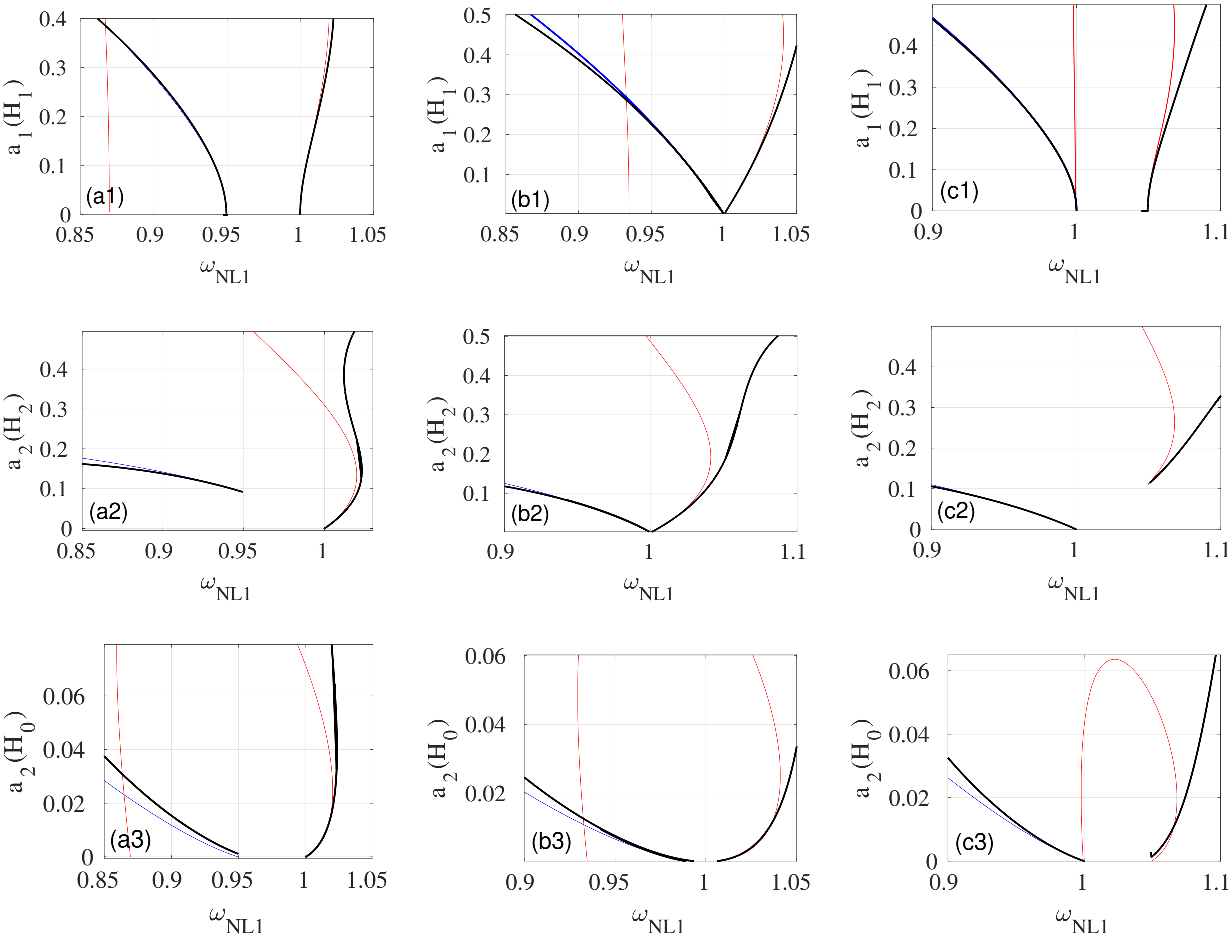

Figure 11.4.5: The comparison of the multiple scale solution (red: $p+$ mode, blue: $p-$ mode) and HBM continuous solution (black), *i.e.*, comparing the coefficients in Eq. (11.1.30) and (11.1.31) with corresponding harmonic component computed by Manlab. Where coefficients of system are chosen as Eq. (11.3.6) and the ω_1 is selected as 1, and the ω_2 is chosen to be 1.9 (a), 2 (b) and 2.1 (c). The first row shows the first harmonic solution for mode 1, the second row represents the second harmonic solution for mode 2 and the third row is the solution of the part with constant coefficient for mode 2.

From Fig. 11.4.5, for all the harmonic components for amplitudes of the modes a_1 and a_2, it is found that backbone curves obtained by the multiple scale methods match well by the continuation method when the amplitude is not very large, also, it is shown that multiple scale solutions retrieve the starting points of the side branch very well. Also, from Fig. 11.4.5 (a) and (c), one can observe that the difference of the results between the two methods is smaller on the calculation of the main branch as compared to the calculation of side one. One should also notice that the $p+$ mode in some of the cases, for example (c3), has both a starting point ($\omega_{NL}^{r} \approx 1.05$) and an ending point ($\omega_{NL}^{r} \approx 1$). In a 3D plot of (a_1, a_2, ω_{NL1}) as shown in Fig 11.4.4(c), the ending point has a large value of a_2. However, because the multiple scale method is applied in the first order such that can be trusted only at the beginning of the backbone curves, the prediction of the ending point here is unreliable.

Fig. 11.4.6 shows another two cases, the idea now is to investigate the system with considerable value of K_{11}^{1} and not a small detuning σ, hence, to highlight the difference of the results between the case with cubic nonlinearity considered and the system with only quadratic nonlinearity, as presented in [101]. Different detuning situation is studied here, in the first case, coefficients of system are given in Eq. (11.3.6), $\omega_1 = 1$, and $\omega_2 = 1.5$ ($\sigma > 0$). In the second case, coefficients of system are given in Eq. (11.4.13) with $\omega_1 = 1$, and $\omega_2 = 2.5$ ($\sigma < 0$).

$$\begin{aligned} &g_{12}^{1} = g_{12}^{2} = 2, \quad g_{11}^{1} = g_{22}^{1} = g_{11}^{2} = g_{22}^{2} = 1; \\ &h_{111}^{1} = h_{112}^{2} = h_{122}^{2} = h_{222}^{2} = 5, \quad h_{122}^{2} = h_{111}^{2} = h_{222}^{1} = h_{112}^{1} = 0. \end{aligned} \tag{11.4.13}$$

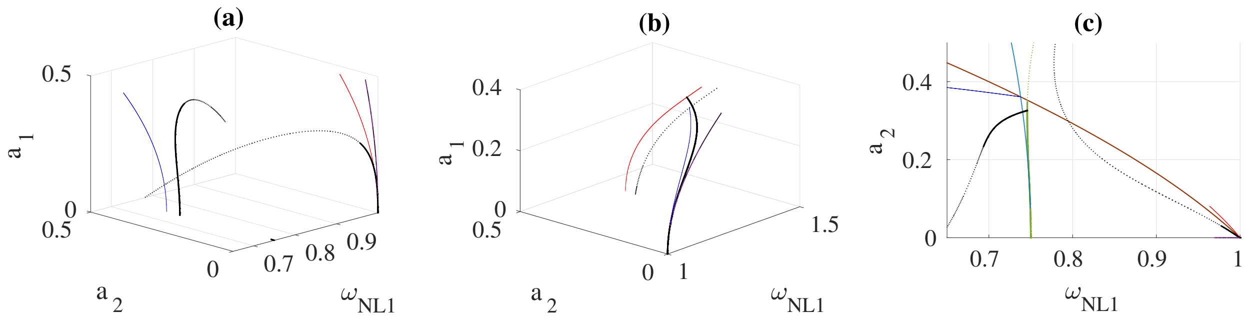

Figure 11.4.6: Backbone curves of the system, (a): coefficients are chosen as Eq. (11.3.6) and $\omega_1 = 1$, $\omega_2 = 1.5$ ($\sigma < 0$), (b): coefficients are chosen as Eq. (11.4.13) and the $\omega_1 = 1$, $\omega_2 = 2.5$ ($\sigma > 0$). (c): Top view of plot (a), with the brown curve is computed by Eq. (11.2.5a) with $a_1 = 0$, the cyan curve is computed by $\frac{1}{2}\omega_{NL2}^{sdof}$, and the green curve presents the $\frac{1}{2}\omega_{NL2}^{sdof}$ computed on the ROM with continuous computation tool. In the figure, the analytical results of the normal form with 1:2 internal resonance are given in blue ($p-$ mode) and red ($p+$ mode), also the result of single NNM is in purple, and the results of the original system calculated by the Manlab are shown in black, with the unstable solution dotted.

In Fig. 11.4.6 (a): $p-$ mode shows hardening behaviour when it is the main branch in the case of $\sigma > 0$ and (b): $p+$ mode shows softening behaviour when it is the main branch in the case of $\sigma < 0$. The cases that shown as the counter-example illustrate the difference and complexity when the cubic terms involved in multiple scale solution of the system with 1:2 resonance, instead of only quadratic terms are considered [101]. In (a) and (b), one can find the starting point of side branch is not well retrieved, to be specific, ω_{NL}^r is correct but a_2^r shows little error as compared to the solution of the continuation method, such error is arisen from the detuning is large and the multiple scale solution for the side branch is not accurate enough in such context. In Fig. 11.4.6(c), it is clear that the starting point of the side branch lay exactly on the cross point of the brown and the cyan curve. Also, it is found that the side branch computed from the original system start with a point of the green curve that given by the nonlinear frequency of the second mode divided by 2, *i.e.* $\frac{1}{2}\omega_{NL2}^{sdof}$. Thus, the example validates again the conclusion obtained in Section 11.4.1.

Fig. 11.4.7 shows the indicator of type of nonlinearity predicted by single NNM with regard to σ (black), the function of Da_2 (pink) given in Eq. (11.3.7) and starting position a_2^r for the side branch (blue). It is shown that when σ tends to be 0, the nonlinear frequency of starting point of the side branch will be close to the ω_1 and thus will approach the main branch, also, from the trend of changing of Da_2, It is clear that from $\sigma < 0$ to $\sigma > 0$ (cross 1:2 divergence), the side branch will first approach the main branch and then leave away, the Da_2 also show a divergence, which represents the main branch switched the type of nonlinearity at a certain point, and the value of Da_2 will be large when $\sigma \approx 0$, it is because the main branch switches from $p+$ mode when $\sigma < 0$ to $p-$ mode when $\sigma > 0$. The figure show a inside view of 1:2 divergence of the result of signal NNM, the change of nonlinearity at crossing 1:2 resonance can be considered as the switch of the main branch and the side branch of the backbone curves such that producing the divergence.

11.5 Application: curved beams with FE discretization

In all previous numerical test cases, the coefficients are chosen freely, in this section, we are going to investigate a more realistic case, *i.e.*, the nonlinear coefficients are obtained from real FE structures thanks to the DNF, instead of ideal values. For that purpose, the nonlinear

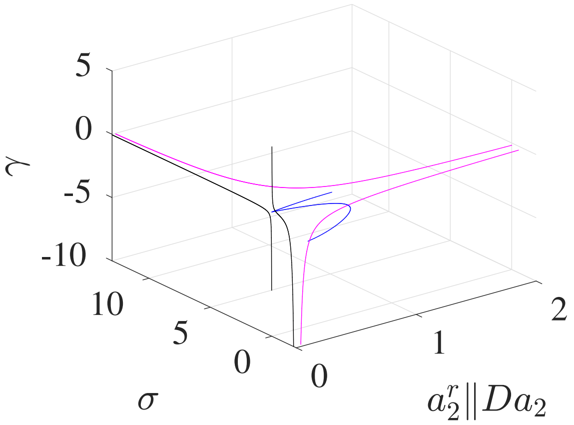

Figure 11.4.7: The indicator γ of type of nonlinearity predicted by single NNM with regards to σ (black), and the function of Da_2 (pink) for the main branch and starting position a_2^r for the side branch (blue). The coefficients of the system are given in Eq. (11.3.6), with $\omega_1 = 1$ and ω_2 selected from 0.1 to 15.

response of the clamped-clamped beams with rectangular cross-section in the neighbourhood of 1:2 internal resonance are investigated, and in order to draw different detuning of the two resonance eigenfrequencies, the investigation is performed on the beams with different curvatures. In the FE model, these beams are discretized with the 3D hexahedral 20 nodes element with 40 elements in the length and 4 elements in the cross-section. The schematic of the beam mesh and the corresponding modes are shown in Fig.11.5.1. Material properties are selected as: density $\rho = 4400kg/m^3$, Young modulus $E = 1.04e11Pa$, and Poisson's ratio $v = 0.3$. The dimensions of the beams with its corresponding response frequencies are shown in the following Tab.11.5.1:

Case	length(m)	thickness(m)	width(m)	height(m)	ω_1(Hz)	ω_2(Hz)	ratio ε
a	1	0.02	0.05	0.12	407.95	674.91	1.65
b	1	0.02	0.05	0.15	393.84	773.25	1.96
c	1	0.02	0.05	0.18	368.28	845.5	2.30

Table 11.5.1: The dimensions and the resonance frequencies of the clamped beams, where $\varepsilon = \omega_2/\omega_1$.

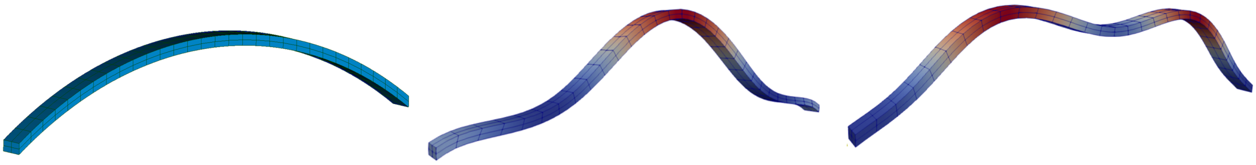

Figure 11.5.1: The schematic of the beam mesh (the left) and the modes (the middle and right).

Fig. 11.5.2 shows the backbone curves of the first transverse mode in the curved direction of the curved beam, as shown in the middle of Fig. 11.5.1. In the figure, the analytical results of the NF with 1:2 internal resonance are given in blue ($p-$ mode) and red ($p+$ mode), and the backbone curves of the two NNMs derived by normal form calculated by Manlab are shown in black, with the unstable solution dotted.

In the figures, it is found that for the main branch of the backbone, the multiple scale solution matches the results obtained by the continuation method well when the amplitude a_1 is not very large. One can also observe that when detuning is small, as shown in the middle plot, the side branch obtained by these two methods agrees well at the beginning of the branch. While it should be noted here that in the left and right plots when detuning is not very small, it is difficult to find the side branch of the result computed by continuation method because of the convergence problem. This is acceptable since in the test cases we are more concerned about the behaviour in the vicinity of 1:2 resonance, also, in the context of the system has large detuning, only the main branch of the backbone curve is investigated.

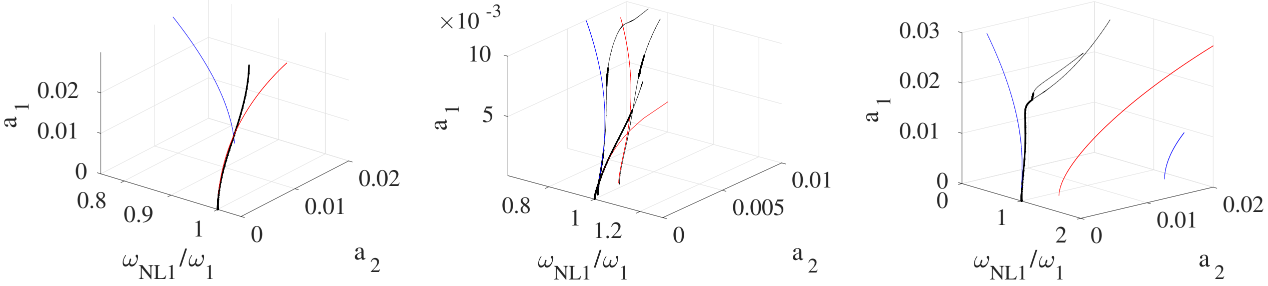

Figure 11.5.2: The backbone curves computed by using normal form reduction with 1:2 resonance of the curved beams. The left: case a, the middle: case b, the right: case c. The blue and the red curves are $p-$ and $p+$ modes respectively computed by multiple scale method, and the black curves are the solution obtained from continuation method.

11.6 Conclusion

In this section, the nonlinear dynamics and nonlinear coordinate transformation under the normal form framework of the system with 1:2 resonance and cubic nonlinearity are investigated. Then, the analytical results for the nonlinear oscillators with 1:2 resonance have been developed by applying the multiple scale method with both quadratic and cubic nonlinearities considered. At last, the first-order analytical results for the backbone curves and the change of nonlinearity at crossing 1:2 resonance of the system have been investigated.

Numerous numerical examples have been done with the different selection of parameters, mainly focusing on the detuning of the resonance eigenfrequencies of two modes, and the situation can thus be divided into two parts with regard to the detuning. Firstly, when the system has a large detuning, it is clearly found that the main branch of the backbone curve will tend to the result obtained by the single normal mode, and when detuning gets smaller and smaller, one can observe that the difference between the first-order results provided by NNM with 1:2 resonance and single NNM will become considerable. Secondly, in the vicinity of 1:2 resonance, for the backbone curve, it is found that the side branch is closed to the main one, also, the starting point of the side branch is investigated and determined analytically. This is meaningful since the starting point gets close to the main branch when ω_2 tends to equal to $2\omega_1$, and then the side branch becomes the main one after crossing the $\omega_2 = 2\omega_1$, consequently, the type of nonlinearity will switch from one to another leading to 1:2 divergence. The analytical solution has been validated by comparing the results provided by numerical continuation procedures (Manlab). In the end, a realistic case has been searched, the ROMs of curved beams on FE model with different detuning has been developed thanks to DNF, and one can observe a good agreement between the analytical solution given by multiple scale method and solution by applying continuous computation on the ROM developed by DNF.

The first contribution of this part is to give the nonlinear dynamics and nonlinear mapping under the normal form framework of the system with 1:2 resonance and cubic nonlinearity. In the past, the analysis shows that the system with such resonance condition can not be linearised, and the corresponding quadratic terms can not be cancelled because it is resonant through the eigenvalue relationship, and thus the two modal coordinates are strongly coupled. In this work, 1:2 resonance condition has been analysed with cubic nonlinearity also considered, and thus draw a clear map about how the quadratic resonant terms will affect the cancellation of cubic terms and nonlinear mapping of the normal form.

The second contribution of this part is to make a comparison between the backbone curves obtained by normal form dynamics with 1:2 resonance and by single dof NNM. From the view of the modal amplitude aspect, in the case of $\omega_2 \gg 2\omega_1$ or $\omega_2 \ll 2\omega_1$, when the first mode is strongly excited, the second mode (with higher eigenfrequencies) just respond a little thus will have a small amplitude, the solution with considering 1:2 resonance should return the same nonlinear features as compared with results obtained by single dof case. While in the context of $\omega_2 \approx 2\omega_1$, in the vicinity of the ω_1, the resonant modes are excited at the same time and thus to be remarkable, such that the backbone curves and the type of nonlinearity of the system will be so different from if only consider single dof NNM.

The third contribution of this part is to clearly explain the resource of 1:2 divergence on the prediction of the hardening/softening behaviour, with analytically investigate the main branch and side branch of the backbone curves. The starting point of the side branches are always getting close to the main one when detuning gets smaller, and they share the same starting point when $\omega_2 = 2\omega_1$. Thus, the change of nonlinearity at crossing 1:2 resonance can be considered as the switch of the main branch and the side branch of the backbone curves such that producing the divergence.

Part V

Conclusion and future work

Chapter 12

Conclusion and future work

In this thesis, reduced-order models as well as reduction methods are investigated for geometrically nonlinear dynamics of thin structures. This chapter discusses the main results of the thesis and emerging research topics for future work.

12.1 Conclusion

In part I, numerous reduction methods have been shortly reviewed. It is found that the non-intrusive methods with linear mapping are sometimes difficult to retrieve the nonlinear phenomena when building ROM, and the problem mainly comes from the implicit coupling relationship between the linear modes. As demonstrated in the circular plate example, the master modes can be coupled with modes in the very high frequency range. Hence, it is found that the methods with nonlinear mapping are more efficient because they introduce a connection between the linear coordinate and the nonlinear one, thus can be used to build ROMs with a small size of modal basis since the curved reduction subspace can retrieve the coupling relationship. The nonlinear reduction methods can be divided into two groups, the first contains these methods relies on invariant manifold theory, for example the normal form approach developed from the Poincaré and Poincaré-Dulac theorem. The second group include the methods that derive a nonlinear mapping without invariant property (the ICE method and the MDs).

In part II, Charter 5 shows a theoretical comparison between the ICE methods with stress manifold and invariant manifold approach, and thus to draw a conclusion that the stress manifold derived by the ICE method theoretically tend to the invariant manifold when a slow/fast assumption fulfilled. Then, the ICE method has been deeply investigated and assessed theoretically and numerically. The beam examples well demonstrate that the ICE method appears particularly appealing when reducing to a single mode since allowing easily a higher-order polynomial fitting, and also in such case the method can follow backbone curves up to larger amplitudes than methods limited to third-order expansions. However, the subsequent plate examples show drawbacks of using ICE method due to the fitting procedure. More specifically, the applied loading scales of the input are difficult to determine, and the result of ROM built by ICE method would to a large extent depend on the fitted curved manifold and thus to be not robustness, also, it is found that the computational burden of using the ICE methods will dramatic increase when the number of master modes is getting large. Chapter 6 of part II introduces the DNF approach, which can directly compute the invariant manifold on the FE model and accurately predict the nonlinear features due to the trajectories of ROM existing in the full system. Modal derivatives is shortly reintroduced after, and a theoretical comparison had been made between these two methods, with special emphasis that was put on the nonlinear dynamics and prediction of type of nonlinearity given by the ROMs. Two simple analytical examples are then used in order to analyse how the different treatments of quadratic nonlinearities by the three methods can affect the predictions. The examples prove again that the ICE and MDs work well only with a slow/fast assumption at hand, while the DNF method always produces the correct first-order assumption as long as the amplitudes are not too large.

In part III, applications of ROMs build by the nonlinear reduction methods (ICE, MDs, DNF) on continuous structures have been done in order to give a full illustrative view of the advantages and drawbacks of each reduction methods. Firstly, flat beam, arch and non-shallow arch are used to emphasize the ability of the methods to handle curvature, and it is found the error of the results obtained by using ICE method and the MDs will get larger with the increasing of the curvature of the beam, but DNF always works well. On the next example (a clamped-clamped beam with two polarizations), it is shown that all the three methods are able to retrieve the 1:1 internal resonance and pitchfork bifurcation. Finally, a cantilever beam with inertia nonlinearity is investigated, and the result shows the MDs gives the best prediction of the nonlinear response, the reason still not very clear and needs further investigation. From all the numerical test cases, one conclude that the DNF works well in the most of situation thanks to the derived invariant manifold, and the other two methods has a drawback that a slow/fast assumption is needed.

In part IV, normal form reduction has been investigated on the nonlinear dynamics of the system with 1:2 resonance and cubic nonlinearity. The second-order internal resonance has the effect on the quadratic nonlinearity, and now it is known that in the nonlinear dynamics, not only the resonant quadratic terms have to be kept, but two new correction cubic terms are introduced. Also, in the nonlinear mapping, the corresponding resonant cubic terms will be slightly modified due to the change of the cancellation procedure of quadratic terms. Apart from that, with the nonlinear dynamics obtained by previous contribution, the first-order results of the backbone curve and the changing of nonlinearity at crossing of 1:2 resonance have also been researched by using the multiple scale method, as the result, the first order multiple scale solution agrees well with the solution of the continuation method. The hardening/softening behaviour of the system with regards to the detuning of 1:2 resonance has also been investigated, as the conclusion, it is found that when the detuning is large, the results tends to the solution obtained by single normal mode, on the other hand, when the detuning is approaching 1:2 divergence, one can observe the side branch of the backbone curve is also getting close to the main one. This work is helpful for whom wants to build ROM of the system with 1:2 resonance by using normal form reduction.

In summary, a comprehensive view of the reduced-order models for geometrically nonlinear vibrations of thin structures has been given in the thesis, and the non-intrusive reduction methods with nonlinear mapping are mainly investigated. Theoretical comparison and numerical tests clearly show the advantages and disadvantages of the ICE method and MDs, and the new introduced DNF approach is found to be very efficient tool to build the accurate ROM on the FE package.

12.2 Future work

This section discusses open problems related to the methods for building ROM for the nonlinear dynamics of structures, in order to describe possible further developments and future work.

The first is to investigate using DNF to building ROM with multiple master modes. It is known that the direct normal form can build accurate ROMs with one or two master coordinates, and it is worth to use the method to tackle more complex dynamics involving a larger number of master modes. For that purpose, a big issue for using the normal form to generate the ROM is that one need discover potential internal resonance situation in the first stage. This can be complexed especially when large amplitudes and multi master modes are considered.

Secondly, although directly normal form approach on the FE model are based invariant manifold theory and thus perform well in the most of situation, but currently it is limited to its third-order asymptotic, so the results are expected to deteriorate at very large amplitudes, which was clearly observed in the cantilever beam example in Part III. To enlarge the application of the methodologies, the theoretical efforts should be devoted into the higher order computation.

Thirdly, in the thesis, the research was mainly focused on the geometrically nonlinear structures, so the nonlinearities were typical expressed as the polynomial terms. So further investigations are planned to deal with different physical problems, like the structures with different types of nonlinearities, for example material nonlinearity, physical configuration nonlinearities; and with different types of nonlinear forces, for instance, the piezoelectric couplings [102] often used in energy-harvesting problems, electrostatic forces in MEMs dynamics, thermal effects [103], nonlinear aeroelastic forces, centrifugal and Coriolis effects in rotating systems with applications to blades, fluid-structure interaction.

Appendix A

Analytical coefficients of asymptotic expansions for the static condensation

In this section we give the exact analytical expressions of the coefficients obtained in the asymptotic expansion for the static condensation of a two degrees of freedom system. The functional relationship between the slave coordinate X_2 and the master one X_1 write $X_2 = c(X_1)$, and c is expanded in polynomial form up to order 9 following Eq. (5.2.4). Identification of like powers term give the following values for the coefficients k_2 to k_9:

$$
\begin{aligned}
k_2 =& -(g_{11}^2/\omega_2^2), && \text{(A.0.1)}\\
k_3 =& (g_{11}^2 g_{12}^2 - h_{111}^2\omega_2^2)/\omega_2^4, && \text{(A.0.2)}\\
k_4 =& (-g_{11}^2(g_{12}^2)^2 - (g_{11}^2)^2 g_{22}^2 + g_{12}^2 h_{111}^2\omega_2^2 + g_{11}^2 h_{112}^2\omega_2^2)/\omega_2^6, && \text{(A.0.3)}\\
k_5 =& (g_{11}^2(g_{12}^2)^3 + 3(g_{11}^2)^2 g_{12}^2 g_{22}^2 - (g_{12}^2)^2 h_{111}^2\omega_2^2 - 2g_{11}^2 g_{22}^2 h_{111}^2\omega_2^2 - 2g_{11}^2 g_{12}^2 h_{112}^2\omega_2^2\\
& - (g_{11}^2)^2 h_{122}^2\omega_2^2 + h_{111}^2 h_{112}^2\omega_2^4)/\omega_2^8, && \text{(A.0.4)}\\
k_6 =& 1/\omega_2^{10}(-g_{11}^2(g_{12}^2)^4 - 6(g_{11}^2)^2(g_{12}^2)^2 g_{22}^2 - 2(g_{11}^2)^3(g_{22}^2)^2 + (g_{12}^2)^3 h_{111}^2\omega_2^2 + 6g_{11}^2(g_{12}^2)g_{22}^2 h_{111}^2\omega_2^2\\
& + 3g_{11}^2(g_{12}^2)^2 h_{112}^2\omega_2^2 + 3(g_{11}^2)^2 g_{22}^2 h_{112}^2\omega_2^2 + 3(g_{11}^2)^2(g_{12}^2)h_{122}^2\omega_2^2\\
& + (g_{11}^2)^3 h_{222}^2\omega_2^2 - g_{22}^2(h_{111}^2)^2\omega_2^4 - 2(g_{12}^2)h_{111}^2 h_{112}^2\omega_2^4 - g_{11}^2(h_{112}^2)^2\omega_2^4 - 2g_{11}^2 h_{111}^2 h_{122}^2\omega_2^4),\\
& && \text{(A.0.5)}\\
k_7 =& 1/\omega_2^{12}(g_{11}^2(g_{12}^2)^5 + 10(g_{11}^2)^2(g_{12}^2)^3 g_{22}^2 + 10(g_{11}^2)^3(g_{12}^2)(g_{22}^2)^2 - (g_{12}^2)^4 h_{111}^2\omega_2^2 -\\
& 12g_{11}^2(g_{12}^2)^2 g_{22}^2 h_{111}^2\omega_2^2 - 6(g_{11}^2)^2(g_{22}^2)^2 h_{111}^2\omega_2^2 - 4g_{11}^2(g_{12}^2)^3 h_{112}^2\omega_2^2 - 12(g_{11}^2)^2(g_{12}^2)g_{22}^2 h_{112}^2\omega_2^2 -\\
& 6(g_{11}^2)^2(g_{12}^2)^2 h_{122}^2\omega_2^2 - 4(g_{11}^2)^3 g_{22}^2 h_{122}^2\omega_2^2 - 4(g_{11}^2)^3(g_{12}^2)h_{222}^2\omega_2^2 + 3(g_{12}^2)g_{22}^2(h_{111}^2)^2\omega_2^4 +\\
& 3(g_{12}^2)^2 h_{111}^2 h_{112}^2\omega_2^4 + 6g_{11}^2 g_{22}^2 h_{111}^2 h_{112}^2\omega_2^4 + 3g_{11}^2(g_{12}^2)(h_{112}^2)^2\omega_2^4 + 6g_{11}^2(g_{12}^2)h_{111}^2 h_{122}^2\omega_2^4 +\\
& 3(g_{11}^2)^2 h_{112}^2 h_{122}^2\omega_2^4 + 3(g_{11}^2)^2 h_{111}^2 h_{222}^2\omega_2^4 - h_{111}^2(h_{112}^2)^2\omega_2^6 - (h_{111}^2)^2 h_{122}^2\omega_2^6), && \text{(A.0.6)}
\end{aligned}
$$

$$
\begin{aligned}
k_8 =&1/\omega_2^{14}(-g_{11}^2(g_{12}^2)^6-13(g_{11}^2)^2(g_{12}^2)^4g_{22}^2-24(g_{11}^2)^3(g_{12}^2)^2(g_{22}^2)^2-5(g_{11}^2)^4(g_{22}^2)^3+\\
&2(g_{11}^2)^2(g_{12}^2)^3g_{22}^2\omega_2^2+6(g_{11}^2)^3(g_{12}^2)(g_{22}^2)^2\omega_2^2+(g_{12}^2)^5h_{111}^2\omega_2^2+16g_{11}^2(g_{12}^2)^3g_{22}^2h_{111}^2\omega_2^2+\\
&20(g_{11}^2)^2(g_{12}^2)(g_{22}^2)^2h_{111}^2\omega_2^2+5g_{11}^2(g_{12}^2)^4h_{112}^2\omega_2^2+26(g_{11}^2)^2(g_{12}^2)^2g_{22}^2h_{112}^2\omega_2^2+10(g_{11}^2)^3(g_{22}^2)^2h_{112}^2\omega_2^2+\\
&10(g_{11}^2)^2(g_{12}^2)^3h_{122}^2\omega_2^2+18(g_{11}^2)^3(g_{12}^2)g_{22}^2h_{122}^2\omega_2^2+18g_{11}^2(g_{12}^2)g_{22}^2h_{111}^2h_{112}^2\omega_2^4-6g_{11}^2(g_{12}^2)^2(h_{112}^2)^2\omega_2^4-\\
&9(g_{11}^2)^3(g_{12}^2)^2h_{222}^2\omega_2^2+5(g_{11}^2)^4g_{22}^2h_{222}^2\omega_2^2-2g_{11}^2(g_{12}^2)^2g_{22}^2h_{111}^2\omega_2^4-4(g_{11}^2)^2(g_{22}^2)^2h_{111}^2\omega_2^4-\\
&4(g_{12}^2)^2g_{22}^2(h_{111}^2)^2\omega_2^4-2g_{11}^2(g_{22}^2)^2(h_{111}^2)^2\omega_2^4-4(g_{11}^2)^2(g_{12}^2)g_{22}^2h_{112}^2\omega_2^4-4(g_{12}^2)^3h_{111}^2h_{112}^2\omega_2^4-\\
&6(g_{11}^2)^2g_{22}^2(h_{112}^2)^2\omega_2^4-2(g_{11}^2)^3g_{22}^2h_{122}^2\omega_2^4-12g_{11}^2(g_{12}^2)^2h_{111}^2h_{122}^2\omega_2^4-10(g_{11}^2)^2g_{22}^2h_{111}^2h_{122}^2\omega_2^4-\\
&12(g_{11}^2)^2(g_{12}^2)h_{112}^2h_{122}^2\omega_2^4-2(g_{11}^2)^3(h_{122}^2)^2\omega_2^4-10(g_{11}^2)^2(g_{12}^2)h_{111}^2h_{222}^2\omega_2^4-4(g_{11}^2)^3h_{112}^2h_{222}^2\omega_2^4+\\
&2g_{11}^2g_{22}^2h_{111}^2h_{112}^2\omega_2^6+g_{22}^2(h_{111}^2)^2h_{112}^2\omega_2^6+3(g_{12}^2)h_{111}^2(h_{112}^2)^2\omega_2^6+g_{11}^2(h_{112}^2)^3\omega_2^6+\\
&3(g_{12}^2)(h_{111}^2)^2h_{122}^2\omega_2^6+6g_{11}^2h_{111}^2h_{112}^2h_{122}^2\omega_2^6+2g_{11}^2(h_{111}^2)^2h_{222}^2\omega_2^6),
\end{aligned}
\tag{A.0.7}
$$

$$
\begin{aligned}
k_9 =&1/\omega_2^{16}(g_{11}^2(g_{12}^2)^7+19(g_{11}^2)^2(g_{12}^2)^5g_{22}^2+64(g_{11}^2)^3(g_{12}^2)^3(g_{22}^2)^2+35(g_{11}^2)^4(g_{12}^2)(g_{22}^2)^3-\\
&2(g_{11}^2)^2(g_{12}^2)^4g_{22}^2\omega_2^2-6(g_{11}^2)^3(g_{12}^2)^2(g_{22}^2)^2\omega_2^2-(g_{12}^2)^6h_{111}^2\omega_2^2-26g_{11}^2(g_{12}^2)^4g_{22}^2h_{111}^2\omega_2^2-\\
&80(g_{11}^2)^2(g_{12}^2)^2(g_{22}^2)^2h_{111}^2\omega_2^2-20(g_{11}^2)^3(g_{22}^2)^3h_{111}^2\omega_2^2-6g_{11}^2(g_{12}^2)^5h_{112}^2\omega_2^2-\\
&56(g_{11}^2)^2(g_{12}^2)^3g_{22}^2h_{112}^2\omega_2^2-60(g_{11}^2)^3(g_{12}^2)(g_{22}^2)^2h_{112}^2\omega_2^2-15(g_{11}^2)^2(g_{12}^2)^4h_{122}^2\omega_2^2-\\
&58(g_{11}^2)^3(g_{12}^2)^2g_{22}^2h_{122}^2\omega_2^2-15(g_{11}^2)^4(g_{22}^2)^2h_{122}^2\omega_2^2-8(g_{12}^2)^3g_{22}^2(h_{111}^2)^2\omega_2^4+\\
&26g_{11}^2(g_{12}^2)(g_{22}^2)^2(h_{111}^2)^2\omega_2^4+19(g_{11}^2)^3(g_{12}^2)^3h_{222}^2\omega_2^2-30(g_{11}^2)^4(g_{12}^2)g_{22}^2h_{222}^2\omega_2^2+\\
&2g_{11}^2(g_{12}^2)^3g_{22}^2h_{111}^2\omega_2^4+4(g_{11}^2)^2(g_{12}^2)(g_{22}^2)^2h_{111}^2\omega_2^4+\\
&4(g_{11}^2)^2(g_{12}^2)^2g_{22}^2h_{112}^2\omega_2^4+5(g_{12}^2)^4h_{111}^2h_{112}^2\omega_2^4+54g_{11}^2(g_{12}^2)^2g_{22}^2h_{111}^2h_{112}^2\omega_2^4+\\
&30(g_{11}^2)^2(g_{22}^2)^2h_{111}^2h_{112}^2\omega_2^4+10g_{11}^2(g_{12}^2)^3(h_{112}^2)^2\omega_2^4+30(g_{11}^2)^2(g_{12}^2)g_{22}^2(h_{112}^2)^2\omega_2^4+\\
&2(g_{11}^2)^3(g_{12}^2)g_{22}^2h_{122}^2\omega_2^4+20g_{11}^2(g_{12}^2)^3h_{111}^2h_{122}^2\omega_2^4+58(g_{11}^2)^2(g_{12}^2)g_{22}^2h_{111}^2h_{122}^2\omega_2^4+\\
&30(g_{11}^2)^2(g_{12}^2)^2h_{112}^2h_{122}^2\omega_2^4+20(g_{11}^2)^3g_{22}^2h_{112}^2h_{122}^2\omega_2^4+\\
&10(g_{11}^2)^3(g_{12}^2)(h_{122}^2)^2\omega_2^4+28(g_{11}^2)^2(g_{12}^2)^2h_{111}^2h_{222}^2\omega_2^4+20(g_{11}^2)^3g_{22}^2h_{111}^2h_{222}^2\omega_2^4+\\
&20(g_{11}^2)^3(g_{12}^2)h_{112}^2h_{222}^2\omega_2^4+5(g_{11}^2)^4h_{122}^2h_{222}^2\omega_2^4-2(g_{22}^2)^2(h_{111}^2)^3\omega_2^6-2g_{11}^2(g_{12}^2)g_{22}^2h_{111}^2h_{112}^2\omega_2^6-\\
&10(g_{12}^2)g_{22}^2(h_{111}^2)^2h_{112}^2\omega_2^6-6(g_{12}^2)^2h_{111}^2(h_{112}^2)^2\omega_2^6-12g_{11}^2g_{22}^2h_{111}^2(h_{112}^2)^2\omega_2^6-4g_{11}^2(g_{12}^2)(h_{112}^2)^3\omega_2^6-\\
&6(g_{12}^2)^2(h_{111}^2)^2h_{122}^2\omega_2^6-12g_{11}^2g_{22}^2(h_{111}^2)^2h_{122}^2\omega_2^6-24g_{11}^2(g_{12}^2)h_{111}^2h_{112}^2h_{122}^2\omega_2^6-\\
&6(g_{11}^2)^2(h_{112}^2)^2h_{122}^2\omega_2^6-6(g_{11}^2)^2h_{111}^2(h_{122}^2)^2\omega_2^6-11g_{11}^2(g_{12}^2)(h_{111}^2)^2h_{222}^2\omega_2^6-\\
&12(g_{11}^2)^2h_{111}^2h_{112}^2h_{222}^2\omega_2^6+h_{111}^2(h_{112}^2)^3\omega_2^8+3(h_{111}^2)^2h_{112}^2h_{122}^2\omega_2^8+(h_{111}^2)^3h_{222}^2\omega_2^8).
\end{aligned}
\tag{A.0.8}
$$

Appendix B

Derivation of normal form on the N dofs system with 1:2 resonance and cubic nonlinearity

In this appendix, the contribution shown in the Chapter 10 is extended to the N dofs nonlinear systems, and the nonlinearly coupled oscillators in the vicinity of 1:2 internal resonance ($\omega_n \approx 2\omega_m$) are considered, as the conclusion, the transformation of coordinates and reduced nonlinear dynamics are given. The equations of motion of the system with quadratic and cubic nonlinearity read as:

$$\begin{aligned} \dot{X}_p &= Y_p, \\ \dot{Y}_p &= -\omega_p^2 X_p - \sum_{i=1}^{N}\sum_{j\geq i}^{N} g_{ij}^p X_i^p X_j^p - \sum_{i=1}^{N}\sum_{j\geq i}^{N}\sum_{k\geq j}^{N} h_{ijk}^p X_i^p X_j^p X_k^p. \end{aligned} \tag{B.0.1}$$

After following the same manner processing shown in Chapter 10, a nonlinear transform can be found in order to cancel the maximum number of quadratic and cubic coupling terms present in the original system. The nonlinear transformation up to order three reads:

$$\begin{aligned} X_p &= R_p + \sum_{i=1}^{N}\sum_{j\geq i}^{N} a_{ij}^p R_i R_j + \sum_{i=1}^{N}\sum_{j\geq i}^{N} b_{ij}^p S_i S_j + \sum_{i=1}^{N}\sum_{j\geq i}^{N}\sum_{k\geq j}^{N} r_{ijk}^p R_i R_j R_k + \sum_{i=1}^{N}\sum_{j=1}^{N}\sum_{k\geq j}^{N} u_{ijk}^p R_i S_j S_k, \\ Y_p &= S_p + \sum_{i=1}^{N}\sum_{j=1}^{N} \gamma_{ij}^p R_i S_j + \sum_{i=1}^{N}\sum_{j\geq i}^{N}\sum_{k\geq j}^{N} \mu_{ijk}^p S_i S_j S_k + \sum_{i=1}^{N}\sum_{j=1}^{N}\sum_{k\geq j}^{N} \nu_{ijk}^p S_i R_j R_k, \end{aligned} \tag{B.0.2}$$

where the quadratic coefficients of $a_{ij}^p, b_{ij}^p, \gamma_{ij}^p$ are given by:

$$\begin{aligned}
&\forall i = 1, ..., N, \forall j \geq i, ..., N : \\
&\qquad a_{ij}^p = \frac{\omega_i^2 + \omega_j^2 - \omega_p^2}{D_{ijp}} g_{ij}^p (1 - \delta_{mp}\delta_{mi}\delta_{nj})(1 - \delta_{np}\delta_{mi}\delta_{mj}) \\
&\qquad b_{ij}^p = \frac{2}{D_{ijp}} g_{ij}^p (1 - \delta_{mp}\delta_{mi}\delta_{nj})(1 - \delta_{np}\delta_{mi}\delta_{mj}) \\
&\qquad \gamma_{ii}^p = \frac{2}{4\omega_i^2 - \omega_p^2} g_{ii}^p (1 - \delta_{np}\delta_{mi}) \\
&\forall i = 1, ..., N, \forall j > i, ..., N : \\
&\qquad \gamma_{ij}^p = \frac{\omega_j^2 - \omega_i^2 - \omega_p^2}{D_{ijp}} g_{ij}^p (1 - \delta_{mp}\delta_{mi}\delta_{nj}) \\
&\qquad \gamma_{ji}^p = \frac{\omega_i^2 - \omega_j^2 - \omega_p^2}{D_{ijp}} g_{ij}^p (1 - \delta_{mp}\delta_{mi}\delta_{nj})
\end{aligned} \tag{B.0.3}$$

with δ_{ij} Dirac delta function and $D_{ijp} = (\omega_i + \omega_j - \omega_p)(\omega_i + \omega_j + \omega_p)(\omega_i - \omega_j + \omega_p)(\omega_i - \omega_j - \omega_p)$. For the cubic coefficients $r_{ijk}^p, u_{ijk}^p, \mu_{ijk}^p, \nu_{ijk}^p$, with $i, j, k, p = 1, ..., N$, their expressions are also not directly given here because they are too complexed, fortunately, as compared with expressions of the coefficients given in [51] with the assumption of no resonance between eigenvalues, the only difference is that for m and nth resonant modes, the external new cubic terms should be considered during the computation. For example, if one want to obtain terms $r_{mmn}^n, u_{mmn}^n, u_{nmm}^n, \mu_{mmn}^n, \nu_{mmn}^n, \nu_{nmm}^n$, one need to replace $(A_{mmn}^n + A_{nmm}^n + h_{mmn}^n)$ in the equations given in [51] to be $(A_{mmn}^n + A_{nmm}^n + h_{mmn}^n - D_{mmn}^n)$ and B_{mmn}^n to be $(B_{mmn}^n - E_{mmn}^n)$.

The new external terms D, E only with regard to the resonance modes are given by:

$$\begin{aligned}
D^m_{mmn} &= \gamma^m_{mm} g^m_{mn} + \gamma^n_{nn} g^n_{mm} - 2b^m_{mm} g^m_{mn} \omega_m^2 - 2b^m_{nn} g^n_{mm} \omega_n^2 \\
D^n_{mmm} &= \gamma^n_{mn} g^n_{mm} - b^n_{mn} g^n_{mm} \omega_m^2 \\
D^n_{mmn} &= \gamma^n_{nn} g^n_{mm} - 2b^n_{nn} g^n_{mm} \omega_n^2 \\
D^n_{mnn} &= \gamma^n_{nm} g^m_{mn} - b^n_{mn} g^m_{mn} \omega_n^2 \\
E^m_{mmn} &= 2b^m_{mm} g^m_{mn} + 4b^m_{nn} g^n_{mm} \\
E^m_{nmm} &= 2b^m_{mm} g^m_{mn} \\
E^n_{mmm} &= 2b^n_{mn} g^n_{mm} \\
E^n_{mnn} &= b^n_{mn} g^m_{mn} \\
E^n_{mmn} &= 4b^n_{nn} g^n_{mm} \\
E^n_{nmn} &= b^n_{mn} g^m_{mn}.
\end{aligned} \tag{B.0.4}$$

After the coordinate transformation, the nonlinear dynamics, up to third order, of the system with the new coordinates (R_p, S_p) should be written as:

$$\begin{aligned}
\dot{R}_p =& S_p, \\
\dot{S}_p =& -\omega_p^2 R_p - g^m_{mn} R_m R_n \delta_{mp} - (h^p_{ppp} + A^p_{ppp}) R_p^3 - B^p_{ppp} R_p S_p^2 \\
& - R_p \left[\sum_{j>p}^{N} [(A^p_{jpj} + A^p_{pjj} + h^p_{pjj}) R_j^2 + B^p_{pjj} S_j^2] + \sum_{i<p} [(A^p_{iip} + A^p_{pii} + h^p_{iip}) R_i^2 + B^p_{pii} S_i^2] \right] \\
& - S_p \left[\sum_{j>p}^{N} B^p_{jpj} R_j S_j + \sum_{i<p} B^p_{iip} R_i S_i \right] + (D^n_{mmn} R_m^2 R_n + E^n_{mmn} R_m S_m S_n - g^n_{mm} R_m^2) \delta_{np}
\end{aligned} \tag{B.0.5}$$

where the terms $A^p_{ijk}, B^p_{ijk}, (i, j, k, p = 1, ..., N)$ are expressed as:

$$\begin{aligned}
A^p_{ijk} &= \sum_{l \geq i}^{N} g^p_{il} a^l_{jk} + \sum_{l \leq i} g^p_{li} a^l_{jk}, \\
B^p_{ijk} &= \sum_{l \geq i}^{N} g^p_{il} b^l_{jk} + \sum_{l \leq i} g^p_{li} b^l_{jk}.
\end{aligned} \tag{B.0.6}$$

Bibliography

[1] M. Schulze, S. Dietz, B. Burgermeister, A. Tuganov, H. Lang, J. Linn, and M. Arnold. Integration of nonlinear models of flexible body deformation in multibody system dynamics. *Journal of Computational and Nonlinear Dynamics*, 9(1):011012, 2014.

[2] G. Kerschen, M. Peeters, J.C. Golinval, and C. Stéphan. Nonlinear modal analysis of a full-scale aircraft. *Journal of Aircraft*, 50(5):1409–1419, 2013.

[3] O. Gözcü and S. Dou. Reduced order models for wind turbine blades with large deflections. *Journal of Physics: Conference Series*, 1618:052046, 2020.

[4] A. Frangi and G. Gobat. Reduced order modelling of the non-linear stiffness in mems resonators. *International Journal of Non-Linear Mechanics*, 116:211 – 218, 2019.

[5] M.I Younis. *MEMS linear and nonlinear statics and dynamics*. Springer, New-York, 2011.

[6] R. W. Gordon and J. J. Hollkamp. Reduced-order models for acoustic response prediction. Technical Report AFRL-RB-WP-TR-2011-3040, Analytical Structural Mechanics Branch Structures Division, 2011.

[7] S. A. Rizzi and A. Przekop. The effect of basis selection on static and random acoustic response prediction using a nonlinear modal simulation. Technical Report TP-2005-213943, NASA Langley Research Center, 2005.

[8] P. Krysl, S. Lall, and J.E. Marsden. Dimensional model reduction in non-linear finite element dynamics of solids and structures. *International Journal for numerical methods in engineering*, 51:479–504, 2001.

[9] M. Amabili, A. Sarkar, and M. P. Païdoussis. Reduced-order models for nonlinear vibrations of cylindrical shells via the proper orthogonal decomposition method. *Journal of Fluids and Structures*, 18(2):227–250, 2003.

[10] G. Kerschen, J.C. Golinval, A.F. Vakakis, and L.A. Bergman. The method of proper orthogonal decomposition for dynamical characterization and order reduction of mechanical systems: an overview. *Nonlinear Dynamics*, 41:147–169, 2005.

[11] A. Vizzaccaro, A. Givois, P. Longobardi, Y. Shen, J.-F. Deü, L. Salles, C. Touzé, and O. Thomas. Non-intrusive reduced order modelling for the dynamics of geometrically nonlinear flat structures using three-dimensional finite elements. *Computational Mechanics*, 66:1293–1319, 2020.

[12] A. Givois, A. Grolet, O. Thomas, and J.-F. Deü. On the frequency response computation of geometrically nonlinear flat structures using reduced-order finite element models. *Nonlinear Dynamics*, 97(2):1747–1781, 2019.

[13] A.A. Muravyov and S.A. Rizzi. Determination of nonlinear stiffness with application to random vibration of geometrically nonlinear structures. *Computers and Structures*, 81:1513–1523, 2003.

[14] A. H. Nayfeh and D. T. Mook. *Nonlinear oscillations*. John Wiley & sons, New-York, 1979.

[15] L Meirovitch. *Fundamentals of vibration*. McGraw Hill, Singapore, 2001.

[16] M. Mc Ewan, J. Wright, J. Cooper, and A. Leung. A finite element/modal technique for nonlinear plate and stiffened panel response prediction. In *19th AIAA Applied Aerodynamics Conference*, 2001.

[17] M. I. Mc Ewan. *A combined modal/finite element technique for the non-linear dynamic simulation of aerospace structures*. PhD thesis, University of Manchester, 2001.

[18] J. J. Hollkamp, R. W. Gordon, and S. M. Spottswood. Non-linear modal models for sonic fatigue response prediction: a comparison of methods. *Journal of Sound and Vibration*, 284:1145–1163, 2005.

[19] J. J. Hollkamp and R. W. Gordon. Reduced-order models for non-linear response prediction: Implicit condensation and expansion. *Journal of Sound and Vibration*, 318:1139–1153, 2008.

[20] S. Jain, P. Tiso, J.B. Rutzmoser, and D.J Rixen. A quadratic manifold for model order reduction of nonlinear structural dynamics. *Computers & Structures*, 188:80 – 94, 2017.

[21] J. B. Rutzmoser, D. J. Rixen, P. Tiso, and S. Jain. Generalization of quadratic manifolds for reduced order modeling of nonlinear structural dynamics. *Computers & Structures*, 192:196 – 209, 2017.

[22] R. M. Rosenberg. The normal modes of nonlinear n-degree-of-freedom systems. *Journal of Applied Mechanics*, 29:7–14, 1962.

[23] R. M. Rosenberg. On non-linear vibrations of systems with many degrees of freedom. *Advances in Applied Mechanics*, 9:155–242, 1966.

[24] G. Kerschen, M. Peeters, J.C. Golinval, and A.F. Vakakis. Non-linear normal modes, part I: a useful framework for the structural dynamicist. *Mechanical Systems and Signal Processing*, 23(1):170–194, 2009.

[25] S. W. Shaw and C. Pierre. Normal modes for non-linear vibratory systems. *Journal of Sound and Vibration*, 164(1):85–124, 1993.

[26] R.D. Borst and C.V. Verhoosel M.A. Crisfield, J.J.C Remmers. *Non-linear finite element analysis of solid and structures*. WILEY, United Kingdom, 2012.

[27] S. W. Shaw and C. Pierre. Non-linear normal modes and invariant manifolds. *Journal of Sound and Vibration*, 150(1):170–173, 1991.

[28] E. Pesheck, C. Pierre, and S. Shaw. A new Galerkin-based approach for accurate non-linear normal modes through invariant manifolds. *Journal of Sound and Vibration*, 249(5):971–993, 2002.

[29] L. E. Malvern. *Introduction to the mechanics of a continuous medium*. Pearson, New-York, 1977.

[30] Y. C. Fung and P. Tong. *Classical and Computational Solid Mechanics*. World Scientific, River Edge, New Jersey, 2001.

[31] M. P. Mignolet, A. Przekop, S. A. Rizzi, and S. M. Spottswood. A review of indirect/non-intrusive reduced order modeling of nonlinear geometric structures. *Journal of Sound and Vibration*, 332:2437–2460, 2013.

[32] C. Touzé, M. Vidrascu, and D. Chapelle. Direct finite element computation of non-linear modal coupling coefficients for reduced-order shell models. *Computational Mechanics*, 54(2):567–580, 2014.

[33] A. Lazarus, O. Thomas, and J.-F. Deü. Finite element reduced order models for nonlinear vibrations of piezoelectric layered beams with applications to nems. *Finite Elements in Analysis and Design*, 49(1):35 – 51, 2012.

[34] F. Chinesta, P. Ladevèze, and E. Cueto. A short review on model order reduction based on proper generalized decomposition. *Archives of Computational Methods in Engineering*, 18(4):395, 2011.

[35] L. Meyrand, E. Sarrouy, B. Cochelin, and G. Ricciardi. Nonlinear normal mode continuation through a proper generalized decomposition approach with modal enrichment. *Journal of Sound and Vibration*, 443:444 – 459, 2019.

[36] R. Perez, X. Q. Wang, and M. P. Mignolet. Nonintrusive Structural Dynamic Reduced Order Modeling for Large Deformations: Enhancements for Complex Structures. *Journal of Computational and Nonlinear Dynamics*, 9(3), 2014.

[37] Électricité de France. *code_aster*, accessed February 10, 2020. https://www.code-aster.org/.

[38] E. Kim and M. Cho. Equivalent model construction for a non-linear dynamic system based on an element-wise stiffness evaluation procedure and reduced analysis of the equivalent system. *Computational Mechanics*, 60:709–724, 2017.

[39] M. Amabili and C. Touzé. Reduced-order models for non-linear vibrations of fluid-filled circular cylindrical shells: comparison of pod and asymptotic non-linear normal modes methods. *Journal of Fluids and Structures*, 23(6):885–903, 2007.

[40] K. Kim, V. Khanna, X. Q. Wang, and M. P. Mignolet. Nonlinear reduced order modeling of flat cantilever structures. In *proc. of 50th AIAA/ASME/ASCE/AHS/ASC Structures, Structural Dynamics, and Materials Conference*, Palm Springs, California, May 2009.

[41] C. Touzé and O. Thomas. Non-linear behaviour of free-edge shallow spherical shells: effect of the geometry. *International Journal of Non-linear Mechanics*, 41(5):678–692, 2006.

[42] A. Vakakis. Non-linear normal modes (nnms) and their applications in vibration theory: an overview. *Mechanical Systems and Signal Processing*, 11(1):3–22, 1997.

[43] S. Ponsioen, T. Pedergnana, and G. Haller. Automated computation of autonomous spectral submanifolds for nonlinear modal analysis. *Journal of Sound and Vibration*, 420:269 – 295, 2018.

[44] G. Haller and S. Ponsioen. Nonlinear normal modes and spectral submanifolds: existence, uniqueness and use in model reduction. *Nonlinear Dynamics*, 86(3):1493–1534, 2016.

[45] T. Breunung and G. Haller. Explicit backbone curves from spectral submanifolds of forced-damped nonlinear mechanical systems. *Proceedings of the Royal Society A: Mathematical, Physical and Engineering Sciences*, 474(2213):20180083, 2018.

[46] A. Haro, M. Canadell, J.L. Figueras, A. Luque, and J.M. Mondelo. *The Parameterization Method for Invariant Manifolds.From rigorous results to effective computations.* Springer, Switzerland, 2016.

[47] S. W. Shaw and C. Pierre. Normal modes of vibration for non-linear continuous systems. *Journal of Sound and Vibration*, 169(3):85–124, 1994.

[48] N. Boivin, C. Pierre, and S. Shaw. Non-linear normal modes, invariance, and modal dynamics approximations of non-linear systems. *Nonlinear Dynamics*, 8:315–346, 1995.

[49] A. Kelley. The stable, center-stable, center, center-unstable and unstable manifolds. *Journal of Differential Equations*, 3:546–570, 1967.

[50] J. Guckenheimer and P. Holmes. *Nonlinear oscillations, dynamical systems and bifurcations of vector fields*. Springer-Verlag, New-York, 1983.

[51] C. Touzé, O. Thomas, and A. Chaigne. Hardening/softening behaviour in non-linear oscillations of structural systems using non-linear normal modes. *Journal of Sound and Vibration*, 273(1-2):77–101, 2004.

[52] C. Touzé and M. Amabili. Non-linear normal modes for damped geometrically nonlinear systems: application to reduced-order modeling of harmonically forced structures. *Journal of Sound and Vibration*, 298(4-5):958–981, 2006.

[53] H. Poincaré. *Les méthodes nouvelles de la mécanique céleste*. Gauthiers-Villars, Paris, 1892.

[54] H. Dulac. Solutions d'un système d'équations différentielles dans le voisinage de valeurs singulières. *Bulletin de la Société Mathématique de France*, 40:324–383, 1912.

[55] C. Touzé. Normal form theory and nonlinear normal modes: theoretical settings and applications. In G. Kerschen, editor, *Modal Analysis of nonlinear Mechanical Systems*, pages 75–160, New York, NY, 2014. Springer Series CISM courses and lectures, vol. 555.

[56] C. Touzé, O. Thomas, and A. Huberdeau. Asymptotic non-linear normal modes for large amplitude vibrations of continuous structures. *Computers and Structures*, 82(31-32):2671–2682, 2004.

[57] R. J. Kuether, B. J. Deaner, J. J. Hollkamp, and M. S. Allen. Evaluation of geometrically nonlinear reduced-order models with nonlinear normal modes. *AIAA Journal*, 53(11):3273–3285, 2015.

[58] Y. Shen, N. Béreux, A. Frangi, and C. Touzé. Reduced order models for geometrically nonlinear structures: assessment of implicit condensation in comparison with invariant manifold approach. *European Journal of Mechanics A/Solids*, 86:104165, 2021.

[59] S.R. Idelsohn and A. Cardona. A reduction method for nonlinear structural dynamic analysis. *Computer Methods in Applied Mechanics and Engineering*, 49(3):253 – 279, 1985.

[60] O. Weeger, U. Wever, and B. Simeon. On the use of modal derivatives for nonlinear model order reduction. *International Journal for Numerical Methods in Engineering*, 108(3):1579–1602, 2016.

[61] A. Vizzaccaro, L. Salles, and C. Touzé. Comparison of nonlinear mappings for reduced-order modelling of vibrating structures: normal form theory and quadratic manifold method with modal derivatives. *Nonlinear Dynamics*, 103:3335–3370, 2021.

[62] D. Jiang, C. Pierre, and S. Shaw. The construction of non-linear normal modes for systems with internal resonance. *International Journal of Non-linear Mechanics*, 40(5):729–746, 2005.

[63] F. Blanc, C. Touzé, J.-F. Mercier, K. Ege, and A.-S. Bonnet Ben-Dhia. On the numerical computation of nonlinear normal modes for reduced-order modelling of conservative vibratory systems. *Mechanical Systems and Signal Processing*, 36(2):520 – 539, 2013.

[64] L. Renson, G. Kerschen, and B. Cochelin. Numerical computation of nonlinear normal modes in mechanical engineering. *Journal of Sound and Vibration*, 364:177 – 206, 2016.

[65] E. Pesheck, N. Boivin, C. Pierre, and S. W. Shaw. Nonlinear modal analysis of structural systems using multi-mode invariant manifolds. *Nonlinear Dynamics*, 25(1):183–205, 2001.

[66] X. Liu and D. J. Wagg. Simultaneous normal form transformation and model-order reduction for systems of coupled nonlinear oscillators. *Proceedings of the Royal Society A: Mathematical, Physical and Engineering Sciences*, 475(2228):20190042, 2019.

[67] L. Guillot, B. Cochelin and C. Vergez. *Manlab*, accessed 30th of August 2019. http://manlab.lma.cnrs-mrs.fr/.

[68] B. Cochelin and C. Vergez. A high order purely frequency-based harmonic balance formulation for continuation of periodic solutions. *Journal of Sound and Vibration*, 324(1):243 – 262, 2009.

[69] A. Lazarus and O. Thomas. A harmonic-based method for computing the stability of periodic solutions of dynamical systems. *Comptes Rendus Mécanique*, 338(9):510 – 517, 2010.

[70] L. Guillot, B. Cochelin, and C. Vergez. A generic and efficient taylor series–based continuation method using a quadratic recast of smooth nonlinear systems. *International Journal for Numerical Methods in Engineering*, 119(4):261–280, 2019.

[71] C. S. M. Sombroek, P. Tiso, L. Renson, and G. Kerschen. Numerical computation of nonlinear normal modes in a modal derivative subspace. *Computers & Structures*, 195:34 – 46, 2018.

[72] G. Iooss and M. Adelmeyer. *Topics in bifurcation theory*. World scientific, New-York, 1998. second edition.

[73] A. de Cheveigné and H. Kawahara. Yin, a fundamental frequency estimator for speech and music. *The Journal of the Acoustical Society of America*, 111(4):1917–1930, 2002.

[74] Z. Veraszto, S. Ponsioen, and G. Haller. Explicit third-order model reduction formulas for general nonlinear mechanical systems. *Journal of Sound and Vibration*, 468:115039, 2020.

[75] A. Vizzaccaro, Y. Shen, L. Salles, and C. Touzé. Model order reduction methods based on normal form for geometrically nonlinear structures: a direct approach. In *proc. of Euromech Non-linear Dynamics Conference, ENOC 2020*, Lyon, July 2020.

[76] A. Vizzaccaro, Y. Shen, L. Salles, J. Blahos, and C. Touzé. Direct computation of nonlinear mapping via normal form for reduced-order models of finite element nonlinear structures. *Computer Methods in Applied Mechanics and Engineering*, 384:113957, 2021.

[77] P. Apiwattanalunggarn, C. Pierre, and D. Jiang. Finite-element-based nonlinear modal reduction of a rotating beam with large-amplitude motion. *Journal of Vibration and Control*, 9:235–263, 2003.

[78] Y. Shen, A. Vizzaccaro, N. Kesmia, T. Yu, L. Salles, O. Thomas, and C. Touzé. Comparison of reduction methods for finite element geometrically nonlinear beam structures. *Vibration*, 4:175–204, 2021.

[79] Y. Shen, N. Kesmia, C. Touzé, A. Vizzaccaro, L. Salles, and O. Thomas. Predicting the type of nonlinearity of shallow spherical shells: comparison of direct normal form with

modal derivatives. In *Proceedings of NODYCON 2021, Second International Nonlinear Dynamics Conference*, Roma, February 2021.

[80] S. W. Shaw. An invariant manifold approach to nonlinear normal modes of oscillation. *Journal of Nonlinear Science*, 4:419–448, 1994.

[81] A. H. Nayfeh and W. Lacarbonara. On the discretization of distributed-parameter systems with quadratic and cubic non-linearities. *Nonlinear Dynamics*, 13:203–220, 1997.

[82] O. Thomas, C. Touzé, and A. Chaigne. Non-linear vibrations of free-edge thin spherical shells: modal interaction rules and 1:1:2 internal resonance. *International Journal of Solids and Structures*, 42(11-12):3339–3373, 2005.

[83] M. W. Johnson and E. Reissner. On transverse vibrations of shallow spherical shells. *Quarterly Applied Mathematics*, 15(4):367–380, 1956.

[84] A. Kalnins. Effect of bending on vibrations of spherical shells. *Journal of the Acoustical Society of America*, 36(1):74–81, 1964.

[85] H-N Chu and G. Herrmann. Influence of large amplitudes on free flexural vibrations of rectangular elastic plates. *Journal of Applied Mechanics*, 23:532–540, 1956.

[86] N. Kesmia. Modèles d'ordre réduit pour les vibrations non-linéaires géométriques. *Rapport de stage, Master 2 MS2SC*, 2021.

[87] J. Blahoš, A. Vizzaccaro, F. El Haddad, and L. Salles. Parallel harmonic balance method for analysis of nonlinear dynamical systems. In *proc. of Turbo Expo, ASME 2020*, volume GT2020-15392, 06 2020.

[88] A. I. Manevitch and L. I. Manevitch. Free oscillations in conservative and dissipative symmetric cubic two-degree-of-freedom systems with closed natural frequencies. *Meccanica*, 38(3):335–348, 2003.

[89] A. Givois, J.J. Tan, C. Touzé, and O. Thomas. Backbone curves of coupled cubic oscillators in one-to-one internal resonance: bifurcation scenario, measurements and parameter identification. *Meccanica*, 55:481–503, 2020.

[90] O. Thomas, A. Sénéchal, and J. F. Deü. Hardening/softening behaviour and reduced order modelling of nonlinear vibrations of rotating cantilever beams. *Nonlinear Dynamics*, 86(2):1293–1318, 2016.

[91] M. R. M. Crespo da Silva and C. C. Glynn. Nonlinear flexural-flexural-torsional dynamics of inextensional beams. part 1: Equations of motion. *J. Struct. Mech.*, 6(4):437–448, 1978.

[92] P. F. Pai and A. H. Nayfeh. Non-linear non-planar oscillations of a cantilever beam under lateral base excitations. *International Journal of Non-Linear Mechanics*, 25(5):455–474, 1990.

[93] C. Touzé and O. Thomas. Reduced-order modeling for a cantilever beam subjected to harmonic forcing. In *proc. of EUROMECH Colloquium 457: nonlinear modes of vibrating systems*, pages 165–168, Fréjus, France, june 2004.

[94] V. Denis, M. Jossic, C. Giraud-Audine, B. Chomette, A. Renault, and O. Thomas. Identification of nonlinear modes using phase-locked-loop experimental continuation and normal form. *Mechanical Systems and Signal Processing*, 106:430–452, 2018.

[95] E. Nicolaidou, T. L. Hill, and S. A. Neild. Indirect reduced-order modelling: Using nonlinear manifolds to conserve kinetic energy. *Proceedings of the Royal Society A: Mathematical, Physical and Engineering Sciences*, 2243(476), 2020.

[96] G. Haller and S. Ponsioen. Exact model reduction by a slow–fast decomposition of nonlinear mechanical systems. *Nonlinear Dynamics*, 90:617–647, 2017.

[97] J.J. Thomsen. *Vibrations and Stability: Advanced Theory, Analysis, and Tools*. Springer-Verlag, New York, 2003. second edition.

[98] W. Lacarbonara, G. Rega, and A. H. Nayfeh. Resonant nonlinear normal modes. part I: analytical treatment for structural one-dimensional systems. *International Journal of Non-linear Mechanics*, 38(6):851–872, 2003.

[99] A. H. Nayfeh, C. Chin, and S. A. Nayfeh. On nonlinear normal modes of systems with internal resonance. *Trans. ASME/Journal of Vibration and Acoustics*, 118:340–345, 1996.

[100] A. H. Nayfeh. Reduced-order models of weakly non-linear spatially continuous systems. *Nonlinear Dynamics*, 16:105–125, 1998.

[101] G. Gobat, L. Guillot, A. Frangi, B. Cochelin, and C. Touzé. Backbone curves, neimark-sacker boundaries and appearance of quasi-periodicity in nonlinear oscillators: application to 1:2 internal resonance and frequency combs in MEMS. *Meccanica*, 2021.

[102] A. Givois, C. Giraud-Audine, J.F. Deü, and O. Thomas. Experimental analysis of nonlinear resonances in piezoelectric plates with geometric nonlinearities. *Nonlinear Dynamics*, 102:1451–1462, 2020.

[103] K. Kim, A. G. Radu, X.Q. Wang, and M. P. Mignolet. Nonlinear reduced order modeling of isotropic and functionally graded plates. *International Journal of Non-Linear Mechanics*, 49:100 – 110, 2013.

ECOLE
DOCTORALE

Titre: Modèles d'ordre réduit pour les vibrations non linéaires géométriquesde structures minces

Mots clés: modèles à ordre réduit, non-linéarité géométrique, formes normales, mode normal non linéaire

Résumé: Lorsqu'elles vibrent avec de grandes amplitudes, les structures minces montrent un comportement non linéaire géométrique, provenant de la relation non linéaire entre les déformations et les déplacements. Les analyses des systèmes complets font appel à des calculs extrêmement couteux de telle sorte que l'établissement de modèles d'ordre réduit efficaces est un sujet d'intérêt majeur pour le calcul prédictif de vibrations de structures minces.

Dans cette thèse, des méthodes non linéaires de réduction de modèle pour les structures discrétisées par la méthode des éléments finis et comportant une non-linéarité géométrique, sont étudiées. Trois méthodes non intrusives sont plus particulièrement examinées et systématiquement comparées : la méthode de condensation implicite, la méthode des dérivées modales, et la réduction sur variétés invariantes du système. Les analyses théoriques montrent que les deux premières méthodes ne peuvent donner de résultats fiables que sous hypothèse d'une séparation spectrale entre les fréquences propres des modes maitres et celles des modes esclaves. La méthode de réduction sur variétés invariantes permet quant à elle d'avoir une méthode directe, ne nécessitant pas de pré-calculs, ni d'hypothèses préalables sur les fréquences propres des modes esclaves, afin de fournir des résultats corrects.

De nombreuses applications et de comparaisons numériques sont montrées sur diverses structures discrétisées avec la méthode des éléments finis. Pour appliquer la méthode des variétés invariantes, une méthode récemment développée, permet de proposer un calcul direct de la forme normale du problème, à partir de la base physique et donc des degrés de liberté du maillage éléments finis. Les exemples montrent clairement les avantage et inconvénients de chaque méthode, validant aussi les résultats théoriques montrés précédemment.

Dans la dernière partie de la thèse, la dynamique non linéaire d'un système présentant une relation de résonance interne 1:2 est analysée, en tenant compte des termes cubiques. La forme normale réelle du problème est d'abord établie. Ensuite les branches de solution du problème sont analysées et comparées avec celles du modèle plus simple négligeant la non-linéarité cubique. Le comportement divergent observé lorsqu'on réduit le problème à un seul mode et que l'on cherche à prédire le comportement raidissant ou assouplissant, est ensuite étudié avec ce modèle plus complet.

Title: Reduced-order models for geometrically nonlinear vibrations of thin structures

Keywords: reduced-order models, geometric nonlinearity, normal forms, nonlinear normal mode

Abstract: When vibrating with large amplitudes, thin structures experience geometric nonlinearity due to the nonlinear relationship between strains and displacements. Because full-order nonlinear analysis on geometrically nonlinear models are computationally very expensive, the derivation of efficient reduced-order models (ROMs) has always been a topic of interest.

In this thesis, nonlinear reduction methods for building ROMs with geometric nonlinearity in the framework of the Finite Element (FE) procedure, are investigated. Three non-intrusive nonlinear reduction methods are specifically investigated and systematically compared. They are: implicit condensation and expansion (ICE), modal derivatives (MD), and the reduction to invariant manifold. Theoretical analysis shows that the first two methods can give reliable results only if a slow/fast assumption between slave and master coordinates holds. On the other hand, reduction to invariant manifolds allows proposing a simulation-free reduction method that can be applied without restricting assumptions on the frequencies of the slave modes.

Numerical comparisons and numerous applications to continuous structures discretized with the FE procedure, are given subsequently. For application of the invariant manifold-based method, the computation is based on a direct application of the normal form to the physical space and hence to the nodes of the FE mesh, a method recently developed. The examples show the advantages and drawbacks of each reduction method when deriving ROM, and the results of the theoretical comparison are validated.

Finally, the analysis of the dynamics of a system with 1:2 internal resonance and cubic nonlinearity is given in the last part of the thesis. The real normal form of the problem is first derived. Then the solution branches of the problem are investigated and compared to simpler solutions with the dynamics truncated at order two. The divergent behaviour of the hardening/softening characteristics for single-mode reduction is investigated with this more complete model.

Institut Polytechnique de Paris
91120 Palaiseau, France